Magnetic zeolite for Cs^{+} and Sr^{2+} to clean up radioactively contaminated water from the Fukushima Daiichi Nuclear Power Plant

by

Azusa Ito

Supervisor: Dr Joseph A. Hriljac

A thesis submitted to the University of Birmingham for the degree of DOCTOR OF PHILOSOPHY

(Chapters 1 to 5 in the total 9 chapters)

The School of Chemistry
College of Engineering and Physical Sciences
University of Birmingham
8 April 2021

Abstract

Magnetic zeolite hybrid systems have been developed for decontaminating radioactive wastewater from the reactors at Fukushima Daiichi Nuclear Power Plant. Superparamagnetic Fe_3O_4 and $CoFe_2O_4$ (M_xO_y) nanoparticles were used to make core-shell M_xO_y/SiO_2/zeolite (MSZ) systems. The MSZ were synthesised by 3 steps; preparing M_xO_y particles by the sol-gel method firstly, the M_xO_y particles were coated by SiO_2 by the Stöber method, then the M_xO_y/SiO_2 particles were mixed with zeolite seeds of zeolite A, zeolite X or CHA-Na. In addition, M_xO_y/Chabazite-Na (CHA-Na) was synthesised by a one-pot synthesis using an autoclave by crystallising the nanoparticles on preformed zeolite particles.

The products were characterised by X-ray diffraction, Raman spectroscopy, transmission electron microscopy (TEM) and scanning electron microscopy. The elemental compositions of the cobalt ferrite, the M_xO_y/CHA-Na and the MSZ were characterised by X-ray fluorescence. The magnetic properties of all products were measured by a magnetic property measurement system or vibrating sample magnetometer. The M_xO_y particle diameters were calculated from the full width at half maximum of the X-ray peaks, observing by the TEM images, or measured by dynamic light scattering. The Cs or Sr adsorption capacities of the M_xO_y/CHA-Na and the MSZ were characterised by inductively coupled plasma mass spectrometry.

Acknowledgments

I would like to thank Dr Joseph Hriljac, under your supervision and great support I have developed as a researcher.

Thanks to all of the 5th floor research group members. It was very fun to do lab work with them, especially Josh and Mohammed. I really liked talking with you while studying and doing lab work. I would like to chat with you again someday.

Thanks to Dr Gnani, for helping me to measure my samples by TEM. I got great TEM-EDS images with your assistance. Thanks to Dr Mingee and Jake for measuring the magnetic properties of my samples by VSM and the MPMS. Thanks to Dr Christopher and Dr Norman for operating the ICP-MS to get the data of the Sr and Cs adsorption.

I would like to really thank Professor Toshihiko Onuki-San and Dr Tomoaki Kato-San for teaching me to prepare ICP samples properly so that I could get great data from them. Thanks to Dr Yukihiko Sato-San, for letting me use your SEM-EDS.

I would like to thank my parents for supporting my study in the UK and paying my tuition fee for 6 years.

This thesis was copy edited for conventions of language, spelling and grammar by Proofreading Birmingham.

Table of Contents

List of Figures

List of Tables

List of Equations

List of Abbreviations

Fukushima Daiichi Nuclear Power Plant (F1)

Simplified active water retrieve and recovery system (SARRY),

Advanced liquid processing system (ALPS).

Chabazite (CHA)

M_xO_y/zeolite (MZ, where M=Fe and CoFe),

M_xO_y/SiO_2/zeolite (MSZ).

Inductively coupled plasma mass spectrometry (ICP-MS)

Tetraethyl orthosilicate (TEOS)

X-ray diffraction (XRD)

X-ray fluorescence (XRF)

Dynamic light scattering (DLS)

Dichloromethane (DCM)

Magnetic property measurement system (MPMS)

Vibrating sample magnetometer (VSM)

Scanning electron microscopy (SEM)

Transmission electron microscope (TEM)

1 INTRODUCTION

1.1 Background

On 11 March 2011, a large tsunami (estimated at 14–15 m) hit the Fukushima Daiichi Nuclear Power Plant (F1), owned by the Tokyo Electric Power Company (TEPCO), in the aftermath of the Great East Japan Earthquake. F1 has six reactors facing the ocean (Units 1 to 6), and Units 4 to 6 were not operating at that time to allow routine checks. All electric power sources used to cool the nuclear fuels in Units 1 to 5 were swept away by the tsunami, leaving a single electric power source for Unit 6, and F1 went into a station blackout (SBO) situation. Following the SBO, nuclear fuels in the reactor pressure vessels and fuel pools in Units 1 to 4 were not cooled and dry-heating of the nuclear reactors occurred due to decay of the nuclear fuels. Units 1 to 3 melted down, and there was fuel debris in the bottom of the reactor containers. Within a few years, it has been planed this debris will be tried to take out from the reactor containers and studied by TEPCO and the Japan Atomic Energy Agency (JAEA). The cooling water in the pressure vessels evaporated and generated hydrogen gas. This increased pressure inside the vessels and attempts were made to release this by wetwell or drywell venting. However, the hydrogen gas remained inside the units, and then the hydrogen within Units 1, 3 and 4 exploded. It was thought that the hydrogen gas in Unit 3 leaked into Unit 4 through air release pipes. F1 is a boiling water reactor. Normally in Japan, Zr alloy cladding is used for fuel rods containing UO_2 pellets. Exothermal reactions occur with the H_2O surrounding the

rods and when the temperature inside the reactor pressure vessel is higher than 900 ºC [1] the following reaction occurs

$$Zr + 2H_2O \rightarrow ZrO_2 + 2H_2 + Heat$$

The hydrogen that was produced by the reaction permeated to the top of the pressure vessels in Units 1, 3 and 4. It reacted with oxygen rapidly after the hydrogen explosion limit in dry mixtures (4%) was exceeded [2], and finally, the hydrogen explosions occurred. Owing to the hydrogen explosions and the damage to the reactor containers due to the meltdown, radioactive nuclides were released into the air and the sea surrounding F1. In particular, a lot of ^{137}Cs, ^{134}Cs and ^{131}I contaminated a broad area, and a few towns around F1 are still difficult-to-return zones.[3, 4] A lot of seawater was pumped into the pressure vessels by fire trucks to cool the fuel rods. The seawater became radioactively contaminated and stored in tanks at the F1 site. Most of the contaminated water has been already filtered by three types of filtration systems: Kurion-Areva/Veolia, simplified active water retrieve and recovery system (SARRY), and advanced liquid processing system (ALPS). [5] ALPS has been mainly used to remove radioactive nuclides from the contaminated water because of the high removal efficiencies for ^{137}Cs, ^{134}Cs, ^{90}Sr, ^{60}Co, ^{125}Sb, ^{106}Ru, ^{129}I, ^{54}Mn and ^{99}Tc. In particular, ^{137}Cs, ^{134}Cs, ^{90}Sr are of most concern due to their long half-lives or the amounts released. The half-lives of ^{137}Cs, ^{134}Cs

and ^{90}Sr are 30, 2.1 and 29 years, respectively. ^{137}Cs and ^{134}Cs can be adsorbed in human bodies because of the similarity with K, and ^{90}Sr can be also adsorbed into bones and teeth because of the similarity with Ca.[6] ^{3}H cannot be removed by the filtration systems. The amount of water treated by ALPS alone was about 1.19×10^{6} m^3 (stored in 979 tanks), and about 860×10^{12} Bq (in 16 g) of ^{3}H has been stored, as of 12 March 2020.[7] However, diluted ^{3}H is less harmful for humans and the environment; therefore, the Japanese government has planned to discharge the diluted ^{3}H into the sea.

The filters of the filtration systems need to be replaced on a regular basis. The filters are not reusable, and the used filters also have to be stored at F1. Final disposal sites for the radioactive contaminated materials have not yet been determined, but the amount of radioactive contaminated waste stored at F1 has increased. To minimise the amount of contaminated material produced by the filtration of contaminated water, reusable filters should be developed and used.

1.2 Adsorption towers at F1

1.2.1 Kurion-Areva/Veolia

The Kurion-Areva/Veolia system was composed of three parts: the adsorption system (made by Kurion Inc., USA), the coprecipitation system (made by Areva/Veolia, France) and the reverse osmosis system (made by Hitachi, Japan). A schematic diagram of the whole system

is shown in Figure 1.1. The Kurion system worked as the first Cs pre-treatment stage. It consisted of three types of adsorption system: the surfactant-modified zeolite skid for removing oil and ^{99}Tc; the herschelite skid for removing ^{137}Cs and ^{134}Cs; and the silver-impregnated engineered herschelite skid for removing ^{129}I.[8] Herschelite is also called Na-chabazite, and it has a high Cs adsorption capacity. The Areva/Veolia system is also known as ActifloTM-Red. The ^{137}Cs and ^{134}Cs that could not be removed by the Kurion system were removed by nickel ferrocyanide, and Sr was also removed by precipitation with barium sulphate.[9] This Kurion-Areva/Veolia system produced a large amount of secondary waste in only three months of operation (in total 820 cm^3: 580 cm^3 was coprecipitated sludge and 240 cm^3 was used zeolite). Therefore, the coprecipitation system (the Areva/Veolia system) was removed, and only the Kurion system continued to operate.[5]

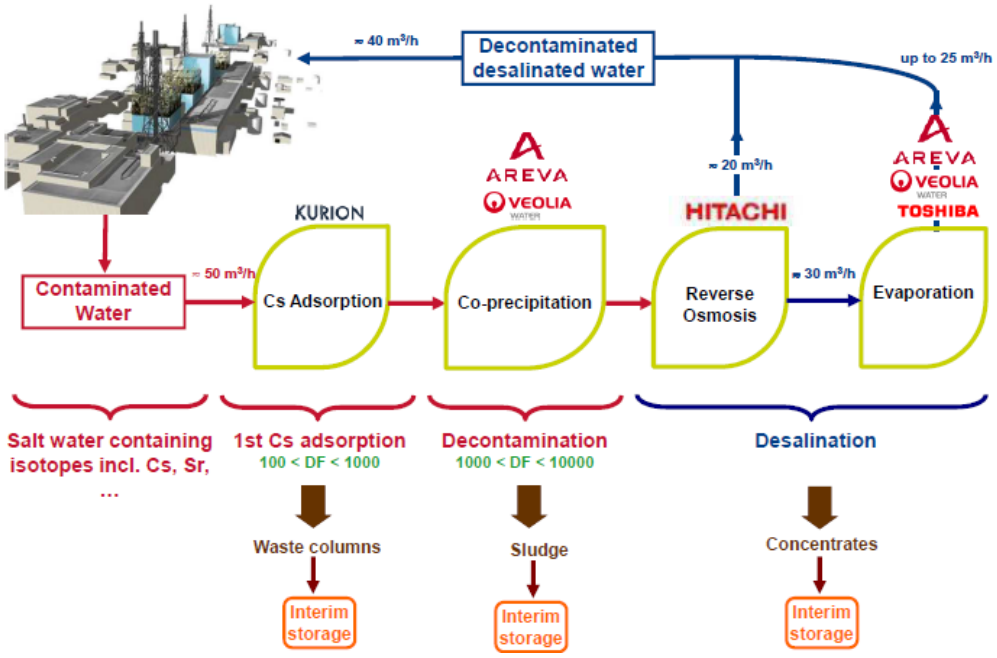

Figure 1.1 *Schematic diagram of the Kurion-Areva/Veolia system.[10] Where DF is a decontamination factor.*

1.1.1 Simplified active water retrieve recovery system (SARRY)

The simplified active water retrieve and recovery system (SARRY) was provided by Shaw, USA, Avantech Inc., USA, and Toshiba, Japan. SARRY is also designed to remove ^{137}Cs and ^{134}Cs, and it has been used in place of the Areva/Veolia system. SARRY is used with the Kurion system to back it up. IONSIV™ R9120 and IONSIV-96, which have already been well studied zeolite as Cs-exchangers, are used in the SARRY system. A schematic diagram of SARRY is shown in Figure 1.2. The total volume of treated wastewater was about 10 times higher than with the Kurion system, and the secondary waste volume was 2.5 times lower than that from the Kurion system.[8] The new SARRY system was introduced in July 2019 (SARRY II). The upgraded SARRY system can also remove ^{90}Sr.[11]

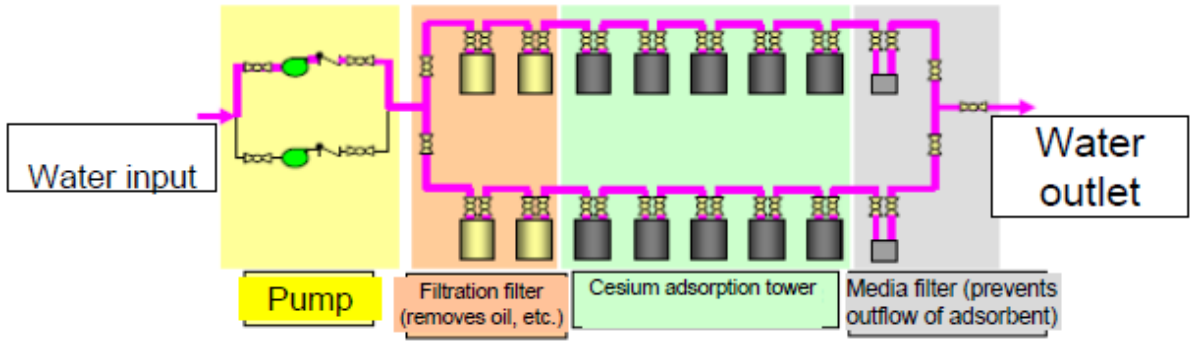

Figure 1.2 *Schematic diagram of SARRY.*[12]

1.1.2 Advanced liquid processing system (ALPS)

The Advanced Liquid Processing System (ALPS), designed by Energy Solutions, was provided by Energy Solutions, USA. The system mainly uses CsTreat®, which is a

hexacyanoferrite, and SrTreat®, which is a titanite, as sorbents, and these came from the Fortum company, Finland. The schematic diagram of ALPS is shown in Figure 1.3. ALPS mainly removes ^{90}Sr from the wastewater, but it can remove most radioactive nuclides generated in the nuclear reactors, excluding ^{3}H. This system first removes slurry using the iron coprecipitation facility and the carbonate precipitation facility, and radioactive nuclides are removed in adsorption towers. CsTreat® has higher Cs capacity than alternatives, such as mordenite and silicotitanate. CsTreat® has 60.2 m^3/kg Cs capacity and SrTreat® has 45.9 m^3/kg Sr capacity if they are used in a 1 m^3 vessel.[13]

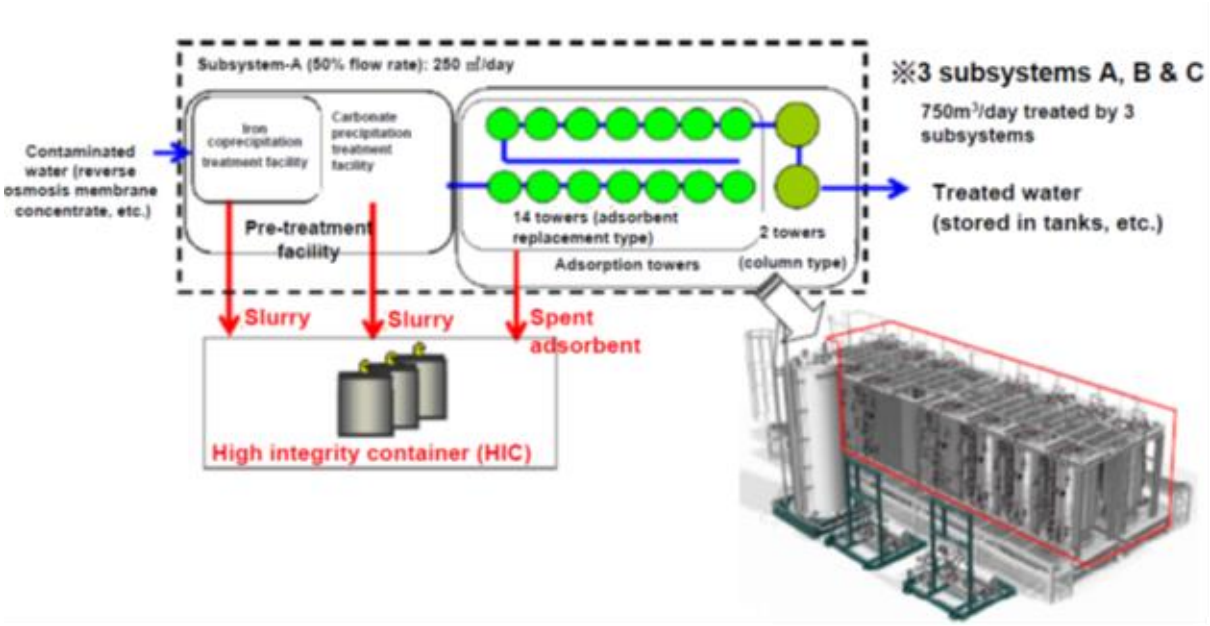

Figure 1.3 *Schematic diagram of ALPS.*[12]

1.2 Zeolite

Zeolites are described as a mineral group, and there are over 60 natural zeolites and over 150 synthesised zeolites.[14] They are widely used as adsorbents for the purification of

gases, as catalysts and as ion exchangers.[15] Some zeolites have been used for removing low- and medium-level radionuclides because of their high abundance and low cost. In particular, zeolites having a low Si:Al ratio are suitable as cation exchangers because of their high exchange capacity. Furthermore, zeolites are regenerative by exchanging a concentrated salt solution with the radionuclides.[16] A zeolite is an inorganic ion exchanger and has a three-dimensional aluminosilicate framework crystal structure: tetrahedral AlO_2 and SiO_2 are linked by oxygen atoms, the substitution of Si^{4+} by Al^{3+} creates net negative charge, and the negative charge of the zeolite framework is neutralised by the presence of exchangeable cations, such as Na^+ and K^+; that is, the cations can be replaced by other cations. Furthermore, a zeolite has high ion exchange capacity, and thermal, mechanical and radiation stability.[17] The cations are located in tiny pores within the tetrahedral frameworks. The ratio of $[AlO_4]^{5-}$ and $[SiO_4]^{4-}$ and the charge densities are changeable in the same stractual framework, for example, both zeolite X and zeolite Y has the same faujasite-type framework and diffrent $Si:Al^-$ ratios.[18] The size of a cation that can enter and stay in the pore depends on the pore size, and the diameter of the pore size ranges from a few Å (angstrom) to a few tens of Å.

1.2.1 Chabazite (CHA)

Chabazites are usually found with dominant cation species of Ca, Na and K, occasionally with Sr and Mg and rarely with Ba. [19] A typical formula of a chabazite is given by

$$(Ca_{0.5}, Na, K)_4[Al_4Si_8O_{24}] \cdot 12H_2O$$

Figures 1.4 and 1.5 shows the crystal structure of typical chabazite. It has six exchangeable cation sites (C1, C2, C3, C4, C4P and C4S). Na^+ and K^+ cannot occupy the C1 sites; however, some C1 sites can be occupied by Sr^{2+}. Cations that have a high electron density can occupy C2 and C3 sites. Many cations can be accepted into the C4 sites due to the charge unbalance of the oxygen sites O2 and O4, and the C4 to oxygen distances. C4P and C4S are near the C4 sites (they are not illustrated in Figure 1.4) and K^+ and Na^+ can occupy C4P and C4S sites partially in only the K and Na form of chabazite.[20]

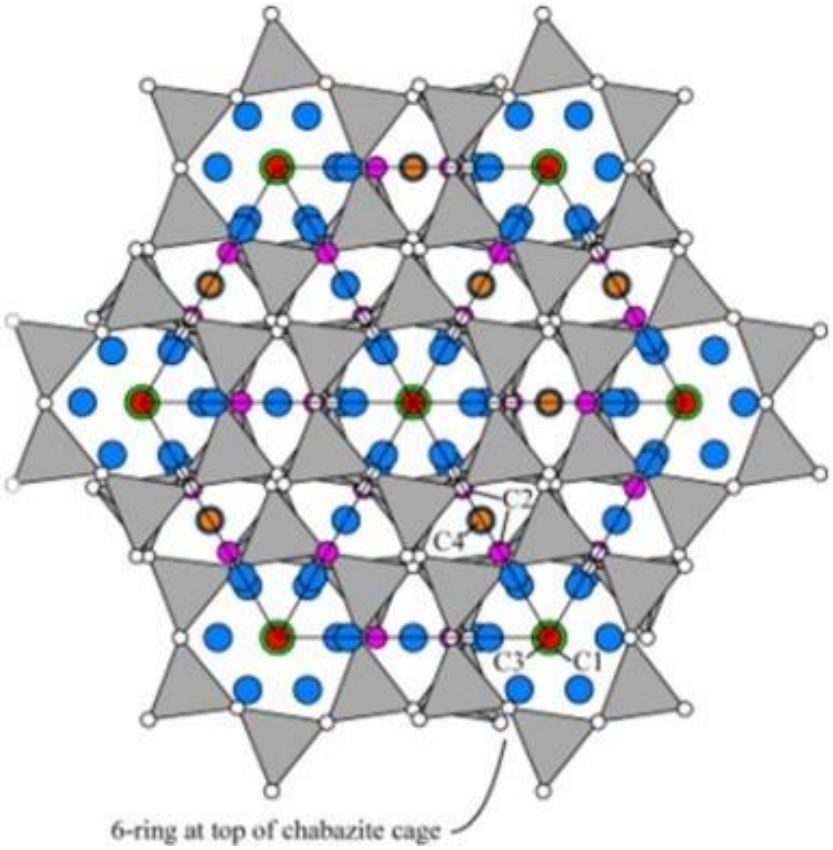

Figure 1.4 *Chabazite framework.[21] Blue circles are water site positions which 6 water sites exist at the 8-ring window.*

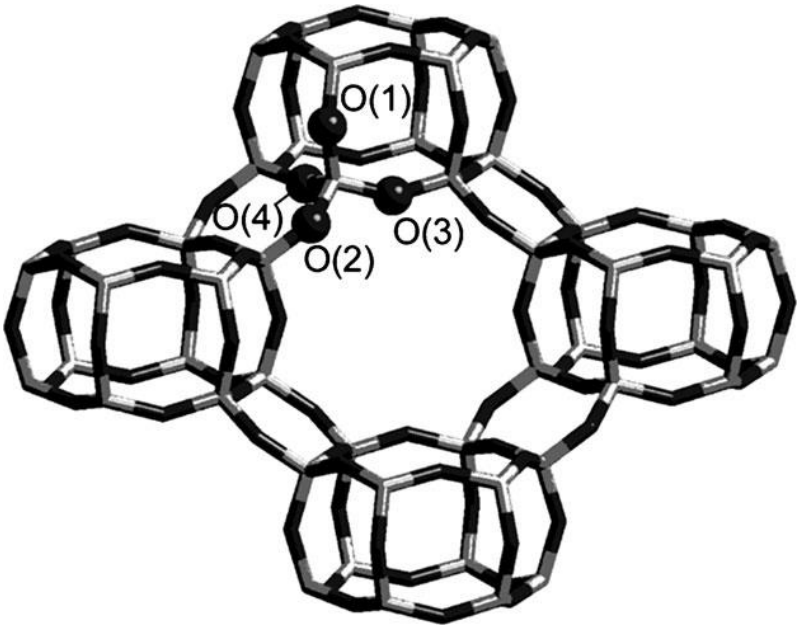

Figure 1.5 *Chabazite framework with oxygen sites.[22]*

Other cations can be introduced by cation exchange. Baek et al. (2018)[23] investigated the cation selectivity of chabazite by cation exchange and found the order of cation selectivity of chabazite was Cs>Na>Li>Sr>K>Rb.[23] The result is due to the chabazite pore aperture of 3.8 × 3.8 Å, and these cation sizes are shown in Figure 1.6. Baek's results showed that chabazite can also take up Sr^{2+}; however, water site 5 in Sr-chabazite does not appear, and the occupation of ions in the other sites is different to that in other types of chabazite.[20]

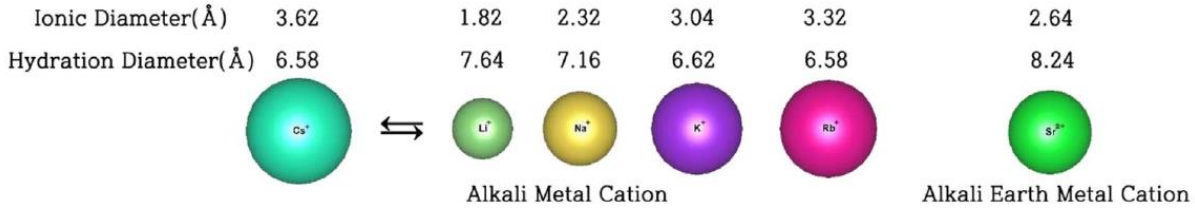

Figure 1.6 *Cation size for cation exchanged chabazite. From left, the cations are Cs^+, Li^+, Na^+, K^+, Rb^+ and Sr^{2+}.[23]*

1.2.2 Zeolite A

$$Na_{12}[(AlO_2)_{12}(SiO_2)_{12}] \cdot 27H_2O$$

Zeolite A (Linde type A) is synthesised in the Na form and has a cubic crystal structure. It has two types of big cage: the α cage (11 Å) and the β cage (~7 Å) (Figure 1.7), and the pore size is around 2 μm.[17] The Si:Al ratio of zeolite A is ~2.[24] This ratio is smaller than for chabazite. Zeolite A can absorb a lot of water in the α cage, while on the other hand, the

chabazite's cage can absorb less water. The zeolitic water in the cages might affect the cation selectivity of the zeolites. Hydrous Sr^{2+} can easily enter the α cage uniformly due to the cage size, and some Na^{+} in zeolite A can be replaced by Cs^{+}.[25] Therefore, the cation selectivity of zeolite A is $Sr^{2+}>Cs^{+}>Na^{+}$, which can be confirmed from these cation's negative free energy values on zeolite A, as Sr^{2+} has a larger negative free energy than the other cations, and the higher value signifies a higher affinity to zeolite A.[26]

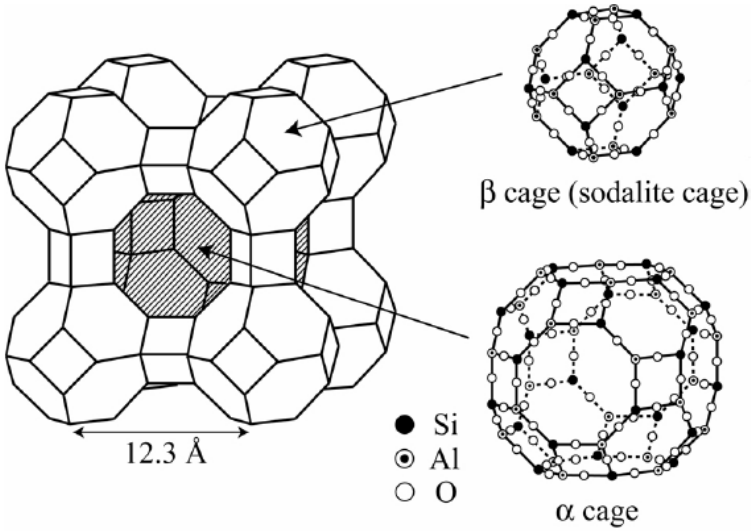

Figure 1.7 *Crystal structure of zeolite A.*[27]

1.2.3 Zeolite X

$$Na_{86}[AlO_2]_{12}(SiO_2)_{12}] \cdot 27H_2O$$

Zeolite X (Linde type X) has the same crystal framework as zeolite Y and it is called the FAU-type (Figure 1.8). The Si:Al ratio of zeolite X is ~1.5. Cations can stay the pores I, I',

II, II', III, III' (S6R and D6R). Kim et al. (2014)[28] studied whether Cs^+ and Sr^{2+} can be accomondated in dehydrated zeolite X pores and found that many Sr^{2+} cations entered site II, while sites I', III and III' did not have any Sr^{2+}. Site III had only Cs^+, and there was no Cs^+ in site I; however, zeolite X had more Sr^{2+} than Cs^+ in total. The supercage sizes relate to the cation selectivity. Some sites are too small or big for Cs^+ and Sr^{2+}, and smaller cations have a higher ionic charge than bigger ones. The supercages prefer the smaller and more highly charged cations, and they can make bonds with the oxygen in the framework more closely, while on the other hand, Cs^+ is too large and insufficiently charged to stay in the pores.

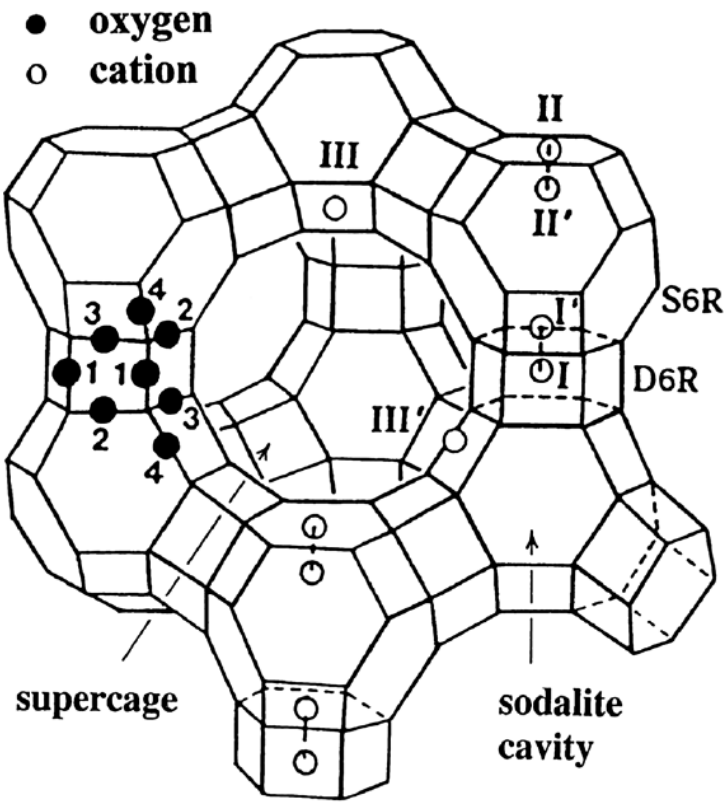

Figure 1.8 *Crystal structure of zeolite X.*[28]

1.3 Magnetic zeolite

Magnetic zeolites have magnetic particles at the cores, such as iron oxides, cobalt ferrite, and nickel ferrite, so they can be strongly attracted by an external magnetic field. The magnetic zeolites have been studied for their ability to remove heavy metals from contaminated water,[29] extracting Cd and drugs form urine samples,[30, 31] and removing organic dye.[32] The zeolite adsorbs target ions and chemicals, and the magnetic particles allow it to be controlled by the external magnetic field. Therefore, a suitable zeolite can be chosen for the magnetic zeolites depending on the target ions and chemicals.

The volume of used zeolite, which is from the adsorption towes, has been increased at the F1 site scince the systems were started operating, and it has not been decided where the used zeolite will be finally disposed yet as well. The magnetic zeolite could be a candidate to reduce the total volume of contaminated wastes at the site by reusing it: the fist step is collcting the radioactive Cs^+ or Sr^{2+} by exchanging with Na^+ on to the magnetic zeolite, the second step is collecting the zeolite by an external magnetic field and exchanging the collected Cs^+ or Sr^{2+} with Na^+ from it in a different batch to condence the Cs^+ or Sr^{2+}, such as evapolating the solution, and finally, the Na^+ exchanged magnetic zeolite is reused for the filteration.The spteps might be repeated many times until the magnetic zeolite does not work for the adsorptions, or loosing the superparamagnetic chracteristic.

1.4 Aim of study

In this study, reusable magnetic zeolites are studied as adsorbents to remove ^{137}Cs, ^{134}Cs and ^{90}Sr from radioactive contaminated water. Two types of magnetic zeolites were studied: one is M_xO_y/zeolite (MZ, where M=Fe and CoFe), and the other is M_xO_y/SiO_2/zeolite (MSZ). The reason why the SiO_2 latyer of the MSZ was adapted is, it could protect the M_xO_y particles from an acidic degradation and not to release Co into the environment directly. Superparamagnetic magnetite (Fe_3O_4) or cobalt ferrite ($Co_{0.3}Fe_{2.7}O_4$ or $Co_{1.1}Fe_{1.9}O_4$) are used as the core of the MZ and MSZ. Na-chabazite that can adsorb Cs was used for MZ and MSZ, and zeolite A and zeolite X that can adsorb Sr were used for MSZ. The cation exchange efficiencies of the two types of adsorbents were compared by Inductively coupled plasma mass spectrometry (ICP-MS) measurements, whether SiO_2 can prevent not to damage the magnetic metal oxides, and which MZ and/or MSZ sample is suitable for the decontamination of radioactive wastewater.

2 EXPERMENTAL DETAILS

2.1 Synthesis

To synthesise the M_xO_y and the M_xO_y/K form of chabazite (CHA-K), the sol-gel method was used, and the SiO_2 coating of the M_xO_y was made using the Stöber method.

2.1.1 Sol-gel method

This method is called the sol-gel method due to its reliance on the transition of a liquid "sol" into a solid "gel" phase. The starting sol is typically an inorganic metal salt or organic compound, and a colloidal suspension or a sol is formed by the sol-gel process involving hydrolysis or polymerisation reactions.[33] For the M_xO_y synthesis, oxygen needs to be supplied by water or organic solvents, such as alcohols. This involves the hydrolysis reaction and when an organic solvent is used, the reaction is called the "nonaqueous sol-gel route".[34] The sol-gel route is also called "solvent controlled synthesis", and the typical synthesis temperature range is normally 50 to 200 ºC.[35] The advantages of this route are that there are fewer organic impurities in the synthesised M_xO_y, the organic solvents are nontoxic, the production of M_xO_y is simpler and more stable, and the organic solvents can access the M_xO_y surface efficiently. However, the disadvantages are the tendency to produce inhomogeneous crystals (in terms of their size and shape), that the particles easily form agglomerates and are less re-dispersible.[36] Because the M_xO_y forms using the oxygen provided from the organic solvents, the solvent acts as a capping agent; therefore, the M_xO_y morphology and agglomeration are affected.[37]

However, the particle size can be controlled by adjusting the synthesis temperature and the ratio of the precursors and organic solvents.

2.1.2 Stöber method

The size controlled uniform spherical SiO_2 particle synthesis method was introduced by Stöber et al. in 1967.[38] The particle was synthesised using tetraethyl orthosilicate (TEOS) as a silica source, ammonium hydroxide as a catalyst to form the spherical particles, and an ethanol-water medium for the hydrolysis reaction of TEOS. M_xO_y particles can be directly coated by SiO_2 with the seeded polymerisation technique of the Stöber method, in which the M_xO_y is added in the SiO_2 reaction by controlling the ionic strength of the media through adjusting the ratio of water and ethanol, and the amounts of TEOS and the catalyst.[39] Furthermore, adjusting the pH of the reaction media using the catalyst, the synthesis temperature and duration, and the reaction method (sonication or agitation) can affect the SiO_2 morphology of the M_xO_y/SiO_2 synthesised.[40-42]

2.2 X-ray diffraction (XRD)

X-ray diffraction (XRD) is used to identify crystal structures of a powder or single crystalline samples. XRD techniques follow Bragg's law.

$$n\lambda = 2d_{hkl}\sin\theta_{hkl}$$

Equation 2-1 *Bragg's equation.*[14]

where n is an integer that refers to the order of reflection, λ is the wavelength of the X-ray, hkl are the Miller indices, d_{hkl} is the perpendicular spacing between the adjacent lattice plains of crystals, and the Bragg angle, θ_{hkl}, is the incident angle (Figure 2.1).

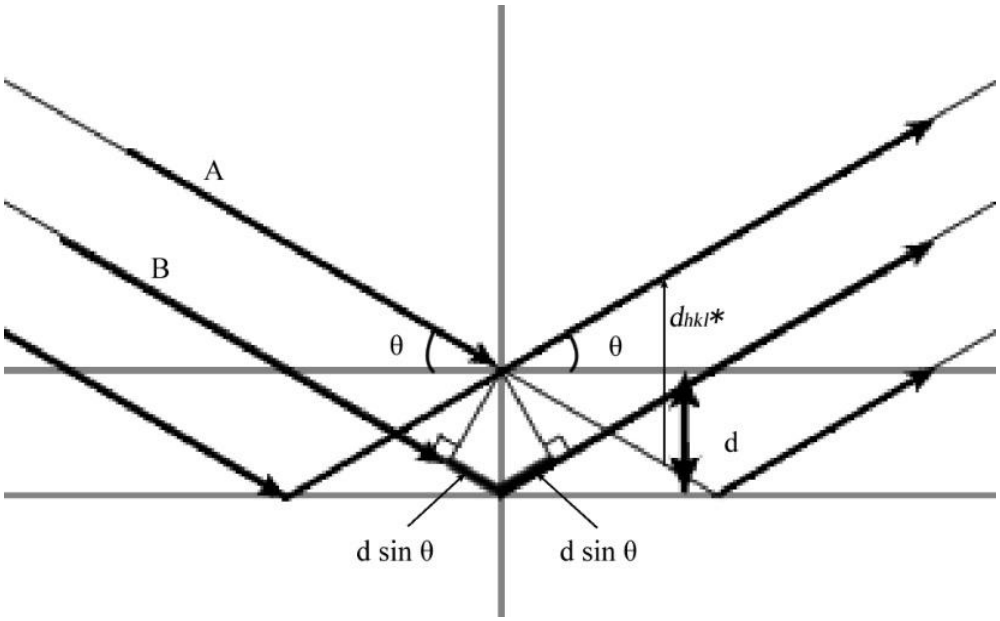

Figure 2.1 *Reflections of x-rays on lattice planes.*

When X-ray photons hit the lattice planes, the photons are diffracted and the incident angle is the same as the angle of reflection. The X-ray scattering is called Bragg scattering, and when it occurs, the X-ray path difference between beam A and beam B is 2d sinθ. The relationship between the d-spacing and Miller indices (hkl) is described by the equations in

Table 2.1. The value of d_{hkl} can be obtained from the diffraction peak positions, which can be used to determine the lattice systems. There are seven types of lattice system depending on the dimensions of the unit cell vectors and angles. The equations for calculating d-spacings (d_{hkl}) of triclinic, monoclinic and rhombohedral are more difficult than the other equations, because they have no 90º angles in their unit cells.

Table 2.1 *Seven lattice systems and the relationship with d-spacings.[14] a, b and c are unit cell edge lengths, and α, β and γ are intersection angles between them.*

System	d-spacing	Unit cell	
Triclinic		a ≠ b ≠ c	(α ≠ β ≠ γ ≠ 90º)
Monoclinic	$\frac{1}{d^2} = \frac{1}{\sin^2\beta}\left(\frac{h^2}{a^2} + \frac{k^2\sin^2\beta}{b^2} + \frac{l^2}{c^2} - \frac{2hl\cos\beta}{ac}\right)$	a ≠ b ≠ c	(α = γ = 90º, β ≠ 90º)
Orthorhombic	$\frac{1}{d^2} = \frac{h^2}{a^2} + \frac{k^2}{b^2} + \frac{l^2}{c^2}$	a ≠ b ≠ c	(α = β = γ = 90º)
Tetragonal	$\frac{1}{d^2} = \frac{h^2+k^2}{a^2} + \frac{l^2}{c^2}$	a = b ≠ c	(α = β = γ = 90º)
Rhombohedral		a = b = c	(α = β = γ ≠ 90º)
Hexagonal	$\frac{1}{d^2} = \frac{4}{3}\left(\frac{h^2 + hk + k^2}{a^2}\right) + \frac{l^2}{c^2}$	a = b ≠ c	(α = β = 90º, γ = 120 º)
Cubic	$\frac{1}{d^2} = \frac{h^2+k^2+l^2}{a^2}$	a = b = c	(α = β = γ = 90º)

The diffraction peaks give not only d_{hkl} values, but also other information about the measured crystals, such as a crystal particle size from the full width at half maximum (FWHM) of the peaks, and the residual strain in the crystals from the peak position and the width. The crystal particle size can be obtained by Scherrer's equation.[43]

$$t = \frac{0.9\lambda}{B_{1/2} cos\theta_B}$$

Equation 2-2 *Scherrer's equation.*

where t is the diameter of crystallites (in Å), $B_{1/2}$ is the FWHM, θ_B is the peak position of observed maximum and λ is described by Bragg's law.

Corundum diffraction patterns are commonly used to subtract the instrumental broadening factor to calculate the crystal particle size using Equation 2-2. It consists of α-Al_2O_3, which has only a few peaks and no strain broadening on XRD, and there are only a few peak overlaps with unknown sample peaks.[44, 45]

A schematic diagram of an X-ray diffractometer is shown in Figure 2.2. X-ray beams are emitted from the X-ray tube, the beams hit and reflect from the sample on the sample holder, and the reflected beams are detected by the position sensitive detector, that can obtain the diffraction data by the simultaneous acquisition within the 2θ detector range.[46]

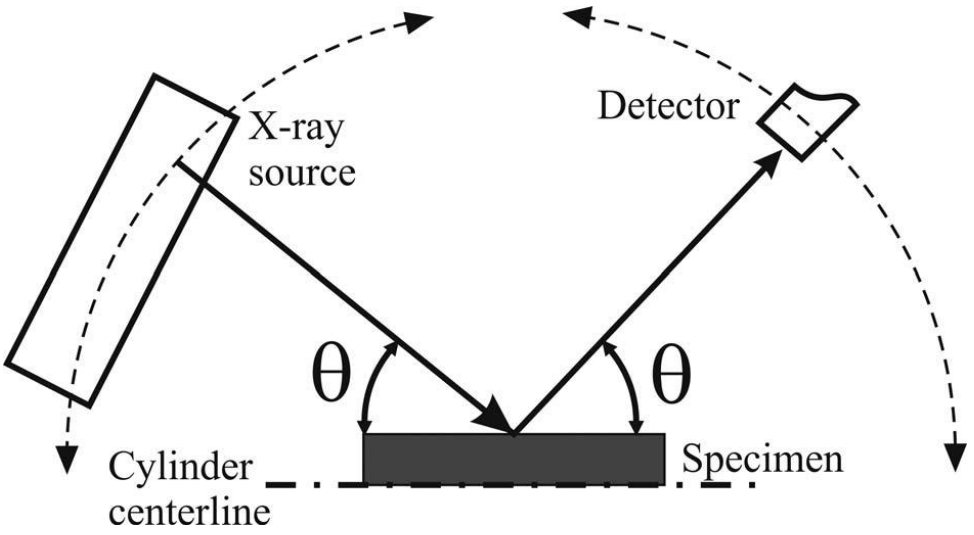

Figure 2.2 *XRD diffractometer image.*[47]

In the vacuum X-ray tube, a tungsten filament (cathode) emits electrons, which are accelerated by high voltage. The accelerated electrons hit the target (anode) that consists of tungsten and other materials, such as Cr, Fe, Co, Cu, Mo and Ag. The materials for the target are selected depending on what materials are intended to be in the measurement sample. Normally, the K_α radiation of the target material is used in XRD as characteristic X-rays, because the K_α radiation energy is higher than that of other radiation, such as K_β or L_α, and photons are emitted as X-rays when electrons are excited and return to their original K orbits. However, if the measurement material receives the same energy as the excitation and return of electrons, the electrons of the measurement material can move from the K to L orbits efficiently, and photoelectric absorption occurs. By this process, fluorescence occurs due to electron transitions to fill the inner shells in the measurement sample. The fluorescence is a

characteristic X-ray and emitted in all directions from the measurement sample; therefore, the background of the XRD measurement is high in this situation.

For, this study, a powder X-ray diffraction (PXRD) instrument (D2, Bruker) with an X-ray tube with a Co source (K_α = 1.80 Å) was used because the measurement samples contain Fe (K_α = 1.94 Å), and the machine has a PSD detector. Co K_α energy (6.924 keV) is lower than Fe K-edge energy (7.112 keV). Fe does not emit fluorescence under this condition.

2.3 X-ray fluorescence

X-ray fluorescence (XRF) spectroscopy is one of the techniques used to analyse elemental compositions of materials. As already mentioned in the XRD technique description, inner shell electrons of a measurement material are excited when higher energy X-rays hit the sample, electrons from higher energy orbital shells fill the vacancies of the excited electrons, and a specific energy X-ray fluorescence is emitted by the transition. The X-ray is generated in the X-ray tube; the cathode filament is normally Cr, Mo, Rh, Pd, W, Au, Ag, or Co and the X-ray is emitted from the Be window towards the sample being measured. In particular, a Rh anode is widely used because the high energy allows good detection of both major and trace elements in geological samples; however, Cr is used for the detection of major elements, and other anodes are used for the efficient detection of trace elements.[48]

XRF can measure solid, powder and liquid samples. There are three ways to measure powder samples: using a disposable cup with a polyester film, such as Mylar®; making a pressed pellet with a wax; and making a fused glass bead. However, the Mylar® film can be damaged by some acids and bases, such as NaOH solution. The accuracy of XRF determination is fused glass bead > pressed pellet > disposable cup.

For this study, an S8 Tiger (Bruker) was used with the disposable cup and pressed pellet methods, and Rh was used for the X-ray source.

2.4 Raman spectroscopy

Raman spectroscopy is commonly used to identify molecular or crystal structures of a target sample by shining a red (633 nm) or green (532 nm) laser onto the sample and observing the Raman scattering by molecular vibrations, rotational or electronic energy changes of the crystal.[49] The range of incident light for Raman spectroscopy is between 244 nm (ultraviolet) and 1064 nm (infrared ray). When the incident light hits the target sample, the molecular dipole moments of the sample vibrate, or the crystal rotational or electronic energy change, and this causes three types of scattering from the sample: Rayleigh, Raman anti-Stokes and Raman Stokes scattering. Raman spectroscopy uses Raman anti-Stokes and Stokes scattering in which photons are scattered from the target sample by the vibrational energy level difference between the laser excitation frequency (υ_0, the incident light and Rayleigh scattering) and the

molecule's vibrational frequency (v_{ex}); each molecule has a different oscillation frequency (Figure 2.3).

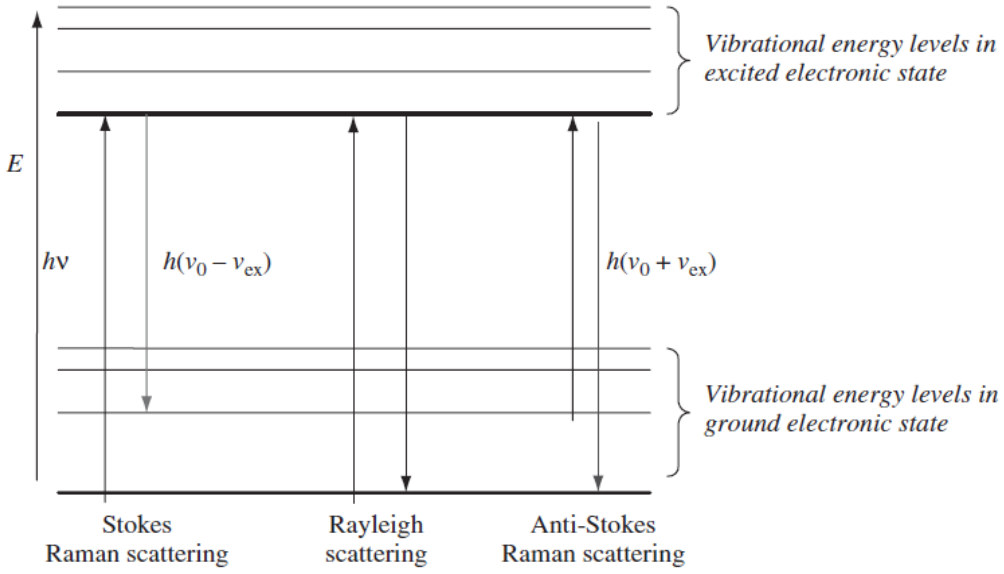

Figure 2.3 *Raman scattering and Rayleigh scattering.*[50]

Raman scattering is caused by the polarisability of the target sample that can be changed by the molecular vibration, and it changes the amplitude of the dipole moment oscillation. The Raman scattering at low frequency is Raman Stokes, and the other at high frequency is Raman anti-Stokes.[51] The scattered photon intensity of Raman scattering (10^{-6}) is far smaller than the intensity of Rayleigh scattering (10^{-3}); therefore, a strong incident light is needed to get strong Raman scattering. Raman scattering can also measure molecules with no dipole moment, such as H_2, N_2 and O_2, that IR spectroscopy cannot measure because IR spectroscopy uses the

incident IR frequency and the molecular dipole moment, so that the specific oscillating IR frequency matches a specific molecular vibration frequency.[51]

The Raman peaks identify the chemical bonding and substances present through their positions; the crystal nature from the peak widths (a wide peak means crystallinity is low and a narrow peak means crystallinity is high); lattice strains by the shifting of peak positions from the original peak positions (if the peaks shift to shorter wavelengths, the crystal lattice is tensile, and if the peaks shift to longer wavelengths, it is compressed); and concentrations of the substance from the intensity of the peaks (if the intensity of peaks is high, the concentration is also high).

2.5 Dynamic light scattering (DLS)

Dynamic light scattering (DLS) measures Brownian motion, in which colloidal particles move randomly and fluctuate with the molecules of the solvent medium. Larger particles move slowly and smaller particles move rapidly in the solution. The particle movements are affected by the solution viscosity and temperature.[52] When a laser hits the particles, the incident laser light is scattered in all directions. The scattered light intensity relates to the particle fluctuations: the intensity of larger particles fluctuates slowly, and the intensity of smaller particles fluctuates rapidly.

DLS can also measure the zeta potential of the particles in the solution medium. The zeta potential is also called electrokinetic potential. Particles are negatively charged at their surfaces in the medium, and there are the positive charges on the negatively charged surface, which is the interfacial double layer. On the double layer, there is the diffuse layer where the ions are loosely bonded and some of the ions move with the particle. This boundary is called a slipping plane.[53] The zeta potential is the voltage of the slipping plane, which is measured in an electric field by applying a voltage to the solution medium that has particles dispersed from negative to positive electrodes. The charged particles are attracted towards the positive electrode by electrophoresis, and the velocity of the particles is proportional to the zeta potential.[54] DLS measures the zeta potential using electrophoresis and laser Doppler velocimetry, which measures the particle's velocity towards the positive electrode.[53] The relationship between the suspension stability of particles and the zeta potential values is shown in Table 2.2. The particles are more dispersed in the solution medium when the zeta potential is bigger. In contrast, the particles tend to aggregate in the medium when the value is smaller.

Table 2.2 *The relationship between suspension stability and zeta potential.*[55]

Stability characteristics	Average zeta potential in mV
Maximum agglomeration and precipitation	0 to +3
Range of strong agglomeration and precipitation	+5 to -5
Threshold of agglomeration	-10 to -15
Threshold of delicate dispersion	-16 to -30
Moderate stability	-31 to -40
Fairly good stability	-41 to -60
Very good stability	-61 to -80
Extremely good stability	-80 to -100

A Zetasizer Nano ZS (Malvern Instruments Ltd.) was used to measure the particle sizes and zeta potentials. Mixtures of ethanol and deionised water (DI water), ethanol and dichloromethane (DCM), or ethanol, DCM and 1-hexanol were used as the solution medium to disperse the particles. The solution temperature was set at 20 to 25 ºC, and the measurement duration was changed depending on the dispersibility of the particles.

2.6 Magnetic property measurement system (MPMS) and vibrating sample magnetometer (VSM)

The basic system of the magnetic property measurement system (MPMS) is almost the same as that of the vibrating sample magnetometer (VSM), in which a rod attached to a magnetic sample is vibrated at selected frequencies in a direct charge (DC) electric field. On the magnetic poles there are detection coils that read the DC induced by electromotive forces

from the changing magnetic flux through the coils, and the flux is proportional to the magnetic moments of the magnetic sample. The MPMS has a superconducting quantum interference device (SQUID) that uses the Josephson junction effect, in which a very thin insulator is sandwiched between two superconductors and Cooper electron pairs can pass through the sandwich junction without any resistance.[56] The SQUID is able to detect very low magnetisms (up to 3×10^{-18} T), and the noise levels also very low.[57] Therefore, the MPMS is suitable for measuring very weak magnetic materials or nanosize superparamagnetic materials. However, the SQUID commonly uses polycrystalline niobium for the Josephson junction electrodes, and it works at liquid helium temperatures.[58] Therefore, the SQUID needs to be cooled down to 4K by liquid helium to maintain superconductivity, and the cost of one measurement is much more than the cost of using VSM, which can be cooled by water. MPMS and VSM can also easily measure the magnetic sample at different temperatures using liquid helium, and the magnetisation behaviours of the magnetic sample under the zero-field-cooled/field-cooled (ZFC/FC) conditions can be observed by changing the temperature while measuring.

For the magnetic sample measurements, a MPMS XL-5 (Quantum Design North America) and MPMS 3 (Quantum Design North America) were used. Using the MPMS XL-5, a magnetic sample was put in a gelatine capsule, with Teflon tape used to ensure the samples were not moved by the magnetisation during the measurement, and the capsule was put in a middle of straw (the position is a little bit the upper side of the straw). Using the MPMS 3, the

magnetic sample was put in VSM powder sample holders supplied by Quantum Design, and the sample was compressed by the two holders to prevent movement. Both types of sample holders were attached to a rod to place it into the machine. The measurements were made by Dr Mingee Chung (University of Birmingham) and Jake Head (University of Birmingham).

2.7 Scanning electron microscopy-energy dispersive X-ray (SEM-EDX) spectroscopy

Micro- and nanoscale structures can be observed in digital images using scanning electron microscopy (SEM). Normally, an optical microscope can magnify only up to 1,000× because it uses visible light. On the other hand, SEM scans a focused electron beam that is able to measure the sample's surface roughness. When the electron beam hits the sample's surface, characteristic X-rays are emitted from the sample. The energy dispersive X-ray (EDX) spectroscope, which is attached to the SEM, detects the X-rays and provides elemental composition results, as with XRF. The schematic diagram of SEM-EDX is shown in Figure 2.4. The electron beam is generated in the electron gun by an accelerated voltage, which depends on the sample type (typically 2 to 30 kV). The electron beam is controlled using the

apertures to adjust the number and angle of the electrons, the adjusted electron beam is focused by the objective lens, and finally the focused beam hits the sample surface.[59]

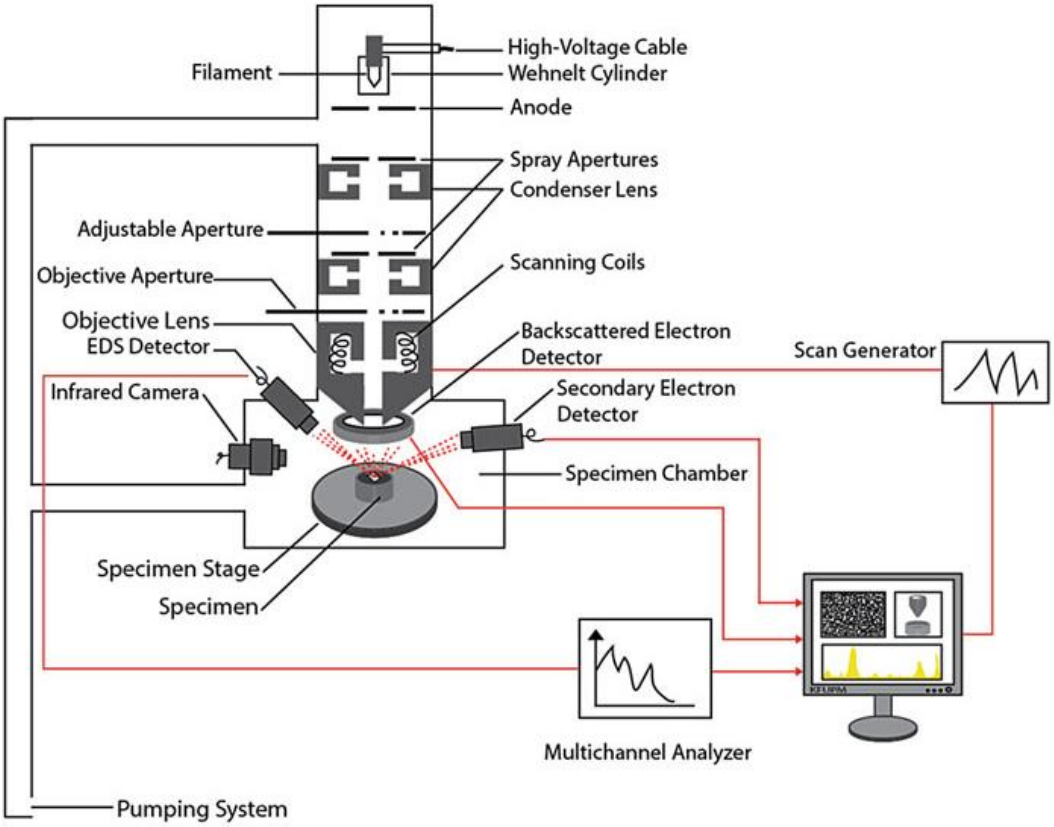

Figure 2.4 *Schematic diagram of SEM-EDX.*[59]

For the SEM-EDX measurements, a JSM-7800F (JEOL) at the Japan Atomic Energy Agency in Japan and a TM4000Plus (Hitachi High-Tech Corporation) were used. The accelerated voltage range of the JSM-7800F is 0.01 to 30 kV, the maximum resolution is 0.8 nm at 15 kV, and the magnification range is 25× to 1,000,000×. The accelerated voltage range of the TM4000Plus is 5 to 15 kV, the maximum resolution is 80 mm (diameter) and 50 mm (thickness), and the magnification range is 25× to 250,000×.

2.8 Transmission electron microscope (TEM)

Smaller scale structures that are not detectable by SEM can be measured by the transmission electron microscope (TEM) in which an electron beam is transmitted through the sample to obtain crystal structure images of the interior of the sample. The TEM is mainly composed of the electron gun, the objective, diffraction, intermediate and projector lenses, the viewing screen, and the photographic film (Figure 2.5). The system needs a higher voltage than the SEM to emit the electron beam and for the vacuum system to accelerate the electrons. In addition, due to the large electric currents, it needs to be cooled by liquid nitrogen. The accelerated voltage range is typically between 60 and 300 kV, the maximum magnification is more than 50,000,000× and the maximum resolution is <50 pm; however, the sample thickness needs to be <150 nm to allow transmission of the electron beam.[60]

To observe nanoparticle diameters, a FEI Talos F200 (Thermo Fissure Scientific) was used. The total beam current was >50 nA, the probe current was 1.5 nA at 1nm probe (200 kV), and the EDX information limit was 0.12 nm. The TEM measurements in this thesis were done by Dr Gnanavel Thirunavukkarasu.

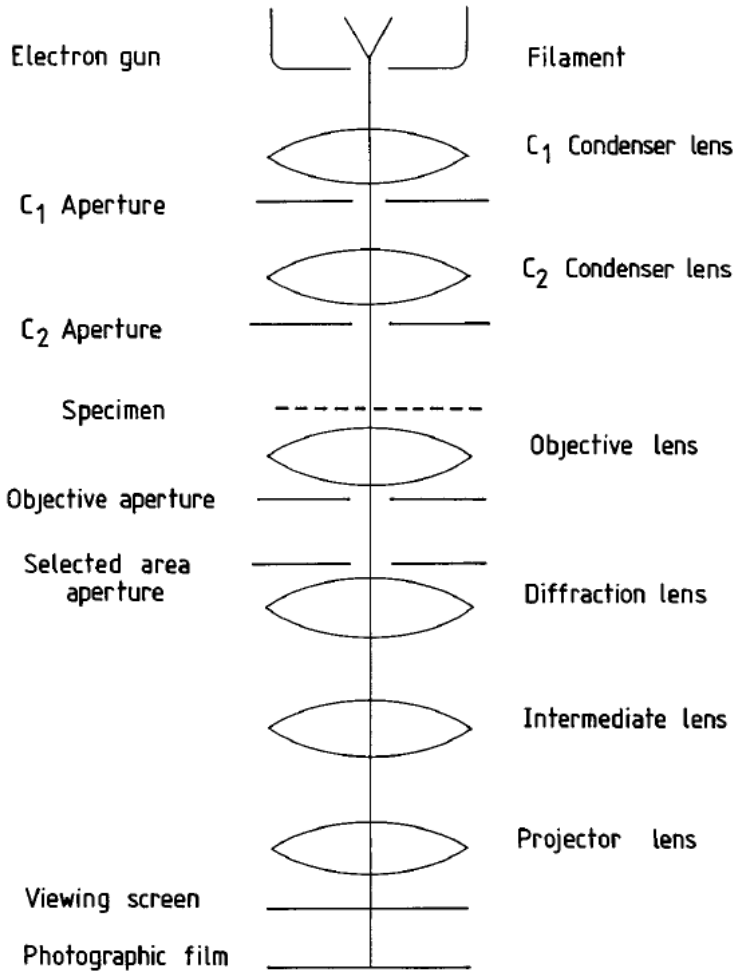

Figure 2.5 *Schematic diagram of TEM.*[61]

2.9 Inductively coupled plasma-mass spectrometry (ICP-MS)

Inductively coupled plasma mass spectrometry (ICP-MS) can detect smaller concentration trace metals than iinductively coupled plasma-atomic emission spectroscopy (ICP-AES) and the limit is > 1 ng/L (ppt) (depending on the elements). The basic system of ICP-MS is the same as that of ICP-AES. The atomic or ionic spectrum enables the measurement of trace metals in a liquid sample. ICP-AES can detect trace metals present in

concentrations of the order of mg/L (ppm). It uses an Argon plasma to decompose and ionise the sample. The atoms in the sample are excited by the impact of high energy electrons in the plasma, and the excited atoms emit a specific intensity of light at specific wavelengths, until they move to lower or ground states. ICP-AES identifies the atoms from the specific wavelengths of light, and determines the atomic concentrations from the specific intensity of light.[62] To make the ICP-AES measurement, the argon plasma is ignited by the radio frequency with aerosol water. After the plasma stabilises for 30 min, the liquid sample is pumped as a mist through the spray chamber. Atoms in the aerosol are excited and they emit light. Finally, the light is detected in the spectrometer to identify the atoms in the sample and their concentrations (Figure 2.6).

The calibration curve method and internal standard method are commonly used to minimise background noise, physical interference and ionisation interference errors. However, the standard solutions need to be of high purity and, for the internal standard, the wavelengths associated with the standard solution must not be the same as the expected measurement sample wavelengths.

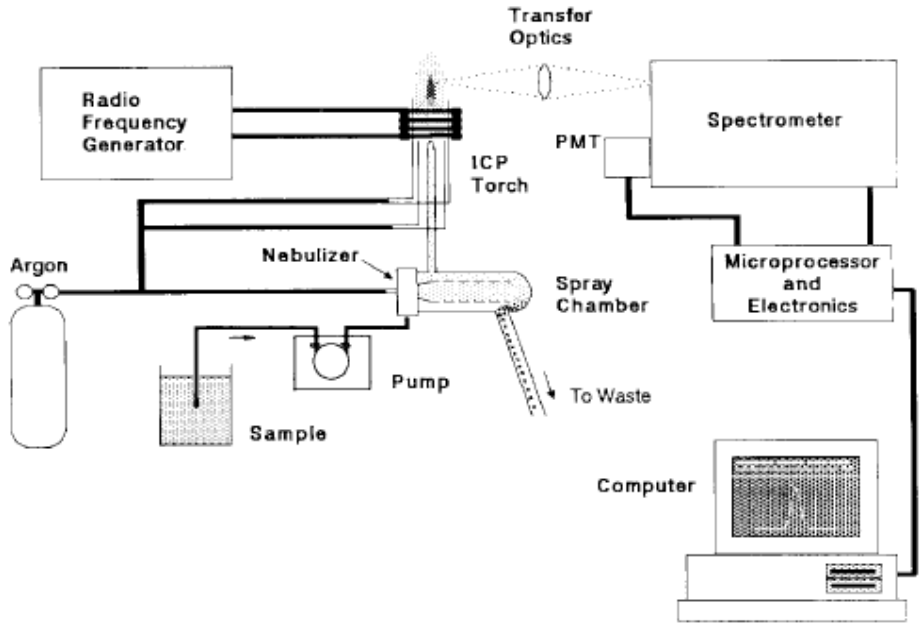

Figure 2.6 *Schematic diagram of ICP-AES.[62] Where PMT is photomultiplier tube.*

Figure 2.7 is a schematic diagram of ICP-MS. Most parts of the ICP-MS are the same as those of the ICP-AES, excluding the detection method. The sample aerosol that goes through the spray chamber is ionised in the argon plasma, and the produced ionised samples pass through the sampler and the skimmer cone in the interface region under a vacuum (1 to 2 torr). The sample is focused into an ion beam by the electrostatic lenses (ion optics), and finally, the ion beam enters the mass separation device (mass spectrometer) under the turbo-molecular pumps, and the ions are converted into an electrical signal.[63] The external standard for the ICP-MS measurement normally uses two standard solutions that have similar mass and ionisation potentials to the atoms expected to be in the sample.[64]

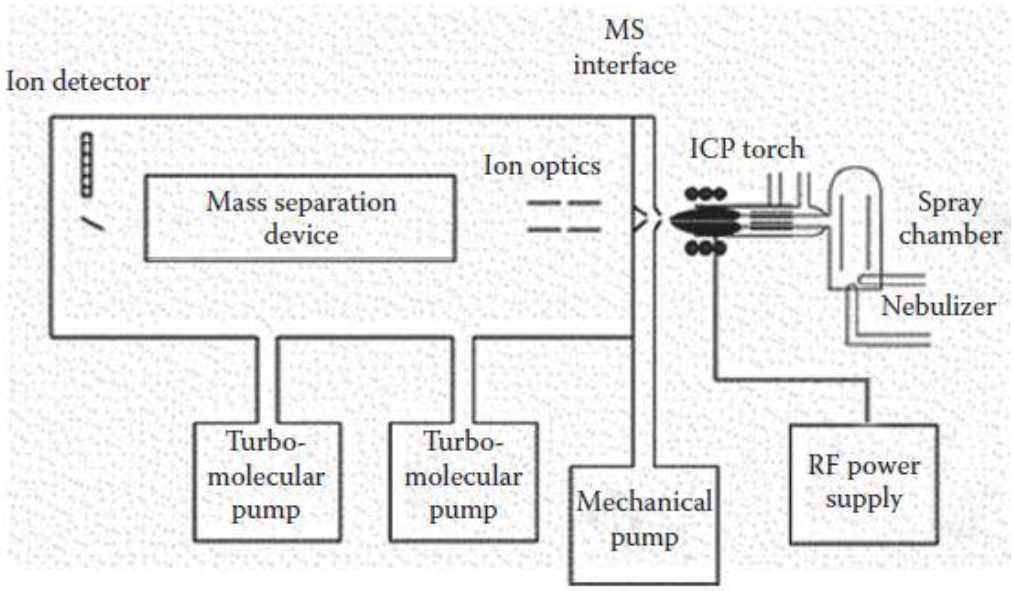

Figure 2.7 *Schematic diagram of ICP-MS.[63] Where RF is radio frequency and MS is mass spectrometry.*

For Cs or Sr detections in cation exchanged solutions, a NexION^{TM} 300X (Perkin Elmer) was used.

2.10 Langmuir adsorption isotherm

The adsorption isotherm model was proposed by Langmuir (1918). It is supposed that gas or vapour molecules theoretically occupy adsorption sites that are unoccupied equivalently by desorption.[65] The adsorption rate onto the adsorption sites is proportional to the gas or vapour pressures at a certain temperature.[66] The isotherm model can be used to determine adsorption capacities of molecules in liquid into solid materials, and it can be calculated by the following equation.

$$qe = \frac{Q_{max} \times Kl \times Ce}{1 + Kl \times Ce}$$

Equation 2-3 *Langmuir adsorption isotherm model equation*

where *qe* is the mass of adsorbed molecules at equilibrium (mg/g), *Ce* is the mass of molecules in the solute at equilibrium (mg/L) Q_{max} is the maximum adsorption capacity of the molecules (mg/g) and *Kl* is the Langmuir constant (L/mg).

2.11 Freundlich adsorption isotherm

The Freundlich adsorption isotherm model is frequently used with the Langmuir model. This model does not consider any limitations, such as an adsorption maximum. Therefore, it cannot be used with a homogeneous adsorbent that the Langmuir model can fit. In contrast, the Freundlich model can be applied to a heterogeneous adsorbent, such as one with a rough surface. The adsorption isotherm can be obtained from the following equation.

$$qe = (K_f \times Ce)^{\frac{1}{n}}$$

Equation 2-4 *Freundlich adsorption isotherm model equation*

where *qe* is the mass of adsorbed molecules at equilibrium (mg/g), *Ce* is the mass of molecules in the solute at equilibrium (mg/L), and K_f and *n* are fitting constants.[67]

3 MANGNETIC NANOPARTICLES (M_xO_y)

3.1 Introduction

3.1.1 Fe_3O_4

Iron (hydroxy)oxides are well known chemical compounds of which there are 16 types, and they are composed of Fe with O and/or OH.[68] In particular, magnetite (Fe_3O_4) and haematite (α-Fe_2O_3) are widely available minerals and have magnetic properties. α-Fe_2O_3 forms a close packed hexagonal structure ($R\bar{3}c$), and the particle colour is black to red. It is completely oxidized. Therefore, the magnetic property is antiferromagnetic or weakly ferromagnetic at room temperature. Fe_3O_4 forms a close packed cubic structure (*Fd3m*) that is composed of both Fe^{2+} and Fe^{3+}. Fe^{2+} occupies the half of the octahedral sites and Fe^{3+} sits in both octahedral and tetrahedral sites evenly in the cubic close packed array. Fe_3O_4 becomes ferrimagnetic with a Curie temperature of 858 K due to the changes in the electron spins of Fe^{2+} and Fe^{3+}.[69] It has a black to dark brown colour and an inverse spinel structure. Normally it is ferrimagnetic, but it is superparamagnetic when the particles are nanosize. When Fe_3O_4 is oxidized and changes its structural form, it becomes maghemite (γ-Fe_2O_3) and α-Fe_2O_3. γ-Fe_2O_3 also forms a close packed cubic structure ($P4_332$) or a tetragonal structure ($P4_12_12$), and the particle colour is brown. It also has ferrimagnetic characteristics, and is strongly attracted by an external magnetic field, such as Fe_3O_4. Fe_3O_4 easily becomes γ-Fe_2O_3 by heating to a high temperature or exposure to a laser; therefore, Fe_3O_4 is not a stable state.

The magnetic characteristics of Fe_3O_4 depend on the particle size. Figure 3.1 shows the relationship between the coercivity and the magnetic domain orientations for Fe_3O_4. Multi-directional (MD) magnetizing occurs when the particle size of Fe_3O_4 > 80 nm, the single domain (SD) region is in the range 10 nm < Fe_3O_4 < 80 nm, and the superparamagnetic (SP) region is < 15-20 nm. Superparamagnetism occurs when the domains of nanosized particles flip in random directions. With an applied external magnetic field, the domains orient in the same direction, and the domain direction follows only the magnetic field; therefore, it does not have coercivity. It is considered nanosized particles in the SP region work even in zeolite. They could help to collect and redisperse the zeolite for the cation exchange process after the radioactive contaminated water treatment.

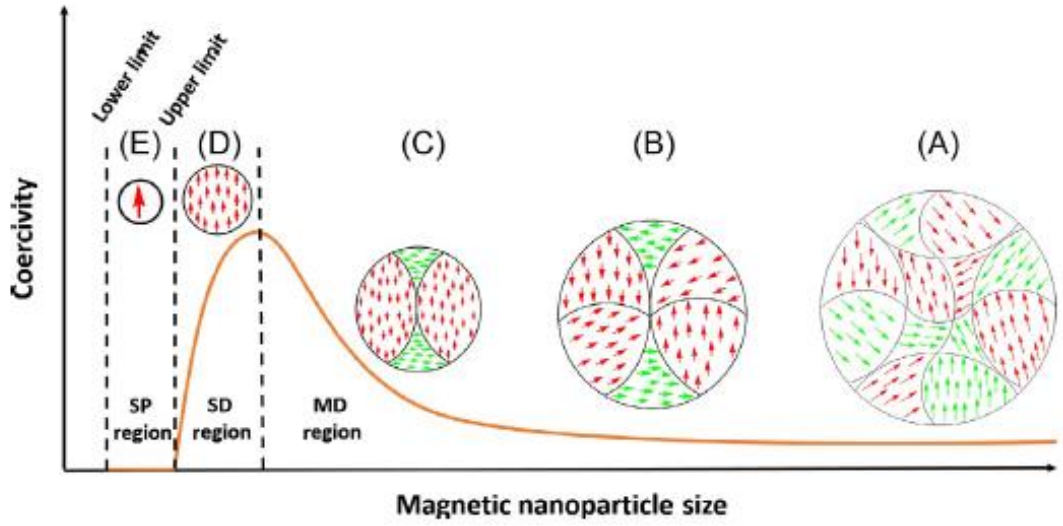

Figure 3.1 *Fe_3O_4 particle size vs the holding force.*[70]

Where A to C are the Fe_3O_4 sizes are more than 80 nm, D is 10 nm < Fe_3O_4< 80 nm, and E is less than 15 to 20 nm.

Nanosized Fe_3O_4 has been combined with other chemicals and materials, such as activated carbon and zeolites, to get the benefits of its magnetic characteristics. Fe_3O_4 works as a magnetic core of the materials used as adsorbents, and it is possible to collect the adsorbents using an external magnetic field[29, 71]. Nanosized Fe_3O_4 can be synthesized easily; for example, through the sol-gel, aqueous nanofluid, coprecipitation and solvothermal methods[72-74].

In this study, nanosized Fe_3O_4 was synthesised by the sol-gel method for magnetic zeolite adsorbents, and the synthesis method for producing pure Fe_3O_4. The particle size and magnetic properties were also studied to choose the best Fe_3O_4 samples for the further syntheses.

3.1.2 $CoFe_2O_4$

Cobalt ferrite ($CoFe_2O_4$) has a cubic closed packed structure in which oxygen occupies one third of the tetrahedral and two thirds of the octahedral sites, Co^{2+} occupies only the octahedral sites and Fe^{3+} occupies both the tetrahedral and octahedral sites equally.[75] It has high magnetocrystalline anisotropy, and it also has superparamagnetic characteristics when the particle diameter is nanosize. However, it cannot be further oxidized, which means that $CoFe_2O_4$ is much more stable than Fe_3O_4.

$CoFe_2O_4$ theoretically has an inverse spinel structure that was calculated as Section 3.2.9. However, it is reported that $CoFe_2O_4$ has partially inverse spinel structures, and its maximum magnetisation changes depending on the Co^{2+} locations in the octahedral and tetrahedral sites.[76] $CoFe_2O_4$ has also been widely used by coating it with zeolite to remove pollutants and radioactive elements from contaminated water by using the strong superparamagnetic characteristics and stability.[77, 78]

In this study, cobalt ferrite was synthesised in almost the same way as Fe_3O_4, but using different precursors, synthesis time and temperature. The elemental compositions of the synthesised cobalt ferrite samples were also characterised to determine the chemical formula. The magnetic and thermal stability were compared with Fe_3O_4 to decide which was suitable for the MSZ and MZ.

3.2 Experimental details

3.2.1 Fe_3O_4

This recipe was made with reference to the work of Pinna et al. (2005).[72] The synthesis preparation before heating was carried out in an argon gas glovebox (O_2 level was ≤ 40 ppm). Between 1.0 and 2.0 g of iron (III) acetylacetonate [$Fe(acac)_3$, ≥ 99.9 %, Sigma Aldrich] as a precursor, and 5.0 to 40.0 ml of benzyl alcohol (99.8 %, Sigma Aldrich) or 1-hexanol (≥99 %, Sigma Aldrich) as a reactant were put in a 45 ml Teflon liner. The ratio of the precursor and the

reactants is shown in Table 3.1. The reagents were put in a glass inner only when the final product was Fe_3O_4, and 5.0 ml of 1-hexanol was filled between the inner and the liner to prevent the overflow of reagents from the inner. The liner was put in an autoclave, and it was heated at various temperatures and for various times by a conventional oven (Table 3.1). The products were washed with ethanol (Fisher Scientific) and dichloromethane (Sigma Aldrich) and centrifuged at 11000 rpm for 10 min three times to collect the final product. Finally, it was dried at 60 ºC for the further synthesis of the Fe_3O_4/SiO_2 and characterisations.

3.2.2 Cobalt ferrite

Most of the synthesis procedure for cobalt ferrite was the same as the Fe_3O_4 recipe, but the precursors and the synthesis temperature were adjusted. For the cobalt ferrite synthesis, 1.70 g of $Fe(acac)_3$, 0.62 g of cobalt (II) acetylacetonate [$Co(acac)_2$, ≥ 99.0 %, Sigma Aldrich] (The mol ratio of $Fe(acac)_3$ and $Co(acac)_2$ was 2:1), and 20.0 ml of 1-hexanol were put in the 45 ml Teflon liner in the glovebox. This was then heated at 180 ºC for various times. The synthesis details are shown in Table 3.3.

3.2.3 Oven temperature

The actual temperature of the conventional oven was measured by a digital needle probe thermometer through the ventilation hole. It was found to be 5.0 to 12.5 ºC higher than the set

temperature; for example, it was 180 to 187.5 C when the temperature control was set at 175 C. It could be thought the actual temperature range for the product synthesis conditions was between +5 to 12.5 C of the set temperature.

3.2.4 X-ray diffraction (XRD)

A PXRD instrument (D2, Bruker) with an X-ray tube with a Co source (K_α = 1.80 Å) was used to obtain Fe_3O_4 and cobalt ferrite XRD patterns. The powder samples were stuck on a Si low background sample holder with Vaseline grease as there was not enough product for a normal sample holder, and to avoid contaminating the machine with the nanoparticles. The patterns that were measured between 20º and 88º showed that Fe_3O_4 and cobalt ferrite have broad XRD peaks, and the total number of steps was 4192.

3.2.5 X-ray fluorescence (XRF)

The Co and Fe ratio in the synthesised cobalt ferrite was characterised by the XRF instrument (S8 Tiger, Bruker) with the Rh anode. The nanoparticles were put in a powder sample cup with Mylar® film. The XRF energy peaks of Co (K_β-line) and Fe (K_α-line) were used to calculate the ratio to avoid overlaps of the elemental energy peaks.

3.2.6 Raman spectroscopy

A Raman spectrometer (inVia, Renishaw) was used to identify whether the iron oxides were Fe_3O_4 or γ-Fe_2O_3 using a 532 nm green laser (Samba 100, Cobalt). Cobalt ferrite was also measured in the same way to characterise the Raman peak positions. The laser hit the samples at 1 % of the maximum power for 10 seconds with cosmic ray removal. The Raman shifts from 200 to 1200 cm^{-1} were due to the main peak positions of Fe_3O_4 and cobalt ferrite.

3.2.7 Dynamic light scattering (DLS)

Synthesised Fe_3O_4 and cobalt ferrite particle sizes and zeta potentials were measured with a Zetasizer Nano ZS (Malvern Instruments Ltd.). The particles were dispersed in DI water, ethanol, a mixture of ethanol and DCM, or a mixture of ethanol, DCM and 1-hexanol at 25 ºC. The mixtures were diluted by ethanol to prevent the DCM damaging the polystyrene sample cuvettes used for the DLS measurements. The solvents have different viscosities: water (0.8914 Pa·s) < ethanol (1.0995 Pa·s) < 1-hexanol (4.477 Pa·s) at 25 °C (Sastry and Valand, 1996; Khattab et al., 2012). The nanoparticles tend to be well dispersed in higher viscosity solutions. Each measurement was repeated three times to see dispersibilities of the nanoparticles.

3.2.8 Magnetic property measurement system (MPMS)

The magnetic characteristics of the synthesised Fe_3O_4 were measured using a MPMS XL-5 (Quantum Design) and those of cobalt ferrite were measured by a MPMS 3 (Quantum Design North America) at 5 and 300K. The magnetisation curves were obtained from -50 to 50 kOe. The ZFC/FC curves were also measured to see how the magnetic behaviours depended on the temperatures, which were changed using liquid nitrogen. The MPMS work was carried out by Dr Mingee Chung (University of Birmingham) and his PhD student Jake Head (University of Birmingham).

3.2.9 Determination of (inverse) spinel structure

Spinel ferrite typically has excellent electromagnetic properties, such as ferrimagnetic ordering.[79] It has the formula AB_2O_4, and the crystal structure is Fd-3m (cubic). Mostly $A=A^{2+}$ (tetrahedral sites) and $B=B^{3+}$ (octahedral sites). The spinel structure, shown in Figure 3.2, has cations in the octahedral and tetrahedral sites in the oxygen sublattice. The oxygen occupies one eighth of the tetrahedral and one half of the octahedral sites; however, the inverse spinel ferrite structure has divalent cations that are in the octahedral sites and iron cations that occupy the tetrahedral and octahedral sites equally.[80]

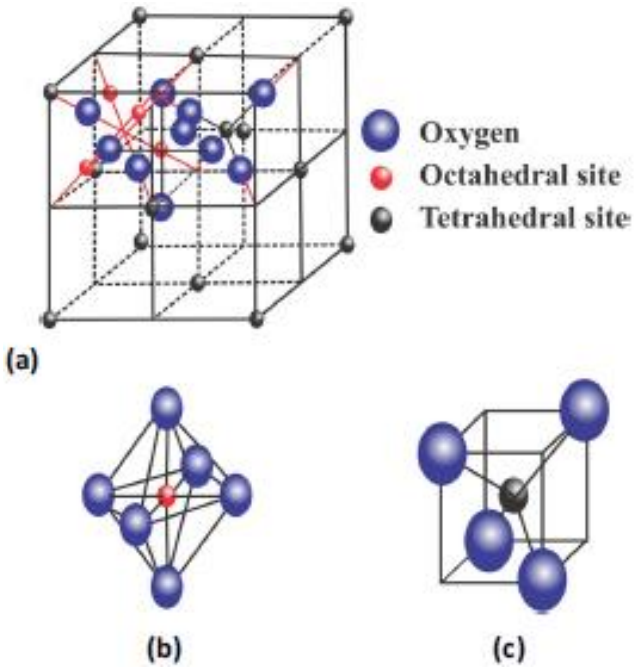

Figure 3.2 *(a) Spinel structure image. (b) Octahedral site. (c) Tetrahedral site.*[80]

The ligand field stabilisation energy (LFSE) of the octahedral and tetrahedral sites of the ferrite samples are used to determine whether it has a spinel structure. The LFSE can be calculated as follows.

For the octahedral site,

$$2(E_0 + A) + 3(E_0 - B) = 5E_0$$

Equation 3-1 *LFSE calculation formula for the octahedral site*

where *A* and *B* are the energy difference of e_g orbit and t_{2g} orbit and E_0 is the average energy before splitting.

$$A + B = \Delta_O$$

where Δ_O is octahedral ligand field splitting parameter. When A and B are plugged into the first equation

$$A = 0.6\Delta_O$$

$$B = 0.4\Delta_O$$

$$\Delta_O = -0.4t_{2g} + 0.6e_g$$

Therefore, e_g is $+0.6\Delta_O$ from E_0 and t_{2g} is $-0.4\Delta_O$ from E_0 (Figure 3.3). Electrons of a complex fill from the low energy field.

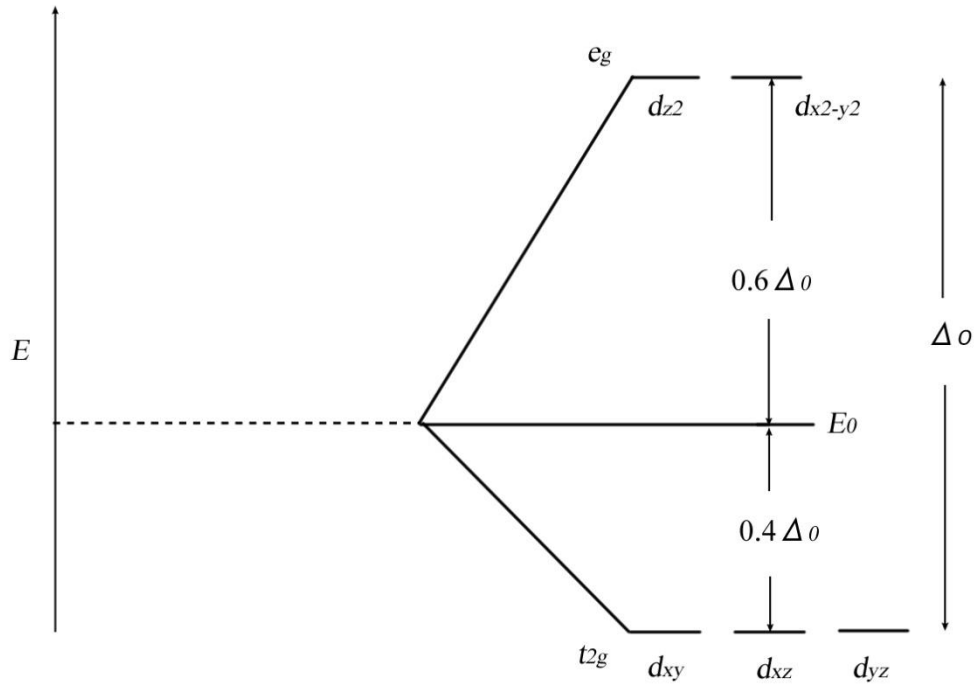

Figure 3.3 *Octahedral crystal field splitting*

For the tetrahedral site, t_2 orbit is higher energy, and e orbit is lower energy due to the tetrahedral structure (Figure 3.4): therefore, Δ_T (tetrahedral ligand field splitting parameter) is < Δ_O.

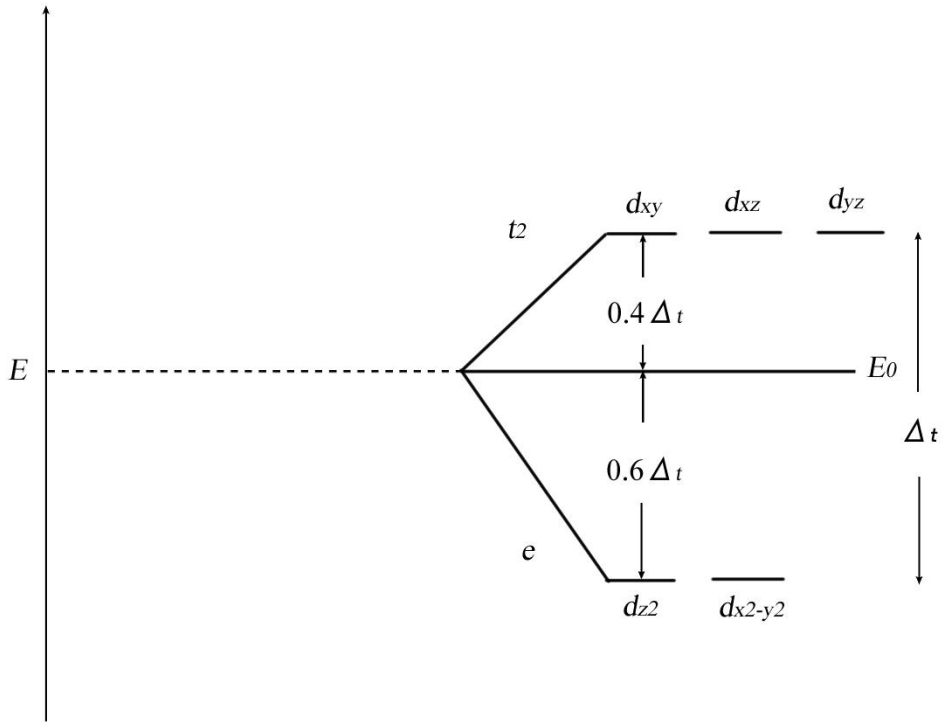

Figure 3.4 *Tetrahedral crystal field splitting*

The LFSE is also called crystal field stabilisation energy (CFSE), and the geometric preferences of d^n having metal ions depends on the tetrahedral and octahedral d^n energy level state. High-spin d^n favours octahedral site rather than low-spin d^n. The energy difference can be calculated by CFSE (octahedral) – CFSE (tetrahedral), which the difference is called the octahedral site preference (or stabilization) energy (OSSE), and d^3 and d^8 have the smallest OSSE (-0.845) that is the most favourable in the octahedral site.[81]

The LFSE of Fe_2O_3, Fe_3O_4 and $CoFe_2O_4$ can then be determined as follows.

The Fe^{3+} of Fe_2O_3 is a d^6 complex, therefore,

$$\Delta_O = -0.4 \times + 0.6 \times 2 = -0.4$$

$$\Delta_T = 0.4 \times 3 - 0.6 \times 3 = -0.6$$

Fe_2O_3 is a normal spinel structure, and Fe^{3+} ions fill the octahedral sites.

The Fe^{2+} of Fe_3O_4 is a d^5 complex, therefore,

$$\Delta_O = -0.4 \times 3 + 0.6 \times 2 = 0$$

$$\Delta_T = 0$$

Fe_3O_4 is an inverse spinel structure.

Co^{2+} of $CoFe_2O_4$ is d^7 complex, so

$$\Delta_O = -0.4 \times 5 + 0.6 \times 2 = -0.8$$

$$\Delta_T = 0.4 \times 3 - 0.6 \times 4 = -1.2$$

Fe^{+3} has $\Delta_O = \Delta_T = 0$

The OSSE of Co^{2+} is $\Delta_T - \Delta_O = -1.2 + 0.8 = -0.4$. |It is larger than d^3 and d^8. The Co^{2+} forms tetrahedral complex having bulky ligands, or ligand falls in the electrochemical series.[81]

3.3 Results

3.3.1 Vapour pressure and synthesis temperature

Three types of iron oxides were synthesised depending on the synthesis temperatures and the ratios of reagents. These were Fe_3O_4, a mixture of α-Fe_2O_3 and γ-Fe_2O_3, and α-Fe_2O_3. The synthesis details of the final products are shown in Table 3.1. When benzyl alcohol was used as the reactant, all final products were a mixture of α-Fe_2O_3 and γ-Fe_2O_3, even when different ratios of the reactant and $Fe(acac)_3$ were tried at various temperatures and for various times. However, when 1-hexanol was used as the reactant, the final products were not always α-Fe_2O_3 and γ-Fe_2O_3. When the synthesis temperature was 175 ºC and the synthesis time was between 5 and 7 hr, Fe_3O_4 was synthesised. γ-Fe_2O_3 was also synthesised when the synthesis time was between 4.5 and 13 hr. The difference in the final products when the synthesis time was between 5 and 7 hr depended on how the conventional oven was used. The autoclave with Fe_3O_4 was taken out of the oven straight after heating and it was cooled at room temperature, which was around 20 ˚C. On the other hand, the autoclave with γ-Fe_2O_3 was not taken out of the oven straight after heating, and it was cooled in the oven on set a dwell program to around

30 ˚C. From the synthesis results of the iron oxides, it could be assumed that Fe_3O_4 was crystallised first from the precursor and 1-hexanol, and it became γ-Fe_2O_3 and α-Fe_2O_3 due to the high temperatures and the longer heating.

Table 3.1 *Synthesis details and final products of iron oxides.*

Reactant	Ratio of reactant and $Fe(acac)_3$	Temperature (ºC)	Time (hr)	Final product
Benzyl alcohol	1:10; 1:20; 1:30 & 1:40	145–250	24–72	α-Fe_2O_3 & γ-Fe_2O_3
1-Hexanol	1:10 & 1:20	175	5–7	Fe_3O_4
	1:10	175	4.5–13	γ-Fe_2O_3
	1:20	160	144	
	1:5		19	
	1:10	175	16–19	α-Fe_2O_3 & γ-Fe_2O_3
	1:20		13–95	
	1:20	200 225	48	

Kominami et al. (1999)[82] investigated how reactants form Fe_3O_4. They synthesised Fe_3O_4 from $Fe(acac)_3$ and 1-hexanol for only 2 hr, but 19 nm Fe_3O_4 was synthesised at 27 ºC. The final product and particle size were related to the synthesis pressure that was increased by temperature and synthesis time. They obtained only amorphous products, or no reaction occurred when the reaction pressure was less than 1.8 MPa with 1-propanol as a reactant. Furthermore, smaller Fe_3O_4 particles were synthesised when the reaction pressure was low. A

similar result was found when 1-hexanol was used and the heating was less than 5 to 7 hr. Regarding the synthesis pressure, Fe_3O_4 transforms into a dense polymorph of Fe_3O_4 (h-Fe_3O_4), and it transforms into FeO and h-Fe_2O_3 (a dense polymorph of α-Fe_2O_3) at higher temperatures and pressures.[83]

Pressures inside the autoclave during the synthesis were calculated from the Antoine equation using 1-hexanol and benzyl alcohol data from Yaws (2015).[84] The Antoine equation is

$$\log_{10} P = A - \frac{B}{C + T}$$

Equation 3-2 *Antoine equation.*

where P is vapour pressure (mmHg), A, B and C are Antoine coefficients for the chemical compound and T is temperature (ºC). The results show the vapour pressure of 1-hexanol is much higher than for benzyl alcohol. The calculated vapour pressures are in Figure 3.5.

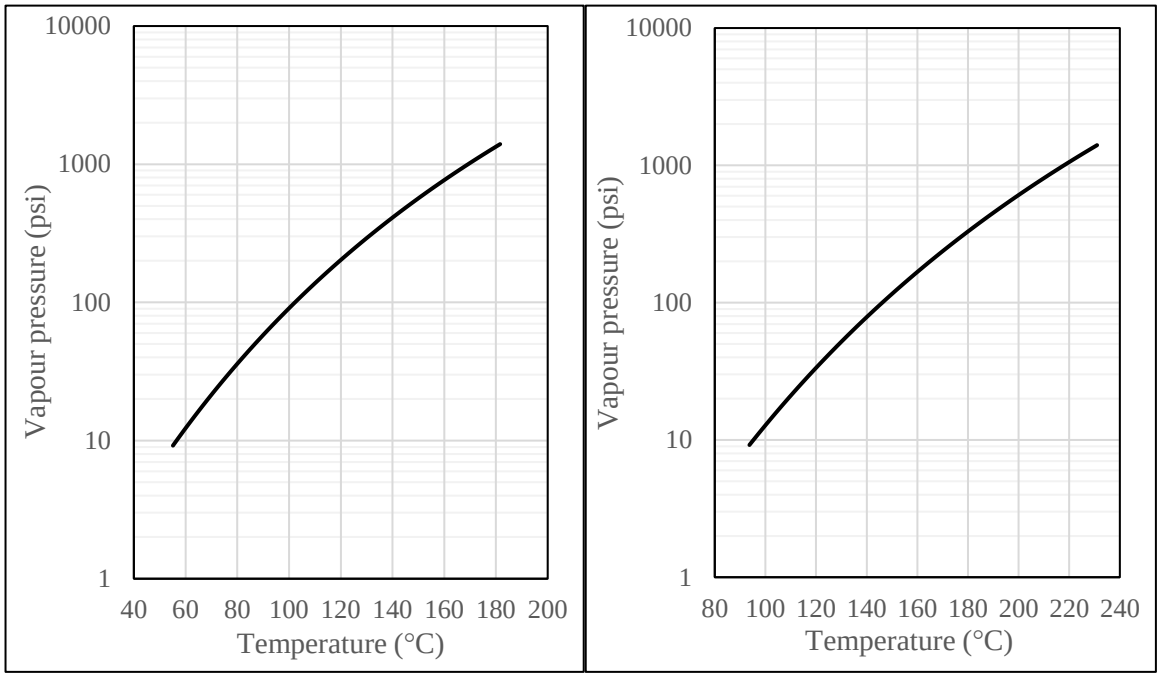

Figure 3.5 *Vapour pressures of 1-hexanol (left) and benzyl alcohol (right) calculated by the Antoine equation.*

The vapour pressure was considered to be in a closed container, the autoclave; therefore, Charles's law was used to estimate volume changes of the reactants. The equation of the Charles's law is

$$\frac{V_1}{T_1} = \frac{V_2}{T_2}$$

Equation 3-3 *Charles's law*

where V_1 and T_1 are the volume (ml) and temperature (K) of the solvent before heating, and V_2 and T_2 are the volume and temperature while heating. The volume expansions were observed from the stains of the reactants on the glass liner after heating.

The calculated vapour pressures in Table 3.2 that are theoretical pressures in a closed container (not in the autoclave). The actual vapour pressures of the reactants were not measured, because the size of an autoclave attached to a pressure meter would be bigger than the sample transfer port of the glovebox. The actual vapour pressures in the autoclave were estimated from the graph of water vapour pressures in the autoclave (Figure 3.3). The water vapour pressure increased with the level of water in the autoclave and the temperature. T_{cr} is the critical temperature of water, and the critical temperatures of 1-hexanol and benzyl alcohol are higher than that of water, at 157 and 205 ºC, respectively. Therefore, the gradients of the relationship between the vapour pressure and temperature of 1-hexanol and benzyl alcohol should be more moderate than for water, but the vapour pressures that gave the final products α-Fe_2O_3 and/or γ-Fe_2O_3 might be reached at around 45 GPa (6.5×10^6 psi) (Figure 3.4). From the diagram, it can be seen that h-Fe_3O_4 can be synthesised at 18 to 30 GPa (2.6×10^6 to 4.3×10^6 psi) and at around 450 K. The combination of heating at 175 ºC and filling over 70 % of the autoclave with 1-hexanol worked to synthesise the Fe_3O_4. However, benzyl alcohol did not work to synthesise the Fe_3O_4 under these conditions, although some authors have reported that the solvent worked as a reactant for crystallising Fe_3O_4.[72, 85] It could be that the vapour pressure of the reactants in the autoclave helps to synthesise Fe_3O_4 with other organic solvents or with different heating temperatures and times.

Table 3.2 *Calculated vapour pressures of 1-hexanol (top) and benzyl alcohol (bottom) that were used to synthesise iron oxides.*

Before heating			While heating		
Amount of 1-hexanol (ml)	Temperature (K)	Vapour pressure (psi)	Amount of 1-hexanol (ml)	Temperature (K)	Vapour pressure (psi)
5	293.15	137.30	7.64	448.15	319.87
15		411.90	22.93		959.60
10		274.60	15.29		639.73
20		549.21	30.57		1279.47

Before heating			While heating		
Amount of benzyl alcohol (ml)	Temperature (K)	Vapour pressure (psi)	Amount of benzyl alcohol (ml)	Temperature (K)	Vapour pressure (psi)
5	293.15	8.69	7.64	448.15	76.51
15		26.07	22.93		229.52
10		17.38	15.29		153.01
20		34.77	30.57		306.03

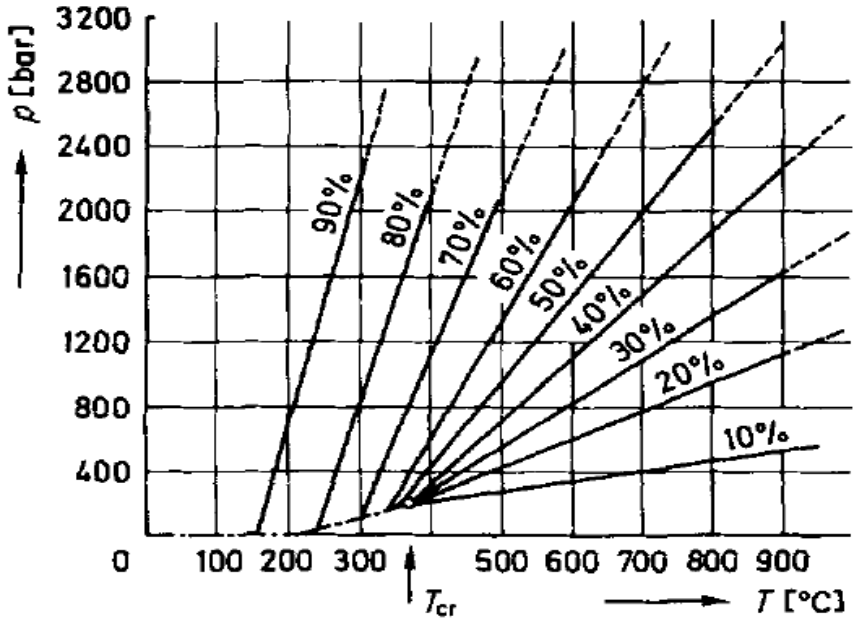

Figure 3.6 *Relationship between temperature and water pressure in an autoclave. The percentage is the filling factor of water in the autoclave, which is normally between 50 and 80 %.*[86]

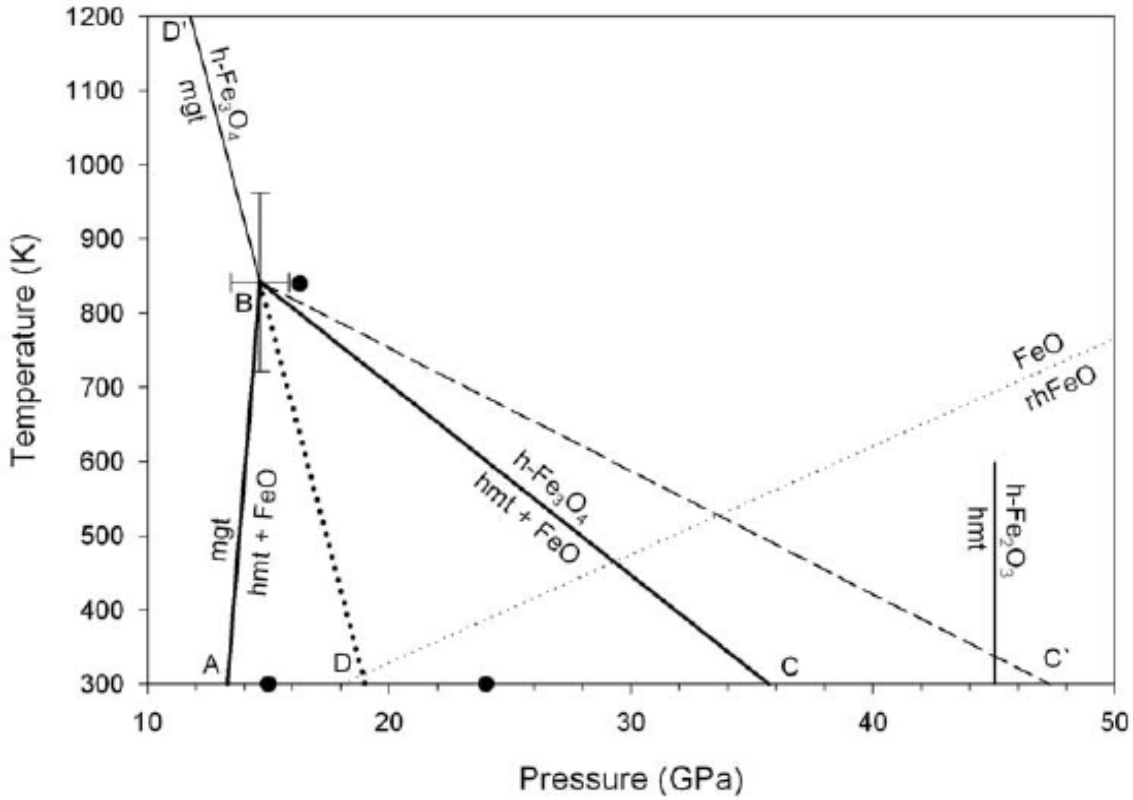

Figure 3.7 *Phase diagram of iron oxides that were obtained from experimental results and thermodynamic calculations,[83] where mgt is short for magnetite, hmt is α-Fe_2O_3, rhFeO is rhombohedrally distorted FeO, and h-Fe_2O_4 and h-Fe_3O_4 are high pressure form of Fe_2O_4 and Fe_3O_4.*

3.3.2 Elemental composition of cobalt ferrite

The elemental compositions of cobalt ferrite that were identified by the XRF measurements are shown in Table 3.3. with the synthesis details. The compositions were related to the synthesis temperature and time. The ratio of Fe to Co tended to be smaller when the heating temperature was higher, and the time was longer. However, the ratio of Fe to Co varied; some cobalt ferrite particles had higher Fe to Co ratios (over 2.00), even when they were heated at a smaller temperature or for a shorter time. It could be that the composition ratio was affected

by small differences in the amounts of the precursors, such as a few tens of milligrams. Ferreira et al. (2003)[87] also reported that the elemental compositions of synthesised cobalt ferrite were slightly different at different heating temperatures, and the crystal defects or chemical heterogeneity of the product were affected the composition, but they did not use an autoclave to synthesise the cobalt ferrite. Rafique et al. (2012)[88] investigated the relationship between the nucleation of cobalt ferrite and the synthesis pressure using an autoclave, and found that higher pressure accelerated the cobalt ferrite nucleation. Therefore, it could also be assumed that the cobalt ferrite with a large amount of Fe was formed by heating for about 10 hours at 175 or 180 ˚C, and Fe was pushed out from it, or the nucleation of cobalt ferrite with a high proportion of Co was formed by the high pressure and the longer heating.

Table 3.3 *Elemental compositions of synthesised cobalt ferrite.*

Synthesis temperature (˚C)	Synthesis time (hr)	Formula	Concentration (wt%)		Amount of material (mmol)	Ratio Fe : Co
175	12	Fe	69.15	(±0.13)	12.38	2.41:1.00
		Co	30.30	(±0.07)	5.14	
	24	Fe	67.50	(±0.12)	12.09	2.19:1.00
		Co	32.50	(±0.08)	5.51	
180	10	Fe	68.82	(±0.13)	12.32	2.65:1.00
		Co	27.38	(±0.07)	4.65	
	15	Fe	67.92	(±0.13)	12.16	2.39:1.00
		Co	29.95	(±0.07)	5.08	
	20	Fe	63.60	(±0.12)	11.39	1.86:1.00
		Co	36.00	(±0.08)	6.11	
	24	Fe	58.85	(±0.12)	10.54	1.56:1.00
		Co	39.75	(±0.09)	6.74	

For the further M_xO_y/SiO_2 and MSZ syntheses, cobalt ferrite that was synthesised at 180˚C for 10 hr was used due to the smaller particles obtained and the speed of synthesis. The chemical formula was $Co_{0.3}Fe_{2.7}O_4$, and it was superparamagnetic (see Section 3.3.6).

3.3.3 Identifying Fe_3O_4, γ-Fe_2O_4 and cobalt ferrite

XRD and Raman spectrometry were used to identify whether the products were Fe_3O_4 or γ-Fe_2O_4. The XRD patterns of Fe_3O_4, the mixture of α-Fe_2O_3 and γ-Fe_2O_3, and α-Fe_2O_3 with the *hkl* indices of their structures are shown in Figure 3.5. The γ-Fe_2O_3 peaks of the mixture of α-Fe_2O_3 and γ-Fe_2O_3 appeared at the same positions as the Fe_3O_4 peak patterns, and the Fe_3O_4

peaks were broader than the other product peaks. Both Fe_3O_4 and γ-Fe_2O_3 have a cubic structure, and their lattice parameters are very similar; therefore, it is very difficult to distinguish them in the XRD patterns, especially as when the particle sizes are small, the peak width increases.[89]

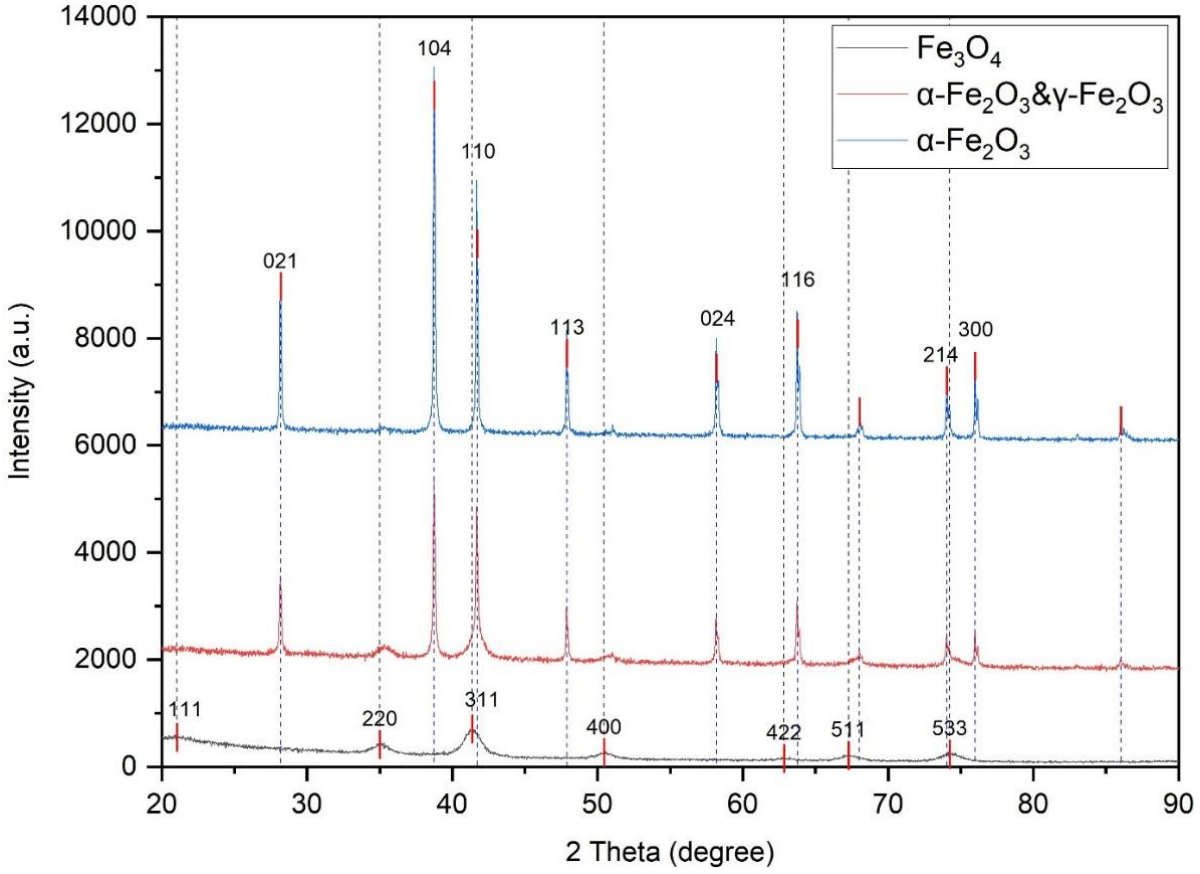

Figure 3.8 *XRD patterns of Fe_3O_4 (bottom), the mixture of α-Fe_2O_3 & γ-Fe_2O_3 (middle) and α-Fe_2O_3 (top).*

The products were also characterised by Raman spectrometry. Figure 3.6 shows the Raman spectra of Fe_3O_4 and γ-Fe_2O_4. Fe_3O_4 was easily oxidised by the laser of the Raman spectrometer; therefore, the peak of Fe_3O_4 was obtained by a green laser to minimise laser exposure. Fe_3O_4 had one big peak at 676.8 cm^{-1}, but γ-Fe_2O_4 had two peaks at 686.3 and 732.7

cm^{-1}. Usually, the Raman peak of Fe_3O_4 appears at around 670 cm^{-1} and γ-Fe_2O_4 appears at 670 and 720 cm^{-1}.[90] Therefore, the products could be identified from the Raman spectra.

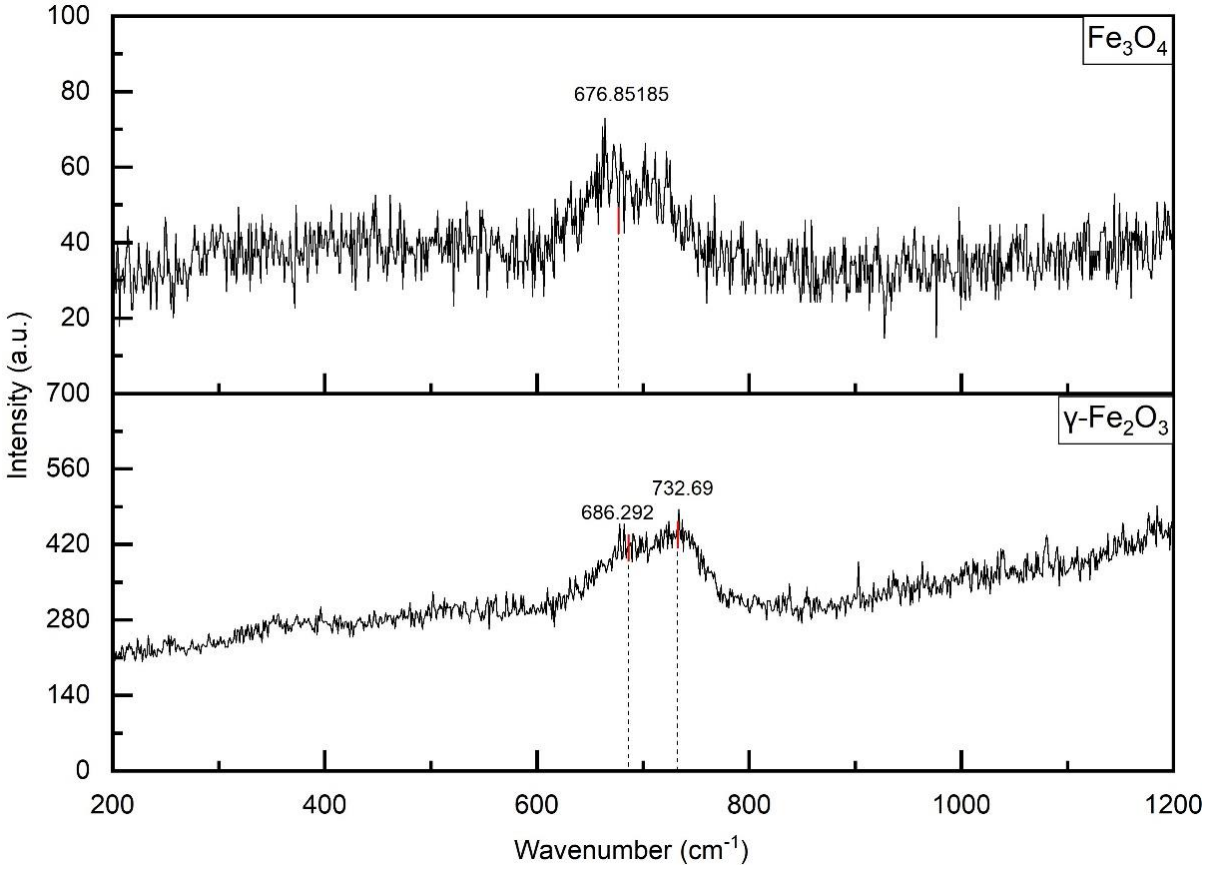

Figure 3.9 *Raman spectra of Fe_3O_4 (top) and γ-Fe_2O_3 (bottom)*

The XRD patterns of $Co_{0.3}Fe_{2.7}O_4$ were also similar to those of Fe_3O_4 because of the crystal structure: both Fe_3O_4 and cobalt ferrite are cubic spinels. The Raman spectra of cobalt ferrite was also obtained just in case (Figure 3.7). The peak positions of the Raman spectra were similar to the cobalt ferrite Raman spectra results that were obtained after the use of the various synthesis methods of Chandramohan et al. (2011).[91] The large Raman peaks of

$Co_{0.3}Fe_{2.7}O_4$ were between 674.8 to 695.3 cm^{-1}, 460.7 to 470.1 cm^{-1}, and 293.2 to 311.8 cm^{-1}. The positions and intensities depended on the particle size and the synthesis route because of the cation distribution of $Co_{0.3}Fe_{2.7}O_4$, and the peaks of smaller particles tend to shift to the lower wavenumber positions.

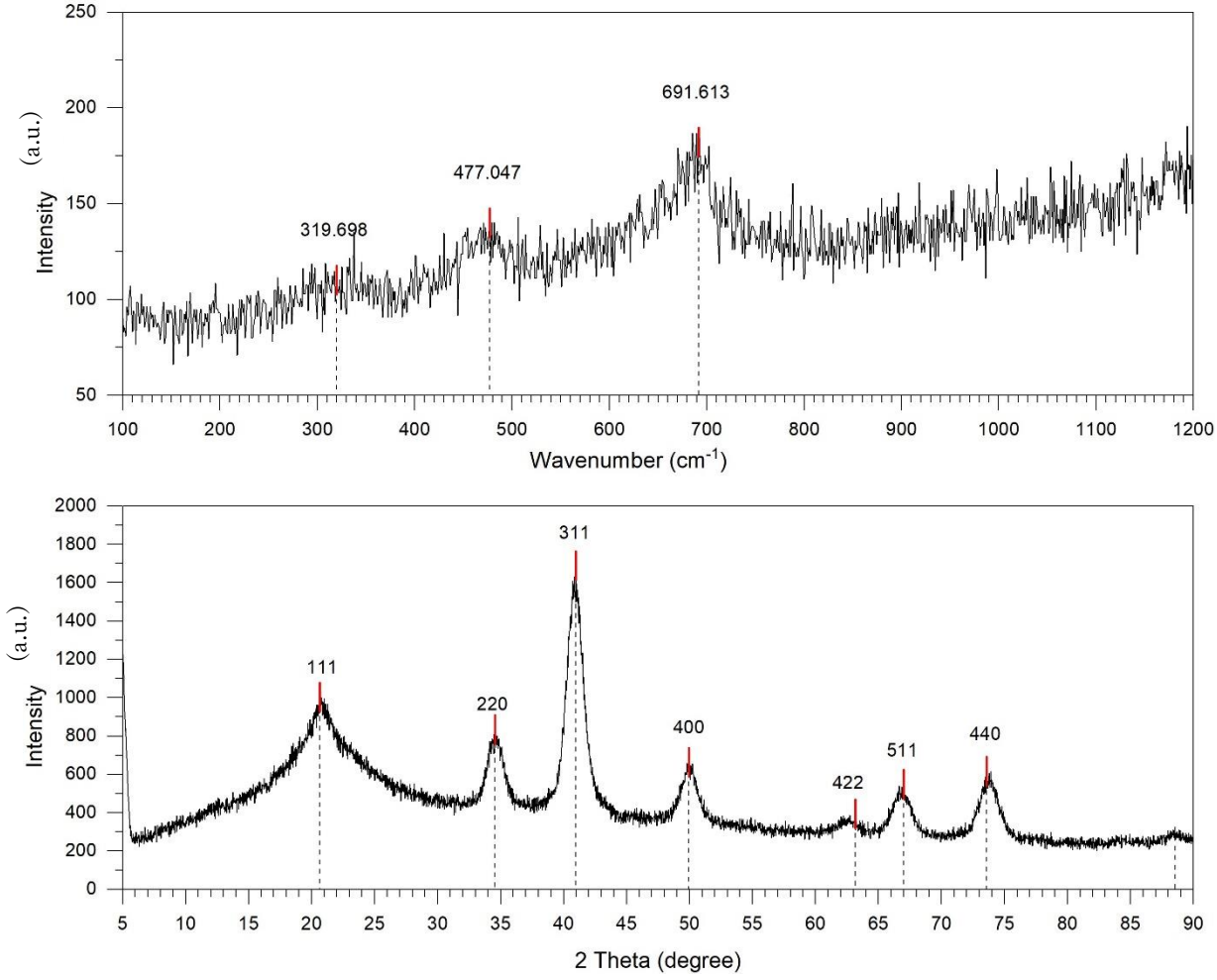

Figure 3.10 *Raman spectra (top) and XRD patterns (bottom) of* $Co_{0.3}Fe_{2.7}O_4$.

3.3.4 Particle size

The particle sizes of Fe_3O_4 and $Co_{0.3}Fe_{2.7}O_4$ were measured by both DLS and TEM, and they were also calculated from the FWHM of the XRD peaks using the Scherrer equation (Equation 2-2). Tables 3.4 and 3.5 show the calculated particle size results from the XRD peaks of the Fe_3O_4 that was synthesised under various synthesis conditions of temperature, time, and precursor and organic solvent ratio. The different conditions worked as parameters for particle size control. Some of the particle sizes were bigger than the heated shorter ones, it was due to the calculation method: the particle sizes were assumed from the product crystallite sizes, and the XRD peaks were border and had less intensities such as the bottom figure of Figure 3.10. It was difficult to calculate the crystallite sizes precisely, therefore, the calculated results were varied.

Smaller particles were synthesised when the synthesis temperatures, time and the ratio were small. It could be assumed the particle size also relates to the synthesis pressure in the autoclave. Higher temperature and solvent volume in the autoclave produce higher pressure, and when it was heated for longer, the crystal growth of Fe_3O_4 could be encouraged. The smallest particles were made when the synthesis ratio of $Fe(acac)_3$ to 1-hexanol was 1:10 and they were heated at 175˚C for between 5 and 7 hours. The Fe_3O_4 particles that were measured by the TEM were synthesised for 5 hr, and the observed average size was 6.8 nm. The smallest and biggest particle sizes calculated by the XRD were about 2 to 3 times bigger than those

observed by the TEM. However, the difference between the average particle sizes calculated by XRD (the average was 9.2 nm) and those observed by the TEM were just 8.0 nm. Therefore, the Fe_3O_4 particle sizes calculated by the XRD also seemed to be reliable.

Table 3.4 *Particle size (Å) measured by XRD (1-hexanol). Where timer is the conventional oven timer was used for both heating and cooling the autoclave. The particle sizes that were smaller than 100 nm are green coloured, smaller than 120 nm are blue coloured, and bigger than 200nm are red coloured.*

	Ratio of $Fe(acac)_3$ (g) to 1-hexanol (ml)	1.5:30	1:05	1:10	1:15	1:20	1.37:20	1.5:1.5	2:20	1:20	1:20
		160 °C				175 °C				200 °C	225 °C
Time (hr)	4.5 (Timer)								100.6		
	5			88.2					101.5		
	6 (Timer)			78.1				93.4			
	7			83.1				92.7			
	7 (Timer)								107.5		
	10								90.4		
	11								91.2		
	12			83.3					96.4		
	13			92.4		89.7					
	16			97.6		100.7					
	18					84.0	103.3				
	19		104.1	91.1	124.6						
	48									251.8	737.5
	72					127.3					
	95					97.8					
	144	416.6									

Table 3.5 *Particle size obtained from XRD peaks and TEM images of Fe_3O_4 that the ratio of $Fe(acac)_3$ to 1-hexanol was 1:10 and heated for 5 hr at 175 °C.*

XRD (nm)			TEM (nm)		
Minimum	Maximum	Average	Minimum	Maximum	Average
8.2	33.8	9.2 (±5.3)	4.4	13.5	8.0 (±1.8)

Table 3.6 *Particle size obtained from XRD peaks and TEM images of $Co_{0.3}Fe_{2.7}O_4$ that was heated for 10 hr at 180 °C.*

XRD (nm)			TEM (nm)		
Minimum	Maximum	Average	Minimum	Maximum	Average
2.4	24.5	9.6 (±4.5)	5.1	11.6	7.5 (±1.5)

The particle sizes of $Co_{0.3}Fe_{2.7}O_4$ that were calculated by XRD were also compared with those obtained by the TEM. The smallest and biggest particle sizes calculated by XRD were very similar to those observed by the TEM, and the average sizes were also close, the difference being just 2.1 nm. Therefore, the result for $Co_{0.3}Fe_{2.7}O_4$ calculated by XRD was also reliable. The DLS measurement results of Fe_3O_4 and $Co_{0.3}Fe_{2.7}O_4$ are shown in Figures 3.8 to 3.15. The nanoparticles were dispersed in DI water, 1-hexanol, ethanol, a mixture of ethanol and DCM (mixture A), or a mixture of 1-hexanol, ethanol and DCM (mixture B). The particles were coated with dopamine, polyvinylpyrrolidone (PVP) and citric acid to try to disperse the particles in the DI water. PVP is amphiphilic and a coating of it helps to stop the particles aggregating.[92] Dopamine works as a monomer, and dopamine coated Fe_3O_4 also has a high affinity in water to help to disperse the particles.[93, 94] However, the peaks of the particle sizes did not overlap, or they had several peaks, excluding the Fe_3O_4 in 1-hexanol. Z-average, which

is also called the cumulants mean, was 46.2 to 56.7 nm in diameter (Figure 3.8 and Table 3.7). The particle sizes calculated by volume were also similar to those calculated by intensity (Figure 3.9). Furthermore, the obtained average diameters were much bigger than the results from XRD and TEM measurements (Table 3.4 and 3.5). Fe_3O_4 and $Co_{0.3}Fe_{2.7}O_4$ tended to aggregate easily in the solutions, even when the particle surfaces were coated, and the measurement durations were just a few minutes. They have high surface areas, and they are easily attracted to each other by dipole-dipole interactions and van der Waals forces.[95, 96]

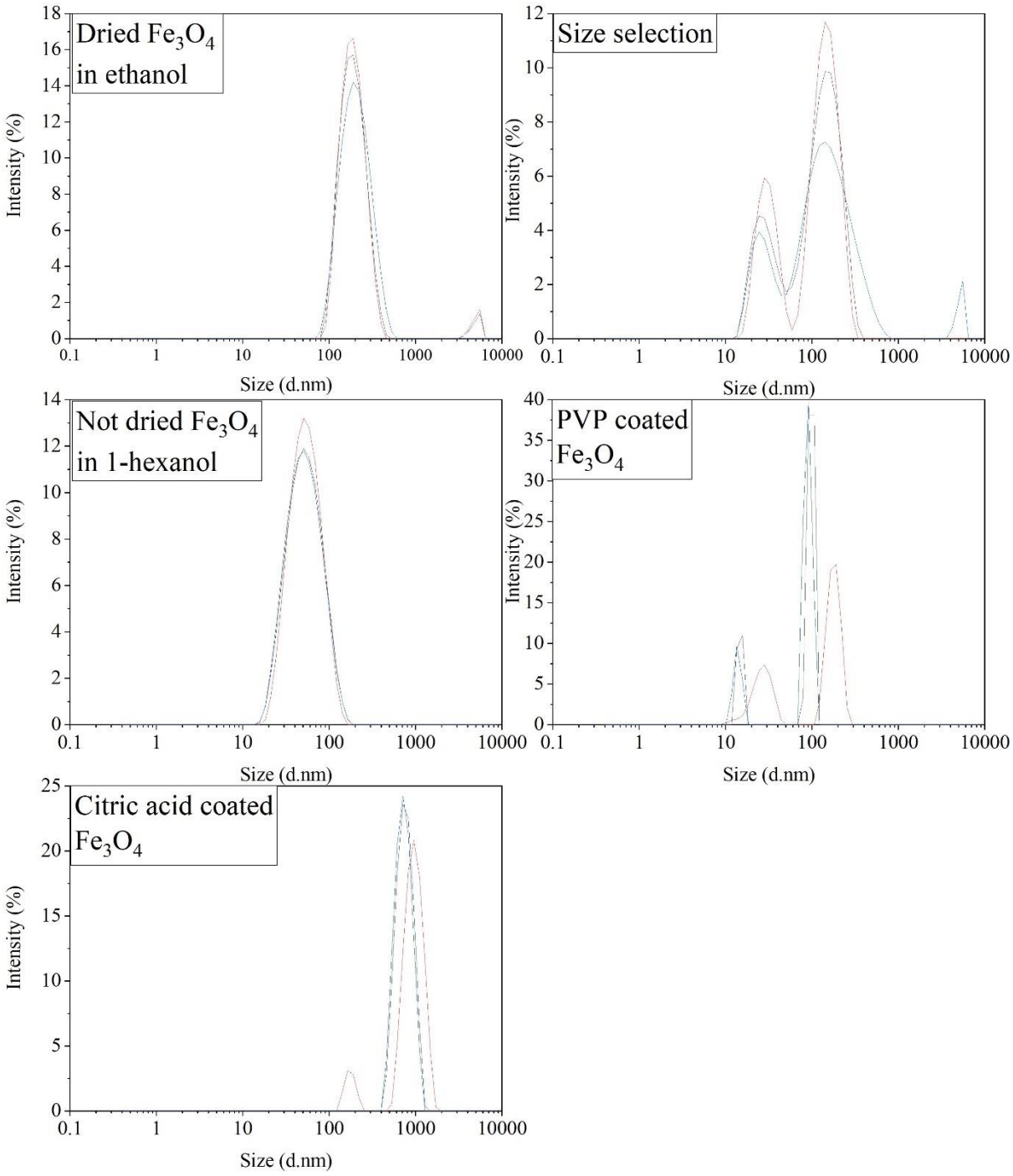

Figure 3.11 *Particle sizes of Fe_3O_4 measured by DLS (calculated by intensity). Where d.nm. is diameter in nm.*

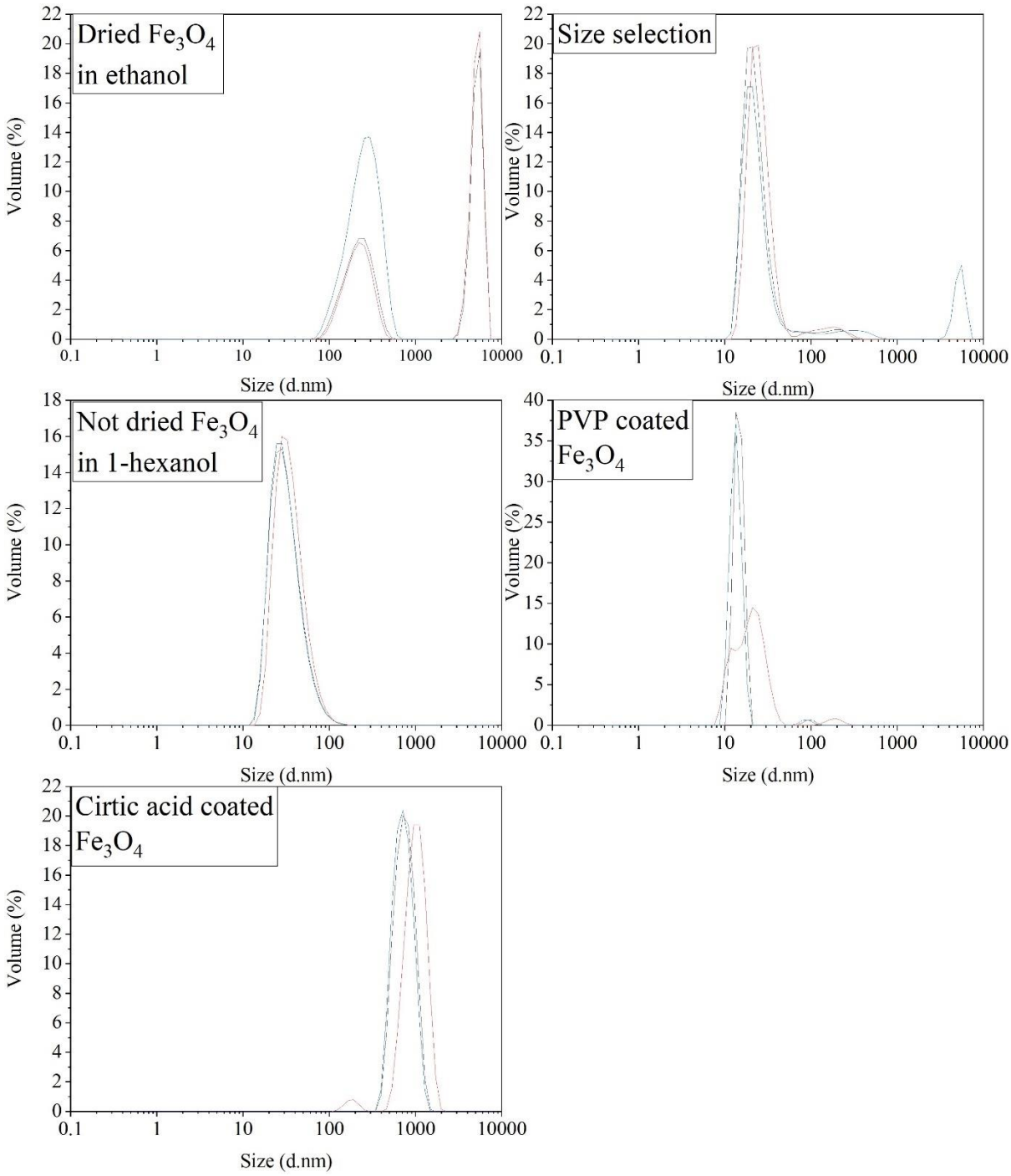

Figure 3.12 *Particle sizes of Fe_3O_4 measured by DLS (calculated by volume). Where d.nm. is diameter in nm.*

Table 3.7 *Particle sizes of Fe_3O_4, which the ratio of $Fe(acac)_3$ to 1-hexanol was 1:10 and heated for 5 hr at 175 °C, under various conditions, obtained by DLS. Where d.nm. is diameter in nm.*

	Intensity (d.nm)			Volume (d.nm)			Z-Average (d.nm)	Polydispersity index*
	Peak 1	Peak 2	Peak 3	Peak 1	Peak 2	Peak 3		
Ethanol	195.7 (97.2 %)	5015 (2.8 %)		229.7 (46.4 %)	5172 (53.6 %)		189.1	0.201
	194.7 (96.6 %)	4972 (3.4 %)		224.2 (41.0 %)	5139 (59.0 %)		191.7	0.213
	214.0 (100 %)			263.8 (100 %)			188.0	0.160
Size selection	149.4 (73.2 %)	29.30 (26.8 %)		189.5 (4.2 %)	23.91 (95.8 %)		114.3	0.299
	151.1 (70.1 %)	30.82 (29.9 %)		158.9 (6.0 %)	25.30 (94.0 %)		137.8	0.250
	179.5 (75.6 %)	27.33 (20.8 %)	5179 (3.6 %)	294.8 (5.3 %)	24.33 (82.2 %)	5290 (12.5 %)	87.09	0.656
1-hexanol	56.81 (100 %)			33.43 (100 %)			47.03	0.151
	56.69 (100%)			36.54 (100%)			46.70	0.162
	56.13 (100%)			33.11 (100 %)			46.20	0.157
PVP coated	97.67 (79.6 %)	14.72 (20.4 %)		96.74 (1.7 %)	14.55 (98.3 %)		733.1	0.769
	179.2 (66.4 %)	26.65 (33.6 %)		11.69 (25.2 %)	22.11 (72.1 %)	188.1 (2.7 %)	350.2	0.488
	90.16 (80.9 %)	13.79 (19.1 %)		88.54 (1.8 %)	13.44 (98.2 %)		804.9	0.706
Citric Acid coated	760.3 (100%)			762.2 (100 %)			1013	0.533
	973.8 (91.6 %)	175.9 (8.4 %)		1027 (97.4 %)	182.0 (2.6 %)		1098	0.567
	734.8 (100 %)			731.9 (100 %)			1037	0.599

**Polydisperse index describes how well disperse the particles, and the rage is from 0.0 (well dispersed) to 1.0 (highly polydispersed).*

**The z-average was calculated by the DLS software automatically.*

The Fe_3O_4 that had not been dried, which were dispersed in mixture A and mixture B were much more stable during the DLS measurements (the measurement for one sample takes about 10 min). The particle sizes in mixture A, which were calculated by intensity, were shown to be a few nm to a few 100 nm by the multiple peaks (Figures3.10 and Table 3.8). However, the values calculated by volume showed fewer peaks, and the biggest peaks were at smaller sizes, around 5 to 6 nm, with the exception of the results for the Fe_3O_4 that was dried and dispersed in mixture B. The particle size calculation using the volume does not include the aggregated particles in the total particle sizes on the graphs. Therefore, the volume graphs obtained almost the same sizes as those measured by XRD and TEM. The effect of changing the ratio of ethanol and DCM in the mixture was also tested, and the maximum peak size for the mixture with more DCM (ethanol:DCM = 1:9.5) was smaller than when the ratio was 1:2. This means that having more DCM in ethanol helped to prevent aggregation of the particles.

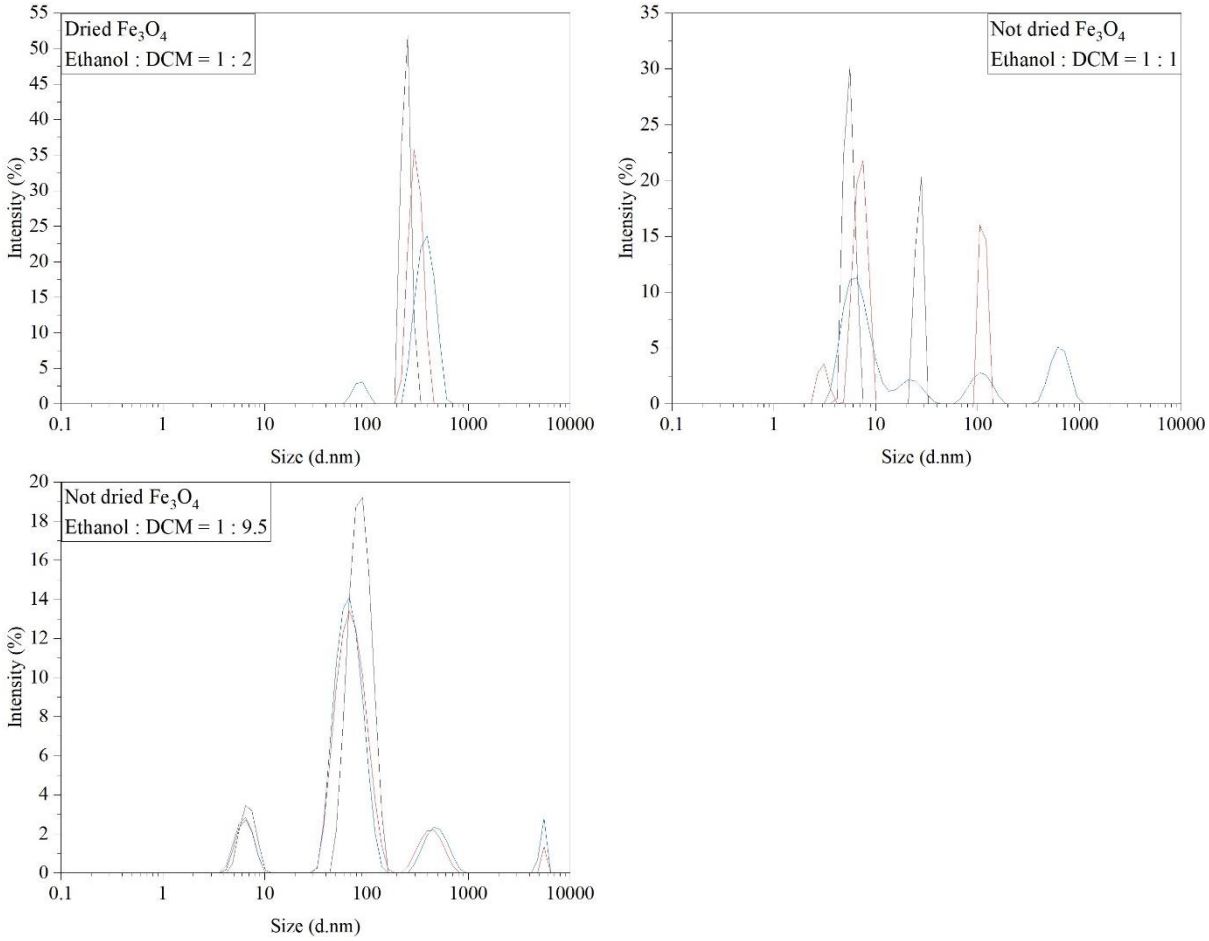

Figure 3.13 *Particle sizes of Fe_3O_4 dispersed in the mixture of ethanol and DCM measured by DLS (calculated by intensity). Where d.nm. is diameter in nm.*

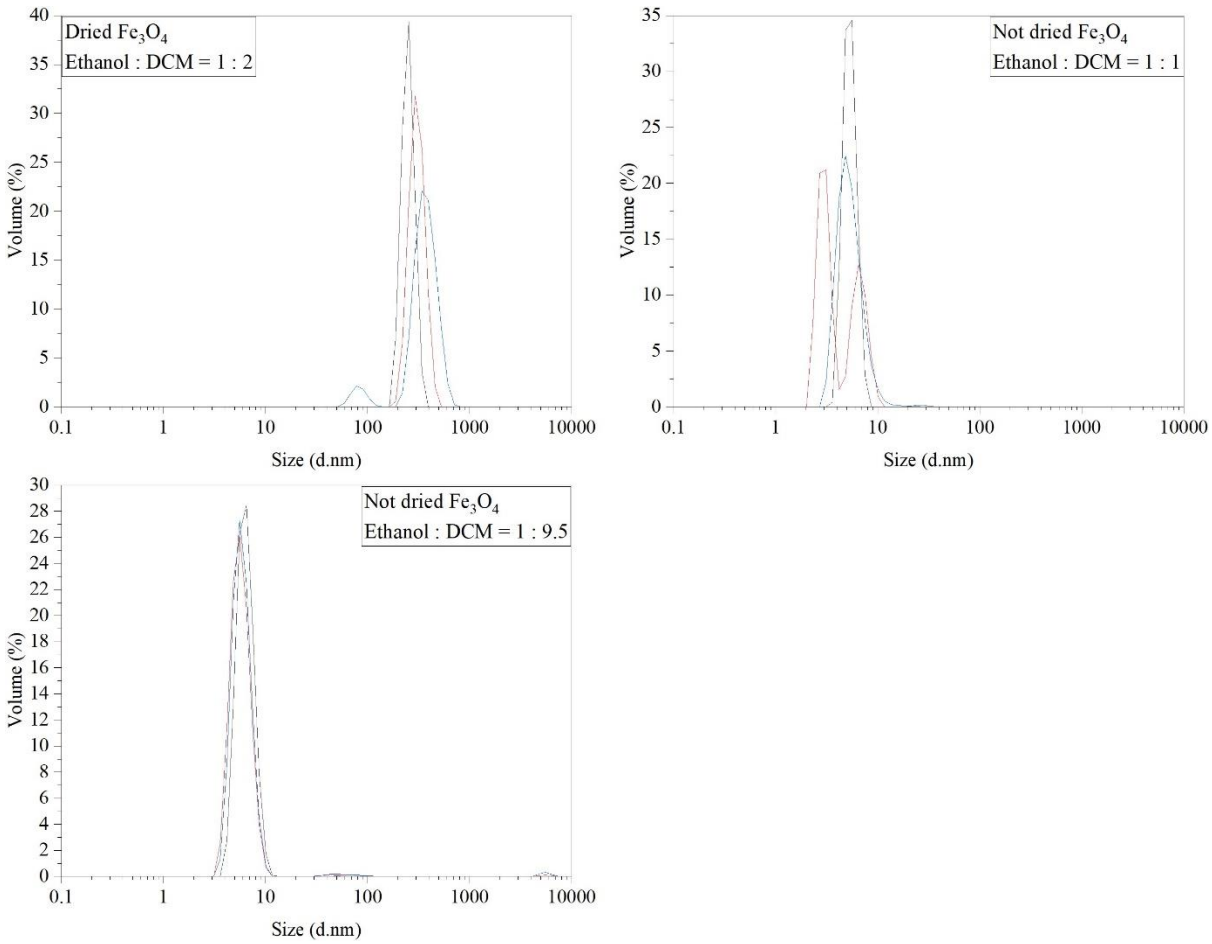

Figure 3.14 *Particle sizes of Fe_3O_4 dispersed in the mixture of ethanol and DCM measured by DLS (calculated by volume). Where d.nm. is diameter in nm.*

Table 3.8 *Particle sizes of Fe_3O_4 in the mixture of ethanol and DCM, obtained by DLS. Where d.nm. is diameter in nm.*

	Intensity (d.nm)			Volume (d.nm)			Z-Average (d.nm)	Polydispersity index
	Peak 1	Peak 2	Peak 3	Peak 1	Peak 2	Peak 3		
Dried Fe_3O_4 Ethanol : DCM (1 : 2)	247.1 (100%)			252.3 (100 %)			677.3	0.984
	307.2 (100%)			308.6 (100 %)			685.7	0.650
	385.1 (91.7 %)	86.75 (8.3 %)		380.6 (93.4 %)	83.44 (6.6 %)		575.1	0.538
Not dried Fe_3O_4 Ethanol : DCM (1 : 2)	5.520 (66.1 %)	26.67 (33.9 %)		5.363 (99.6 %)	26.39 (0.4 %)		2382	1.000
	7.148 (61.8 %)	113.7 (30.6 %)	3.054 (7.7%)	2.978 (59.2 %)	6.684 (40.8 %)		1409	1.000
	6.792 (59.1 %)	647.6 (18.6 %)	110.4 (11.6 %)	5.479 (100 %)			492.4	0.662
Not dried Fe_3O_4 Ethanol : DCM (1 : 9.5)	88.60 (89.0 %)	6.918 (11.0 %)		77.19 (0.5 %)	6.422 (99.5 %)		82.02	0.355
	73.77 (78.1 %)	441.2 (10.4 %)	6.379 (10.1 %)	57.61 (0.8 %)	450.3 (0.1 %)	5.778 (99.0 %)	83.28	0.336
	69.61 (76.5 %)	493.6 (10.7 %)	6.475 (9.3 %)	56.17 (0.9 %)	521.2 (0.1 %)	5.921 (98.3 %)	88.52	0.411

***** *The Fe3O4 synthesis condition was the ratio of $Fe(acac)_3$ to 1-hexanol was 1:10 and heated for 5 hr at 175 °C.*

Two types of mixture B were tested: with the ratio of 1-hexanol to ethanol to DCM set at 1:1:5 and at 1:1:9. The particle size graph calculated by volume in which the mixture ratio was 1:1:5 showed big peaks at around 4.38 to 5.30 nm and tiny peaks at around 33.77 to 39.35 nm (Figure 3.13). The tiny peaks could be assumed to be aggregated Fe_3O_4 particles. The particle sizes calculated by intensity show more peaks at larger sizes (Figure 3.12). The mixture with the ratio of 1:1:9 also showed peaks at similar positions; however, the peaks that were calculated by intensity overlapped less, and therefore, the z-average sizes were a few 100 nm bigger (Table 3.9).

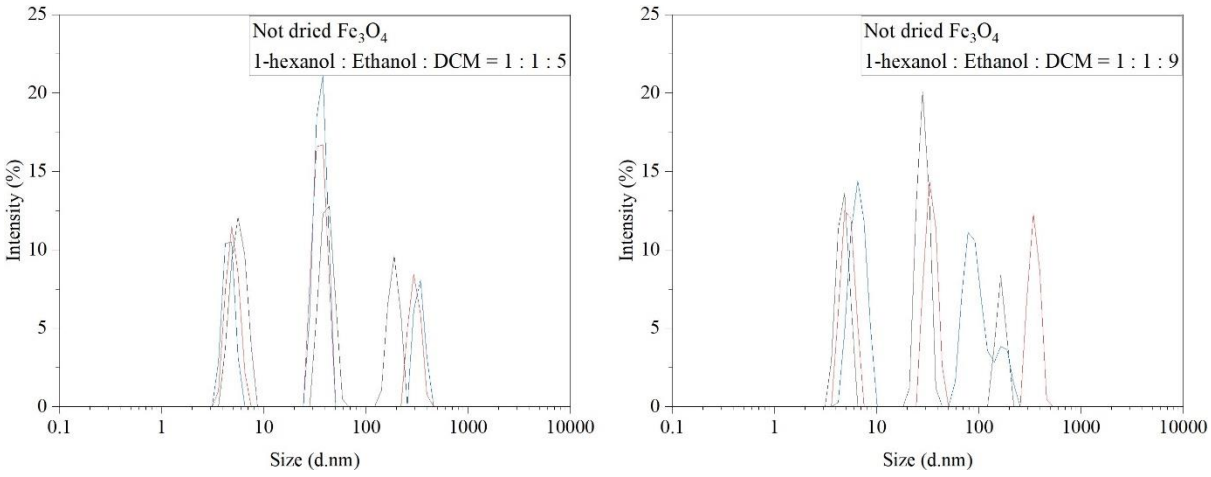

Figure 3.15 *Particle sizes of Fe_3O_4 dispersed in the mixture of 1-hexanol, ethanol and DCM measured by DLS (calculated by intensity) Where d.nm. is diameter in nm.*

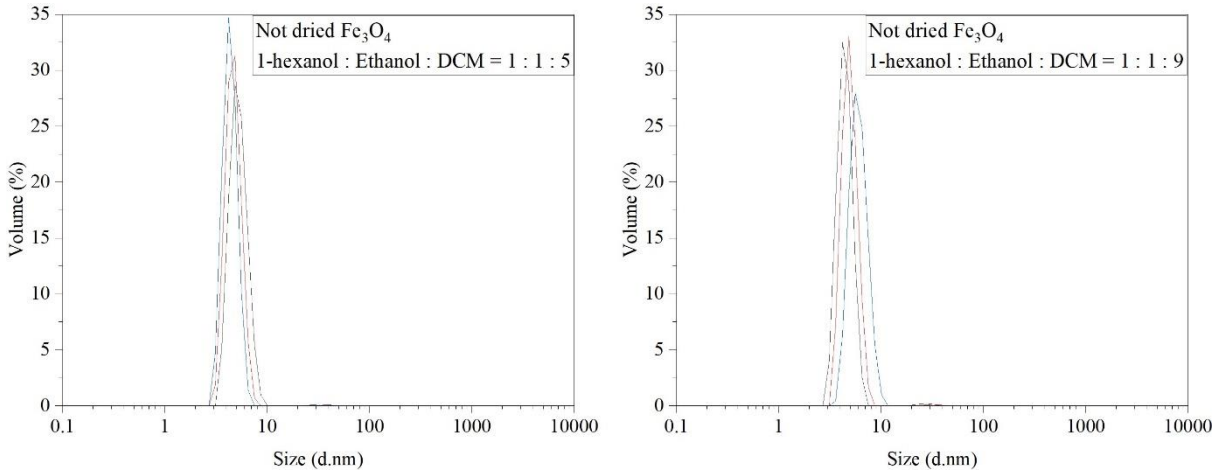

Figure 3.16 *Particle sizes of Fe_3O_4 dispersed in the mixture of 1-hexanol, ethanol and DCM measured by DLS (calculated by volume) Where d.nm. is diameter in nm.*

Table 3.9 *Particle sizes of Fe_3O_4 in the mixture of 1-hexanol, ethanol and DCM, obtained by DLS. Where d.nm. is diameter in nm.*

	Intensity (d.nm)			Volume (d.nm)		Z-Average (d.nm)	Polydisperse index
	Peak 1	Peak 2	Peak 3	Peak 1	Peak 2		
1-hexanol,	5.710 (38.6 %)	41.59 (38.3 %)	188.2 (23.1 %)	5.292 (99.7 %)	39.35 (0.3 %)	251.6	0.464
ethanol and DCM	35.55 (49.3 %)	4.979 (30.6 %)	302.9 (20.1 %)	33.77 (0.4 %)	4.720 (99.5 %)	190.0	0.365
(1 : 5)	36.20 (55.6 %)	4.555 (27.0 %)	335.3 (17.4 %)	34.56 (0.4 %)	4.379 (99.6 %)	230.5	0.428
1-hexanol,	28.46 (48.7 %)	4.678 (34.6 %)	165.6 (16.7 %)	4.474 (99.4 %)	27.31 (0.6 %)	419.3	0.591
ethanol and DCM	34.18 (36.1 %)	5.236 (35.7 %)	349.4 (28.1 %)	32.79 (0.4 %)	4.981 (99.6 %)	368.5	0.650
(1 : 1 : 9)	6.611 (46.1 %)	91.24 (42.5 %)	173.5 (11.4 %)	6.088 (99.9 %)	83.56 (0.1 %)	427.1	0.597

***** *The Fe3O4 synthesis condition was the ratio of $Fe(acac)_3$ to 1-hexanol was 1:10 and heated for 5 hr at 175 °C.*

The $Co_{0.3}Fe_{2.7}O_4$ was also dispersed in mixture A and mixture B, and the particle sizes were measured by DLS (Figures 3.14 and 3.15). When dried and dispersed in mixture A, the sample gave rise to single overlapped peaks at 900 to 1000 nm (Table 3-10). Even when the particles were dispersed in mixture B, there were multiple peaks of two sizes at 46.96 to 49.07 nm and 296.0 to 459.6 nm when calculated by intensity, and 32.84 to 34.98 nm and 314.6 to 466.1 nm when calculated by volume. The actual particle sizes that were observed using the TEM were 5.9 to 11.5 nm (Table 3.10). The DLS results showed aggregated $Co_{0.3}Fe_{2.7}O_4$ particles. The mixtures A and B did not work for $Co_{0.3}Fe_{2.7}O_4$ particles, although mixture B caused less aggregation of the particles.

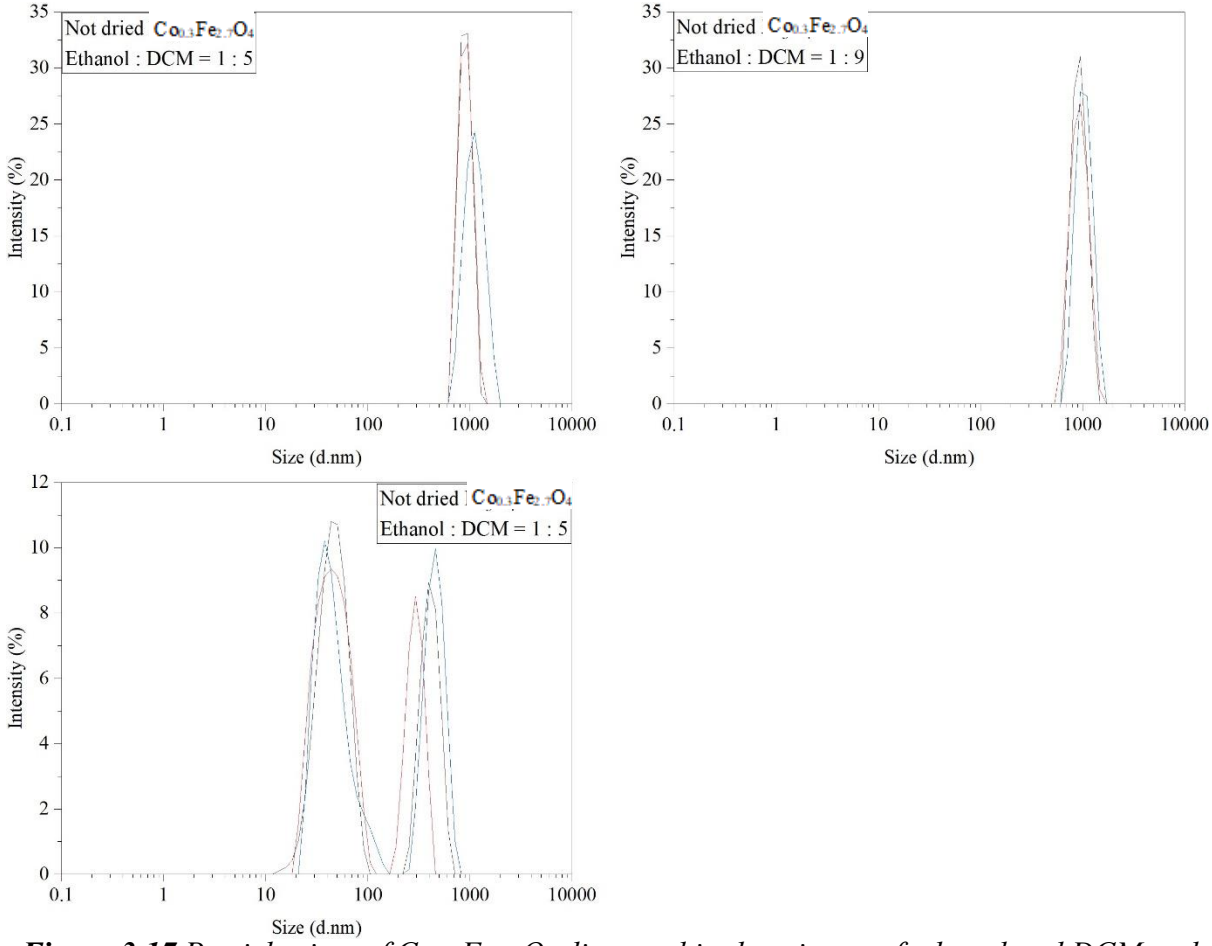

Figure 3.17 *Particle sizes of $Co_{0.3}Fe_{2.7}O_4$ dispersed in the mixture of ethanol and DCM and the mixture of 1-hexanol, ethanol and DCM, measured by DLS (calculated by intensity). Where d.nm. is diameter in nm.*

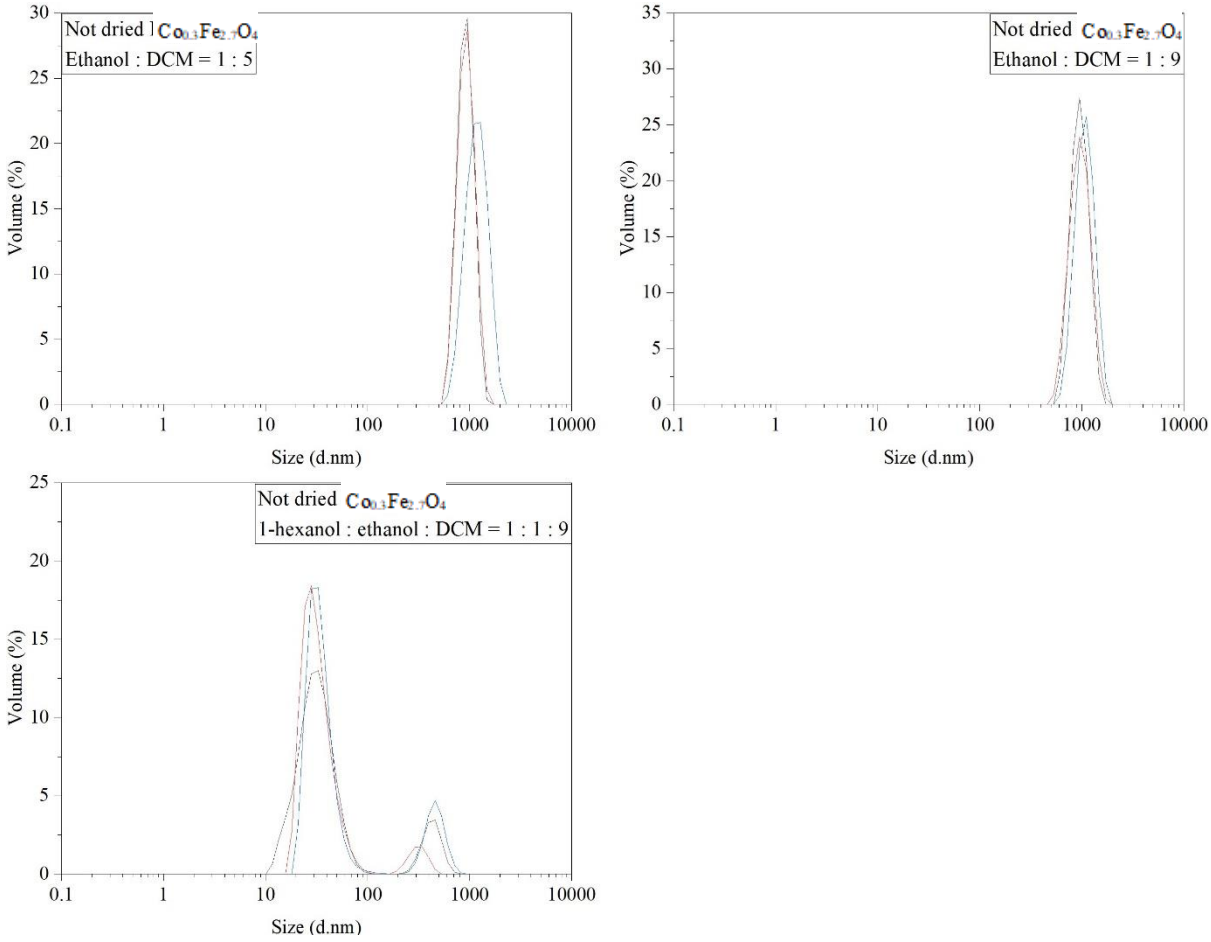

Figure 3.18 *Particle sizes of $Co_{0.3}Fe_{2.7}O_4$ dispersed in the mixture of ethanol and DCM and the mixture of 1-hexanol, ethanol and DCM, measured by DLS (calculated by volume). Where d.nm. is diameter in nm.*

Table 3.10 *Particle sizes of $Co_{0.3}Fe_{2.7}O_4$ in the mixture of ethanol and DCM and the mixture of 1-hexanol, ethanol and DCM, obtained by DLS. Where d.nm. is diameter in nm.*

	Intensity (d.nm)		Volume (d.nm)		Z-Average (d.nm)	Polydisperse index
	Peak 1	Peak 2	Peak 1	Peak 2		
Ethanol and DCM (1 : 5)	902.5 (100 %)		922.1 (100 %)		858.3	0.043
	916.4 (100 %)		939.6 (100 %)		902.9	0.108
	1127 (100 %)		1198 (100 %)		1064	0.120
Ethanol and DCM (1 : 9)	940.7 (100 %)		968.8 (100 %)		897.0	0.144
	944.4 (100 %)		980.2 (100 %)		990.5	0.230
	1047 (100 %)		1091 (100 %)		961.9	0.167
1-hexanol, ethanol and DCM (1 : 1 : 9)	46.96 (65.3 %)	413.4 (34.7 %)	32.84 (86.9 %)	430.1 (13.1 %)	448.4	0.588
	47.33 (70.1 %)	295.0 (29.9 %)	33.10 (93.3 %)	314.6 (6.7 %)	469.7	0.619
	48.07 (59.8 %)	459.6 (40.2 %)	34.98 (82.6 %)	466.1 (17.4 %)	311.8	0.755

*The *$Co_{0.3}Fe_{2.7}O_4$ synthesis condition was the ratio of $Fe(acac)_3$:$Co(acac)_2$:1-hexanol was 1.70:0.62:20.0, and it was heated at 180 ºC for 10 hr.*

Ye et al. (2013)[97] reported that $BaTiO_3$ was able to uniformly disperse in the mixture of ethanol and DCM. It is supposed that the ethanol and DCM mixture attached hydroxyl radicals onto the particle surfaces, and they had high affinity surfaces (Figure 3.16).

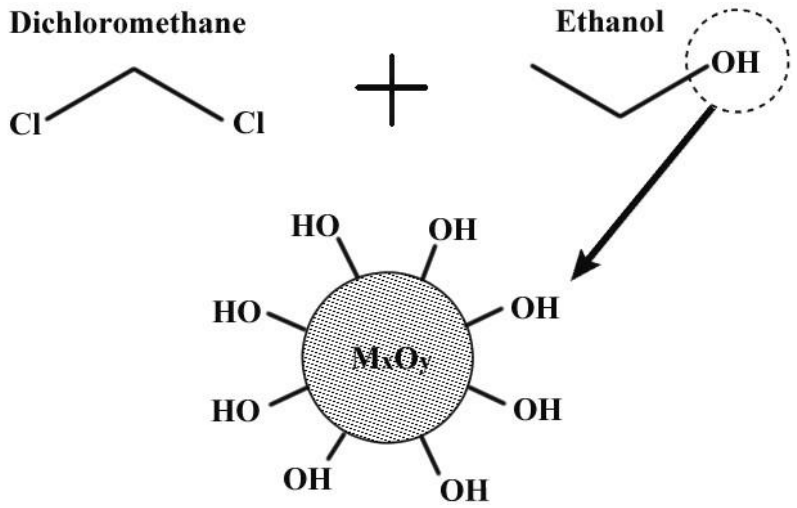

Figure 3.19 *Schematic diagram of the DCM and ethanol reaction.*

The colour of the mixtures A and B were still dark for the DLS measurements after diluting them by ethanol, and the measurement qualities were poor due to the sample fluorescence and absorbance even after the mixtures were diluted with much ethanol. Furthermore, the nanoparticles in the diluted mixtures were too polydisperse for the particle distribution analysis. If the mixtures would be diluted by DCM, the measurement qualities might be improved, and more reliable particle size measurement data could be obtained by the DLS.

3.3.5 Zeta potential

Zeta potentials of the dopamine coated Fe_3O_4, which the ratio of $Fe(acac)_3$ to 1-hexanol was 1:10 and heated for 5 hr at 175 °C, and $Co_{0.3}Fe_{2.7}O_4$ which was heated for 10 hr at 180 °C, were measured by DLS to determine the nanoparticle's stabilities. Zeta potentials of the bare nanoparticles were not measured. It could be thought that getting aggregations of the bare nanoparticles would be faster than for the nanoparticles coated by PVP and dopamine. The zeta potential measurements took longer than the size measurements, and the PVP coated NPs were more aggregated than the dopamine coated NPs. The zeta potential results are shown Figure 3.17 to 3.19. The average zeta potential of dopamine/Fe_3O_4 was 23 mV (the maximum was 23.6 mV and the minimum was 22.4 mV) and for dopamine/$Co_{0.3}Fe_{2.7}O_4$ it was 24.9 mV (the maximum was 25.7 mV and the minimum was 24.4 mV). As can be seen in Table 3.7, the zeta potential values mean the nanoparticles tended to start aggregating; therefore, it could be assumed the size distribution graphs had two to three peaks. Some of the NPs were kept dispersed in DI water during the measurements, but the others started aggregating. It can also been seen from these zeta potential results that the Fe_3O_4 and $Co_{0.3}Fe_{2.7}O_4$ had characteristics of easily aggregating in solutions even if they were coated with polymers or dopamine to prevent aggregation.

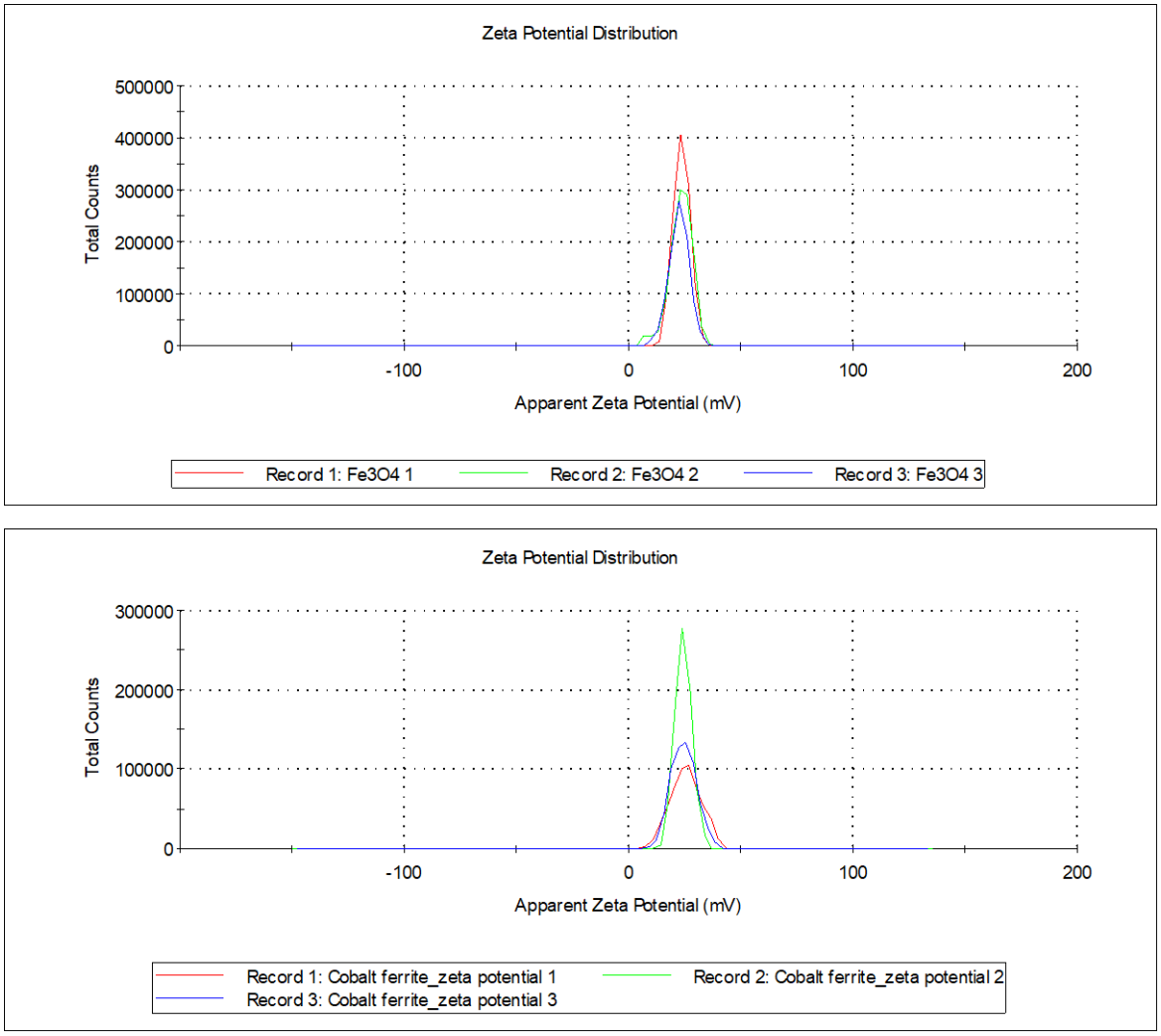

Figure 3.20 *Zeta potentials of dopamine coated Fe_3O_4 (top)and $Co_{0.3}Fe_{2.7}O_4$ (bottom).*

Figure 3.18 shows the zeta potentials of Fe_3O_4 in mixtures A and B. The zeta potential in mixture A was 33.4 to 36.6 mV (The zeta deviation was 11.6 to 12.8 which was also calculated by the DLS software automatically), and in mixture B it was 34.6 to 39.7 mV. (The zeta deviation was 12.9 to 16.4) from the particle sizes measured by DLS, Fe_3O_4 particles were most stable in mixture B. The zeta potential results were close to those of mixture A; however,

mixture B had higher zeta potential values, and there was almost “good stability”, meaning that DLS can measure a single particle size in the mixture.

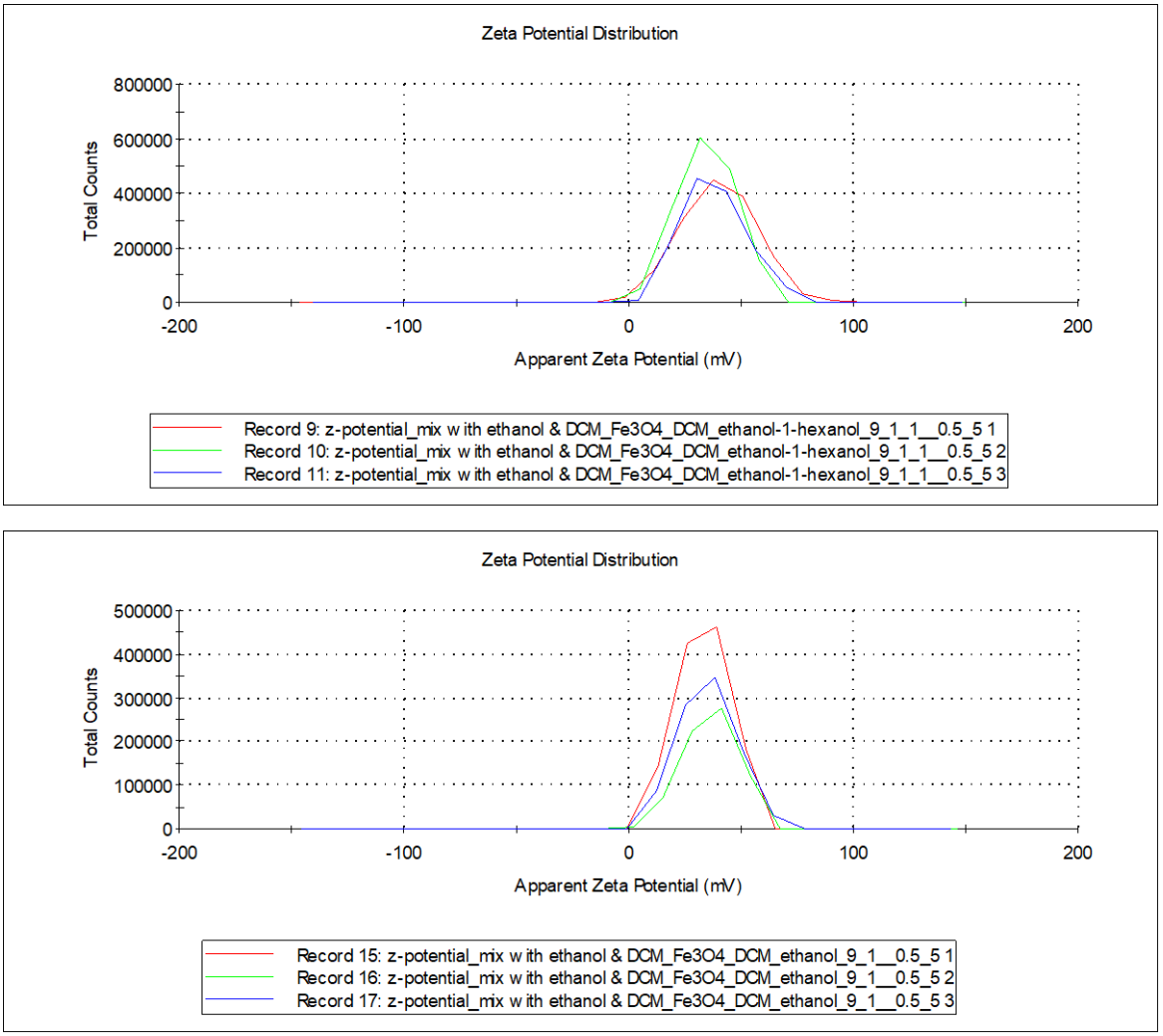

Figure 3.21 *The zeta potentials of Fe_3O_4. The top is not washed and mixed with ethanol and DCM. The bottom is washed with ethanol and dispersed in the mixture of ethanol and DCM*

Zeta potentials of $Co_{0.3}Fe_{2.7}O_4$ in the mixtures A and B were also measured to reveal the aggregation of the particles even in the mixtures. The zeta potential of $Co_{0.3}Fe_{2.7}O_4$ in mixture B was between 33.8 and 32.8 mV (The zeta deviation was 13.7 to 11.6), and in mixture

A it was between 26.8 and 28.5 mV (The zeta deviation was 9.39 to 10.4) (Figure 3.19). These values were lower than for Fe_3O_4 in the mixtures, and the particles in mixture A were at the "threshold of delicate stability" – this means that the particles still tend to aggregate in the mixture, and the aggregated particles tend to be counted as big particles by the size measurement. The zeta potential values of mixture B were close to those of mixture A, but it could be assumed that 1-hexanol in the mixture helped to form bigger aggregated particles and, therefore, the zeta potential was slightly higher than for mixture A.

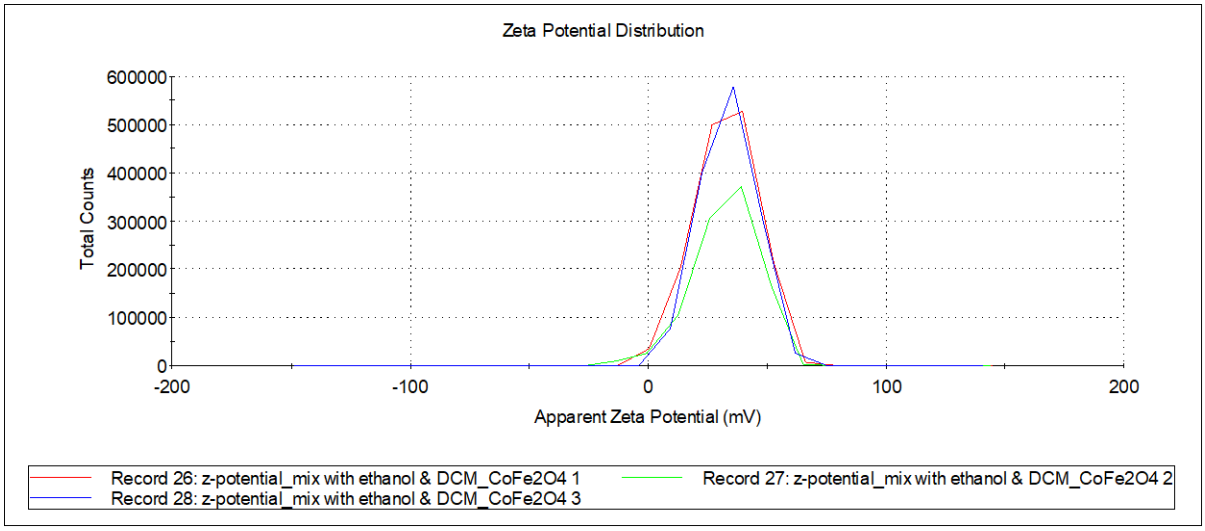

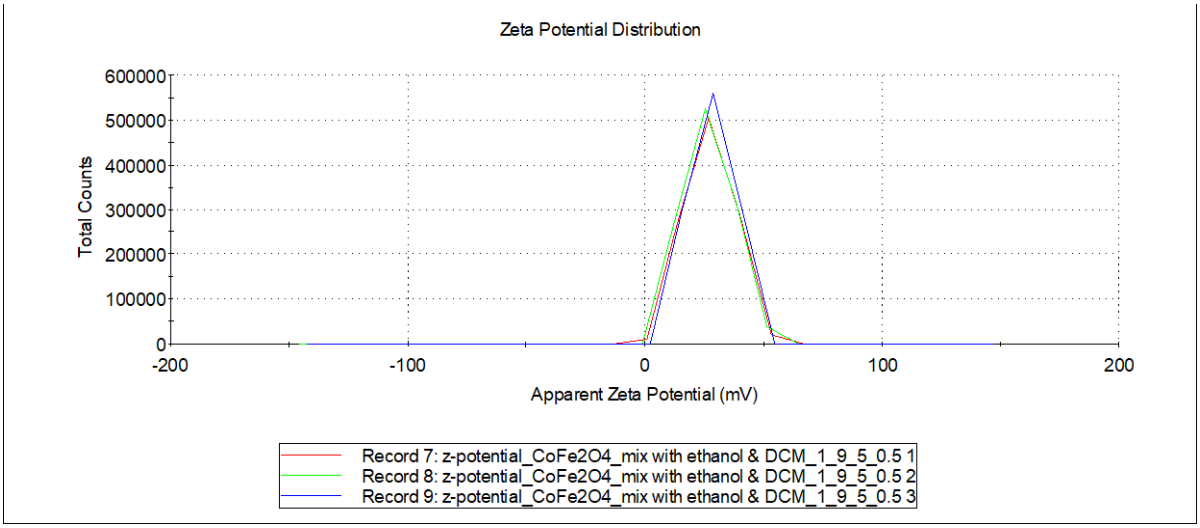

Figure 3.22 *The zeta potentials of $Co_{0.3}Fe_{2.7}O_4$. The top is not washed and mixed with ethanol and DCM. The bottom is washed with ethanol and dispersed in the mixture of ethanol and DCM*

Bare iron oxides and cobalt ferrite are hard particles, meaning that the charged layer around the particle is thinner than for soft particles, and the particle surface charge of hard particles is normally opposite to that around the slipping plain. This is why the particles have low zeta potentials and are easily aggregated in solution. However, soft particles have a thick charged layer, and if there are both positive and negative charges in the charged layer, have a high zeta potential and are easily dispersed in solution.[98] It could be thought the mixtures A and B made a thicker charged layer on the iron oxide particles so they became soft particles. However, cobalt ferrite had a thinner charged layer even with the mixtures; therefore, it could be assumed that the particles were aggregated.

From the results, it could be thought the iron oxides and cobalt ferrite surface charges were changed by drying, and the surface charges were not changed by the mixtures.

Furthermore, a higher dispersibility of the particles could be achieved by coating the surfaces with the original synthesised particle solution. For dispersing cobalt ferrite in solution, it is necessary to study why the particles aggregated even in the mixtures, or whether the mixtures could be optimised to disperse cobalt ferrite particles.

3.3.6 Magnetic properties

The magnetisation curves of Fe_3O_4 and $Co_{0.3}Fe_{2.7}O_4$ are shown in Figures 3.20 and 3.21, and the curves are symmetric. The maximum magnetisations of Fe_3O_4 and $Co_{0.3}Fe_{2.7}O_4$ were 58.9 and 69.6 emu/g, respectively, at 50 kOe (Table 3.11). They showed a tiny hysteresis around the origin points. The hysteresis of Fe_3O_4 passed through the origin point, but the hysteresis of $Co_{0.3}Fe_{2.7}O_4$ shifted to the negative magnetic field side. The magnetisation curve was measured by VSM, and the superconducting magnet normally traps flux while decreasing the magnetic field, thus causing a few Oe to a few tens of Oe of residual field. It is reasonable to suppose this affected the hysteresis shift.

The gap size of the hysteresis has a relationship with the particle superparamagnetism. The coercive field (H_c), maximum magnetisation (M_s) and remnant magnetisation (M_r) of Fe_3O_4 and $Co_{0.3}Fe_{2.7}O_4$ were obtained from the hysteresis curves and are shown in Table 3.11. M_r/M_s for the particles was less than 0.1, meaning it is superparamagnetic.[99] However, M_r/M_s for Fe_3O_4 was -0.005 due to the hysteresis shift.

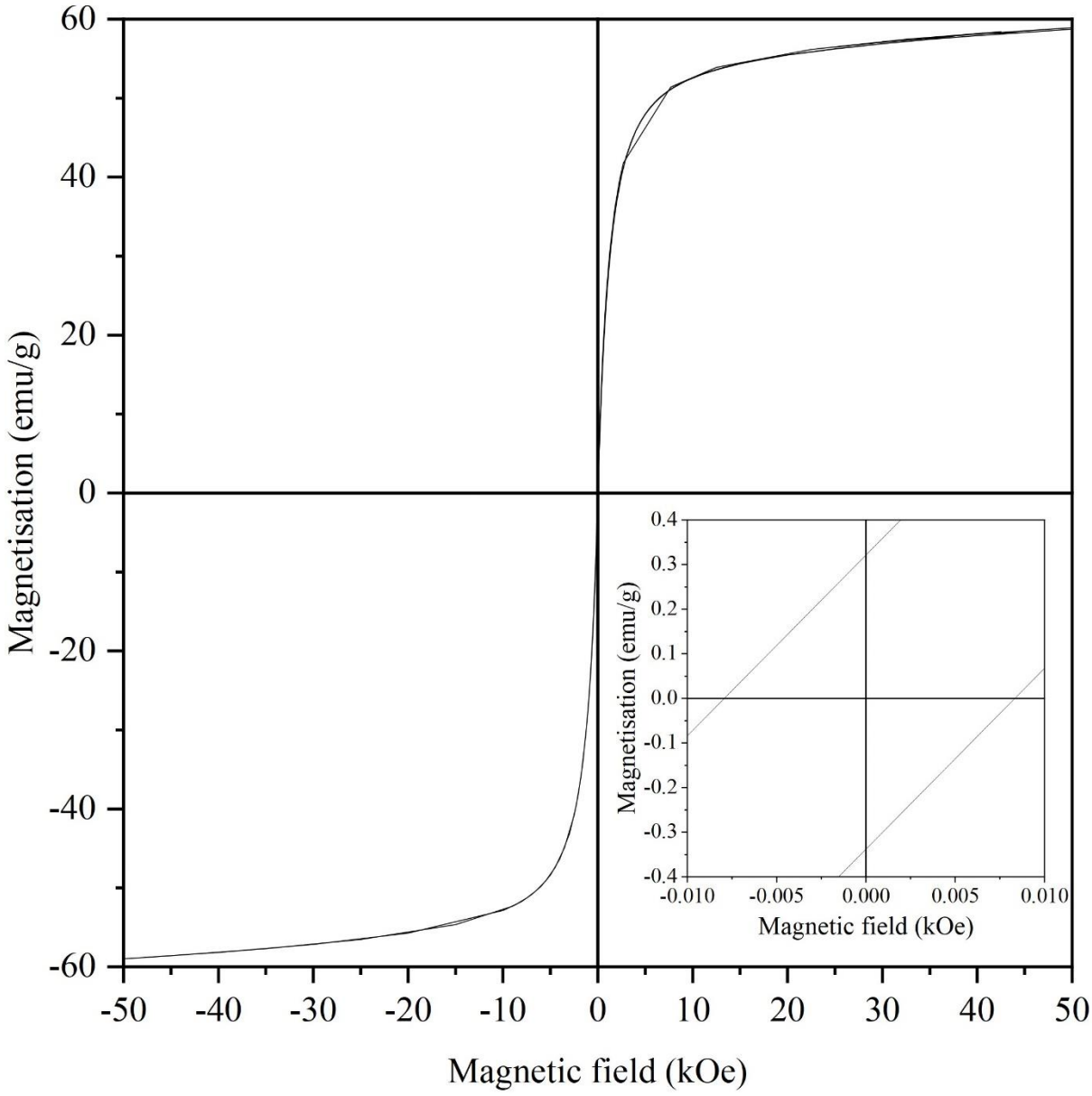

Figure 3.23 *Magnetisation curve and hysteresis loop of Fe_3O_4 measured by MPMS*

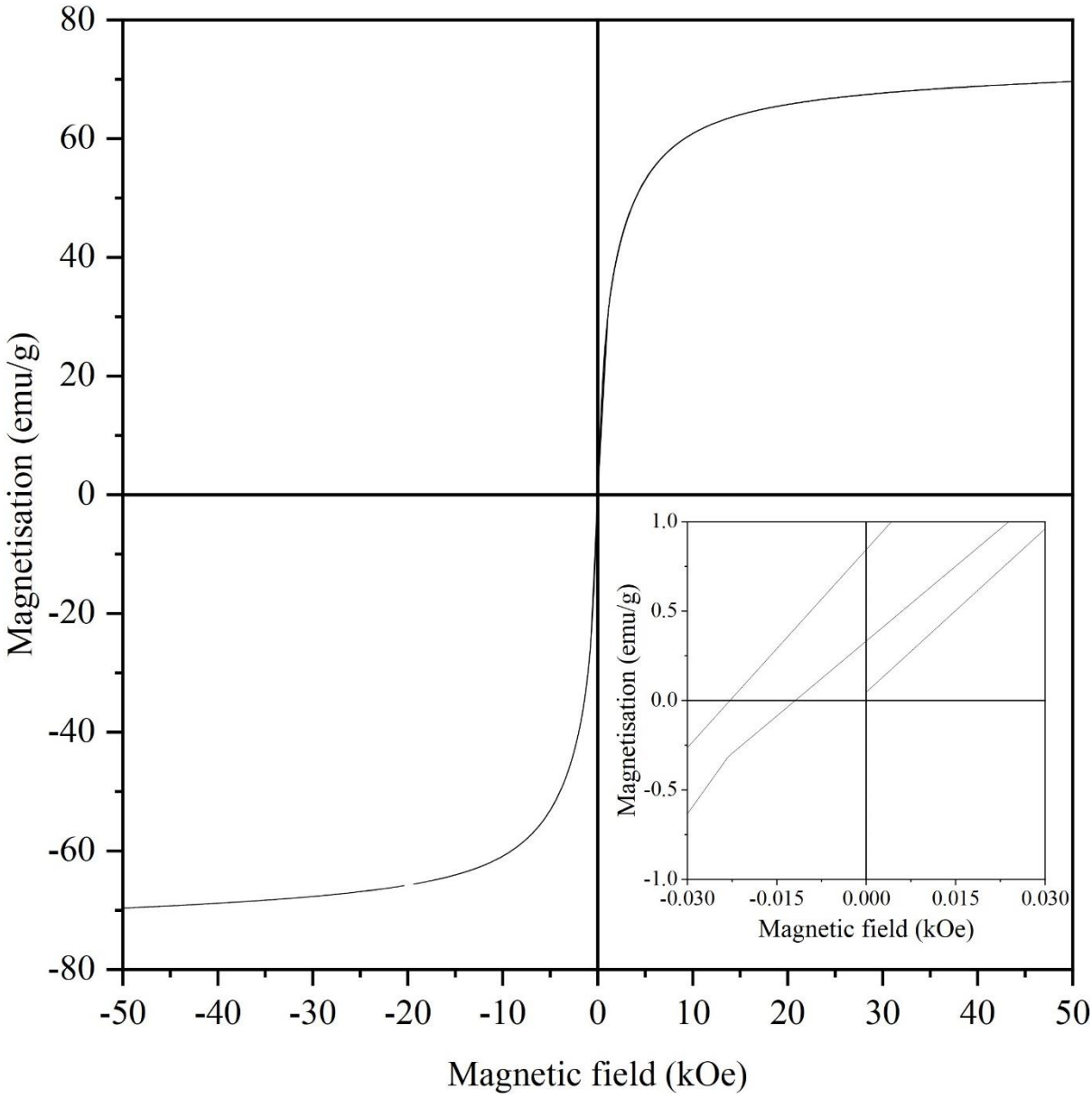

Figure 3.24 *Magnetisation curve and hysteresis loop of $Co_{0.3}Fe_{2.7}O_4$ measured by VSM*

Table 3.11 *Relationship of the magnetisation hysteresis gaps and superparamagnetism*

	Temperature (K)	H_c (kOe)	M_s (emu/g)	M_r (emu/g)	M_r/M_s
Fe_3O_4	300	-0.002	58.916	0.320	0.005
		0.008	-58.978	-0.338	0.006
$Co_{0.3}Fe_{2.7}O_4$	300	-0.023	69.600	0.840	0.012
		-0.012	-69.600	0.330	-0.005

The superparamagnetism of the particles were checked using the ZFC/FC curves. The blocking temperature, T_B, is also one of the indications of superparamgetism. Magnetic nanoparticle moments, which each nanoparticle has respectively, can escape from an energy well above this temperature, such that the particle is normally paramagnetic because of its thermal stability, or it is blocked below the temperature such that it becomes superparamagnetic because of sufficiently large thermal fluctuations in the absence of an external field (Livesey et al., 2018). The T_B of Fe_3O_4 and $Co_{0.3}Fe_{2.7}O_4$ are 140.36 and 257.69 K, respectively (Figures 3.22 and 3.23). As these temperatures are less than 300 K, the particles were superparamagnetic at room temperature. However, the T_B of Fe_3O_4 was over 100 K lower than that of $Co_{0.3}Fe_{2.7}O_4$, which means Fe_3O_4 is superparamagnetic even below 273.15 K.

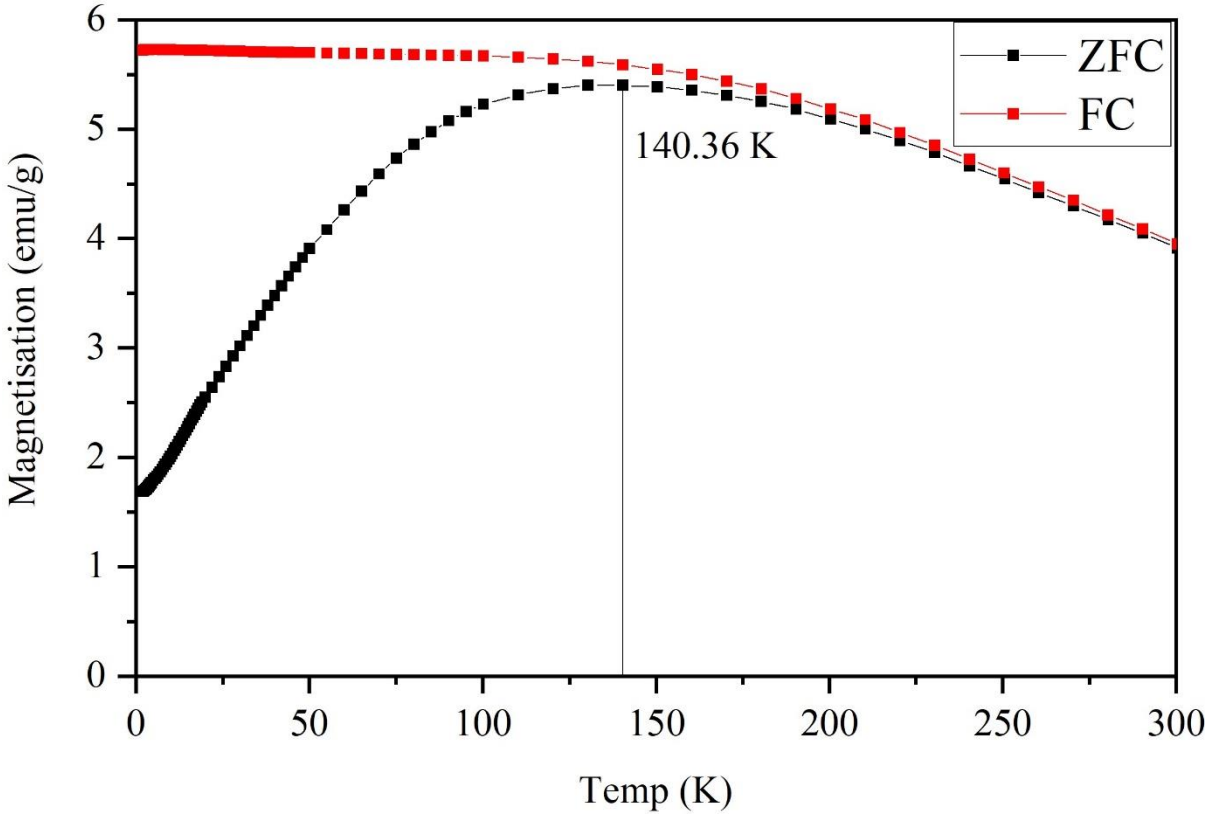

Figure 3.25 *ZFC/FC curves of* Fe_3O_4

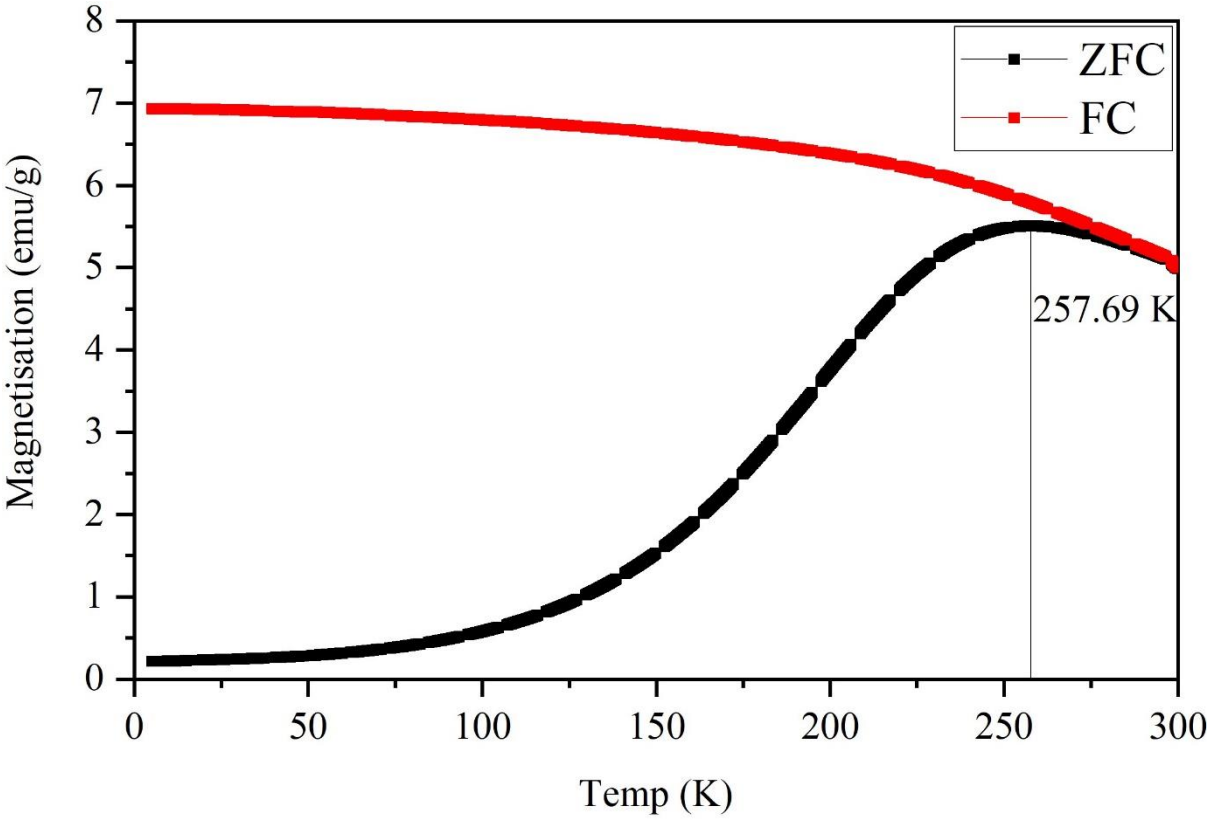

Figure 3.26 *ZFC/FC curves of* $Co_{0.3}Fe_{2.7}O_4$

Typically, the maximum magnetisation of nanosize $CoFe_2O_4$ was smaller than for Fe_3O_4, and the hysteresis was also bigger.[100-102] However, the synthesised $Co_{0.3}Fe_{2.7}O_4$ had a larger maximum magnetisation than Fe_3O_4. The reason could be assumed to be the synthesis route, reagents and the elemental composition of $Co_{0.3}Fe_{2.7}O_4$. The maximum magnetisation decreased with increasing the particle size, but it was affected by the formation of cobalt ferrite, which went through a nonmagnetic ferrihydrite phase due to its synthesis from reagents with Fe^{3+} salts.[75] The $Co_{0.3}Fe_{2.7}O_4$ was synthesised from the reagents having no Fe^{3+} salts, and the

particle sizes were less than 7.7 nm on average. Therefore, it could be assumed the $Co_{0.3}Fe_{2.7}O_4$ had a larger maximum magnetisation.

3.4 Conclusion

Fe_3O_4 and $Co_{0.3}Fe_{2.7}O_4$ were synthesised by the sol-gel method, and the best reactant was determined from the experimental results. The Fe_3O_4 could be synthesised by 1-hexanol with $Fe(acac)_3$, but a mix of Fe_3O_4 with α-Fe_2O_3 and/or γ-Fe_2O_3 was always synthesised when benzyl alcohol was used as the reactant. The difference of the final products by the reactants was determined from their vapour pressures by the calculations. The vapour pressure in the closed container of 1-hexanol was higher than benzyl alcohol, and the actual pressures in the autoclave could also assumed 1- hexanol was higher than benzyl alcohol from the calculation and the final products whether Fe_3O_4 or the mixture with α-Fe_2O_3 and/or γ-Fe_2O_3.

From the experimental and calculation results, it was revealed higher pressure was needed to synthesis the Fe_3O_4 while the heating process: The synthesis condition was the ratio of $Fe(acac)_3$ to 1-hexanol was 1:10 and heated for 5 hr at 175 ºC (Table 3.12).

Table 3.12 *Summary of the synthesis conditions of Fe_3O_4 and $Co_{0.3}Fe_{2.7}O_4$*

Product	Reagent ratio			Synthesis condition		Average particle size by TEM (nm)
	$Fe(acac)_3$ (g)	$Co(acac)_2$ (g)	1-hexanol (ml)	Temperature (ºC)	Heating time (hr)	
Fe_3O_4	1.00		10	170	5	8.0
$Co_{0.3}Fe_{2.7}O_4$	1.70	0.62	20	180	10	7.5

Both Fe_3O_4 and $Co_{0.3}Fe_{2.7}O_4$ were characterised by XRD, Raman and/or XRF to identify the chemical formula. The $Co_{0.3}Fe_{2.7}O_4$ was more Fe rich than normal cobalt ferrite ($CoFe_2O_4$), however, the magnetisation was about 10 emu/g higher than the Fe_3O_4 at 50 kOe, and the average particle diameters of both products were less than 8 nm. From the tiny hysteresis of the magnetisation curves and the blocking temperature of the ZFC/FC curves, it was confirmed both products were superparamagnetic

Attempts were made to obtain the particle diameters of both products by DLS. Once already washed and dried, particles of both Fe_3O_4 and $Co_{0.3}Fe_{2.7}O_4$ were easily aggregated during the measurement, even if their surfaces were coated by dopamine, PVP or citric acid. However, unwashed Fe_3O_4 particles were well dispersed in the mixture A (ethanol and DCM), and the mixture B (1-hexanol, ethanol and DCM), especially in mixture B. The reason was revealed by the zeta potentials of the DLS measurements. The zeta potential of mixture B was highest.

The $Co_{0.3}Fe_{2.7}O_4$ was always aggregated even in the mixtures, but the zeta potentials were similar to that of the Fe_3O_4. The reason was assumed to be from the charged layer on the $Co_{0.3}Fe_{2.7}O_4$ particle surfaces.

4 M_xO_y/SiO_2

4.1 Introduction

SiO_2, introduced via either silanol or TEOS reaction, can be used to coat nanosized metal oxide (M_xO_y) particles to enable grafting or to functionalise them via, for example, with amines or polymers for drug delivery and bioengineering applications.[103-105] The SiO_2 coating not only functionalises the M_xO_y particles but also protects them from further oxidation, further stabilising them in solution, and preventing or minimising their aggregation by their magnetic dipole forces.[106] Bumb et al. (2008)[107] also reported that silica helps the nanoparticle cores to not self-aggregate and behave ferromagnetically. Furthermore, a coating of SiO_2 can prevent the release of cobalt from $CoFe_2O_4$.[108]

The Stöber method has been commonly applied to synthesise M_xO_y/SiO_2 nanoparticles. A uniform and nano mater scale thin SiO_2 layer on the M_xO_y is desirable to prevent a decrease in the maximum magnetisation of the nanoparticles. Generally, SiO_2 encapsulates some M_xO_y particles, and they become located at the centre of a SiO_2 coating because of their hydrophobic interactions,[41] and the M_xO_y/SiO_2 particles are formed as uniformly sized spherical particles. However, with a thinner SiO_2 coat it is possible to aggregate the M_xO_y/SiO_2 particles and form irregularly shaped particles due to the encapsulation of more M_xO_y in the SiO_2; this could be led by the microemulsion of the SiO_2 reaction medium, such as when the concentration of TEOS in water is higher.[109] The aggregated M_xO_y/SiO_2 could also show hysteresis as the

aggregation of M_xO_y particles in the SiO_2 means they behave like bigger particles, and they are not superparamagnetic. The particle aggregation depends on the M_xO_y/SiO_2 dispersal method used during the synthesis: the particles made with mechanical stirring aggregate more than those made with ultrasonication.[40] In contrast, when the SiO_2 coating of M_xO_y is thinner (less than 2.5 nm) and the particles are not aggregated, they exhibit superparamagnetic behaviour, and the SiO_2 layer inhibits the maximum magnetisation less.[107]

4.2 Experimental details

4.2.1 M_xO_y/SiO_2

The Stöber method was used for the M_xO_y/SiO_2 syntheses: 200 ml of ethanol (Fisher Scientific) was diluted by 50 ml of DI water (the ratio of ethanol to DI water was 4:1). The pH of the solution was adjusted to 10.50 or 11.0 using a few drops of 28 % ammonia solution (Fisher Scientific). The solution pH was measured by LAQUAtwin (HORIBA), and it was measured using an auto-hold mode that a pH value held that moves within 3 digit for 10 sec. The solution was degassed using nitrogen gas for 10 min using a Schlenk line. Then 250 mg of Fe_3O_4 or $Co_{0.3}Fe_{2.7}O_4$ nanoparticles were put in the degassed solution, and it was sonicated for 10 min to disperse the NPs. Next, 1.0 to 2.0 ml of TEOS (≥99.0 %, Sigma Aldrich) was put in the mixture, and it was sonicated at 20, 30 or 40 °C for 2 hours. The product was washed with

ethanol and centrifuged at 11000 rpm for 15 min three times. Finally, it was dried at 60 °C for the further M_xO_y/SiO_2/zeolite syntheses and characterisation.

4.2.2 XRD, Raman spectroscopy and VSM

The measurements were carried out by the same instruments and under the same conditions used for the M_xO_y measurements (See Chapter 3.24, 3.2.6 and 3.2.8). The VSM work was carried out by Dr Mingee Chung (University of Birmingham) and his PhD student Jake Head (University of Birmingham).

4.2.3 XRF

This characterisation was also carried out using the S8 Tiger (Bruker) under the same conditions as M_xO_y. The ratio of M_xO_y and SiO_2 was calculated from the obtained elemental weight percent (w%).

4.2.4 TEM-EDS

Images of more small parts of the samples and the surface elemental compositions were also captured by the TEM-EDS, and the method of sample preparation onto the TEM copper grids was the same as for the other TEM sample measurements. The TEM-EDS work was carried out with Dr Gnanavel Thirunavukkarasu (University of Birmingham).

4.2.5 Theoretical SiO2 thickness calculation

The theoretical SiO_2 thickness was calculated from the TEM observations of the SiO_2 thickness and the M_xO_y diameters. The masses of SiO_2 and M_xO_y were calculated from the following equation:

$$m = \frac{4}{3}\pi r^3 \times \rho$$

Equation 4-1 *The equation for a spherical particle volume.*

where m is the mass of SiO_2 or M_xO_y, r is the radius of the particles, and ρ is the nanoparticle density (for Fe_3O_4, ρ = 5.24 g/cm^3; for $CoFe_2O_4$, ρ = 5.23 g/cm^3; and for SiO_2, ρ = 2.05 g/cm^3).

The theoretical mass of SiO_2 (m_{shell}) and the mass of the core part of SiO_2 that needs to be substituted with the mass of M_xO_y (m_{core}) were calculated to find the mass of the outer layer SiO_2 ($m_{outer\ layer}$):

$$m_{outer\ layer} = m_{shell} - m_{core}$$

The ratio of SiO_2 to Fe_3O_4 or $Co_{0.3}Fe_{2.7}O_4$ was calculated from $m_{outer\ layer}$ and the mass of M_xO_y (m_{MxOy}):

$$The\ ratio = \frac{m_{outer\ layer}}{m_{MxOy}}$$

To calculate the theoretical SiO_2 thickness, the ratio of SiO_2 to Fe_3O_4 or $Co_{0.3}Fe_{2.7}O_4$ that was calculated from the XRF measurements was substituted into the equations.

4.3 Results

4.3.1 XRD and Raman peaks of M_xO_y/SiO_2

The XRD patterns of Fe_3O_4/SiO_2 and $Co_{0.3}Fe_{2.7}O_4/SiO_2$ were compared with those of the bare Fe_3O_4 and $Co_{0.3}Fe_{2.7}O_4$ to check whether their shapes or compositions had changed in terms of peak shifts and widths. Figures 4.1 and 4.2 show that the Fe_3O_4/SiO_2 and $Co_{0.3}Fe_{2.7}O_4/SiO_2$ peaks appeared in almost the same positions as they had for the bare particles.

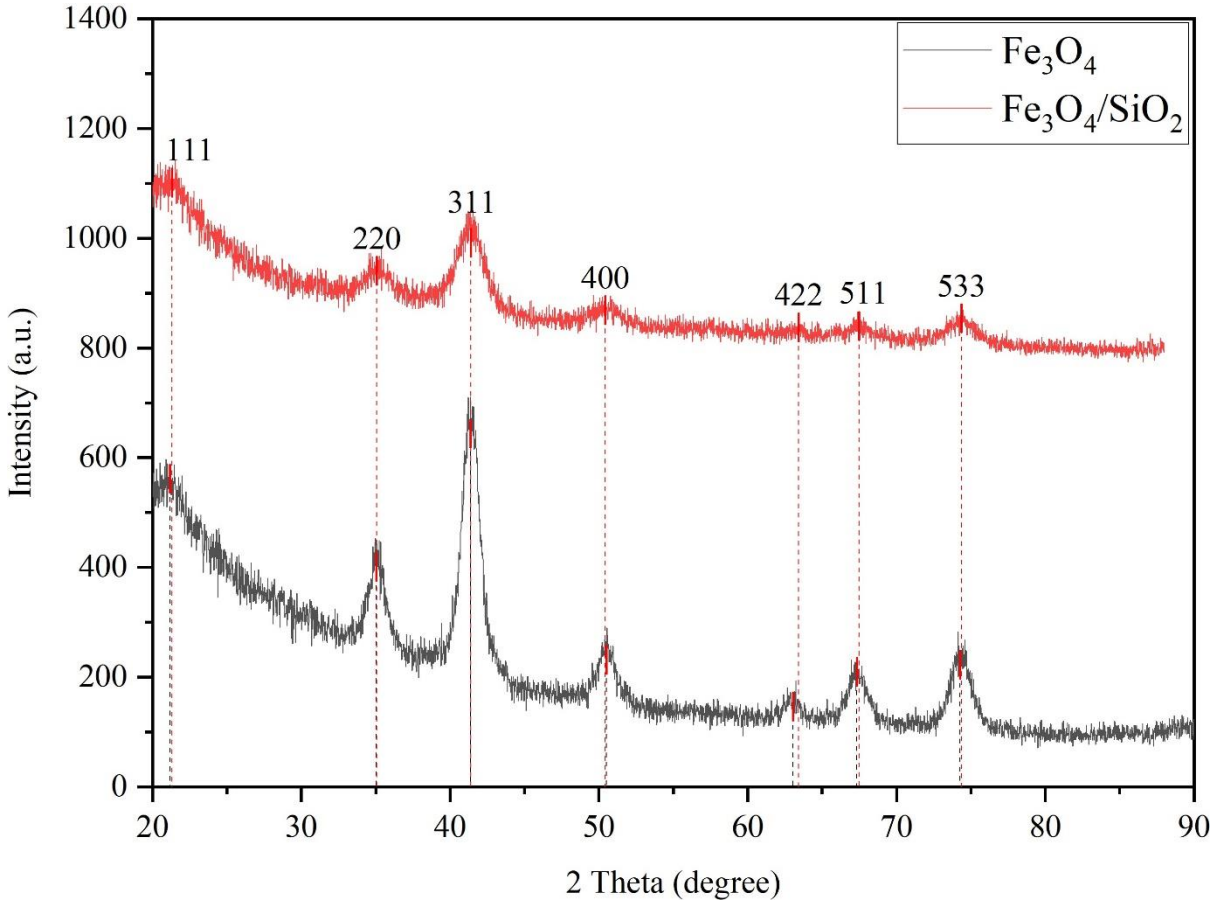

Figure 4.1 *XRD patterns of Fe_3O_4 (bottom) and Fe_3O_4/SiO_2 (top) with the hkl indices*

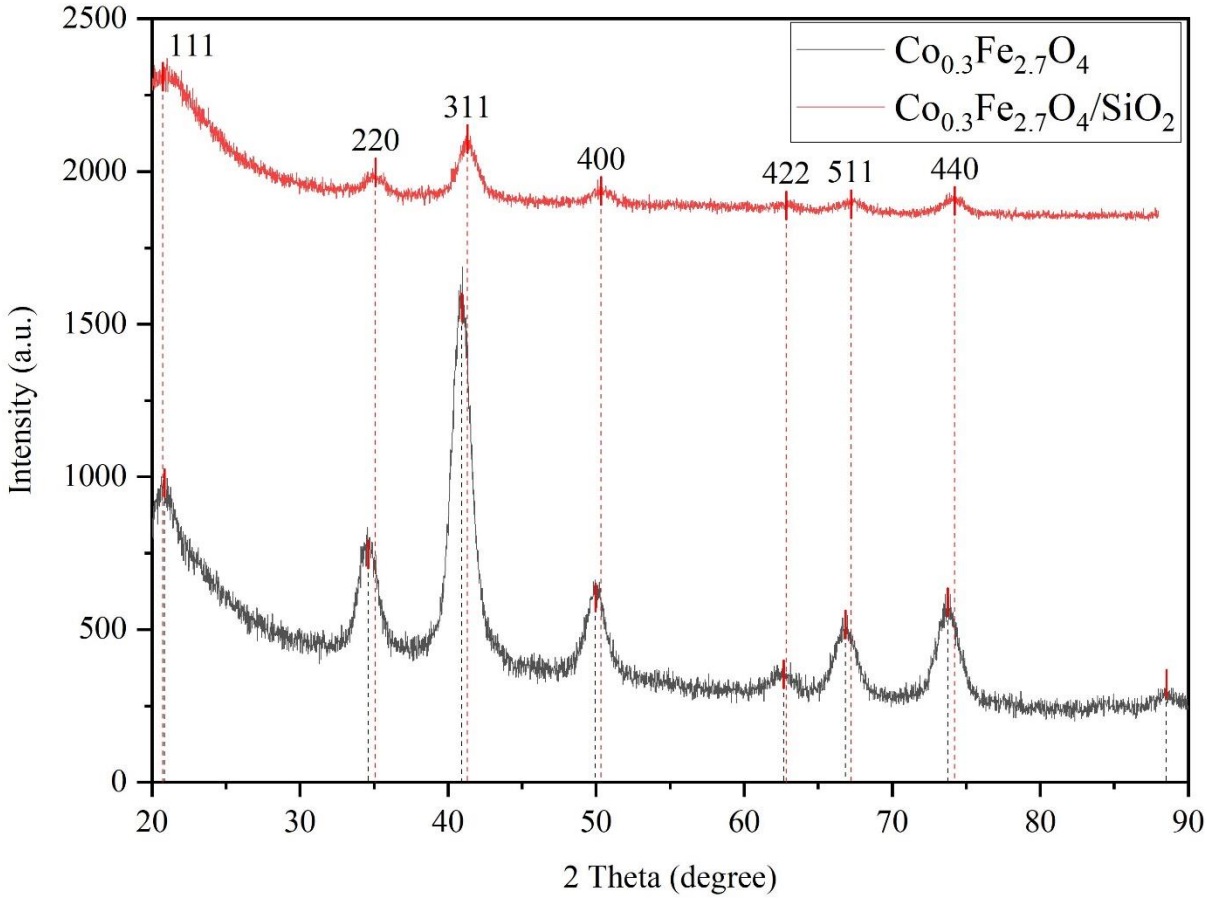

Figure 4.2 *XRD patterns of $Co_{0.3}Fe_{2.7}O_4$ (bottom) and $Co_{0.3}Fe_{2.7}O_4/SiO_2$ (top) with the hkl indices*

To check if the Fe_3O_4 was oxidised and changed by the SiO_2 coating synthesis, Fe_3O_4/SiO_2 was also measured by Raman spectroscopy (Figure 4.3). There were three Raman peaks at 693.811, 497.720 and 357.655 cm^{-1}. According to Wei et al. (2015),[110] Fe_3O_4 has Raman peaks at around 665, 540 and 311 cm^{-1} and γ-Fe_2O_3 has Raman peaks at around 700, 500 and 350 cm^{-1}. Therefore, the iron oxide of Fe_3O_4/SiO_2 may have been changed to γ-Fe_2O_3. The iron oxide transformation as also identified through the hysteresis of the magnetisation curves (see Section 4.3.3).

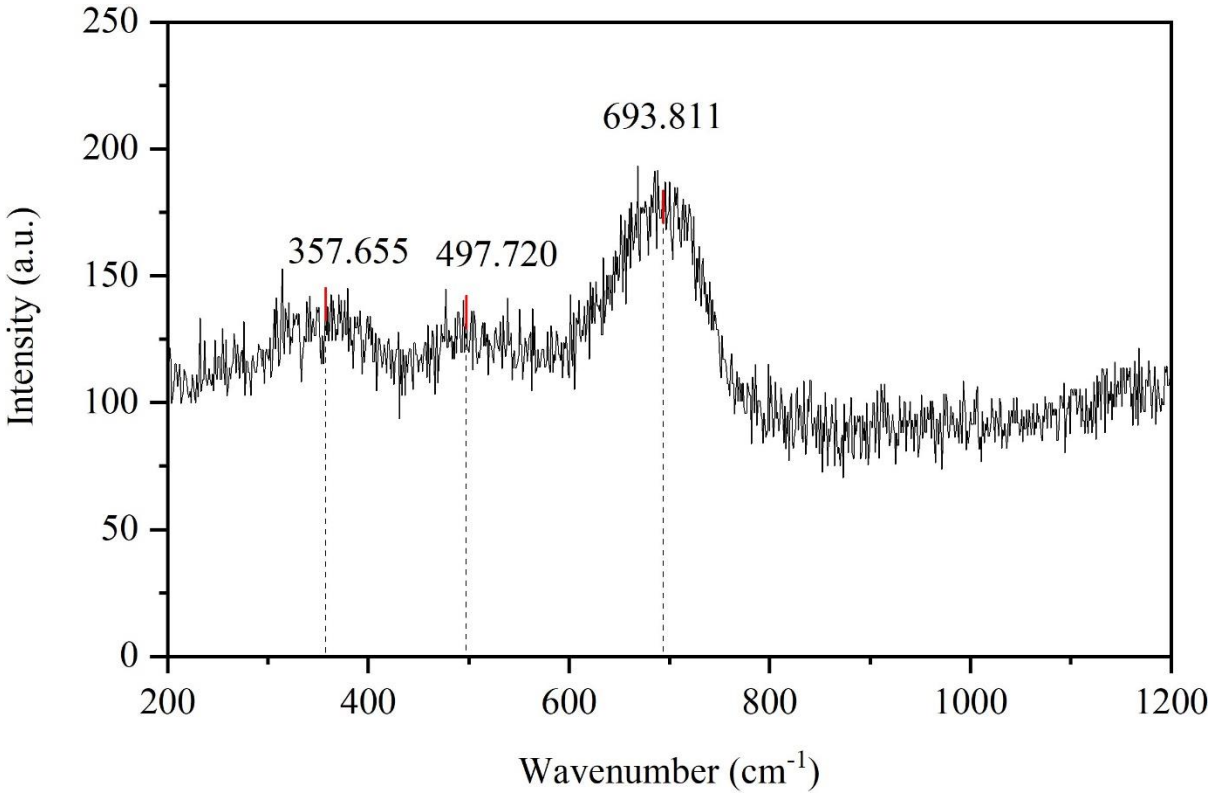

Figure 4.3 *Raman spectra peaks of Fe_3O_4/SiO_2*

4.3.2 Thickness and particles size of M_xO_y/SiO_2

The thickness of SiO_2 on Fe_3O_4/SiO_2 and $Co_{0.3}Fe_{2.7}O_4/SiO_2$ was observed by TEM. The images are in Figure 4.4, and the comparison of the theoretical SiO_2 thickness and that observed in the TEM images is in Table 4.1. The theoretical SiO_2 thickness was calculated from the elemental compositions of M_xO_y/SiO_2 obtained by the XRF measurements. The SiO_2 could not be observed when the thickness was less than about 1 nm. The TEM image of $Co_{0.3}Fe_{2.7}O_4/SiO_2$ (bottom right) captured the thinnest SiO_2 layer, which was less than 2 nm. From the tabulated thickness comparisons, the thicknesses determined from the TEM images were almost same as

the calculated theoretical thicknesses of 1.95 nm. When the theoretical thicknesses were less than 1.95 nm the TEM images did not capture any SiO_2 on the M_xO_y particles (top right and bottom left images). However, the image with the thickest SiO_2 layer (top left) did not match the theoretical thickness: the theoretical thickness was 4.71 nm, but that observed in the image was over 30 nm. The images show that some of the thicker SiO_2 layers encapsulated a lot of Fe_3O_4 nanoparticles, but some of the thicker SiO_2 particles did not contain any Fe_3O_4 particles. However, the thinner SiO_2 layer on the $Co_{0.3}Fe_{2.7}O_4$ were coated all of the particles, and the layer thicknesses were almost even. The theoretical thickness calculation assumes that all nanoparticles are evenly coated by the SiO_2. Therefore, it is assumed that the theoretical thickness is reliable when the M_xO_y/SiO_2 has less SiO_2, such as when the real thickness is around 2 nm.

Table 4.1 *Comparison of theoretical SiO_2 thicknesses M_xO_y/SiO_2 particles with those observed by the TEM.*

	Theoretical SiO_2 thickness (nm)	SiO_2 thickness observed by the TEM (nm)
Fe_3O_4	4.71	> 30
	1.62	Not observed
$CoFe_{2.66}O_{4.99}$	1.95	< 2
	0.44	Not observed

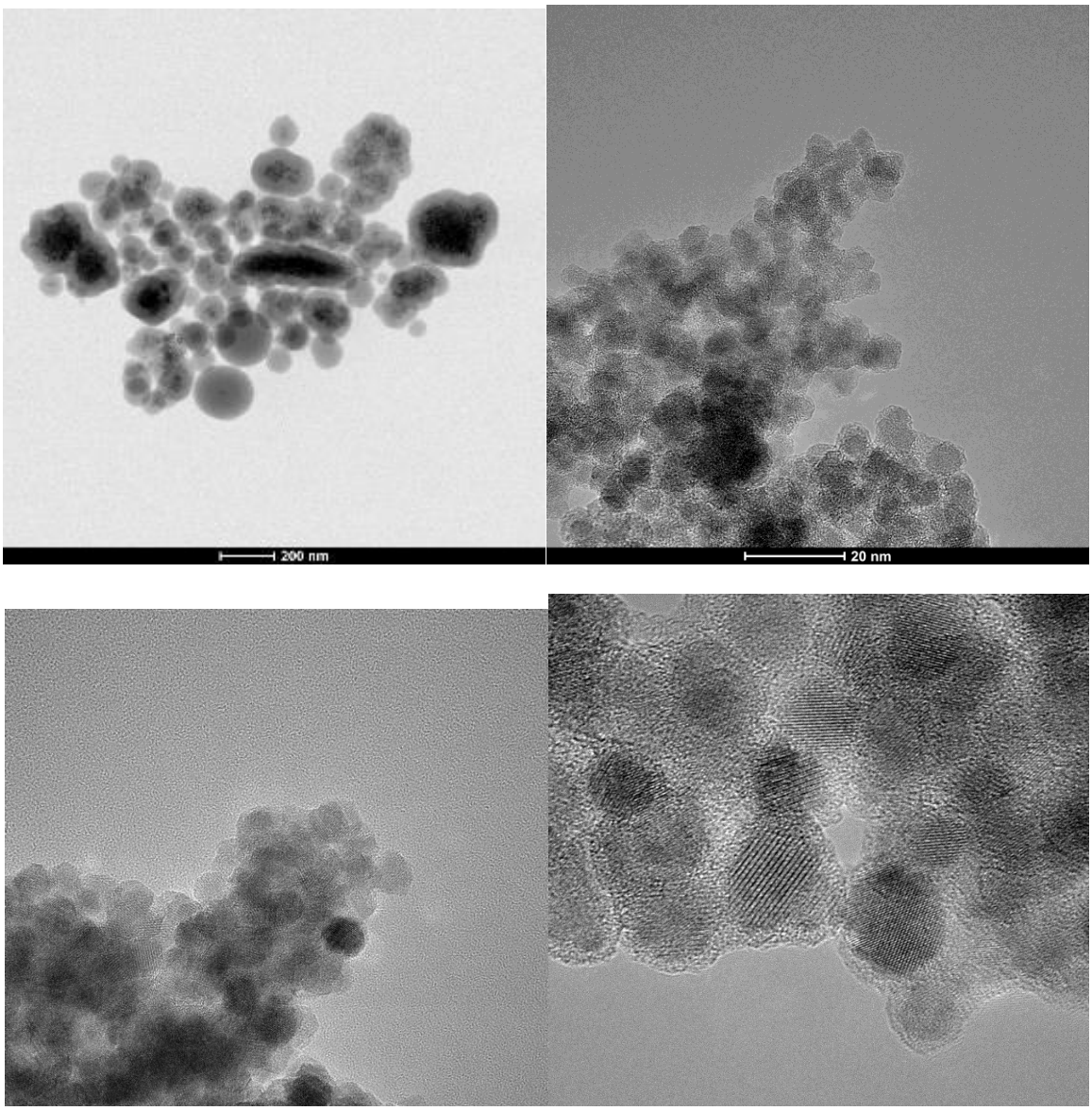

Figure 4.4 *TEM images of Fe_3O_4/SiO_2 (top) and $Co_{0.3}Fe_{2.7}O_4/SiO_2$ (bottom). The black parts are Fe_3O_4 or $Co_{0.3}Fe_{2.7}O_4$, and the grey parts around the black parts were SiO_2.*

The elemental composition of the $Co_{0.3}Fe_{2.7}O_4/SiO_2$ with the measured SiO_2 thickness of around 2 nm was observed by TEM-EDS (Figure 4.5). The images show all the elements within $Co_{0.3}Fe_{2.7}O_4/SiO_2$. Furthermore, there was a lot of Si around the Co and Fe of the nanoparticles, which means the particles were sufficiently coated by the SiO_2.

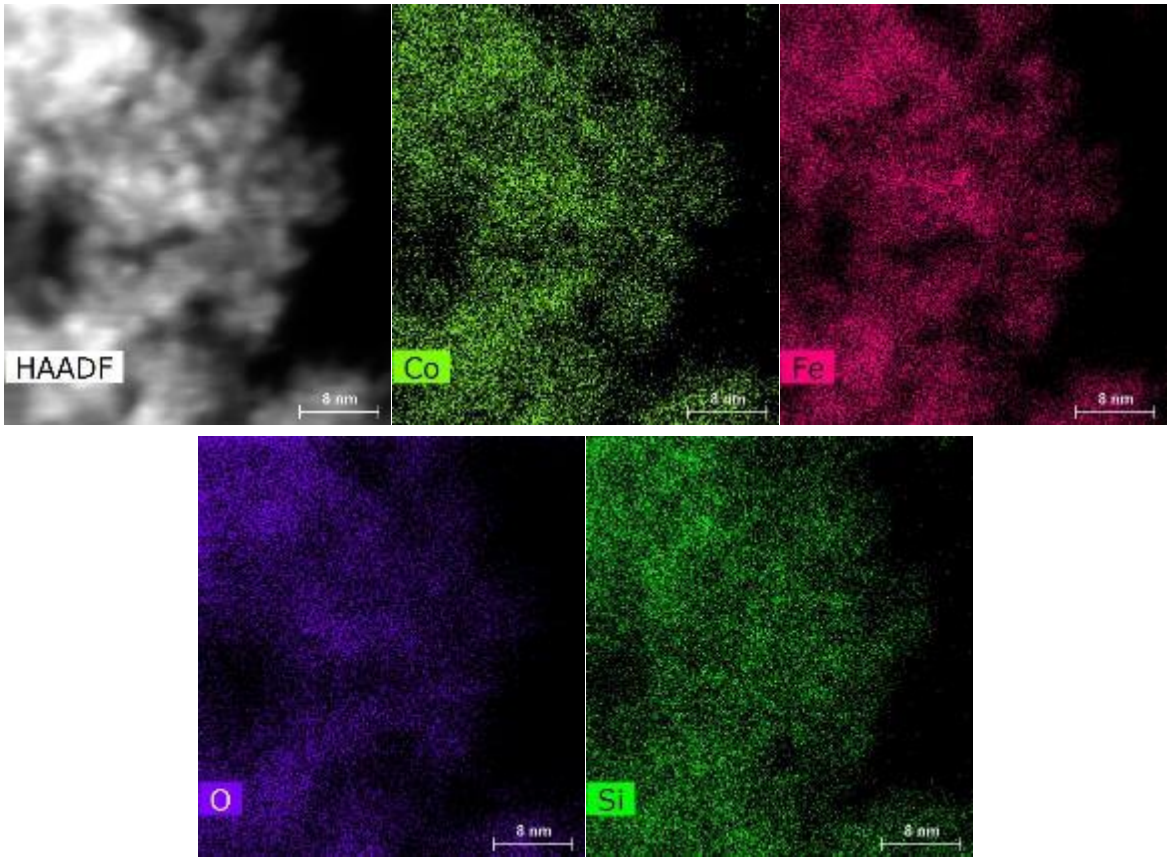

Figure 4.5 *TEM-EDS mapping images of $Co_{0.3}Fe_{2.7}O_4$ where SiO_2 thickness was around 2 nm. Where HAADF is High Angle Annular Dark Field.*

The SiO_2 thicknesses were controlled by the synthesis temperature, the amount of TEOS that was the SiO_2 source, and the dispersant pH. The results are shown in Figure 4.6. The dispersant pH did not affect the thickness, but the synthesis temperature did: thicker SiO_2 was formed at higher synthesis temperatures. Dang et al. (2010)[40] also reported SiO_2 thickness, showing that agglomeration was increased at higher synthesis temperatures; in particular, agglomeration increased dramatically between 40 and 50 ˚C. They also investigated the effect

of the dispersant pH on the SiO_2 thickness, but found that it did not contribute much to the SiO_2 growth.

The thicknesses varied due to the coarse control of the water bath temperature of the sonicator. The temperature changed between 4.2 and 14.9 ºC from the set temperature of the sonicator (both increasing and decreasing the temperature). This might depend on the water level in the bath, or the cooler or sample flask positions, but it was difficult to determine which affected the SiO_2 thickness due to the equipment.

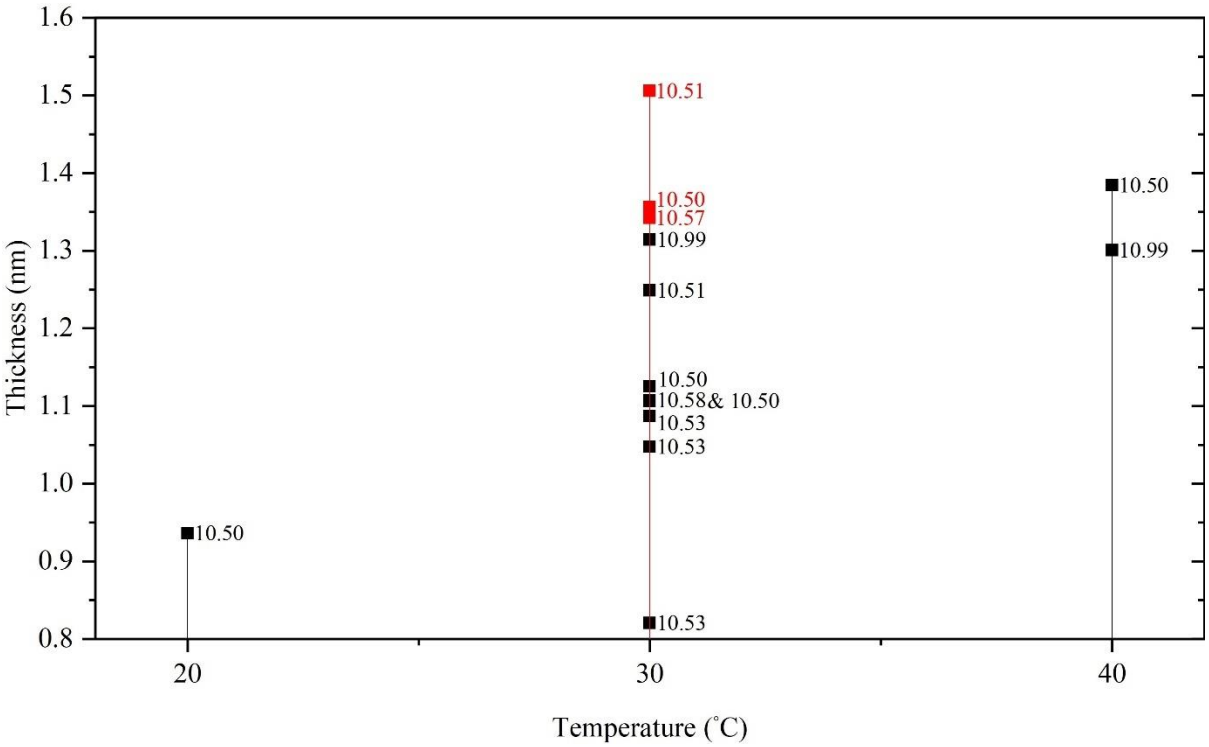

Figure 4.6 *Relationship of theoretical SiO_2 thickness on Fe_3O_4 (black) and $CoFe_{2.66}O_{4.99}$ (red) with the synthesis temperature and pH (the numbers by the side of the dots).*

The amount of TEOS that was used for the M_xO_y/SiO_2 synthesis was also compared with the theoretical SiO_2 thickness and the dispersant pH (Figure 4.7). When the amount of

TEOS was increased, the SiO_2 thickness also increased; in particular, it dramatically increased when the amount of TEOS increased from 1.0 to 2.0 ml (0.7 to 2.5 nm). Lu et al. (2002)[42] also reported that the SiO_2 thickness on Fe_3O_4 increased when the amount of TEOS was increased, and that the Fe_3O_4/SiO_2 that used more TEOS was monodispersed because of a strong chemical affinity between Fe_3O_4 and the higher concentration of silicate; therefore, a single SiO_2 particle can encapsulate Fe_3O_4 particles in the centre.

To make the same SiO_2 thickness on the Fe_3O_4 and $Co_{0.3}Fe_{2.7}O_4$, 2.0 ml of TEOS was used for Fe_3O_4/SiO_2/zeolite and 1.0 ml of TEOS was used for $Co_{0.3}Fe_{2.7}O_4/SiO_2$/zeolite.

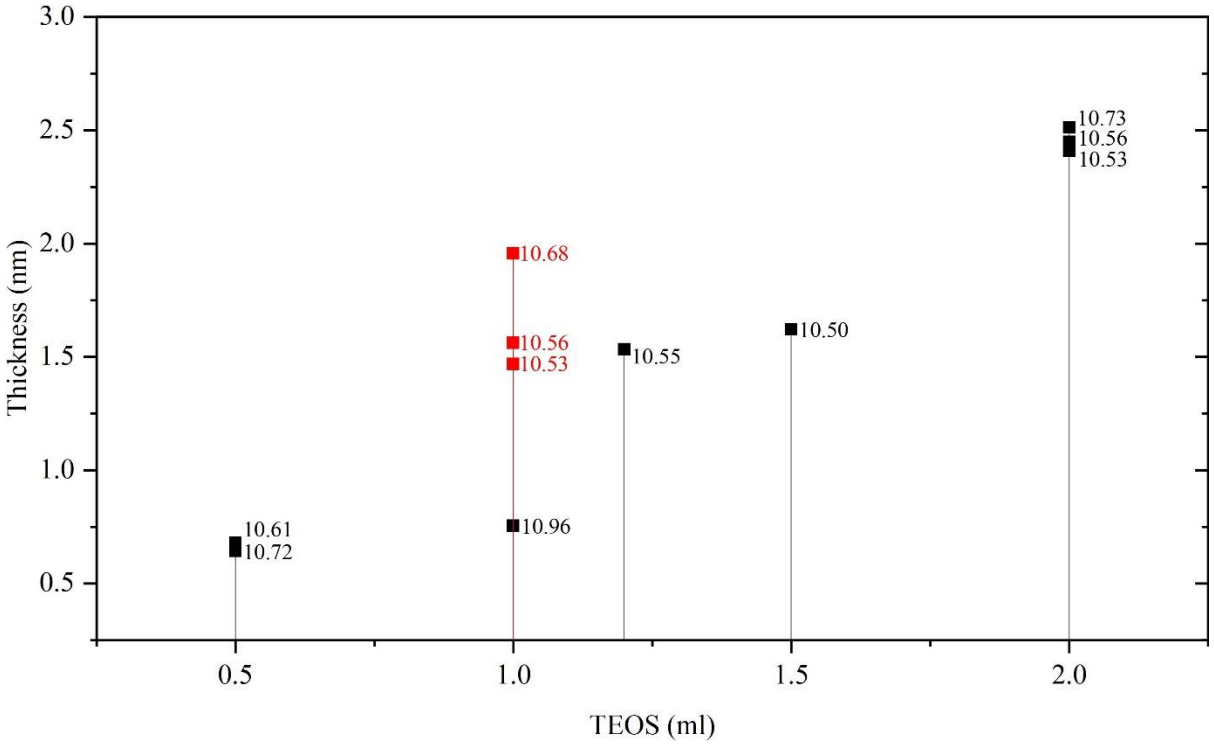

Figure 4.7 *Relationship of theoretical SiO_2 thickness on Fe_3O_4 (black) and $Co_{0.3}Fe_{2.7}O_4$ (red) with the amount of TEOS used and pH (the sonicator water bath temperature was 30˚C).*

4.3.3 Magnetic properties

The magnetisation curves of both Fe_3O_4/SiO_2 and $Co_{0.3}Fe_{2.7}O_4/SiO_2$ were saturated at the origin points, but the hysteresis was shifted to the positive magnetic field side (Figures 4.8 and 4.9). The measurement was done by the VSM and it could be thought that the shifts were due to the trapped flux. The hysteresis gaps were narrow, and the M_r/M_s values of the particles were less than 0.1 (Table 4.2).

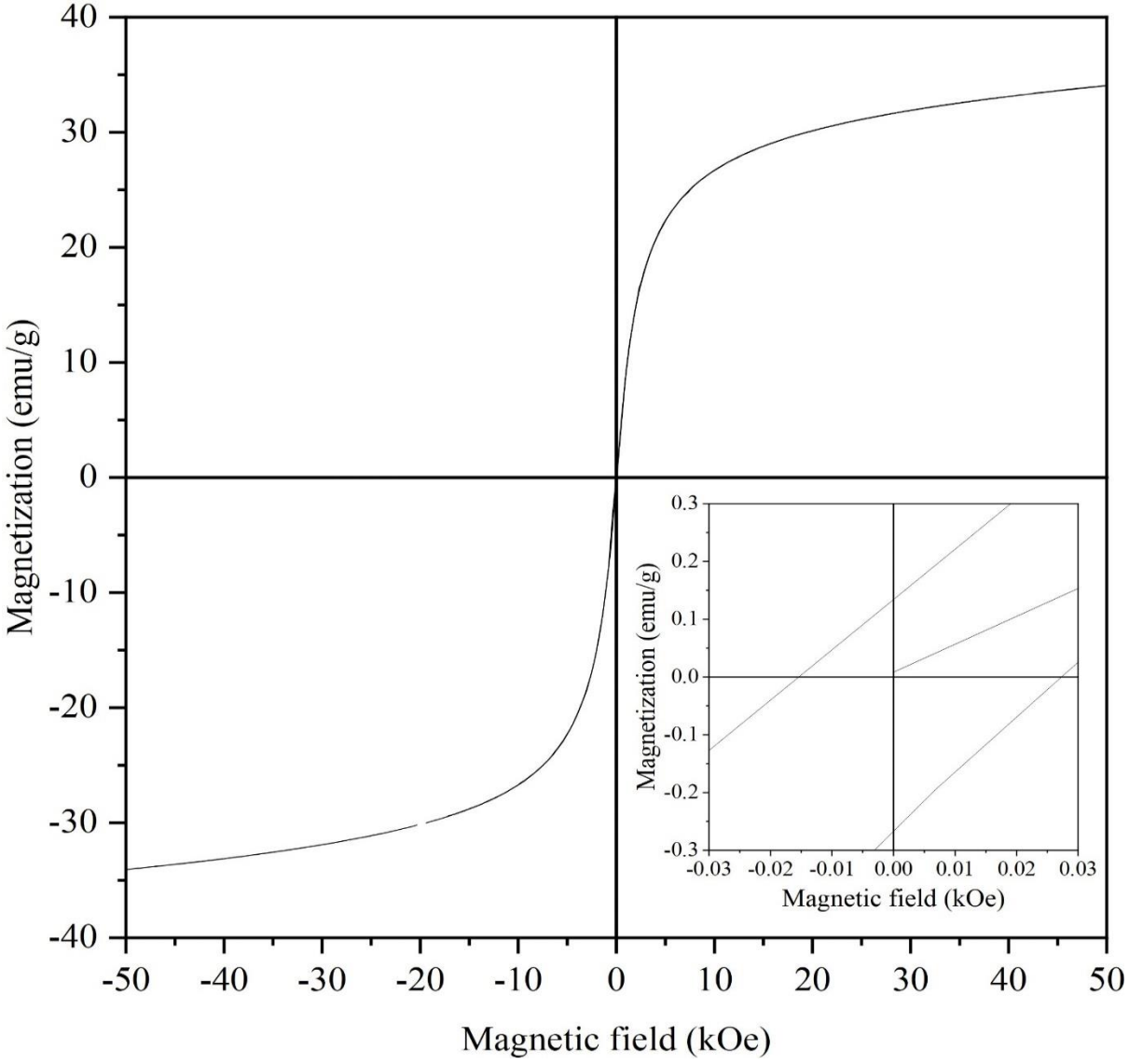

Figure 4.8 *Magnetisation curve of Fe_3O_4/SiO_2*

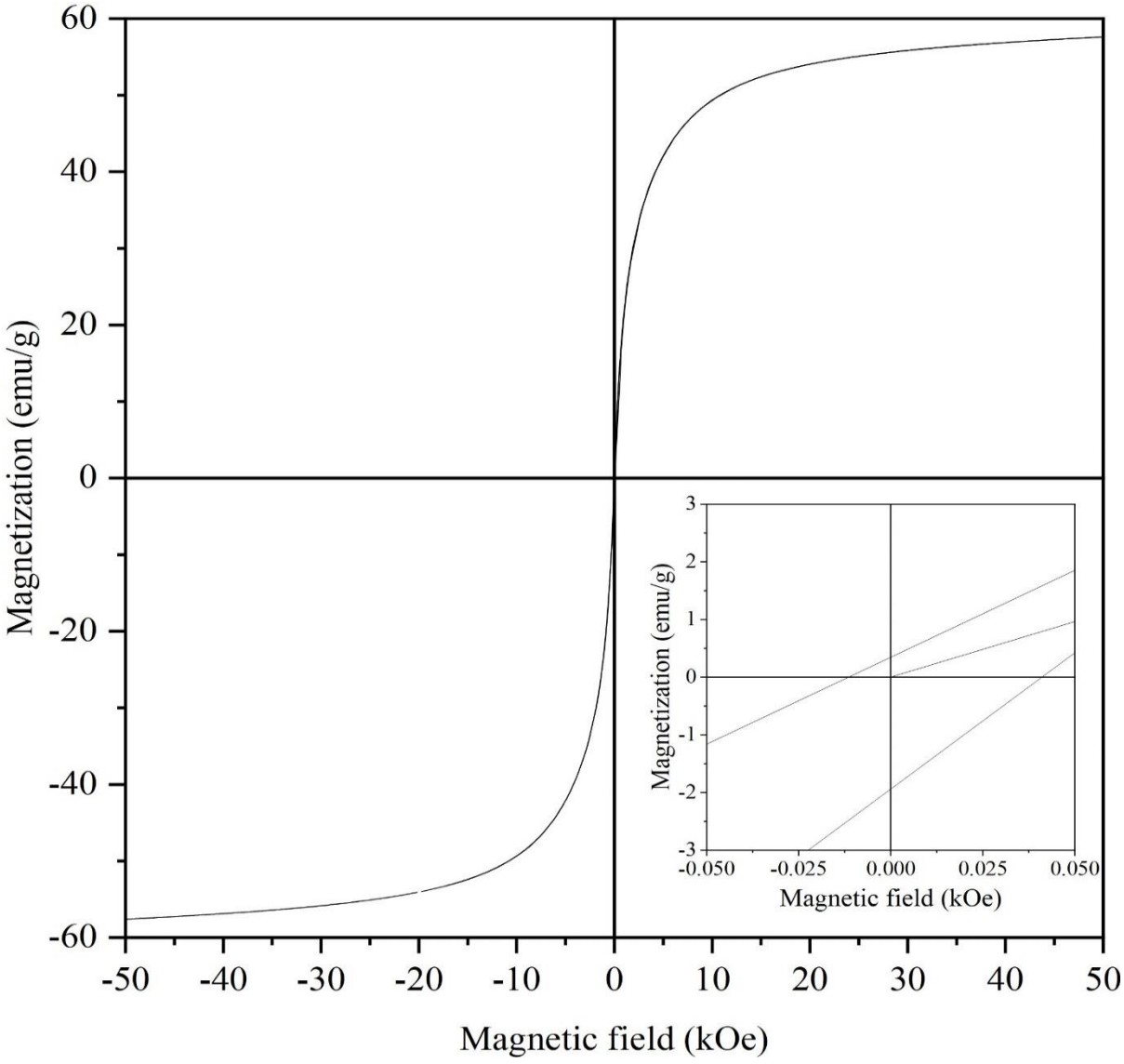

Figure 4.9 *Magnetisation curve of $Co_{0.3}Fe_{2.7}O_4$*

Table 4.2 *Relationship of the magnetisation hysteresis gaps with superparamagnetism. The measurement temperature was 300 K.*

	H_c (kOe)	M_s (emu/g)	M_r (emu/g)	M_r/M_s
Fe_3O_4/SiO_2	-0.015	34.051	0.130	0.004
	0.028	-34.062	-0.132	0.004
$Co_{0.3}Fe_{2.7}O_4/SiO_2$	-0.011	57.601	0.350	0.006
	0.042	-57.602	-1.950	0.034

Furthermore, the blocking temperatures of ZFC/FC of both products (Figures 4.10 and 4.11) were less than room temperature, and the blocking temperature of the $Co_{0.3}Fe_{2.7}O_4/SiO_2$ was about only 8 K greater than that of Fe_3O_4/SiO_2. The blocking temperature of the bare $Co_{0.3}Fe_{2.7}O_4$ was 257.69 K, which was 209.9 K higher than for the $Co_{0.3}Fe_{2.7}O_4/SiO_2$. It could be assumed the $Co_{0.3}Fe_{2.7}O_4$ particles were aggregated when they were measured by the VSM, but they might be dispersed during the SiO_2 coating synthesis process; therefore, the blocking temperature would be greatly decreased from that of the bare particles. The maximum magnetisation of the $Co_{0.3}Fe_{2.7}O_4/SiO_2$ was decreased from that of the bare particles, from 69.6 to 57.6 emu/g. The results can also support reducing the aggregated particle size from the bare $Co_{0.3}Fe_{2.7}O_4$.

The blocking temperature of the Fe_3O_4/SiO_2 was 64.13 K, which was less than the blocking temperature of the bare Fe_3O_4 (140.36 K), and the maximum magnetisation also decreased from 58.9 to 34.1 emu/g. It could be thought that the SiO_2 coating also helped to disperse the aggregated Fe_3O_4 particles. However, the maximum magnetisation was decreased due to the dispersion and the SiO_2 layer.

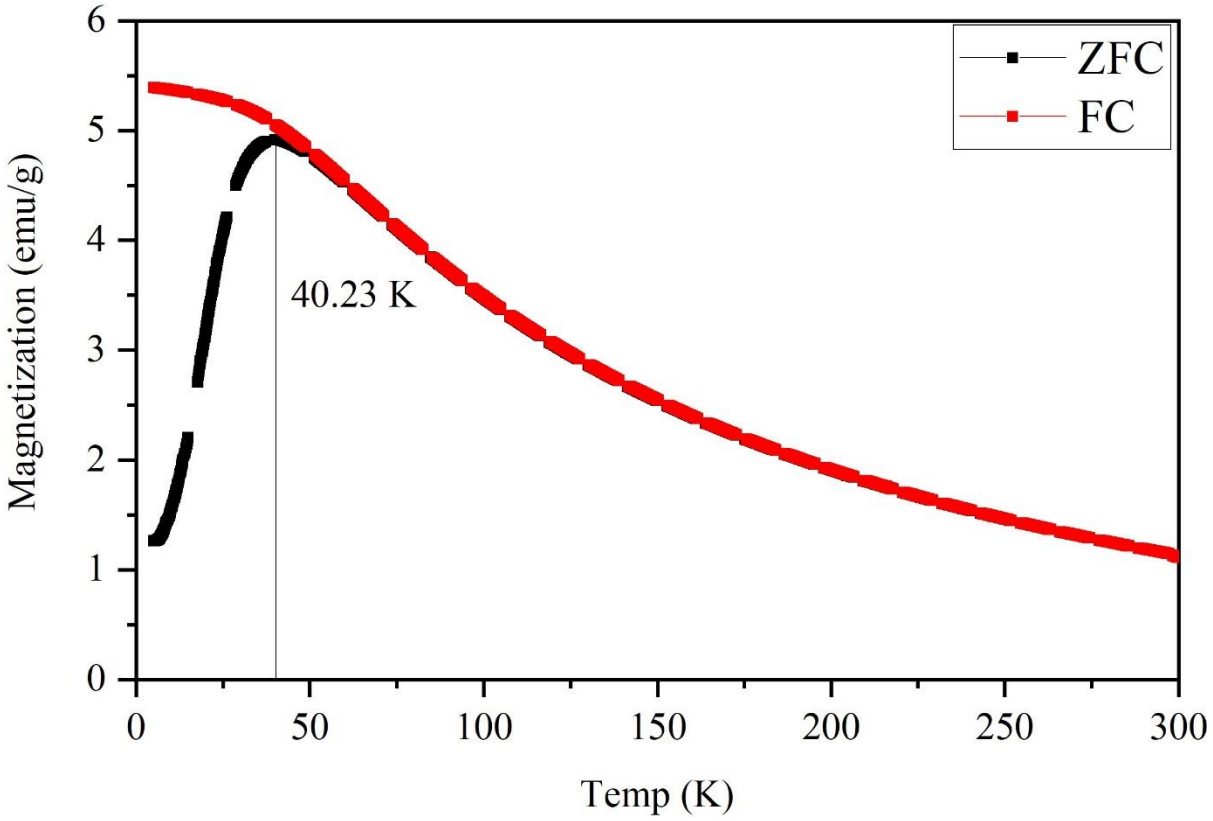

Figure 4.10 *ZFC/FC curves of Fe_3O_4/SiO_2*

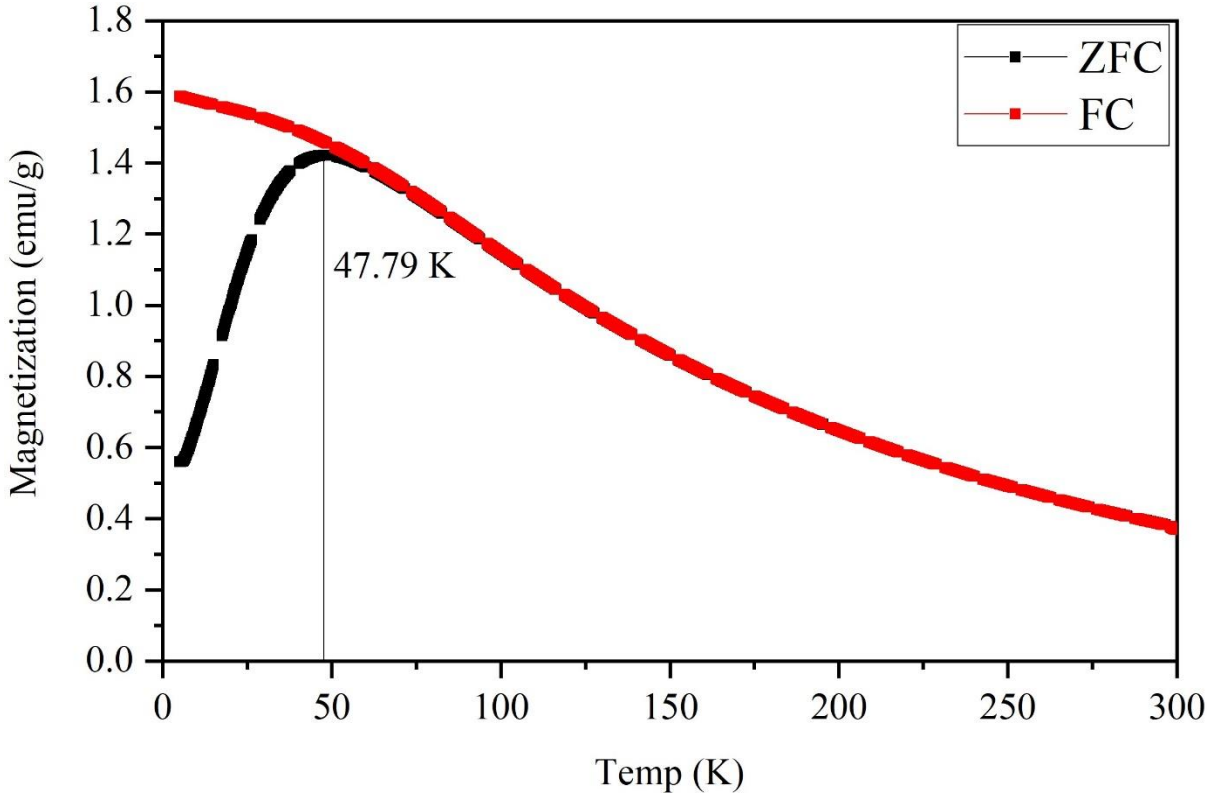

Figure 4.11 *ZFC/FC curves of $Co_{0.3}Fe_{2.7}O_4/SiO_2$*

4.4 Conclusion

The synthesised bare Fe_3O_4 and $Co_{0.3}Fe_{2.7}O_4$ particles were coated by SiO_2 by the Stöber method. The thickness of the SiO_2 coating on the particles was controlled by the ratio of DI water and ethanol, the amount of SiO_2 and the dispersant pH.

A 2 nm SiO_2 layer was observed by TEM, it was the thinnest SiO_2 that can be observed. A thinner SiO_2 layer was synthesised based on an estimate from the calculations of the Si/Fe and/or Co ratio and the Fe_3O_4 and $Co_{0.3}Fe_{2.7}O_4$ particles densities. The estimated thinnest SiO_2 thickness was less than 2 nm.

Both synthesised Fe_3O_4/SiO_2 and $Co_{0.3}Fe_{2.7}O_4/SiO_2$ were also superparamagnetic as revealed by VSM. The Fe_3O_4 seemed to be changed to γ-Fe_2O_3 based on the Raman spectra. The maximum magnetisations of both products were decreased from the bare M_xO_y, and it could be assumed the particle aggregations and SiO_2 layer affected the magnetization properties due to the syntheses.

5 M_xO_y/CHA-Na

5.1 Introduction

Magnetised zeolites (MZ) have been studied in relation to treating polluted water, and the type of zeolite within the MZ can be chosen depending on the target elements to be extracted from the polluted water. Typically, nanosized metal oxides are used as the magnetic particles in the MZ; in particular, Fe_3O_4 and Fe_2O_3 have been used. The level of magnetisation of MZ depends on the type and amount of the metal oxides in the MZ; for example, the maximum magnetisation of cobalt ferrite is higher than Fe_3O_4, based on the results of the M_xO_y magnetisation loops.

Several ways to synthesise MZ have been used: a ready-made zeolite can be mixed with precursors of the metal oxides to form the metal oxides on the zeolite by heating with a catalyst;[17, 29, 111] in contrast, ready-made metal oxide particles in a zeolite seed solution were heated to crystallise the MZ[112]; and in another process, a zeolite was put in a ready-made metal oxide solution, and then the mixture was stirred to form the MZ.[32, 113] For these synthesis processes it was necessary to stir for a few hours under a nitrogen atmosphere, stabilise the mixture's pH or add a reactant while stirring. Karmaoui and Hriljac (2016)[114] introduced a simpler MZ one-pot synthesis method using an autoclave, and CHA-Na was used for the MZ. The metal oxide particle size can be controlled by the crystallisation process by heating the autoclave. However, the metal oxide in the MZ synthesised by their recipe was γ-Fe_2O_3. The

CHA-Na can be easily synthesised from the ammonium form of zeolite Y and KOH; it has a high Cs capacity and is already well studied.[115-117] The advantage of this one-pod synthesis method is taking fewer synthesis steps than the other MZ synthesis methods, and it can save the synthesis time. The disadvantage is it is difficult to control the amount of metal oxide particles in the MZ precisely, because they are made from the metal oxide reagents simultaneously with synthesising the MZ.

In this study, the recipe of Karmaoui and Hriljac (2016)[114] was improved to synthesise Fe_3O_4/CHA-Na nanocomposites by optimising the synthesis temperature and heating duration. Furthermore, cobalt ferrite/CHA-Na was also synthesised to compare the morphologies, magnetic characteristics, and Cs adsorption capacities with those of Fe_3O_4/CHA-Na. The capacities were also compared with the synthesised M_xO_y/SiO_2/zeolite (MSZ) (see Chapter 6).

5.2 Experimental details

5.2.1 M_xO_y/CHA-Na

This recipe for the M_xO_y/CHA-Na was designed in reference to the recipe of Karmoui and Hriljac (2016)[114], and it is almost the same as the M_xO_y recipe (Chapter 3.2.1). The synthesis steps of the M_xO_y/CHA-Na is much simpler and taking less time than synthesising M_xO_y and CHA-Na separately, therefore, the recipe was adapted. The recipe for CHA-K that was the CHA-Na source was taken from the zeolite recipe database of IZA-SC (IZA-SC, n.d.).

The ammonium form of zeolite Y was used as the CHA-Na source. It was calcined at 550 ˚C (the ramp rate was 2 ˚C/min) for 2 hours to change it to zeolite H-Y in a furnace. Then, 25 g of the zeolite Y was mixed with a solution of 26.8 ml of KOH and 198.2 ml DI water, and the mixture was shaken for 30 min by hand, and then heated at 95 ˚C for 4 days in the conventional oven. The product was washed with DI water three times and dried at 60˚C.

The CHA-Na was synthesised from the synthesised CHA-K by exchanging the potassium with sodium. First, 20 g of the CHA-K was put in 400 ml of 2 mol/l NaCl (46.73 g of NaCl in 400 ml of DI water), and it was shaken by a shaker at 140 rpm for 15 min and heated at 100 ˚C, and then the product was washed with DI water once. The process was repeated six times, and the final product was washed with DI water three times and dried at 60 ˚C. The reason why this step is needed is the cation selectivity of chabazite (Cs>Na>K) as Chapter 1.2.1. The synthesised CHA-Na was dehydrated by the furnace at 300 ˚C (the ramp rate was 2 ˚C/min) for 3 hours under vacuum, using a Schlenk line. The dehydrated CHA-Na was put in the glovebox for the M_xO_y/CHA-Na synthesis.

Between 0.71 and 1.00 g of the dehydrated CHA-Na was put with the reagents for synthesising the M_xO_y. They were the same as the reagents used for the syntheses of the bare Fe_3O_4 and $Co_{0.3}Fe_{2.7}O_4$ (See Chapter 3.21 and 3.2.2). The mixture was synthesised in the same way as M_xO_y. The autoclave was heated in the conventional oven or a rotation oven. The rotation oven was used to try to disperse M_xO_y in CHA-Na evenly.

5.2.2 Cs adsorption experiments

To obtain the Cs adsorption isotherms of Fe_3O_4/CHA-Na, cobalt ferrite/CHA-Na and bare CHA-Na, 10 mg of each sample was put into a separate 50 ml conical tube. Then, 30 to 161 ppm concentrated Cs solutions were prepared from $CsNO_3$ and ultrapure (Milli-Q) water. Each of the concentrated Cs solutions was added to each conical tube containing an individual sample. The conical tubes were shaken for about 24 hr by the shaker at 140 rpm at ambient temperature. The solutions, which had exchanged Cs with the Na in the samples, were filtered by 0.22 μm filters, and a few tens of ml of the filtered solutions were put in separate 15 ml conical tubes. The pH values of the exchanged solutions were also measured from the filtered solutions. About 10 ml of 2 % HNO_3 was added to the conical tubes to dilute and stabilise the filtered solution for Cs concentration analysis using ICP-MS.

To obtain the time-dependent Cs adsorption capacities onto Fe_3O_4/CHA-Na, cobalt ferrite/CHA-Na and CHA-Na, 30 mg of each sample was put into a separate 50 ml conical tube. Then, 76 and 78 ppm of concentrated Cs solutions were also prepared from $CsNO_3$ and Milli-Q water. The conical tubes were shaken by a vortex mixer at 900 rpm. It was stopped at 10, 30, 60, 120 and about 1440 min after starting the shaking, and each time a few millilitres of the mixture was taken out from each conical tube. The mixtures were also filtered and then diluted

with 2 % HNO_3 in the same way as for obtaining the Cs adsorption isotherms, for the remaining Cs concentration analysis.

To obtain the pH-dependent Cs adsorption capacities onto Fe_3O_4/CHA-Na, cobalt ferrite/CHA-Na and CHA-Na, the adsorption experimental method was almost the same as that for obtaining the Cs adsorption isotherms. However, concentrated Cs solutions were made from $CsNO_3$ and 4-(2-hydroxyethyl)-1-piperazineethanesulfonic acid (HEPES) or N-cyclohexyl-3-aminopropanesulfonic acid (CAPS) solutions. HEPES can be used to stabilise the solution pH between 6.80 and 8.20, and CAPS can be used to stabilise it between 9.70 and 11.10; their stabilities as buffers are suitable for alkaline earth metals and transition metals (Ferreira et al. 2015). In this study, the pH 4 buffered solution was made with HEPES, because of the ease of access to the chemical, and because it could be used at pH 3.5 (Velikyan et al., 2008).[118]

First, 50 mM HEPES or CAPS were prepared. The buffer solutions were prepared by considering the initial concentrated Cs solutions, as higher concentrations of the buffers can more stabilise the solution pH. The pH stabilisation capabilities of the buffers were also checked after the Cs adsorptions. Second, the solution pH was adjusted to pH 4, 7 or 10 by 1 to 0.1 M NaOH or 1 M HCl, and then the Cs concentration in each solution was adjusted by $CsNO_3$ individually. The mixtures of the samples and pH adjusted concentrated Cs solutions were also shaken for 24 hr by the shaker at 140 rpm, and they were prepared for the ICP-MS measurements using the same method as the other adsorption experiments.

The correlation coefficient for the ICP-MS measurement was 0.998779 when obtaining the Cs adsorption isotherms, and for the time-dependent Cs adsorption capacities using the pH stabilised concentrated Cs solution the correlation coefficient was 0.999832. This coefficient is normally between -1 and 1, and the ICP-MS measurement is reliable when the value is over 0.99. The coefficient values of the Cs concentration measurements were both over 0.99; therefore, the ICP-MS measurements were reliable.

5.2.3 Buffer

The pH ranges of most buffers are below 6 and over 8, and this was found by extending the buffer studies of Good et al. (1966). They proposed twelve buffers that would be suitable for biological studies, and these buffers are called Good's buffers. The criteria of Good's buffers are below.

1) The pH (pK_a) range should be between 6 and 8.
2) The maximum water solubility and minimum solubility in all other solvents of the buffers should be considered. This consideration is to avoid accumulations of nonpolar buffers in biological systems.
3) For the above reason, the buffers should have lower permeabilities than the biological membranes.

4) Salt effects to the buffers should be minimised. Highly ionic buffers by adding salts can be cancelled by adding suitable ions to the salts.

5) The buffers should be used in the following conditions to avoid dissociations of the buffers: a minimum influence of buffer concentration, temperature, and ionic composition.

6) Complexation with the buffers should be understood or avoided.

7) The buffers should be as stable as possible, and enzymatic and nonenzymatic degradations should be avoided.

8) The buffer's solutions should not adsorb visible or ultraviolet light that are greater than 230–240 nm.

9) The buffers should be easily prepared, not expensive, and easily purified.

Furthermore, Ferreira et al. (2015) reviewed which buffers interact with metal ions and found that the pH range is between 5.50 and 11.40. CAPS and HEPES meet these criteria.

5.2.4 XRD

The synthesised Fe_3O_4/CHA-Na, cobalt ferrite/CHA-Na and bare CHA-Na were also measured using the same procedures as the other measurements (Chapter 3.2.4), and the phases were identified from the X-ray diffraction peaks by DIFFRAC.EVA against the ICDD database

of XRD peaks. The peak FWHM and positions of the same type products were also compared using Origin Pro.

5.2.5 Raman spectroscopy

Raman spectra were measured to confirm the presence of Fe_3O_4 and cobalt ferrite in the products, and the CHA-Na in the samples was confirmed by this measurement as well. The green laser power was optimised between 1 and 10 %, and it was applied to the samples for 10 to 30 seconds using cosmic ray removal. The RRUFF project Raman database[119] was used as a reference to identify the obtained Raman peaks of the Fe_3O_4, the cobalt ferrite and the CHA-Na.

5.2.6 XRF

These samples were also measured by XRF to identify the elemental compositions. In particular, the elemental composition of cobalt ferrite in the CHA-Na was calculated from this measurement. The cation exchange reaction times for the CHA-K with Na was estimated from the XRF measurement results.

5.2.7 SEM-EDS and TEM-EDS

The SEM images of the Fe_3O_4/CHA-Na and the cobalt ferrite/CHA-Na were captured by a TM4000Plus (Hitachi High-Tech Corporation). The sample elemental compositions were also measured by SEM- EDS using an AZtecOne (Oxford Instruments).

The sample surface and M_xO_y shapes were observed by TEM. The sample preparation for the measurement was the same as for M_xO_y/SiO_2. The TEM-EDS work was carried out with Dr Gnanavel Thirunavukkarasu (University of Birmingham).

5.2.8 VSM

The magnetic properties of Fe_3O_4/CHA-Na and cobalt ferrite/CHA-Na were also measured by VSM from -50 to 50 kOe at ambient temperature. The VSM work was carried out by Dr Mingee Chung (University of Birmingham) and his PhD student Jake Head (University of Birmingham).

5.2.9 ICP-MS

The Cs concentration measurements of the Cs adsorption experiments of the products and the bare CHA-Na were performed using ICP-MS. A 2 % solution of HNO_3 was used as the blank and carrier solutions. For the internal solution, Rb was used to reduce the matrix effect.

The machine was operated by Dr Christopher Stark (University of Birmingham) and Dr Norman Day (University of Birmingham).

5.3 Results

5.3.1 Phase identification of M_xO_y/CHA-Na

The Fe_3O_4/CHA-Na synthesised using different ratios of reagents and with different temperatures and times were first characterised through the obtained XRD patterns. The synthesis condition details of the products are in Table 5.1, and the XRD patterns are shown in Figure 5.1, which also shows the XRD patterns of bare Fe_3O_4 and CHA-Na for comparison. Most products had large Fe_3O_4 peaks with the CHA-Na peaks; therefore, the peaks were just used to estimate the ratio of Fe_3O_4 and CHA-Na in the products. The Fe_3O_4 peak of the products at 41.4° was not completely coincident with the CHA-Na peaks, and the samples with more Fe_3O_4 had a higher peak at that position, such as iron oxides/CHA-Na-1 (C-Fe1), C-Fe2 and C-Fe4. C-Fe1 used the same amount of $Fe(acac)_3$ (0.5 g) as C-Fe3; however, the amounts of 1-hexanol and CHA-Na were higher than for C-Fe3. From the Fe_3O_4 synthesis results, the amount of 1-hexanol affected the final products, and it could be considered that the ratio of $Fe(acac)_3$, CHA-Na and 1-hexanol for C-Fe4 was better. C-Fe2 and C-Fe4 also had higher Fe_3O_4 peaks at the position, but the amounts of $Fe(acac)_3$ and/or 1-hexanol were lower than for C-Fe1, and for C-Fe4, which had been heated for 24 hours. However, the Raman spectra peaks of C-Fe4 were

at 477 and 687 cm^{-1}, showing that it contained Fe_3O_4 (Figure 5.2). Furthermore, even C-Fe4 had few Fe_3O_4 nanoparticles outside the Fe_3O_4/CHA-Na that were observed on the TEM image (see Figure 5.5). The particles outside the Fe_3O_4/CHA-Na could be negligible due to the small amounts, but it could be thought that the maximum amount of Fe_3O_4 in Fe_3O_4/CHA-Na had the same ratio as C-Fe4. The CHA-Na peaks of C-Fe4 were smaller than those for C-Fe1 and C-Fe2. This means C-Fe4 had more Fe_3O_4 nanoparticles and, therefore, it was strongly attracted by a neodymium magnet; the magnetic properties were also measured (see Section 5.3.2).

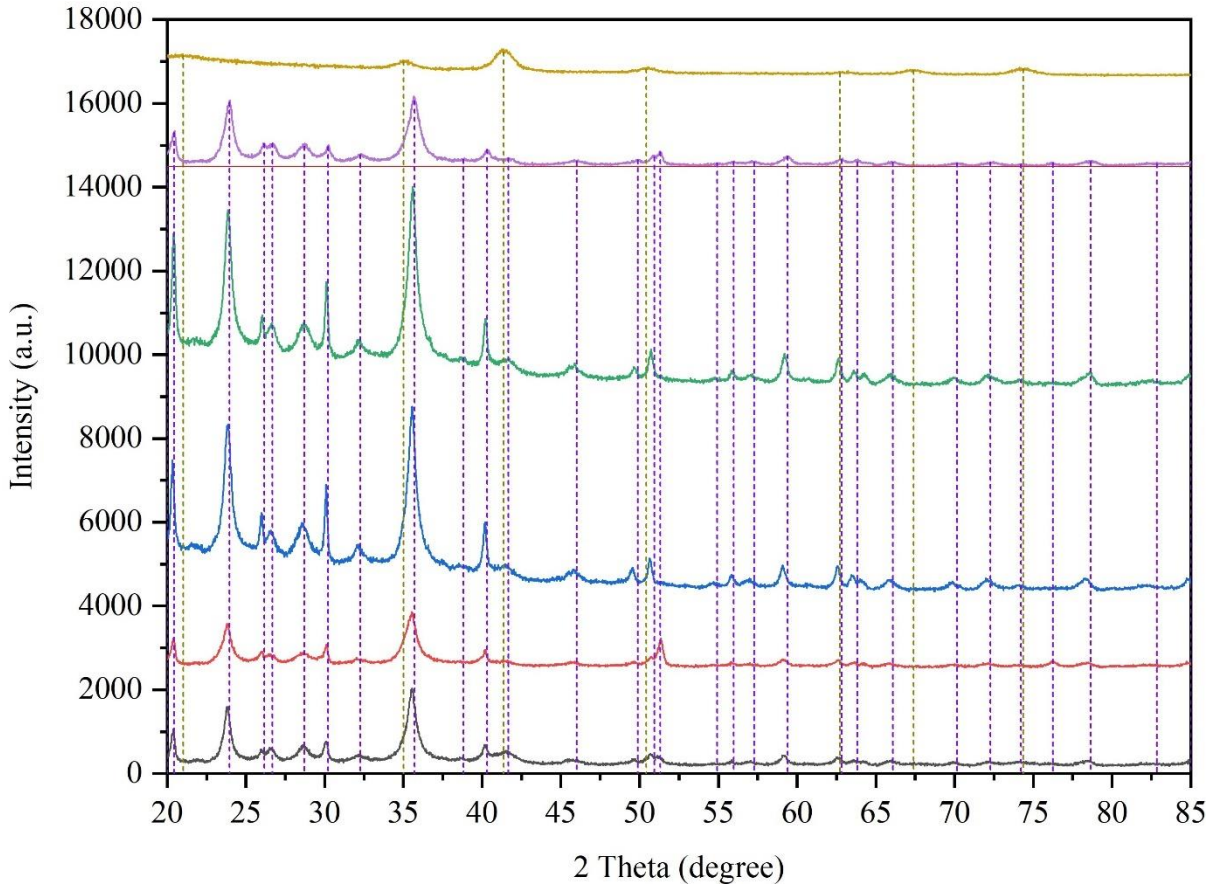

Figure 5.1 *XRD patterns of Fe_3O_4 (yellow), CHA-Na (purple) and iron oxides/CHA-Na samples: C-Fe1 (green), C-Fe2 (blue), C-Fe3 (red), C-Fe4 (black) (only C-Fe4 was heated in a rotation oven).*

Table 5.1 *The amounts of reagents and synthesis times for iron oxides/CHA-Na when the synthesis temperature was 175 ºC.*

Sample	Amount of $Fe(acac)_3$ (g)	Amount of CHA-Na (g)	Amount of 1-Hexanol (ml)	Synthesis temperature (ºC)	Synthesis time (hr)
C-Fe1	0.50	1.00	20.00	175	5
C-Fe2	0.80		20.00*		
C-Fe3	0.50	0.71	5.00*		
C-Fe4	0.80	1.00	5.00		24

*(*a glass inner was used in the Teflon liner, and 5 ml of 1-hexanol was put between the inner and the liner)*

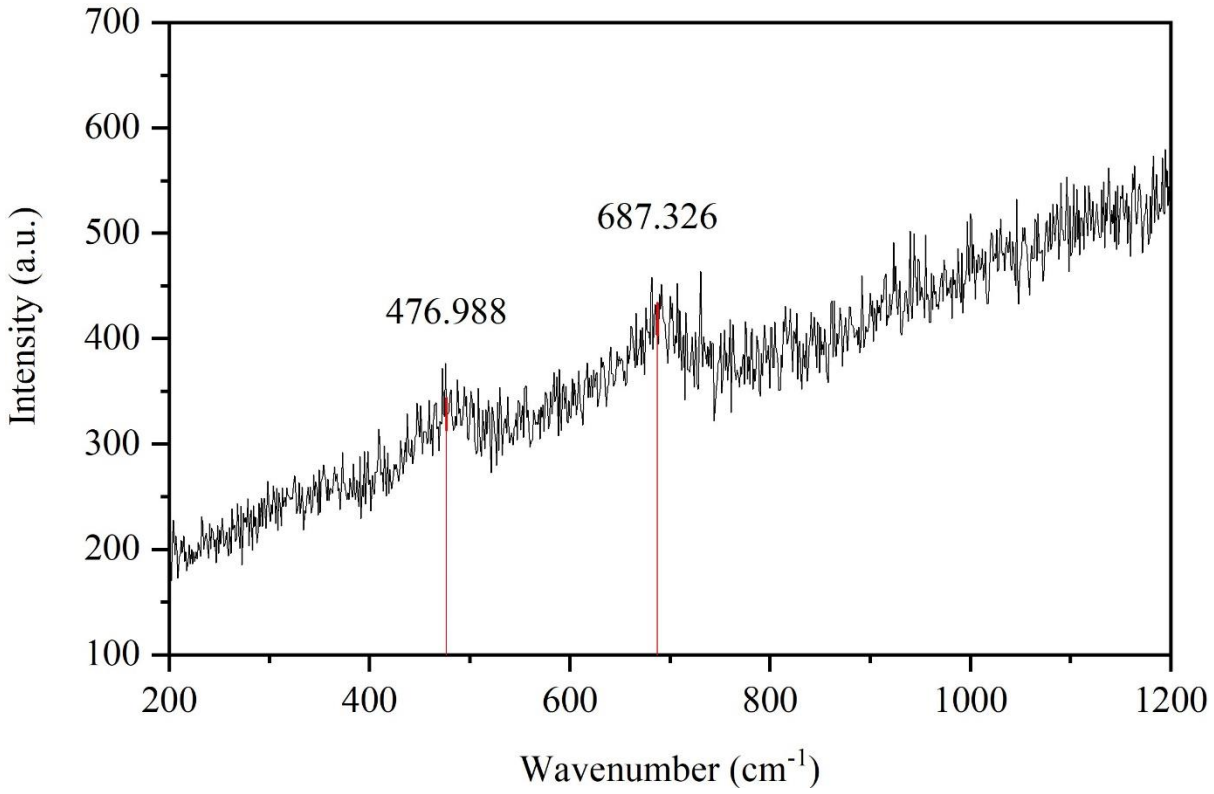

Figure 5.2 *Raman peak of Fe_3O_4 of C-Fe4*

The XRD patterns of cobalt ferrite/CHA-Na, which were made with different ratios of reagents, and with different synthesis temperatures and times, are shown in Figure 5.3 with the

XRD patterns of bare $Co_{0.3}Fe_{2.7}O_4$ and CHA-Na. The synthesis condition details of $CoFe_2O_4$/CHA-Na are in Table 5.2. The ratios of reagents and synthesis temperature of the samples were the same (the * denotes that 5 ml of 1-hexanol was put between the inner and the liner to prevent the overflow of the reagents from the glass inner due to the solvent boiling). The cobalt ferrite in the magnetic composites was also compared with the bare $Co_{0.3}Fe_{2.7}O_4$ by the XRD peak at 41.1°. The ratio of Co and Fe was slightly different, but the XRD patterns were the same as for $Co_{0.3}Fe_{2.7}O_4$. Except for cobalt ferrite/CHA-Na (C-Co1), the peaks of all of the synthesised products at this position could be observed: there were just tiny peaks of the products at the position. C-Co2 and C-Co3 were compared by their magnetic attractions to the neodymium magnet. The results showed that C-Co3 was more attracted to the magnet; therefore, it was chosen for the further Cs adsorption experiments. C-Co3 had the highest peak corresponding to CHA-Na at 51.3°. It could be assumed this peek is from zerovalent iron (Fe(0)). The appearance is around 52.381° that is reported by Crane and Sapsford (2019).[120] The Fe(0) can be generated from $Fe(acac)_3$. [121, 122] It is supposed the genration can be caused while the Fe oxidisation process: Nene, et al., (2016) reported Fe_3O_4, which was synthesised from $Fe(acac)_3$, diphenyl-ether, ascorbic acid, ethanol, and ultrapure water, did not have any Fe(0) peak on the XRD patterns, however, the without using ultrapure water one had a Fe(0) peak, and it is assumed it was caused by the Fe oxidisation in air atomospher while handling due to without water potection on the Fe particle surfaces.[123] The Fe(0) in C-Co3 might be

also generated by contacting with air atomospher while the synthesis process such as affecting O^2 level on the groveboox (≤ 40 ppm) and handling the reagents inside it.

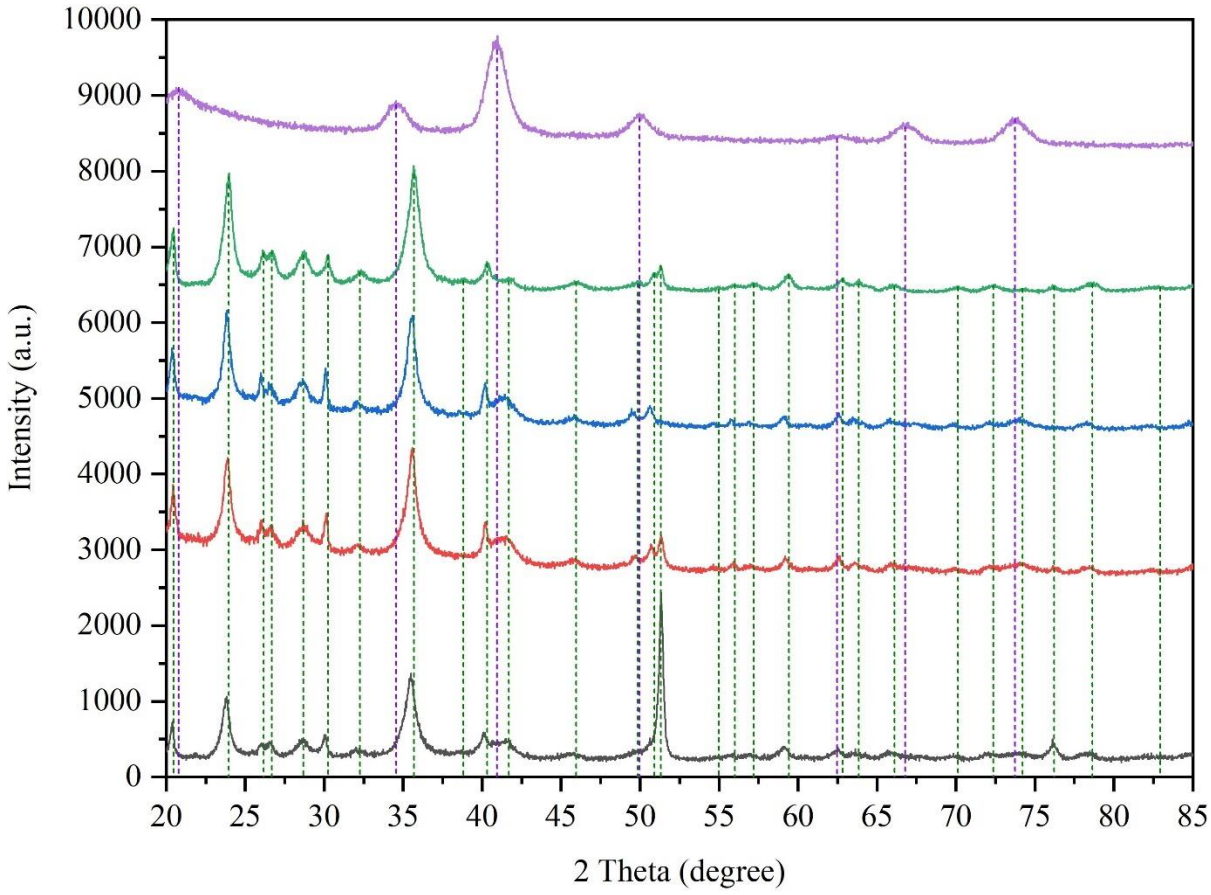

Figure 5.3 *XRD patterns of $Co_{0.3}Fe_{2.7}O_4$ (purple), CHA-Na (green) and cobalt ferrite/CHA-Na samples: C-Co1 (blue), C-Co2 (red), C-Co3 (black) (only C-Co3 was heated in the rotation oven).*

Table 5.2 *The amounts of reagents and synthesis times for cobalt ferrite/CHA-Na when the synthesis temperature was 180 ºC.*

Sample	Amount of $Fe(acac)_3$ (g)	Amount of $Co(acac)_2$ (g)	Amount of CHA-Na (g)	Amount of 1-Hexanol (ml)	Synthesis temperature (ºC)	Synthesis time (hr)
C-Co1	0.57	0.21	1	5*	180	48
C-Co2						72
C-Co3				5		96

** a glass inner was used in the Teflon liner, and 5 ml of 1-hexanol was put between the inner and the liner*

The Raman peaks of the Fe_3O_4/CHA-Na, the cobalt ferrite/CHA-Na and the bare CHA-Na are shown in Figure 5.4. The laser power used to obtain the peaks was high enough to change Fe_3O_4 to Fe_2O_3 by heat; therefore, there were also Fe_2O_3 peaks with the Fe_3O_4/CHA-Na Raman peaks. The Raman peaks of CHA-Na appeared at 342, 488, 787 and 1097 cm^{-1}. The Fe_3O_4/CHA-Na and the cobalt ferrite/CHA-Na also had peaks around the CHA-Na peak positions, but the Fe_3O_4/CHA-Na also had a peak at 558 cm^{-1}, and the cobalt ferrite/CHA-Na a peak at 570 cm^{-1}. It could be assumed that they were from the metal oxides. From the RRUFF database[119] and Chandramohan et al. (2011)[91], those peaks were haematite and cobalt ferrite. The synthesised $Co_{0.3}Fe_{2.7}O_4$ did not have a peak at around 570 cm^{-1}, but Raman peak positions of cobalt ferrite may be changed by the particle size and the cation distribution in cobalt ferrite, they can also be changed by the laser heating during the measurement.

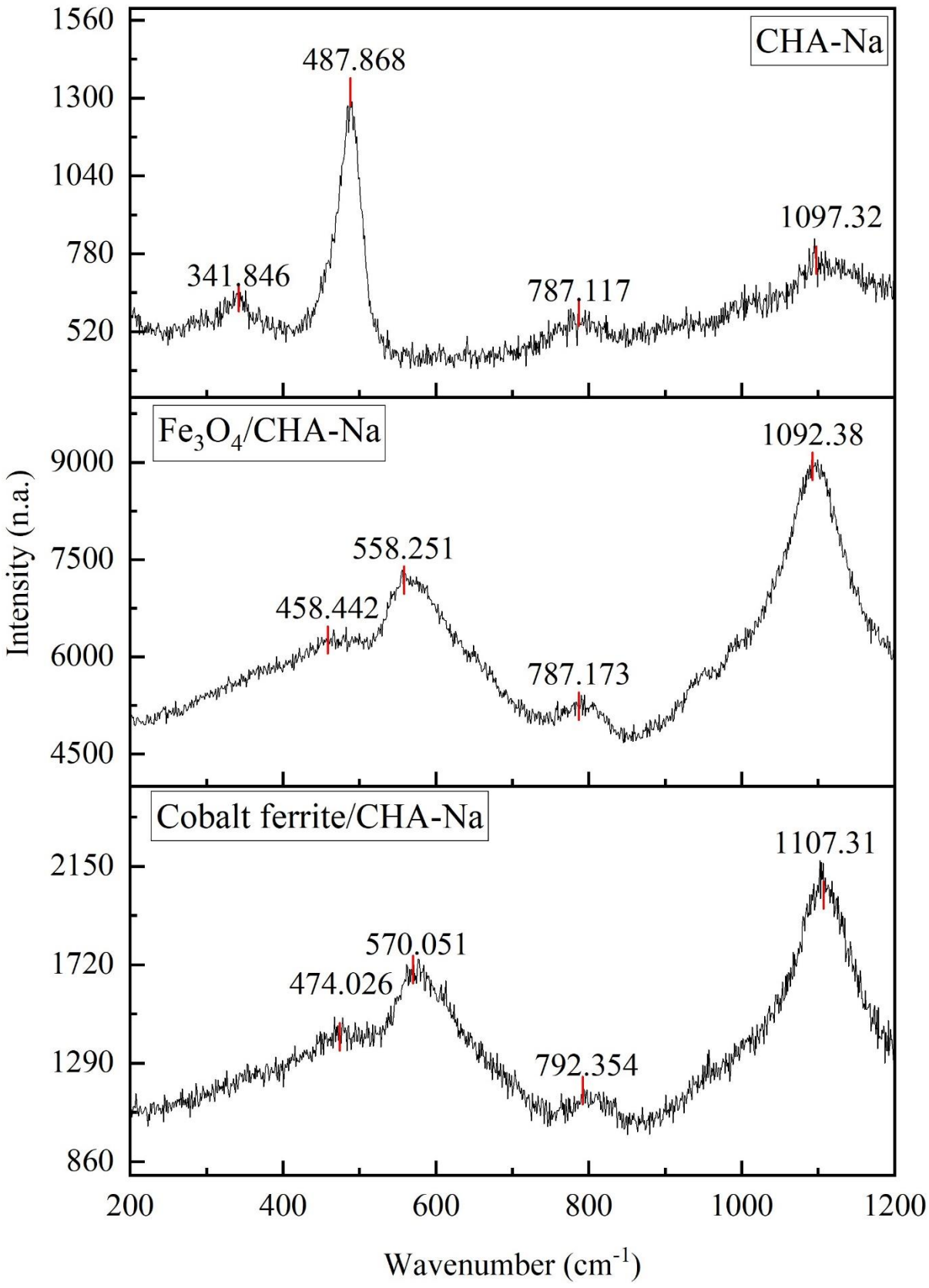

Figure 5.4 *Raman spectra of CHA-Na, Fe_3O_4/CHA-Na and cobalt ferrite/CHA-Na*

The products were also characterised using XRF to identify their elemental compositions. Table 5.3 shows the elemental composition of the CHA-Na that was used for the synthesis of Fe_3O_4/CHA-Na and cobalt ferrite/CHA-Na. The theoretical composition of CHA-Na and CHA-K is (Na, K)[$AlSi_2O_6$]•3(H_2O). For the synthesised bare CHA-Na the elemental ratio of Al : Si : Na : K was 1 : 3.21 : 0.46 : 0.25. There were slightly fewer cations than in the theoretical composition and it was more silica rich.

Table 5.3 *Elemental composition of CHA-Na used for the syntheses of Fe_3O_4/CHA-Na and cobalt ferrite/CHA-Na.*

Formula		Concentration (wt%)	Amount of material (mmol)	Ratio
Al	19.60	(±0.41)	0.73	1.00
Si	65.50	(±0.87)	2.33	3.21
Na	7.66	(±0.31)	0.33	0.46
K	7.11	(±0.21)	0.18	0.25

The elemental compositions of C-Fe1 to C-Fe4 are shown in Table 5.4. The elemental compositions of CHA-Na in the products were all similar due to the same CHA-Na being used for the syntheses; the small differences can be ignored, because they were measured using the pressed pellet method that included mixing with wax. However, the ratio of Si to Al decreased by about 0.32 to 0.66 from the bare CHA-Na, and the ratio of K to Al also decreased by about 0.019 to 0.021. Cao et al. (2008)[112] also reported that the zeolite P elemental composition of

synthesised Fe_3O_4/zeolite P was different from standard zeolite P, and they thought the Fe_3O_4 particles affected the zeolite P constitution. The Fe_3O_4/zeolite P was crystallised with bare Fe_3O_4 particles. The Fe_3O_4/CHA-Na was crystallised before mixing with the bare Fe_3O_4. However, the products might be also affected by the heating from the synthesis of Fe_3O_4/CHA-Na: the Si and K might be pushed away from the CHA-Na framework to put Fe and O instead by the heating pressures. C-Fe4 had the highest Fe to Al ratio in the elemental compositions. From this result, the ratio of reagents and the synthesis conditions of C-Fe4 was best to synthesise the strongly magnetic Fe_3O_4/CHA-Na.

Table 5.4 *Elemental compositions of iron oxides/CHA-Na. The standard errors are acceptable, especially the errors of K and Fe were not different each product.*

Formula			Concentration (wt%)	Amount of material (mmol)	Ratio
C-Fe1	Al	17.20	(±0.25)	6.38	1.00
	Si	46.30	(±0.46)	16.48	2.59
	Na	10.50	(±0.27)	4.57	0.72
	K	0.92	(±0.04)	0.24	0.04
	Fe	25.00	(±0.11)	4.48	0.70
C-Fe2	Al	18.20	(±0.25)	6.75	1.00
	Si	48.40	(±0.45)	17.23	2.55
	Na	11.30	(±0.26)	4.92	0.73
	K	1.05	(±0.04)	0.27	0.04
	Fe	21.00	(±0.09)	3.76	0.56
C-Fe3	Al	18.60	(±0.26)	6.89	1.00
	Si	50.50	(±0.49)	17.98	2.61
	Na	10.70	(±0.27)	4.65	0.68
	K	1.10	(±0.05)	0.28	0.04
	Fe	19.10	(±0.10)	3.42	0.50
C-Fe4	Al	6.89	(±0.14)	2.55	1.00
	Si	20.70	(±0.26)	7.37	2.89
	Na	3.73	(±0.14)	1.62	0.64
	K	1.66	(±0.05)	0.42	0.17
	Fe	36.00	(±0.14)	6.45	2.52

The measured elemental compositions of the synthesised cobalt ferrite/CHA-Na are shown in Table 5.5. The elemental compositions of CHA-Na in the products were almost the same as in the Fe_3O_4/CHA-Na. The ratios of K to Al and Si to Al in the CHA-Na were also decreased by about 0.33 to 0.50 and by 0.18 to 0.20, respectively. This could also be assumed to be due to the changing CHA-Na morphology or the pushing away of some of the elements

from the frameworks. The Co and Fe ratio of cobalt ferrite/CHA-Na was calculated from these measurement results. From the synthesis details (Table 5.2), the cobalt ferrite of C-Co1 that was heated for 48 hr was $Co_{1.2}Fe_{1.8}O_4$, for C-Co2 that was heated for 72 hr it was $Co_{0.9}Fe_{2.1}O_4$, and for C-Co3 that was heated for 96 hr it was $Co_{0.50}Fe_{2.5}O_4$. C-Co2 was closest to the ideal cobalt ferrite chemical formula ($CoFe_2O_4$). However, the selected C-Co3 particles for the Cs adsorption experiments was $Co_{1.1}Fe_{1.9}O_4$ (see Table 5.8), and C-Co3 was used for the further experiments regarding adsorption.

Table 5.5 *Elemental composition of cobalt ferrite/CHA-Na (those highlighted in yellow are the ratio of Co and Fe used to identify the cobalt ferrite in the magnetic CHA-Na).*

Sample	Formula	Concentration (wt%)		Amount of material (mmol)	Ratio
C-Co1	Al	11.70	(±0.25)	4.34	1.00
	Si	33.00	(±0.44)	11.75	2.71
	Na	6.12	(±0.25)	2.66	0.61
	K	0.89	(±0.05)	0.23	0.05
	Fe	28.00	(±0.13)	5.01	1.46
	Co	20.20	(±0.11)	3.43	1.00
C-Co2	Al	8.79	(±0.21)	3.26	1.00
	Si	25.60	(±0.38)	9.11	2.80
	Na	5.12	(±0.22)	2.23	0.68
	K	0.71	(±0.04)	0.18	0.06
	Fe	41.20	(±0.19)	7.38	2.35
	Co	18.50	(±0.10)	3.14	1.00
C-Co03	Al	7.79	(±0.16)	2.89	1.00
	Si	22.30	(±0.28)	7.94	2.75
	Na	3.87	(±0.15)	1.68	0.58
	K	1.47	(±0.05)	0.38	0.13
	Fe	27.00	(±0.13)	4.83	2.52
	Co	11.30	(±0.06)	1.92	1.00

The TEM images of the *synthesised Fe_3O_4/CHA-Na are* shown in Figure 5.5. The nanosized Fe_3O_4 particles that were in the CHA-Na could be observed in the images; however, few Fe_3O_4 particles were outside the CHA-Na. As mentioned in the previous results, the maximum capacity of Fe_3O_4 in CHA-Na was synthesised from the reagents of C-Co3. The average Fe_3O_4 particle size was 9.0 nm that was obtained from Figure 5.5 (Table 5.6). It was bigger than the synthesised bare Fe_3O_4 (6.8 nm); however, it was still superparamagnetic.

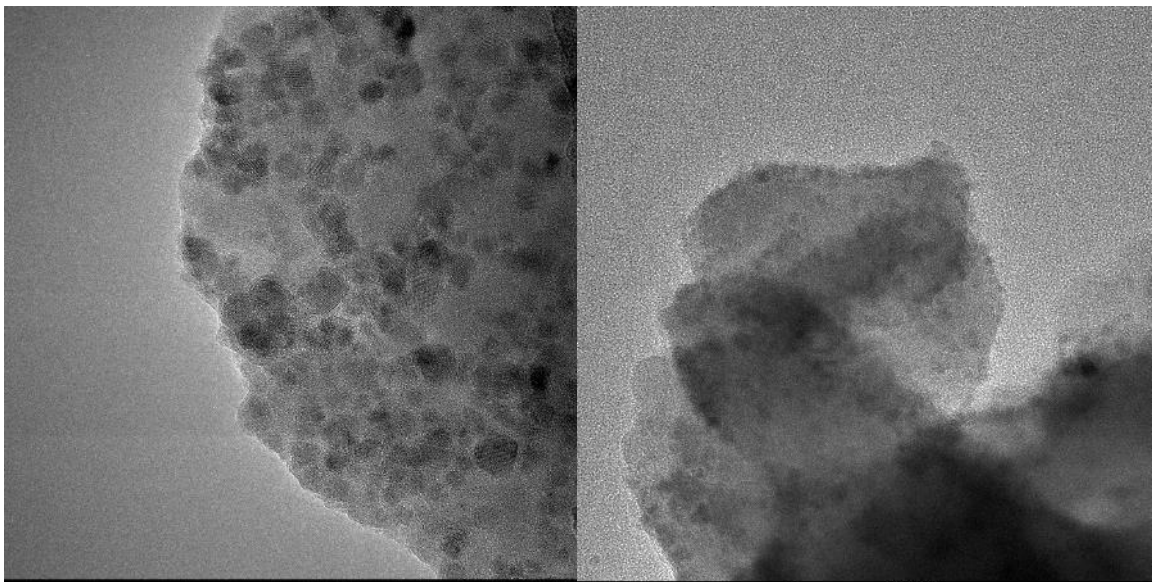

Figure 5.5 *TEM image of Fe_3O_4/CHA-Na. The sample of the right-side image had few Fe_3O_4 particles outside Fe_3O_4/CHA-Na. (They were captured different places of the same sample on the cupper grid for the TEM measurement).*

Table 5.6 *Particle size (nm) of Fe_3O_4 in the Fe_3O_4/CHA-Na*

Smallest	Biggest	Average
6.1	13.5	9.0 (±2.2)

The elemental mapping of the product, which was captured by TEM-EDS, is shown in Figure 5.6. The images captured all the elements of the product, excluding K, because there was so little of it. The mapping image of Fe showed that Fe_3O_4 nanoparticles were evenly dispersed in the CHA-Na.

The $Co_{1.1}Fe_{1.9}O_4$/CHA-Na was not characterised by the TEM-EDS, but it could be assumed the synthesis method of C-Co3 worked to encapsulate most $CoFe_2O_4$ nanoparticles in the CHA-Na because there was almost the same theoretical amount as for the Fe_3O_4 (the theoretical amount of Fe_3O_4 in the CHA-Na is 0.17 g, and for $CoFe_2O_4$ it is 0.14 g).

The SEM-EDS images of the synthesised Fe_3O_4/CHA-Na and $Co_{1.1}Fe_{1.9}O_4$/CHA-Na are shown in Figures 5.7 to 5.10. The product particle sizes seemed to be uniform, and they did not form irregular or large CHA-Na particles. The Fe appeared on the Al, Si and Na, meaning that the Fe_3O_4 particles were evenly distributed.

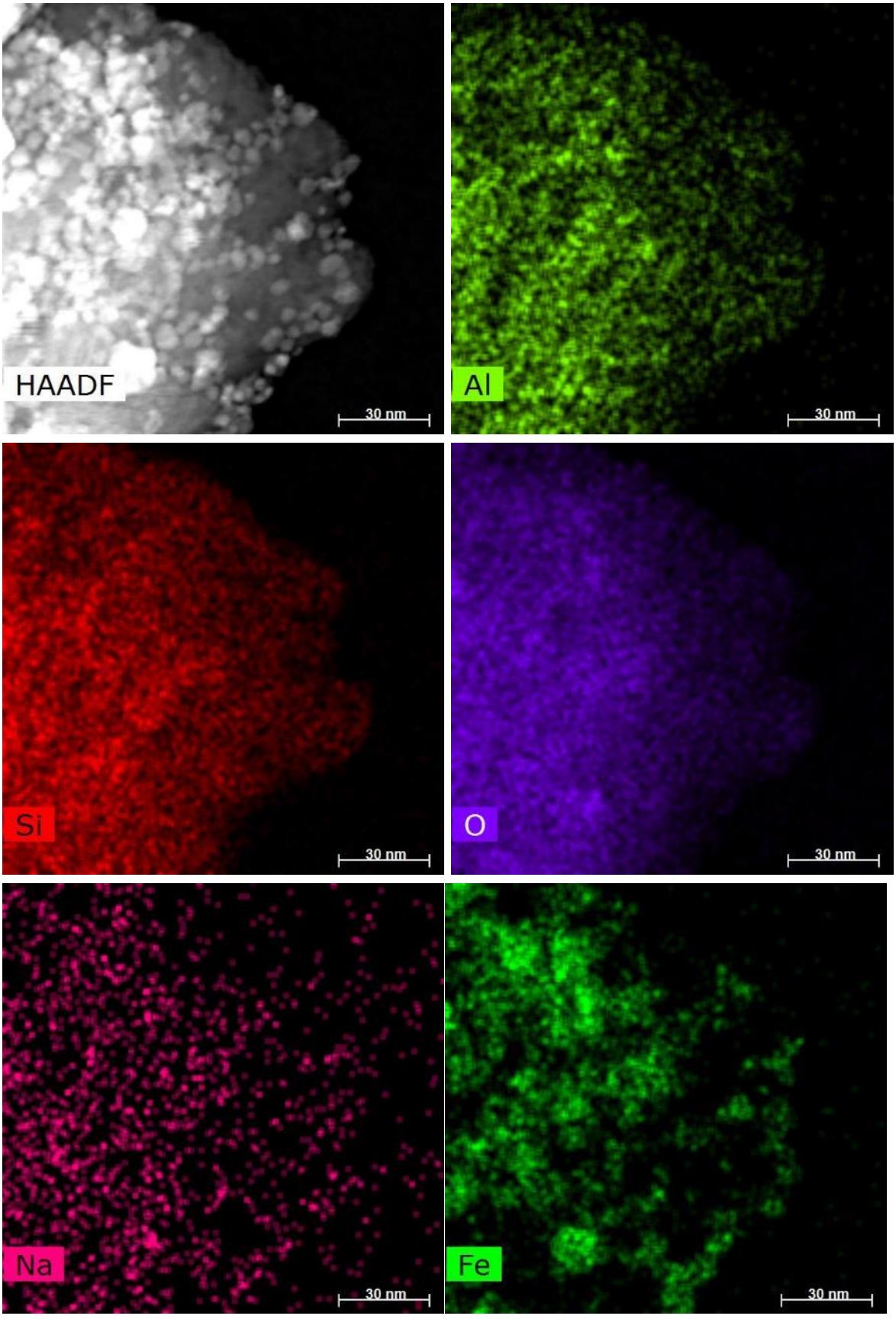

Figure 5.6 *TEM-EDX images of Fe_3O_4/CHA-Na*

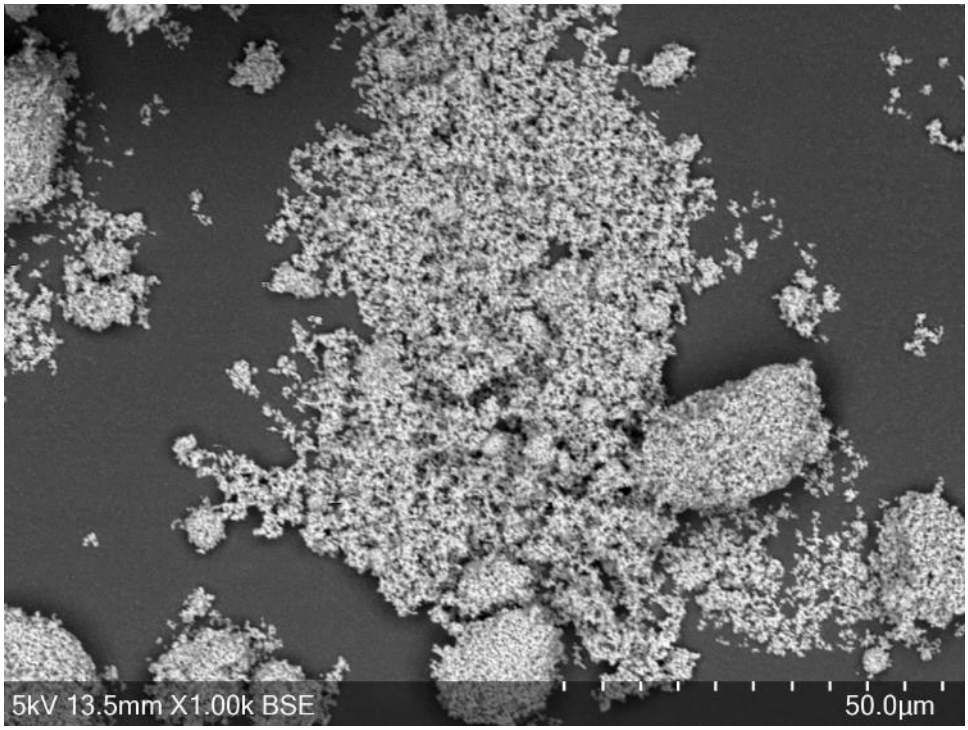

Figure 5.7 *SEM image of Fe_3O_4/CHA-Na*

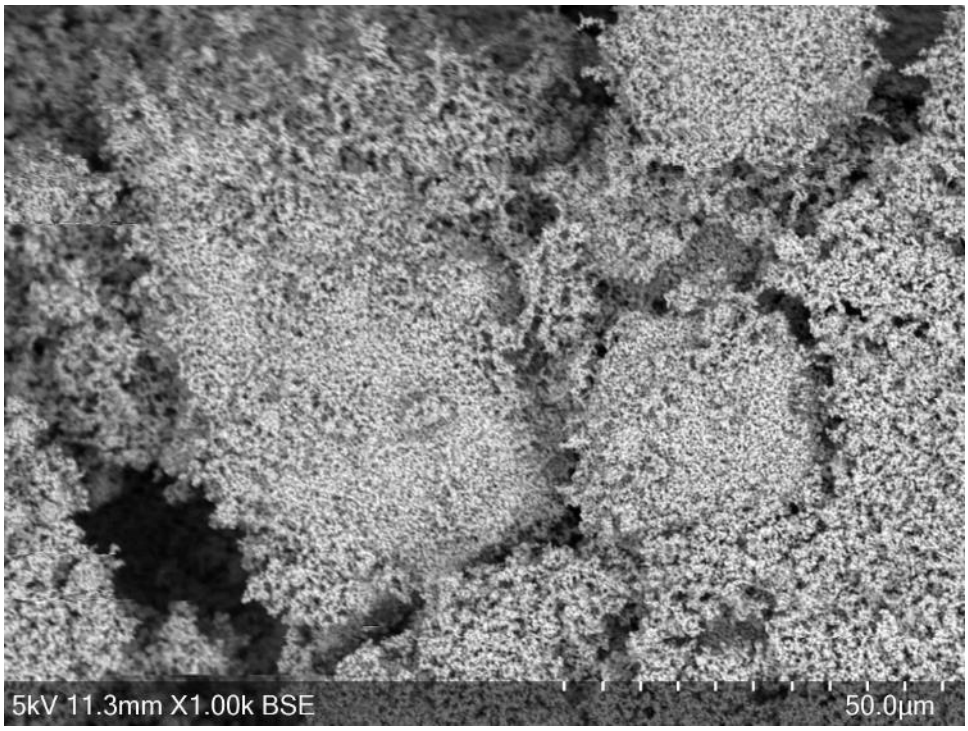

Figure 5.8 *SEM image of $Co_{1.1}Fe_{1.9}O_4$/CHA-Na*

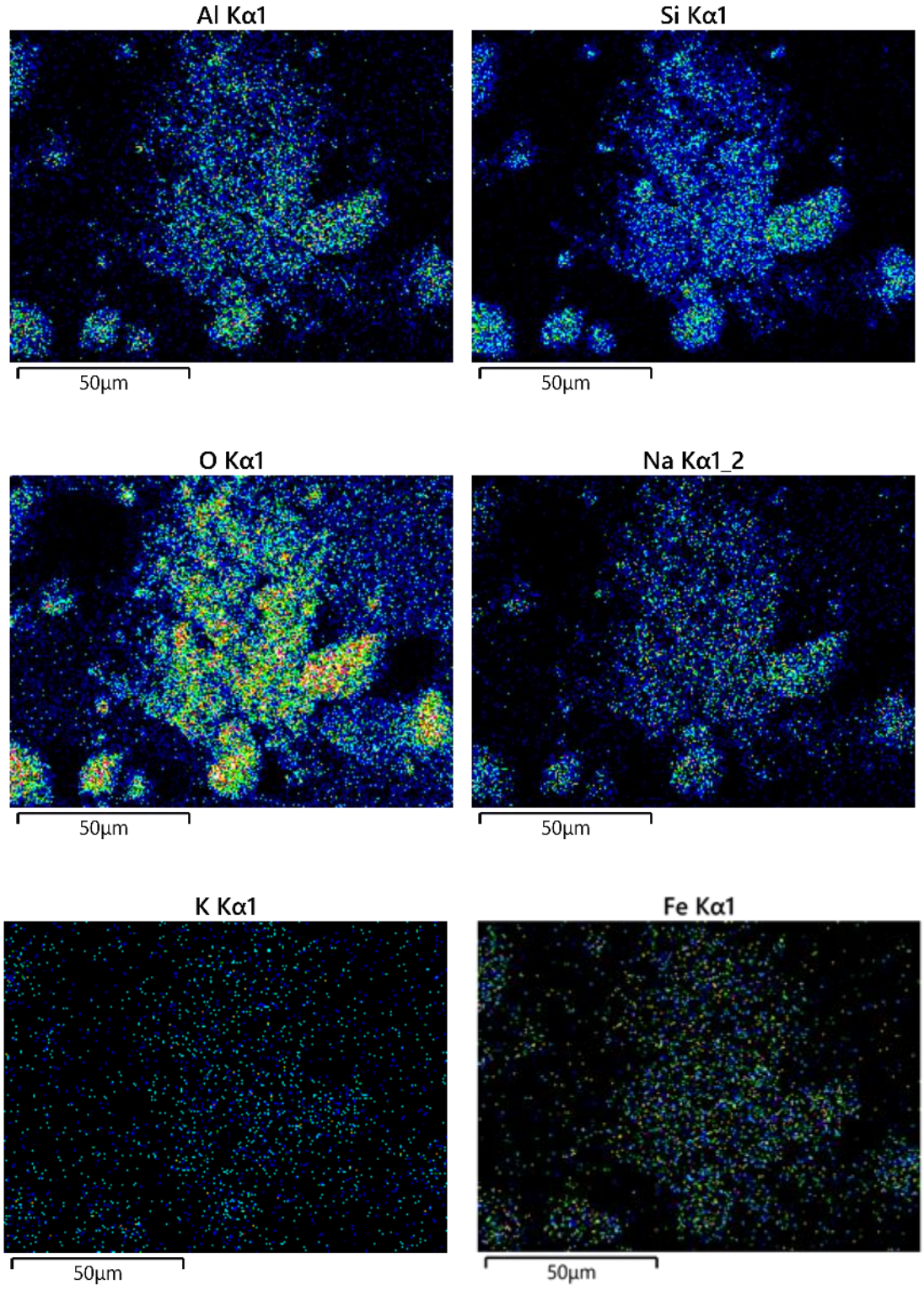

Figure 5.9 SEM-EDS images of Fe_3O_4/CHA-Na

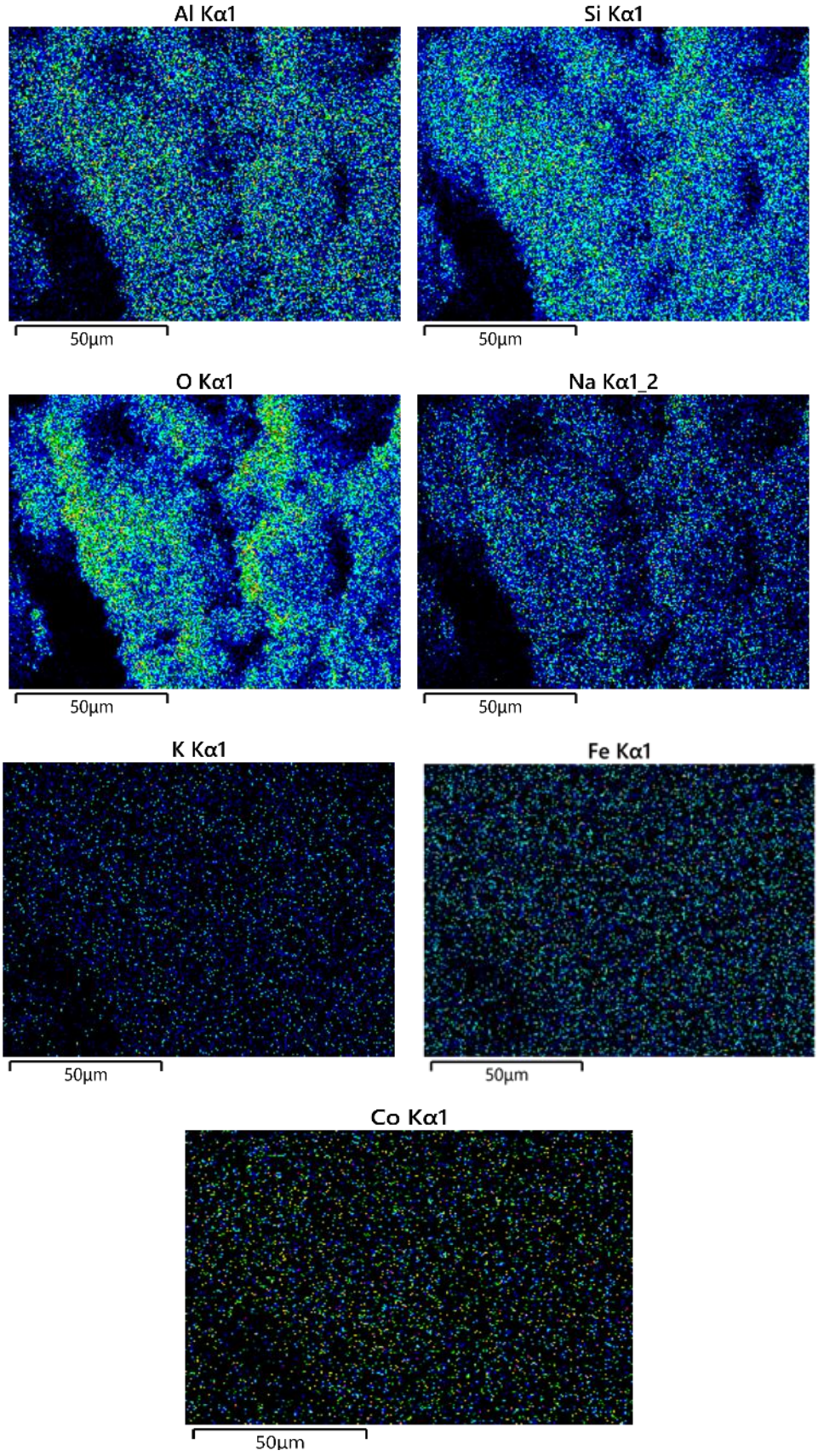

Figure 5.10 *SEM-EDS images of* $Co_{1.1}Fe_{1.9}O_4$*/CHA-Na*

5.3.2 Magnetic properties

The Fe_3O_4/CHA-Na and $Co_{1.1}Fe_{1.9}O_4$/CHA-Na selected by the neodymium magnet for the Cs adsorption experiments were also characterised by XRF, and the results are given in Table 5.7. The compositions of cobalt ferrite in the $Co_{1.1}Fe_{1.9}O_4$/CHA-Na for the Cs adsorption experiments and C-Co3 are shown in Table 5.8. The ratio of Fe to Al in Fe_3O_4/CHA-Na was increased to 3.66 from 2.52, and the ratios of Co to Al and Fe to Al in $Co_{1.1}Fe_{1.9}O_4$/CHA-Na increased to 3.85 from 0.66, and to 7.25 from 1.67, respectively. These results show the amounts of Fe_3O_4 or $Co_{1.1}Fe_{1.9}O_4$ nanoparticles in the Fe_3O_4/CHA-Na and $Co_{1.1}Fe_{1.9}O_4$CHA-Na synthesised using the rotation oven seem to be slightly increased.

Table 5.7 *The elemental compositions of Fe_3O_4/CHA-Na and $Co_{1.1}Fe_{1.9}O_4$/CHA-Na that were used for the Cs adsorption experiments.*

	Formula	Concentration (wt%)		Amount of material (mmol)	Ratio
Fe_3O_4/CHA-Na	Al	8.04	(±0.23)	2.98	1.00
	Si	24.70	(±0.42)	8.79	2.95
	Na	3.65	(±0.21)	1.59	0.53
	K	2.52	(±0.09)	0.64	0.22
	Fe	60.90	(±0.27)	10.90	3.66
$Co_{1.1}Fe_{1.9}O_4$/CHA-Na	Al	7.86	(±0.23)	2.91	1.00
	Si	23.60	(±0.42)	8.40	2.88
	Na	3.05	(±0.19)	1.33	0.46
	K	2.19	(±0.09)	0.56	0.19
	Fe	40.60	(±0.23)	7.27	1.89
	Co	22.70	(±0.16)	3.85	1.00

Table 5.8 *The elemental compositions of cobalt ferrite in the CHA-Na for the Cs adsorption experiments and C-Co3*

	Formula	Concentration (wt%)		Amount of material (mmol)	Ratio
For the Cs adsorption experiments	Fe	40.60	(±0.23)	7.27	1.89
	Co	22.70	(±0.16)	3.85	1.00
C-Co03	Fe	27.00	(±0.13)	4.83	2.52
	Co	11.30	(±0.06)	1.92	1.00

The measured magnetic properties of the Fe_3O_4/CHA-Na and the $Co_{1.1}Fe_{1.9}O_4$/CHA-Na for the Cs adsorption experiments are shown in Figures 5.11 and 5.12, and the magnetisation loops and the hysteresis details are in Table 5.9. Both products had small hysteresis, and the hysteresis of $Co_{1.1}Fe_{1.9}O_4$/CHA-Na was shifted to the negative magnetic field side. However, the gaps (M_r/M_s) were less than 0.1, meaning they were superparamagnetic. The maximum magnetisation of the Fe_3O_4/CHA-Na was 5.3 emu/g, which was 53.6 emu/g smaller than for the bare Fe_3O_4 at 50 kOe. The $Co_{1.1}Fe_{1.9}O_4$/CHA-Na was 6.3 emu/g, which was 63.3 emu/g smaller than for the bare $Co_{0.3}Fe_{2.7}O_4$ at 50 kOe. It could be assumed the decreased maximum magnetisation was caused by the CHA-Na layer around the Fe_3O_4 and $Co_{1.1}Fe_{1.9}O_4$ due to the magnetic phase transition, and the nanoparticle sizes, because the average Fe_3O_4 in the CHA-Na was bigger than the bare particles. Furthermore, the Fe_3O_4 might form as aggregated

particles in the CHA-Na. However, the maximum magnetisation was about 2.5 emu/g higher than chabazite/iron oxides synthesised by Karmaoui and Hriljac (2016).[114]

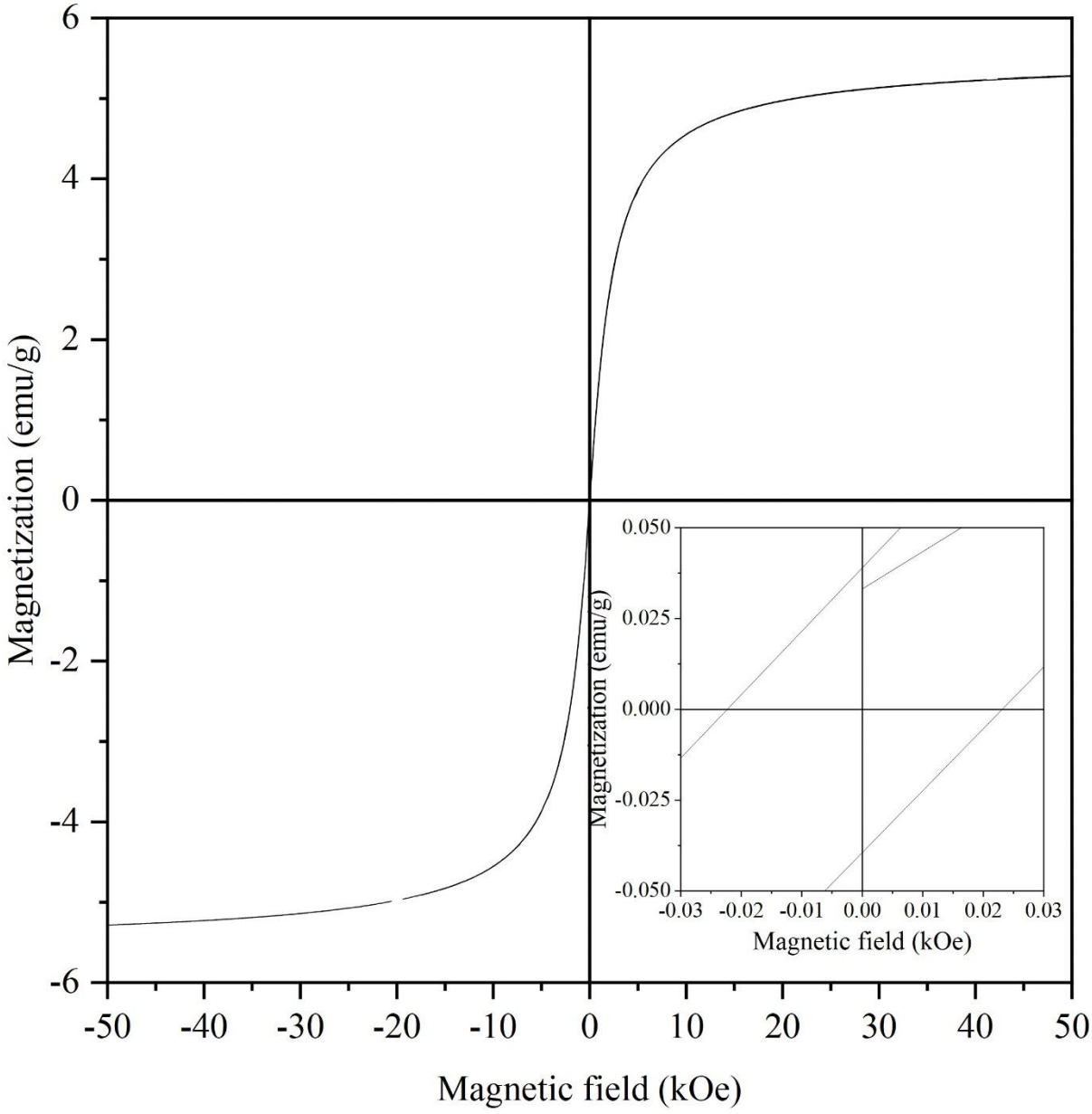

Figure 5.11 *Magnetisation loop of Fe_3O_4/CHA-Na*

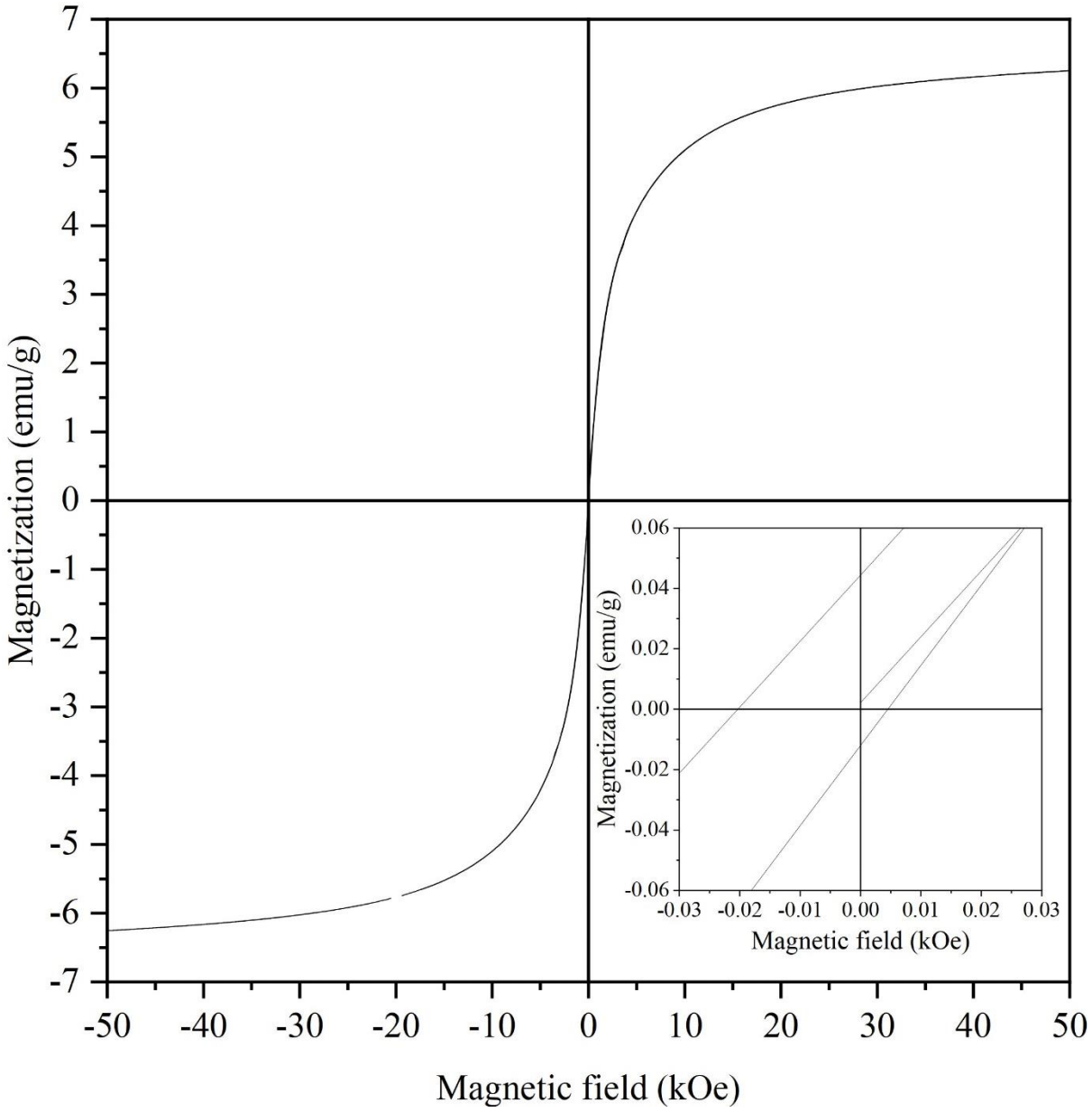

Figure 5.12 *Magnetisation loop of $Co_{1.1}Fe_{1.9}O_4$/CHA-Na*

Table 5.9 *Relationship of the magnetisation hysteresis gaps and the superparamagnetism of Fe_3O_4/CHA-Na and $Co_{1.1}Fe_{1.9}O_4$/CHA-Na.*

	H_c (kOe)	M_s (emu/g)	M_r (emu/g)	M_r/M_s
Fe_3O_4/CHA-Na	-0.022	5.300	0.039	0.007
	0.023	-5.300	-0.034	0.006
$Co_{1.1}Fe_{1.9}O_4$/CHA-Na	-0.020	6.300	0.044	0.007
	0.005	-6.300	-0.012	0.002

The superparamagnetic properties of the products were also characterised by the ZFC/FC curves (Figures 5.13 and 5.14). The blocking temperature of Fe_3O_4/CHA-Na was 119.61 K smaller than that of the bare Fe_3O_4, and for the $Co_{1.1}Fe_{1.9}O_4$/CHA-Na it was also 92.79 K smaller than for the bare $Co_{0.3}Fe_{2.7}O_4$. It could be supposed that the Fe_3O_4 and $Co_{1.1}Fe_{1.9}O_4$ in the CHA-Na were aggregated during the synthesis process even when the rotation oven was used, or that the distances between the nanoparticles in the CHA-Na might not be large enough to maintain a single magnetic moment domain in some parts. Therefore, it could be expected that the blocking temperature was much higher than it was for the bare nanoparticles. However, the blocking temperature was lower than room temperature, so these products were still superparamagnetic.

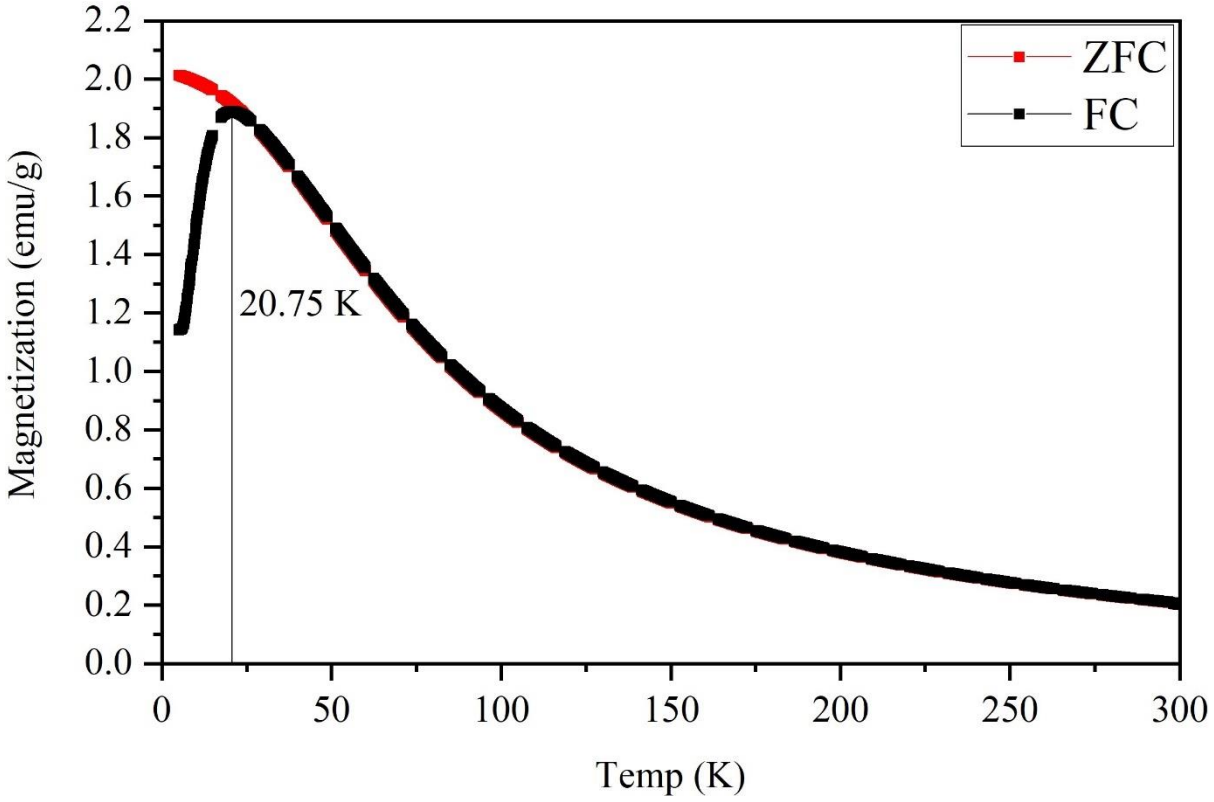

Figure 5.13 *ZFC/FC curves of Fe_3O_4/CHA-Na*

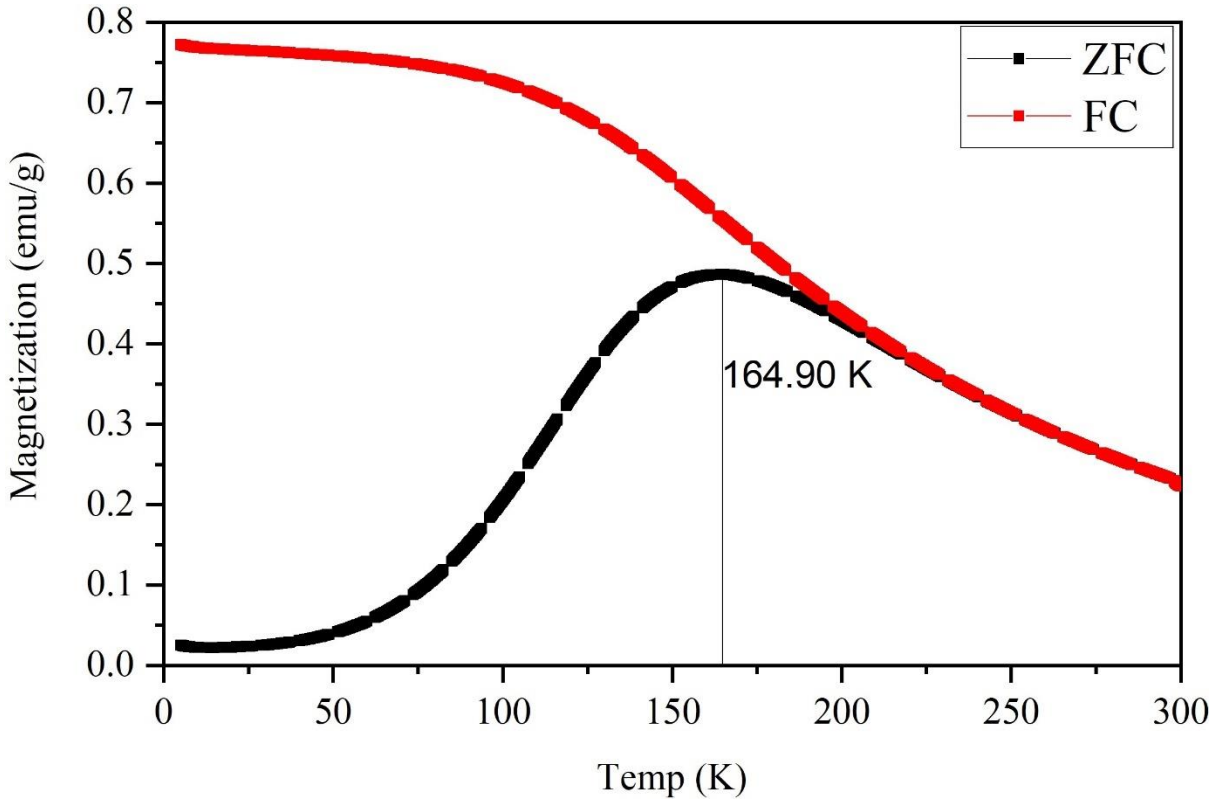

Figure 5.14 *ZFC/FC curves of $Co_{1.1}Fe_{1.9}O_4$/CHA-Na*

5.3.3 Cs adsorption

5.3.3.1 Adsorption isotherms

Figure 5.15 shows the Cs adsorption isotherms of the Fe_3O_4/CHA-Na, the $Co_{1.1}Fe_{1.9}O_4$/CHA-Na and the bare CHA-Na. The initial Cs concentrations and the pH values of the concentrated Cs solutions before and after the Cs adsorption experiments are shown in Table 5.10. The isotherm curves of Fe_3O_4/CHA-Na and $Co_{1.1}Fe_{1.9}O_4$/CHA-Na were almost the same. The equilibrium concentration (Ce) of Cs of CHA-Na was the highest until the initial Cs concentration was around 121 ppm; after that, the curve was almost the same for both products. It could be assumed most Cs was adsorbed onto the CHA-Na in the solutions with the smaller initial Cs concentrations. However, the Cs capacity was almost the same for all the products when the initial Cs concentration was higher.

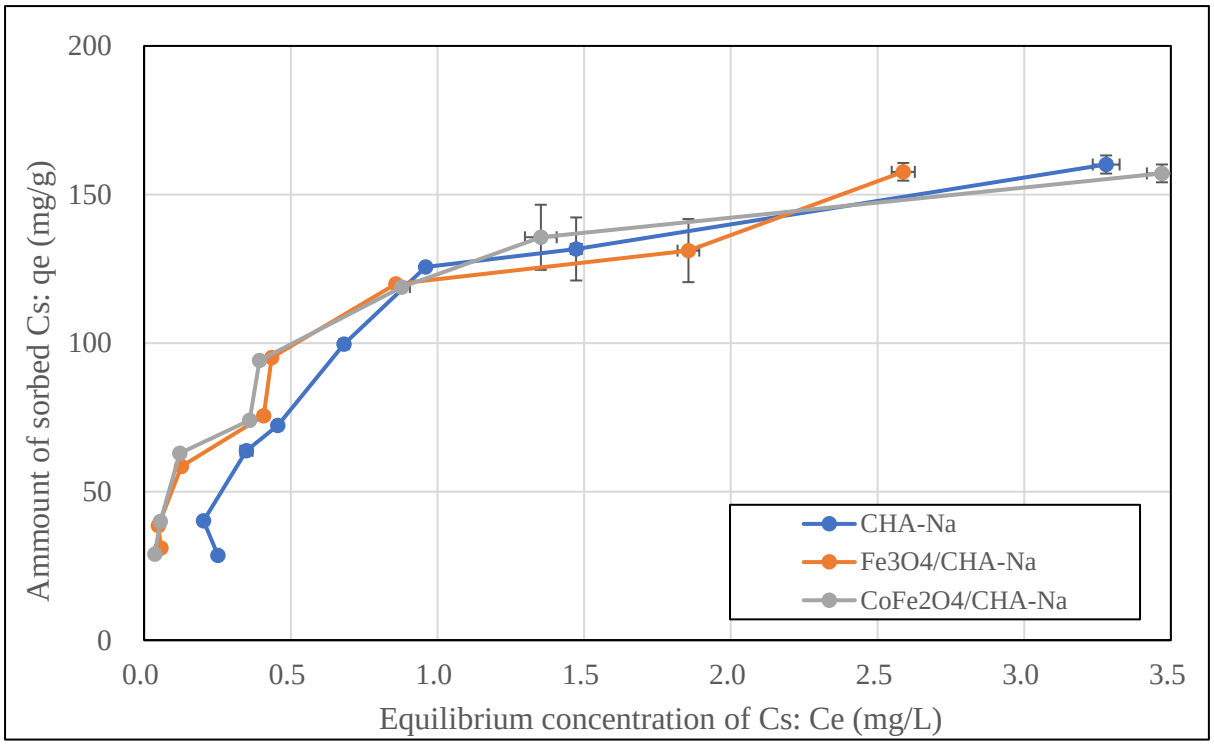

Figure 5.15 *Adsorption isotherms of M_xO_y/CHA-Na. (See Appendix about the standard error details, Table 9.12).*

The final pH values of the concentrated Cs solutions of Fe_3O_4/CHA-Na were the smallest, and the $Co_{1.1}Fe_{1.9}O_4$/CHA-Na had similar pH values to the bare CHA-Na. The results were consistent with the adsorption isotherm results: the final pH values were higher for the products with the higher Ce values at the highest initial Cs concentration; conversely, the smaller pH values were associated with the smaller Ce values. The optimal pH value for Cs adsorption onto CHA-Na is about 5.5, and the Cs capacity decreases gradually with increasing pH.[25]

Table 5.10 *Initial and final pH of Cs exchange solution for the adsorption isotherms. The measurement was used the auto-hold mode that the pH values were measured when they moved within ± 3 digit for 10 sec.*

ppm	initial pH	Final pH		
		CHA-Na	Fe_3O_4/CHA-Na	$CoFe_2O_4$/CHA-Na
160.70 (±2.95)	5.34	5.63	5.30	5.70
138.76 (±11.05)	5.29	5.83	5.53	5.56
121.45 (±0.78)	5.46	6.24	5.12	6.22
95.87 (±0.84)	5.48	6.18	5.95	6.06
75.75 (±1.20)	5.46	6.43	5.83	6.22
63.12 (±0.85)	5.71	6.02	6.08	6.22
40.36 (±0.42)	5.96	6.43	6.14	6.71
30.30 (±0.61)	5.60	6.48	6.02	6.36

The obtained Cs adsorption isotherms were fitted with the Langmuir and Freundlich isotherm models (Figures 5.16 to 5.18). All of them were a closer fit with the Langumir model, and the results show that all of them had maximum Cs capacities, because

if the Freundlich mode can be applied for the simulations, it means the zeolite has heterogeneous surface for the adsorptions. The model also tells that the products had evenly distributed Cs asorption sites. This means the Fe_3O_4 and $Co_{1.1}Fe_{1.9}O_4$ nanoparticles did not distort the CHA-Na Cs adsorption sites.

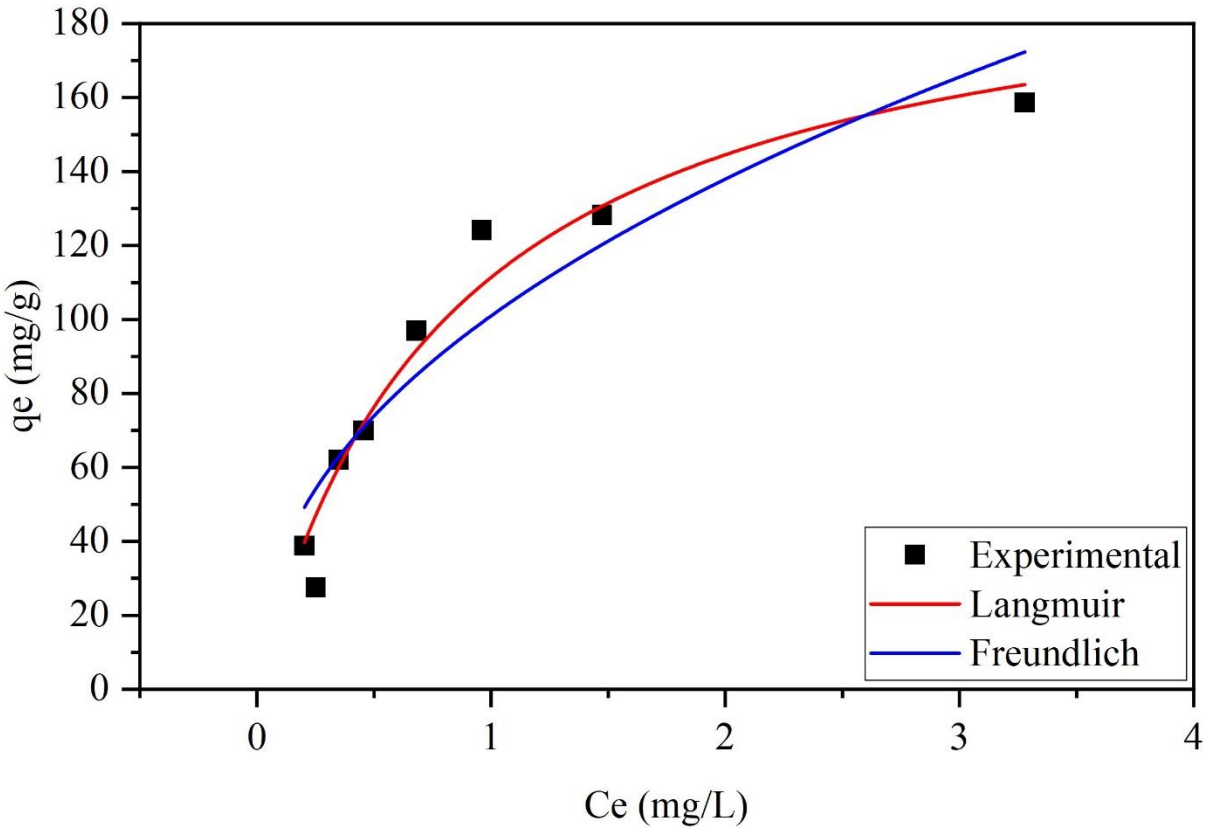

Figure 5.16 *Langmuir and Freundlich fitting curves of CHA-Na*

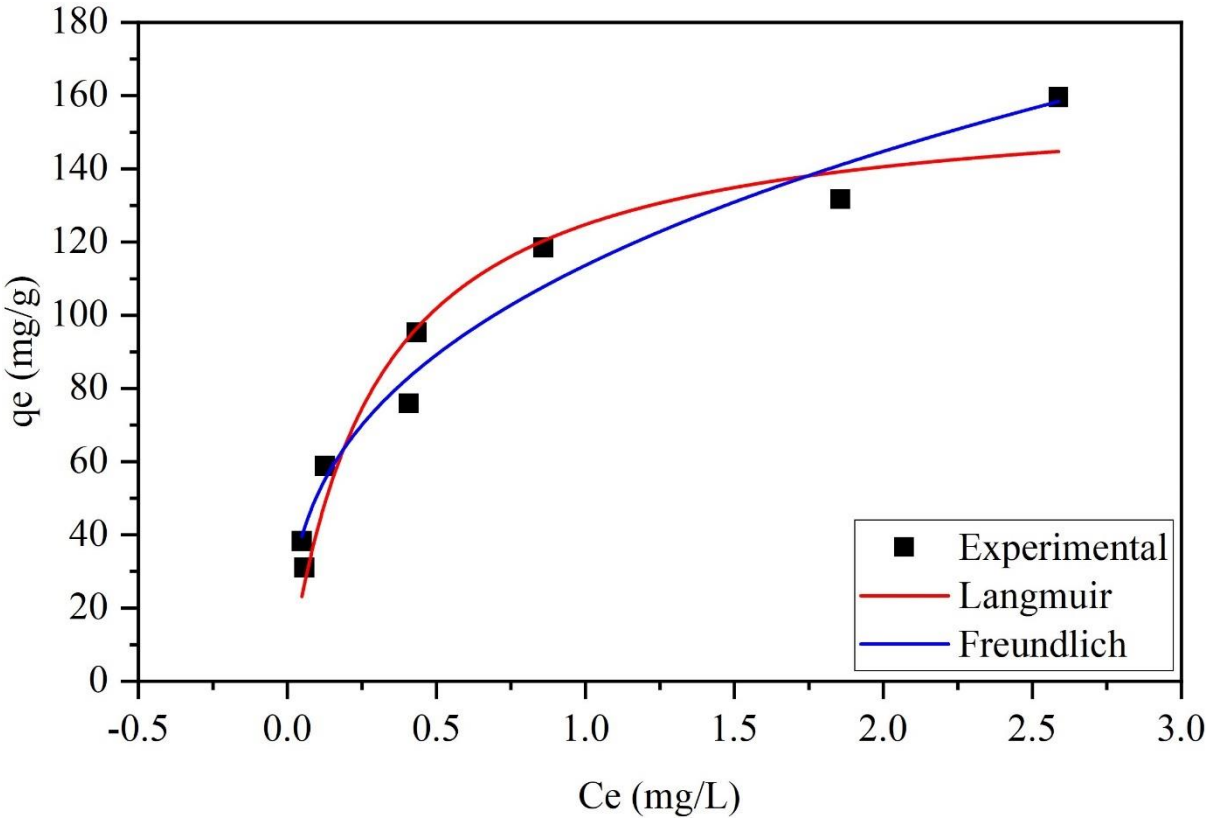

Figure 5.17 *Langmuir and Freundlich fitting curves of Fe_3O_4/CHA-Na*

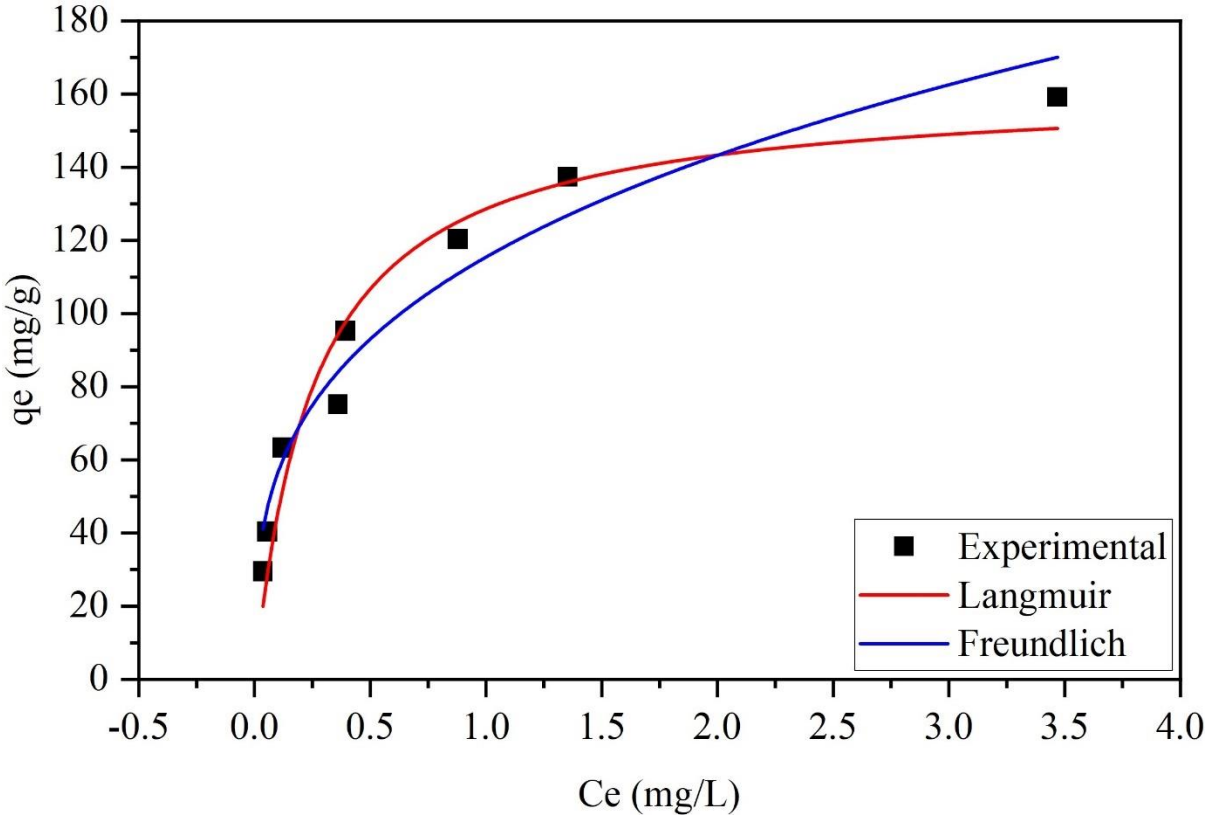

Figure 5.18 *Langmuir and Freundlich fitting curves of $Co_{1.1}Fe_{1.9}O_4$/CHA-Na*

5.3.3.2 Time-dependent Cs adsorption

The time-dependent Cs adsorption was also determined, and the results are shown in Figures 5.19 and 5.20. Most Cs was adsorbed onto the samples within 10 min of starting this experiment, and the adsorption equilibria of all samples were reached within about 30 to 120 min. Table 5.11 shows the pH values measured at the start and at each sample time. The pH dropped when the samples made contact with the concentrated Cs solutions. However, the values increased and stabilised about 30 min after the start, and the final pH values had moved within 1.0 unit.

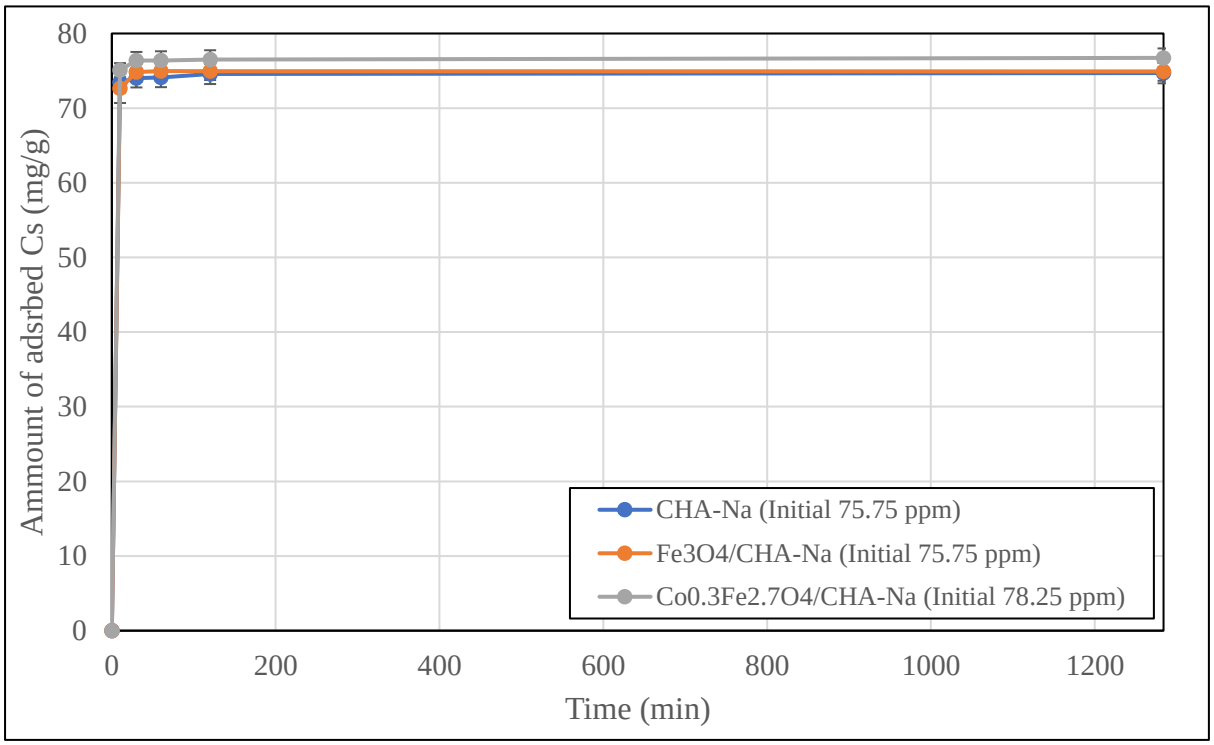

Figure 5.19 *Cs adsorption of M_xO_y/CHA-Na with time. The numbers after the samples were the duplicate experiments. (See Appendix about the standard error details, Table 9.13).*

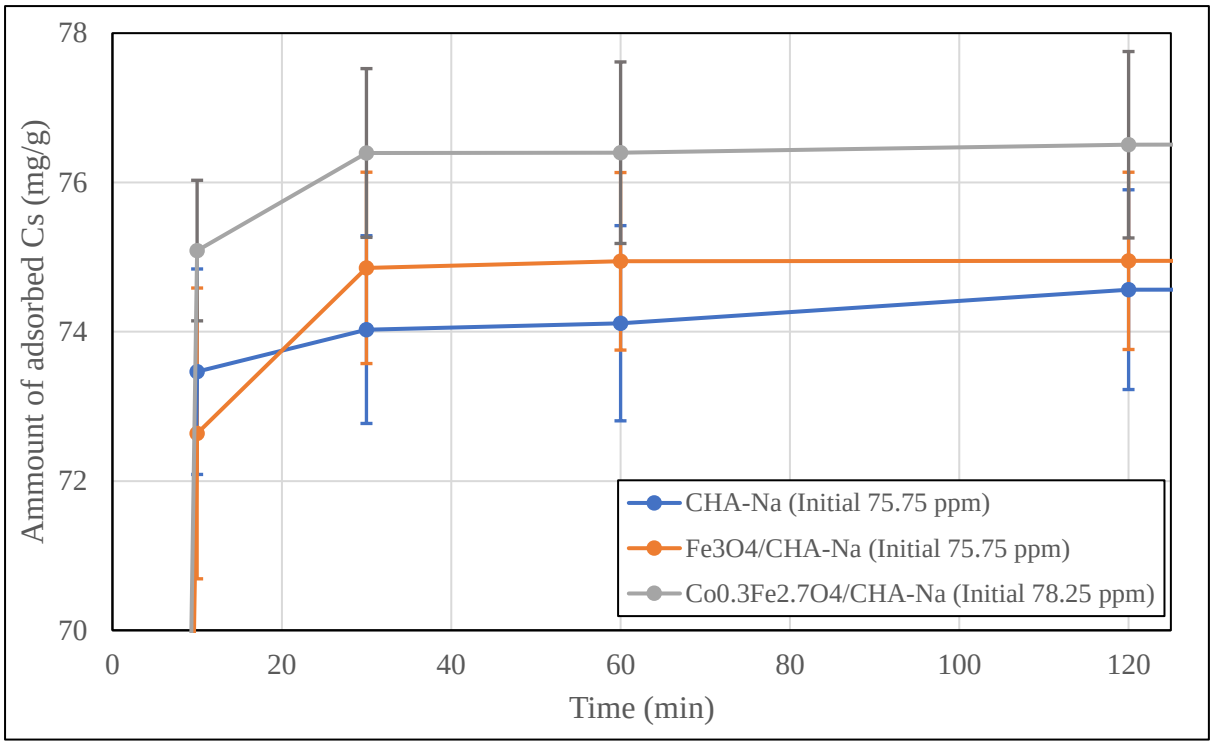

Figure 5.20 *Cs adsorption of M_xO_y/CHA-Na with time (Greater data of Figure 5.19). The numbers after the samples were the duplicate experiments.*

Table 5.11 *Initial and final pH of Cs exchange solution for the Cs adsorption over time.*

Time	CHA-Na		Fe_3O_4/CHA-Na		$Co_{1.1}Fe_{1.9}O_4$/CHA-Na	
0	5.46	*	5.46	*	5.68	*
10	5.43	*	4.89	(±0.00)	5.11	(±0.06)
30	4.76	(±0.38)	4.96	(±0.08)	5.26	(±0.04)
60	5.21	(±0.32)	5.17	(±0.09)	5.19	(±0.01)
120	5.49	(±0.11)	5.17	(±0.04)	5.28	(±0.06)
1440	5.90	(±0.27)	5.33	(±0.15)	5.98	(±0.04)

** The measurement was used the auto-hold mode that the pH values were measured when they moved within ± 3 digit for 10 sec.*

The elemental compositions of the products and bare CHA-Na before and after the Cs adsorption experiment are presented in Tables 5.12 to 5.14. Samples of a few tens of milligrams were mixed with few grams of wax to make pellets for the XRF measurements.

Therefore, the elemental ratios would have varied due to the impurities; however, the elemental ratios of CHA-Na in the products and the bare CHA-Na did not seem to change before and after the Cs adsorption. Most of the K in the bare CHA-Na seemed to have been exchanged with Cs. The amount of Na was also decreased, and the Fe_3O_4/CHA-Na and the $Co_{1.1}Fe_{1.9}O_4$/CHA-Na adsorbed Cs well.

Table 5.12 *Elemental compositions of the bare CHA-Na before and after the Cs adsorption experiment depending time.*

	Formula	Concentration (wt%)		Amount of material (mmol)	Ratio
CHA-Na	Al	19.60	(±0.41)	0.73	1.00
	Si	65.50	(±0.87)	2.33	3.21
	Na	7.66	(±0.31)	0.33	0.46
	K	7.11	(±0.21)	0.18	0.25
Cs-exchanged CHA-Cs	Al	4.74	(±0.24)	1.76	1.00
	Si	14.80	(±0.46)	5.27	3.00
	Na	1.30	(±0.15)	0.57	0.32
	K	1.16	(±0.09)	0.30	0.17
	Cs	77.90	(±1.33)	5.86	3.34

The amount of Na in the Fe_3O_4/CHA-Na was decreased about by half after the adsorption; however, the amount of K seemed to be unchanged. The amount of adsorbed Cs did not seem to be much different from the bare CHA-Na, and this is also shown by the Cs adsorption curves.

Table 5.13 *Elemental compositions of the Fe_3O_4/CHA-Na before and after the time-dependent Cs adsorption experiment.*

	Formula	Concentration (wt%)		Atomic weight (g/mol)	Amount of material (mmol)	Ratio
Fe3O4/CHA-Na	Al	8.04	(±0.23)	26.98	2.98	1.00
	Si	24.70	(±0.42)	28.09	8.79	2.95
	Na	3.65	(±0.21)	22.99	1.59	0.53
	K	2.52	(±0.09)	39.10	0.64	0.22
	Fe	60.90	(±0.27)	55.85	10.90	3.66
Cs-exchanged Fe_3O_4/CHA-Na	Al	4.03	(±0.04)	26.98	1.49	1.00
	Si	13.00	(±0.02)	28.09	4.63	3.10
	Na	1.13	(±0.09)	22.99	0.49	0.33
	K	1.22	(±0.08)	39.10	0.31	0.21
	Cs	51.35	(±0.01)	132.91	3.86	2.59
	Fe	29.25	(±0.01)	55.85	5.24	3.51

The elemental composition results of the $Co_{1.1}Fe_{1.9}O_4$/CHA-Na were also similar to those for Fe_3O_4/CHA-Na. The ratios of Co and Fe seemed to be unchanged before the experiment. The $Co_{1.1}Fe_{1.9}O_4$/CHA-Na adsorbed more Cs, but it can be thought that the sample's impurity by mixing with the small amount of sample and the wax caused the higher K in $Co_{1.1}Fe_{1.9}O_4$/CHA-Na (See the other elemental composition data by XRF in Appendix, Table 9.1 to 9.3). The difference in the Cs exchange with Na and K can be assumed to be due to the adsorption and desorption sites of Na and K when adding the Fe_3O_4 and $Co_{1.1}Fe_{1.9}O_4$.

Table 5.14 *Elemental compositions of the $Co_{1.1}Fe_{1.9}O_4$/CHA-Na before and after the time - dependent Cs adsorption experiment (the ratio of Co and Fe are highlighted in blue).*

	Formula	Concentration (wt%)		Atomic weight (g/mol)	Amount of material (mmol)	Ratio
$Co_{1.1}Fe_{1.9}O_4$/CHA-Na	Al	7.86	(±0.23)	26.98	2.91	1.00
	Si	23.60	(±0.45)	28.09	8.40	2.88
	Na	3.05	(±0.19)	22.99	1.33	0.46
	K	2.19	(±0.09)	39.10	0.56	0.19
	Fe	40.60	(±0.23)	55.85	7.27	1.89
	Co	22.70	(±0.16)	58.93	3.85	1.00
Cs-exchanged $Co_{1.1}Fe_{1.9}O_4$/CHA-Na	Al	3.56	(±0.14)	26.98	1.32	1.00
	Si	11.96	(±0.28)	28.09	4.26	3.23
	Na	0.94	(±0.09)	22.99	0.41	0.31
	K	1.17	(±0.06)	39.10	0.30	0.23
	Cs	51.55	(±0.90)	132.91	3.88	2.94
	Fe	20.45	(±0.17)	55.85	3.66	2.12
	Co	10.17	(±0.10)	58.93	1.73	1.00

The Cs adsorption onto the Fe_3O_4/CHA-Na, $Co_{1.1}Fe_{1.9}O_4$/CHA-Na and CHA-Na in which the pH of concentrated Cs solutions was stabilised were also conducted, and the result is shown in Figure 5.21. The initial pH is presented in 5.15, and the initial and final pH values are shown in 5.16. The highest Cs adsorption performances of the samples was seen at pH 4.04, even when the initial Cs concentration was higher in the other pH solutions. The final pH also stayed within 0.3 of the initial value. At pH 6.89 and pH 10.03, the adsorption capacities of Cs of the samples varied at the different initial pH values, such as the standard errors of the CHA-Na at pH 4.04 and 10.03 were ±1.55 ppm, but the errors at pH 6.89 was ±4.77 ppm. Both Fe_3O_4/CHA-Na and $Co_{1.1}Fe_{1.9}O_4$/CHA-Na had the almost same standard errors as CHA-Na.

The final pH of the concentrated Cs solution at pH 6.89 and 10.03 also changed slightly. Therefore, it could be thought the Fe_3O_4/CHA-Na and $CoFe_2O_4$/CHA-Na had a different CHA-Na pore mesh due to the Fe_3O_4 and $CoFe_2O_4$, or the Cs was adsorbed and desorbed particularly well at pH 10.03.

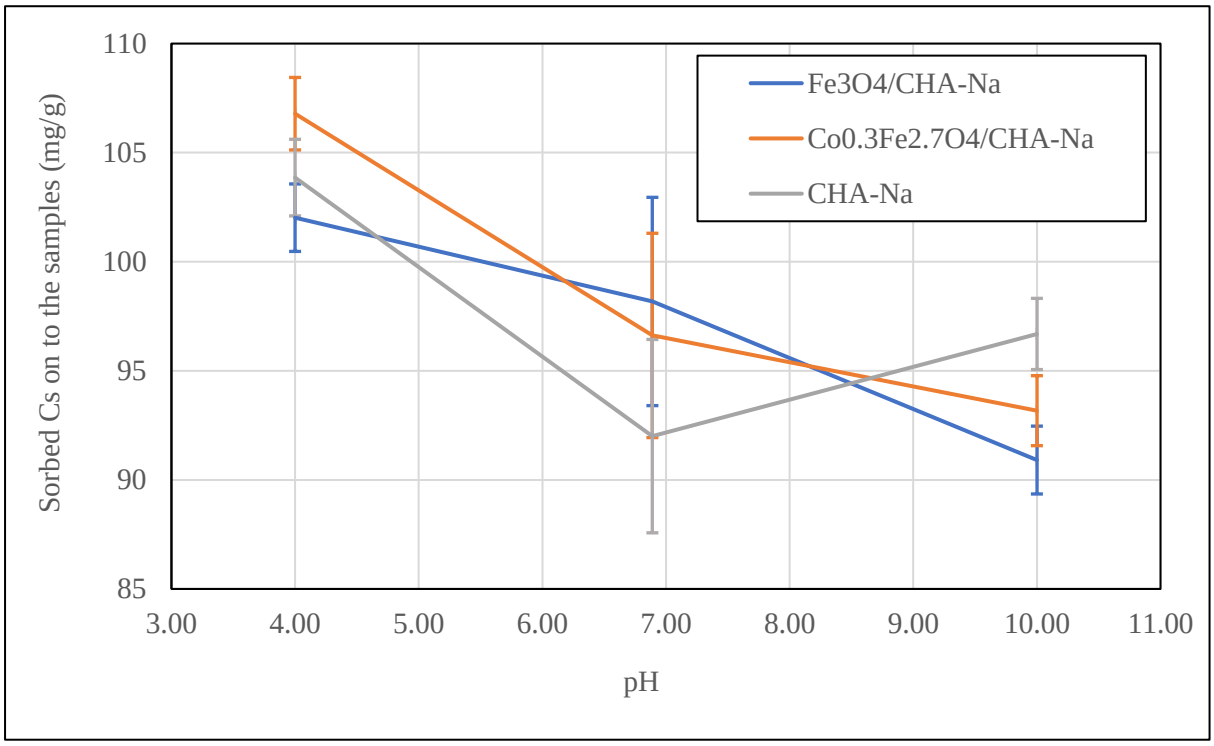

Figure 5.21 *Cs adsorption on to M_xO_y/CHA-Na depending on different initial pH. The numbers after the samples were the duplicate experiments. (See Appendix about the standard error details, Table 9.14).*

Table 5.15 *Initial pH for the Cs adsorption stabilising the pH*

pH	Cs (ppm)
4.04	107.06 (±1.52)
6.89	98.88 (±4.64)
10.03	96.30 (±1.59)

Table 5.16 *Initial and final pH of M_xO_y/SiO_2/zeolite X depending on different initial pH*

Initial	Fe_3O_4/CHA-Na	$Co_{1.1}Fe_{1.9}O_4$/CHA-Na	CHA-Na
4.04*	4.29 (±0.04)	4.29 (±0.00)	4.28 (±0.04)
6.89*	6.93 (±0.03)	6.90 (±0.01)	6.97 (±0.01)
10.03*	9.97 (±0.01)	10.01 (±0.01)	10.01 (±0.05)

**The measurement was used the auto-hold mode that the pH values were measured when they moved within ± 3 digit for 10 sec.*

The elemental composition changes of the products and the bare CHA-Na were also measured by XRF, but the samples were less than the samples that were used for the Cs adsorption depending on time (see the tables in the appendix, Table 9.14). Therefore, the results were only used to check the elemental compositions were not changed significantly after the adsorptions. From the results, the products and the bare CHA-Na seemed not to be damaged by the pH 4 solution.

5.4 Conclusion

Both Fe_3O_4/CHA-Na and $Co_{1.1}Fe_{1.9}O_4$/CHA-Na were synthesised by a one-pot method that was almost the same as the M_xO_y recipe. Fe_3O_4 was successfully formed with CHA-Na as confirmed by Raman spectroscopy. The $Co_{1.1}Fe_{1.9}O_4$ in the CHA-Na had a composition close to the theoretical cobalt ferrite formula ($CoFe_2O_4$).

More Fe_3O_4 particles were encapsulated in the CHA-Na, and the maximum magnetisations of both products were over 50 emu/g smaller than the bare M_xO_y particles. Both products were superparamagnetic that was revealed form the tiny hysteresis of the magnetization curves and the blocking temperatures of the ZFC/FC curves.

The Cs adsorption isotherms of the products were very similar to the bare CHA-Na, it means the M_xO_y particles in the CHA-Na did not affect the Cs adsorption. The pH dependence of the Cs adsorption was also very similar to the bare CHA-Na and the Cs adsorption capacities were highest at pH 4.

Magnetic zeolite for Cs^{+} and Sr^{2+} to clean up radioactively contaminated water from the Fukushima Daiichi Nuclear Power Plant

by

Azusa Ito

Supervisor: Dr Joseph A. Hriljac

A thesis submitted to the University of Birmingham for the degree of DOCTOR OF PHILOSOPHY

(Chapters 6 to 9 in the total 9 chapters)

The School of Chemistry
College of Engineering and Physical Sciences
University of Birmingham
08 April 2021

6 M_xO_y/SiO_2/zeolite

6.1 Introduction

M_xO_y/SiO_2/zeolite has an additional silica layer between the M_xO_y and zeolite to protect the M_xO_y particles. From the results of M_xO_y/CHA-Na, it could be seen that a small number of Fe_3O_4 nanoparticles were outside the CHA-Na (See Chapter 5.3.1). It could be thought some Fe_3O_4 particles were not totally covered by the CHA-Na and were on the surfaces. If so, the Fe_3O_4 and $Co_{1.1}Fe_{1.9}O_4$ might be damaged during the Cs adsorption by the M_xO_y/CHA-Na; in particular, Fe_3O_4 is easily oxidised by heat or under extremely alkaline conditions.[124] Cobalt ferrite can also be damaged and form sol flocculates under acidic conditions.[125] In this situation, it would be better to coat the M_xO_y with another layer such as silica. Therefore, another type of magnetic zeolite nanocomposite was studied, M_xO_y/SiO_2, and the results are presented in this chapter. Zeolite A, zeolite X or CHA-Na were used for Sr or Cs adsorptions. Zeolite A and zeolite X are also commonly used for synthesising MZ via cation exchanges with metal ions to encapsulate metal oxides for use in cleaning up contaminated water and drug delivery. It was found that the MZ had superparamagnetic characteristics at ambient temperatures.[17, 113, 126, 127] The zeolite A and zeolite X also have great adsorption and desorption characteristics for specific chemicals and cations such as lithium and divalent cations. They have good Sr adsorption capacities for cleaning up

radioactive contaminated water. Furthermore, their synthesis methods and reagents are very similar to each other.

In this study, three types of MSZ were synthesised using M_xO_y/SiO_2 and zeolite (zeolite A, zeolite X or CHA-Na). The Sr and Cs adsorption results of the products were evaluated and compared with those of M_xO_y/CHA-Na.

6.2 Experimental details

6.2.1 M_xO_y/SiO_2/zeolite A

The zeolite A recipe used was similar to that of Robson (1998).[128] First, 0.022 g of NaOH was dissolved in 2.4 ml of DI water. The solution was divided into two. Then, 0.25 g of sodium aluminate was put into the one of the solutions, and 0.47 g of sodium metasilicate pentahydrate was put into the other solution. After dissolving the reagents in the solutions, the mixtures were slowly combined, and this was shaken by a vortex mixer for 1 hr. Then 0.1 g of Fe_3O_4/SiO_2 or $Co_{0.3}Fe_{2.7}O_4/SiO_2$ was put into in the zeolite A seed, and it was shaken by the vortex mixer for 1 hr again. The mixture was then heated in the conventional rotation or the rotation oven at 99˚C for 5 hr. The final product was washed with DI water three times and dried at 60˚C.

6.2.2 M_xO_y/SiO_2/zeolite X

The zeolite Linde X type recipe of Robson (1998)[128] was also referenced to synthesise the M_xO_y/SiO_2/zeolite X. First, 0.68 g of sodium metasilicate pentahydrate was dissolved in 1.5 ml of DI water and 0.22 g of sodium aluminate was dissolved in 1.0 ml of DI water. After the reagents were completely dissolved, the solutions were mixed slowly, and the mixture was shaken by the vortex mixer for 1 hr to make the zeolite X seed. After this process, M_xO_y/SiO_2/zeolite X was synthesised in the same way as M_xO_y/SiO_2/zeolite A.

6.2.3 M_xO_y/SiO_2/CHA-Na

The CHA-K seed was made in the same way as M_xO_y/CHA-Na (see Chapter 5.2.1). First, 0.36 g of zeolite Y was put in 3.24 ml of KOH solution (0.39 ml of KOH and 2.85 ml of DI water), and the mixture was shaken by the vortex mixer for 1 hr. After this process, the synthesis proceeded in the same way as for M_xO_y/SiO_2/zeolite A. The M_xO_y/SiO_2/CHA-K was exchanged to form M_xO_y/SiO_2/CHA-Na in the same way as in the recipe for CHA-Na.

6.2.4 Sr or Cs adsorption experiments

Technically, the preparations and the Sr and Cs adsorption methods were the same as for the Cs adsorption experiments of M_xO_y/CHA-Na. For the Sr adsorption onto

M_xO_y/SiO_2/zeolite A and M_xO_y/SiO_2/zeolite X, $Sr(NO_3)_2$ was used to make the concentrated Sr solutions. The Sr or Cs exchanged with Na (K) solutions were also measured by ICP-MS.

ICP-MS was used to obtain Sr adsorption isotherms and dependency on time for M_xO_y/SiO_2/zeolite A, and the correlation coefficient was found to be was 0.999906. For the Sr adsorption isotherms and dependency on time of M_xO_y/SiO_2/zeolite X, and on pH using stabilised concentrated Sr solution of both MxOy/SiO2/zeolite A and MxOy/SiO2/zeolite X, the correlation coefficient was 0.999602. For the Cs adsorption onto the M_xO_y/SiO_2/CHA-Na under all of the different adsorption conditions, the correlation coefficient was 0.999832. These values of correlation coefficient suggest that the ICP-MS measurement results should be reliable. The machine was operated by Dr Christopher Stark (University of Birmingham) and Dr Norman Day (University of Birmingham).

6.2.5 XRD and Raman spectroscopy

The morphologies of the magnetic zeolite samples were also characterised using the same settings as the other products (see Chapter 3.2.4 and 5.2.4), and the obtained peak patterns were identified by DIFFRAC.EVA as well. The peak FWHM and positions of the same type products were also compared using the Origin Pro.

The Raman peaks of the products were obtained using a 10 mW green laser, irradiated for 30 seconds, and cosmic ray removal was also applied. The obtained peaks were used for confirmation of the presence of M_xO_y in the zeolite and the zeolite form.

6.2.6 XRF and SEM-EDS

The elemental compositions of the products were also characterised by XRF, including the Co and Fe ratios of cobalt ferrite in the products. The particle shape images of the products and the surface elemental composition images were also captured by SEM-EDS.

6.2.7 TEM-EDS

Only Fe_3O_4/SiO_2/zeolite A and Fe_3O_4/SiO_2/zeolite X were analysed by TEM-EDS to confirm the presence of Fe_3O_4 in the zeolite. The ratios of the $Co_{0.3}Fe_{2.7}O_4/SiO_2$ and zeolite seed were also confirmed from these results. The TEM-EDS work was carried out with Dr Gnanavel Thirunavukkarasu (University of Birmingham).

6.2.8 VSM

The magnetisation loops and the ZFC/FC curves of the products were obtained by the VSM to check whether the Fe_3O_4 and $Co_{0.3}Fe_{2.7}O_4$ in the products were still

superparamagnetic. The VSM work was carried out by Dr Mingee Chung (University of Birmingham) and his PhD student Jake Head (University of Birmingham).

6.3 Results

6.3.1 M_xO_y/SiO_2/zeolite A

6.3.1.1 Phase identification of M_xO_y/SiO_2/zeolite A

The XRD patterns of Fe_3O_4/SiO_2, zeolite A and Fe_3O_4/SiO_2/zeolite A are shown in Figure 6.1. Regarding the Fe_3O_4/SiO_2 XRD patterns, the Fe_3O_4 peak positions did not move after the SiO_2 coating was applied. As described in the Fe_3O_4/CHA-Na result (see Chapter 5.3.1), the Fe_3O_4 in this product was also identified from the peak at 41.4°. There was a tiny peak at the position, and the product seemed to contain Fe_3O_4. The zeolite A peaks of the Fe_3O_4/SiO_2/zeolite A were obtained from the synthesised zeolite A that was made using the same recipe as the product. The product has XRD peaks at the same positions at the synthesised zeolite A, apart from the peak at 51.3°. The sharp peak also seems to be Fe(0), and it might be caused while the synthesis process of Fe_3O_4/SiO_2/zeolite A, such as the Fe oxidisation (See Chapter 5.3.1).

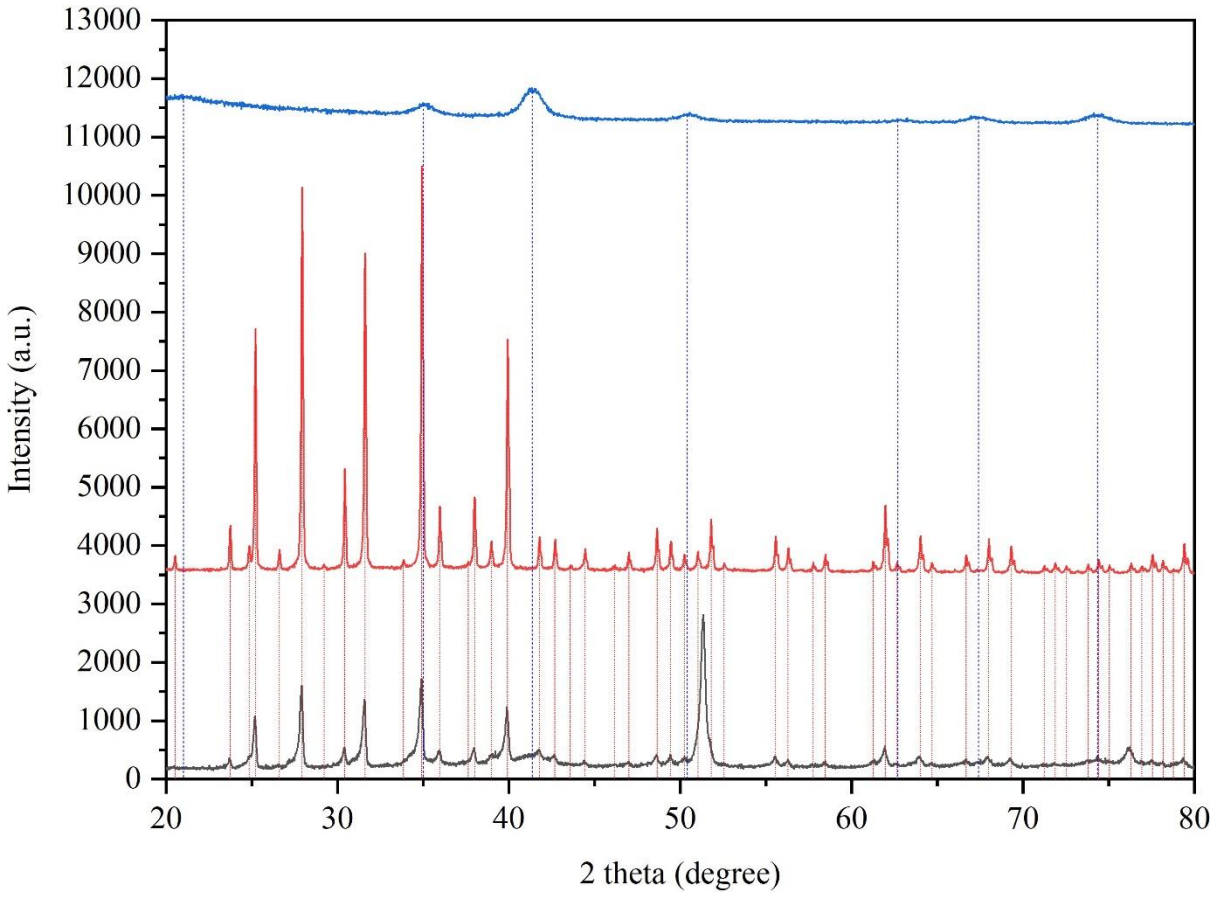

Figure 6.1 *XRD patterns of Fe_3O_4 (blue), zeolite A (red) and Fe_3O_4/SiO_2/zeolite A (black).*

The XRD patterns of $Co_{0.3}Fe_{2.7}O_4/SiO_2$/zeolite A shown in Figure 6.2 also have the $CoFe_2O_4/SiO_2$ and zeolite A patterns. The $Co_{0.3}Fe_{2.7}O_4$ in this product was also identified from the peak at 41.1°, as for $Co_{1.1}Fe_{1.9}O_4$/CHA-Na (see Chapter 5.3.1). This product also seemed to contain $Co_{0.3}Fe_{2.7}O_4$, inferred from the tiny peak around this position. The synthesised zeolite A peaks were the same as for the Fe_3O_4/SiO_2/zeolite A. The product had peaks at the same positions as zeolite A, and it seemed to be unchanged by the $Co_{0.3}Fe_{2.7}O_4/SiO_2$.

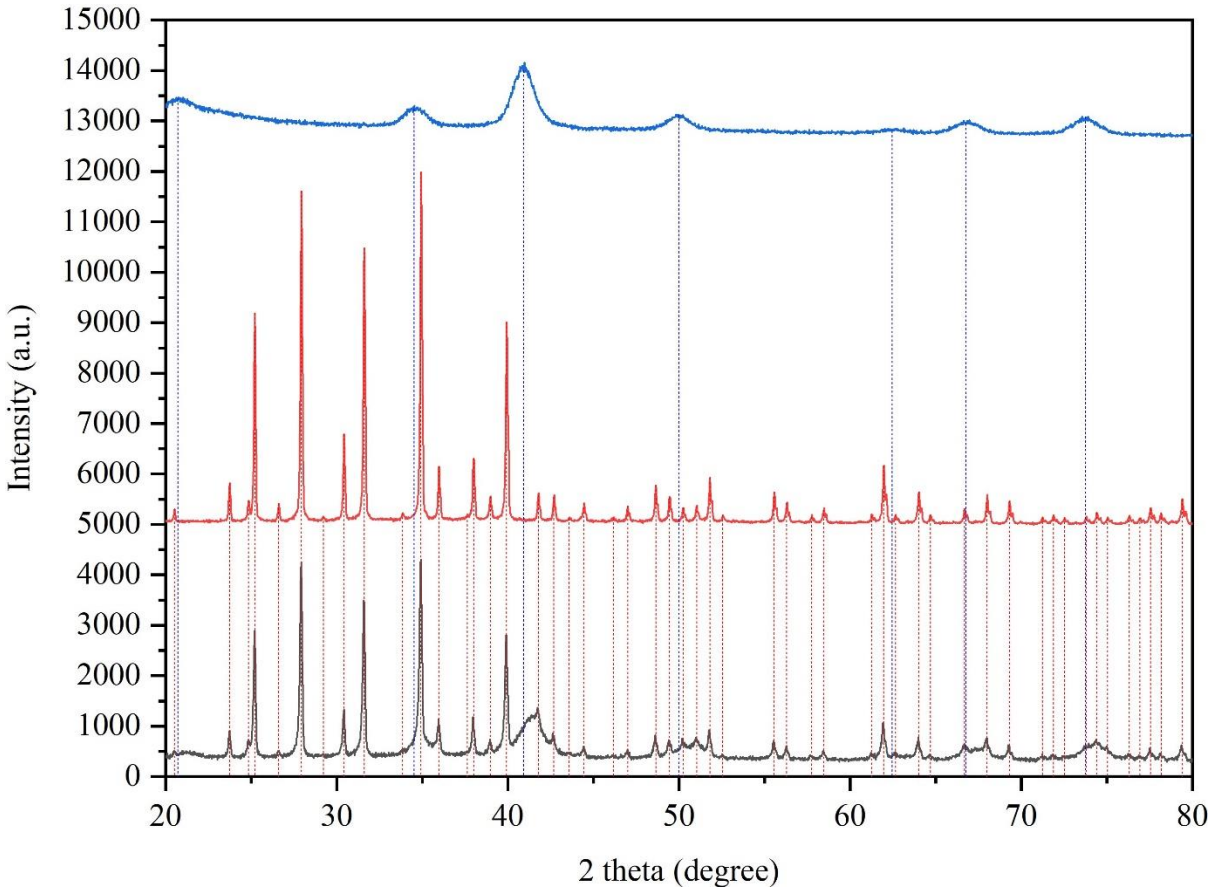

Figure 6.2 *XRD patterns of $Co_{0.3}Fe_{2.7}O_4$ (blue), zeolite A (red) and $Co_{0.3}Fe_{2.7}O_4/SiO_2$/zeolite A (black).*

These products were also characterised by Raman spectroscopy, and their peaks were compared with the Raman peaks of synthesised zeolite A (Figure 6.3). The Fe_3O_4/SiO_2/zeolite A had a Fe_3O_4 peak at 807.95 cm^{-1} that was confirmed from the RRUFF database. However, $Co_{0.3}Fe_{2.7}O_4$ was not observed in the $Co_{0.3}Fe_{2.7}O_4/SiO_2$/zeolite A Raman peak patterns. The reason could be that the zeolite A peaks are higher than those of $Co_{0.3}Fe_{2.7}O_4$, or that the zeolite A layer was thicker. The zeolite A typically has main Raman peaks at 341, 491, 695, 966, 1040 and 1097 cm^{-1}.[129] The products and the synthesised bare zeolite A also had peaks around those positions.

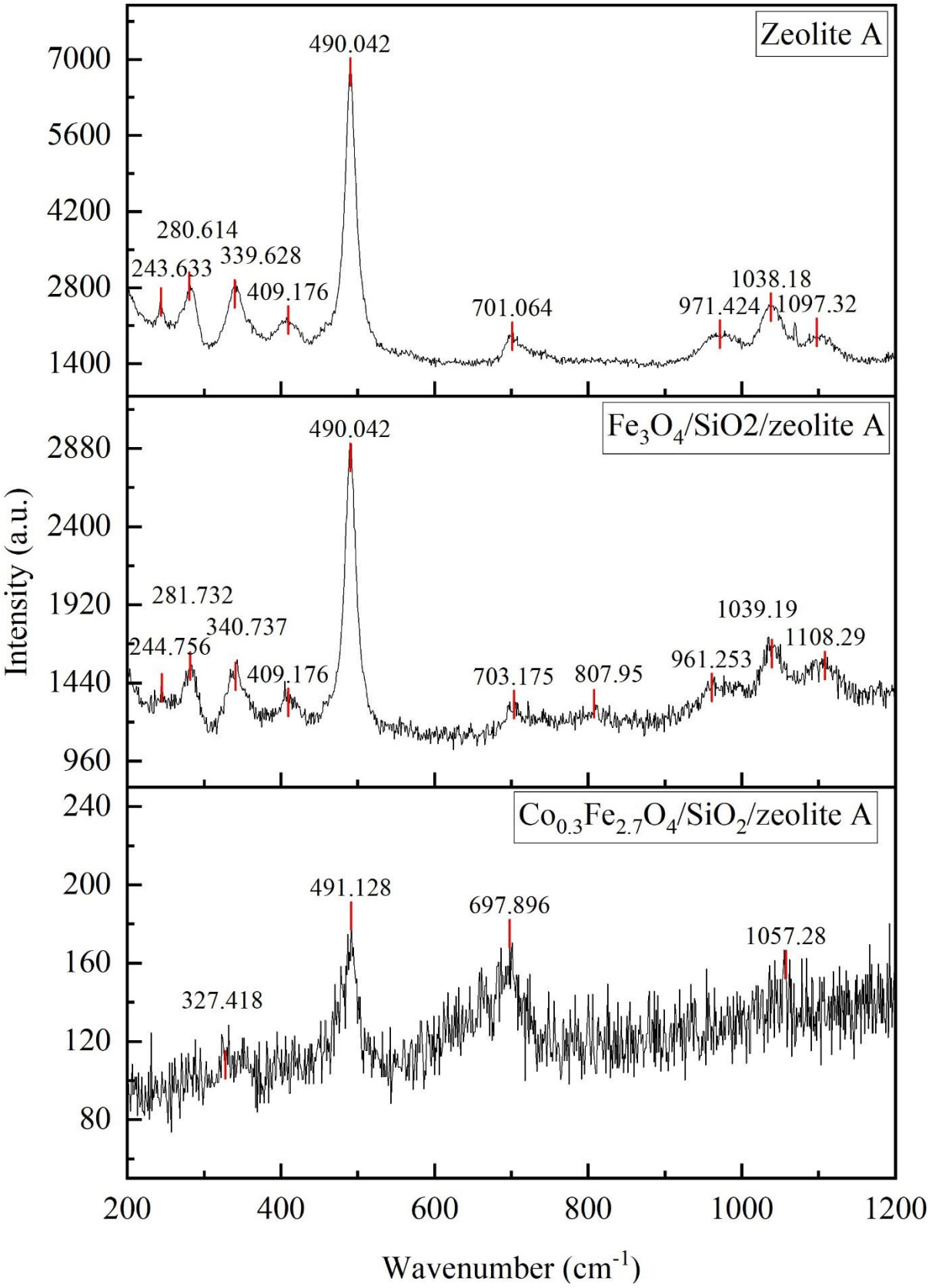

Figure 6.3 *Raman spectra of zeolite A, Fe_3O_4/SiO_2/zeolite A and $Co_{0.3}Fe_{2.7}O_4/SiO_2$/zeolite A*

The SEM images of the Fe_3O_4/SiO_2/zeolite A show cubic shaped particles that can be assumed to be zeolite A (Figure 6.4). The Fe_3O_4/SiO_2 seemed not to affect the form of zeolite A significantly. The SEM-EDS captured all the elements that the product should have. The particle surfaces had less Fe, but it appeared to be on the zeolite A particles. The Fe_3O_4/SiO_2 seemed to be evenly incorporated into the zeolite A particles.

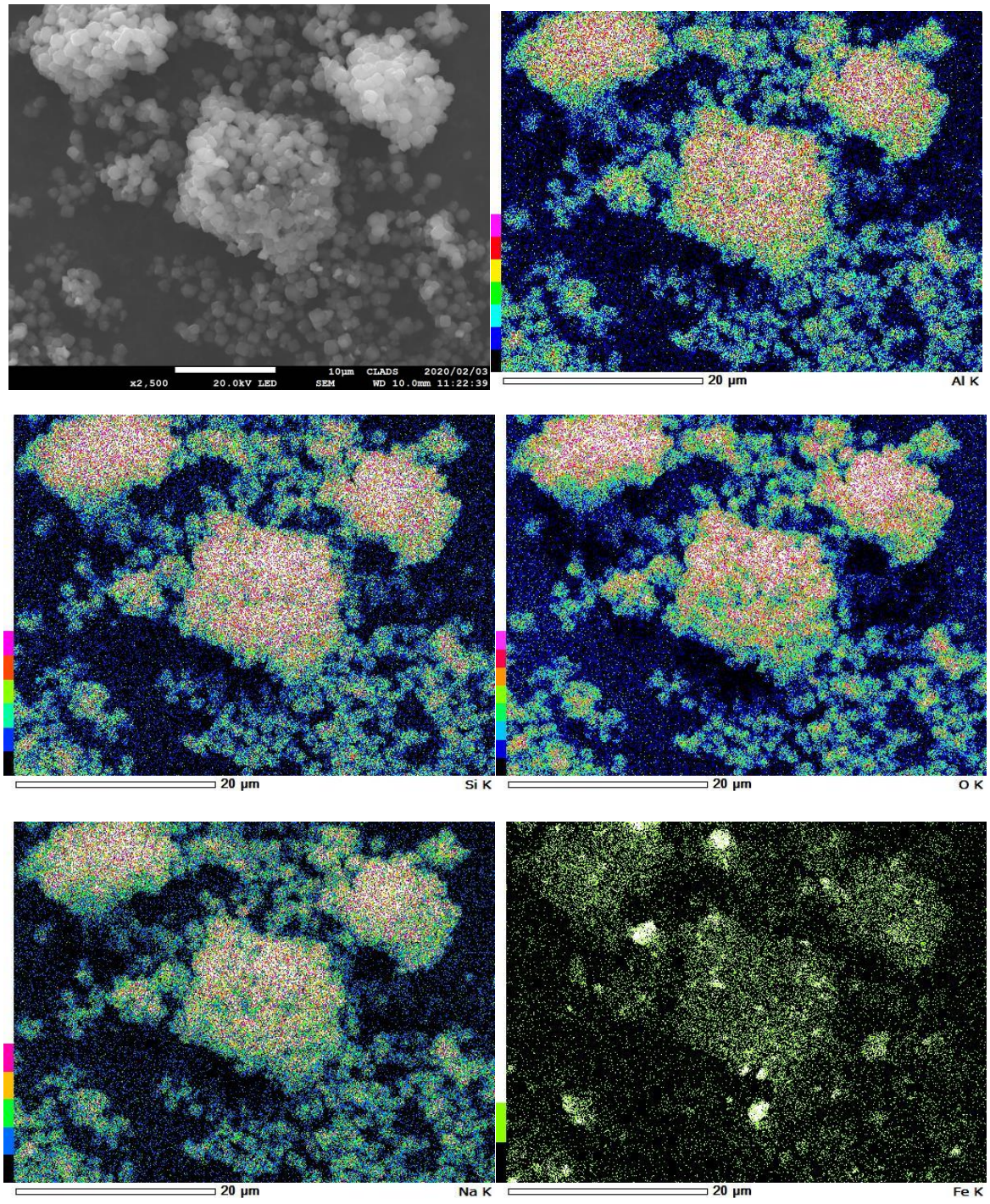

Figure 6.4 *SEM-EDS images of Fe_3O_4/SiO_2/zeolite A*

The $Co_{0.3}Fe_{2.7}O_4/SiO_2$/zeolite A particle shape images captured by the SEM show both zeolite A particle shapes and a big ellipse shaped particle. The big particle had fewer zeolite

A elements (Al, Si and Na) and more $Co_{0.3}Fe_{2.7}O_4$ elements (O, Fe and Co). It could be assumed the $Co_{0.3}Fe_{2.7}O_4/SiO_2$ particles were aggregated before or during the $Co_{0.3}Fe_{2.7}O_4/SiO_2$/zeolite A crystallisation process, even though the zeolite A seed and the $Co_{0.3}Fe_{2.7}O_4/SiO_2$ were mixed vigorously. The product was heated in the conventional oven, so the $Co_{0.3}Fe_{2.7}O_4/SiO_2$ might have been aggregated during the crystallisation process.

Pamnudi et al. (2020)[130] also reported that when less Fe_3O_4 was formed in MZ by an impregnation method that was similar to the recipe for M_xO_y/SiO_2/zeolite A, fewer aggregated Fe_3O_4 particles were formed in zeolite. In contrast, when the amount of Fe_3O_4 increased, there was more aggregation of the particles in the zeolite. However, the Fe_3O_4 aggregations in the MZ were sorted out using a coprecipitation method that was similar to that used in the recipe for M_xO_y/CHA-Na. Therefore, the aggregation of the $Co_{0.3}Fe_{2.7}O_4/SiO_2$ particles of the $Co_{0.3}Fe_{2.7}O_4/SiO_2$/zeolite A might be also due to the synthesis method. Because the M_xO_y particles were dried before using the Stober method, and it revealed the dried M_xO_y particles easily aggregates from the DLS and zeta potential results. It could be thought the process affected the aggregations in the zeolite.

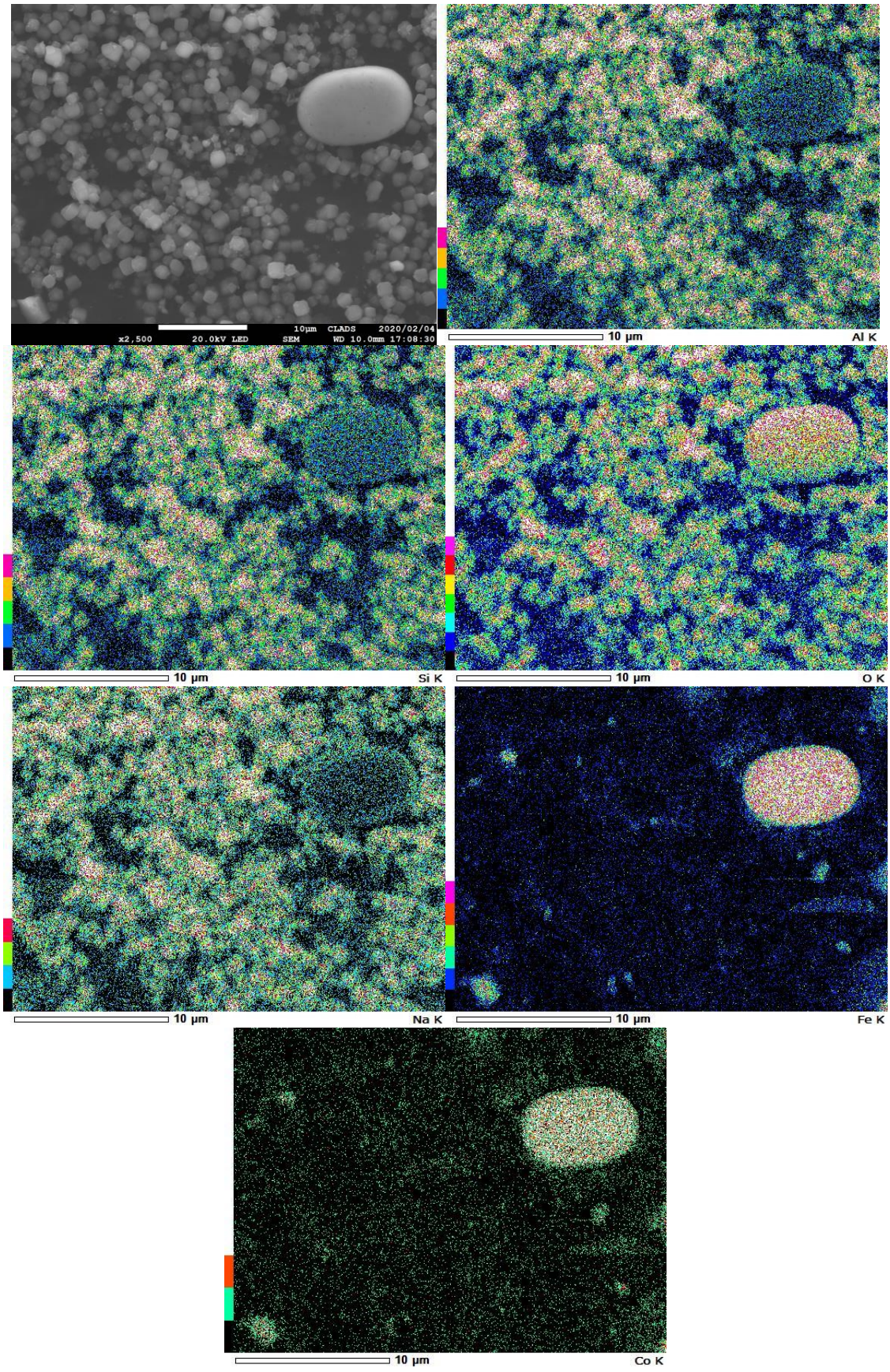

Figure 6.5 *SEM-EDS images of* $Co_{0.3}Fe_{2.7}O_4/SiO_2$*/zeolite A*

The elemental compositions of the synthesised Fe_3O_4/SiO_2/zeolite A, $Co_{0.3}Fe_{2.7}O_4/SiO_2$/zeolite A, and bare zeolite A are presented in Table 6.1 (the particles were already separated by a neodymium magnet for the further Sr adsorption experiments). Surprisingly, the Si to Al ratio in the Fe_3O_4/SiO_2/zeolite A and $Co_{0.3}Fe_{2.7}O_4/SiO_2$/zeolite A was about 0.30 less than in the bare zeolite A. It could be thought that the Si of the M_xO_y/SiO_2 might be also used for crystallising the zeolite A, therefore, the ratio would be less than in the bare zeolite A. From the result, the SiO_2 coat onto the M_xO_y particles might become thinner than before using the zeolite A formation, however, the SiO_2 might work to support the incorporation of the M_xO_y/SiO_2 particles in the zeolite by making bonds with the zeolite frameworks.The total ratio of Fe to Al and/or Co to Al in both Fe_3O_4/SiO_2/zeolite A and $Co_{0.3}Fe_{2.7}O_4/SiO_2$/zeolite A was about 4.20. They contained almost the same proportion of magnetic nanoparticles as zeolite A.

Table 6.1 *Elemental compositions of zeolite A, Fe_3O_4/SiO_2/zeolite A and $Co_{0.3}Fe_{2.7}O_4/SiO_2$/zeolite A (the ratio of Co and Fe are highlighted in yellow).*

Sample	Formula	Concentration (wt%)		Amount of material (kmol)	Ratio
Zeolite A	Al	33.70	(±0.53)	1.25	1.00
	Si	52.60	(±0.80)	1.87	1.50
	Na	13.30	(±0.39)	0.58	0.46
Fe_3O_4/SiO_2/zeolite A	Al	8.80	(±0.24)	3.26	1.00
	Si	11.60	(±0.29)	4.13	1.27
	Na	3.86	(±0.20)	1.68	0.51
	Fe	75.70	(±0.31)	13.55	4.16
$Co_{0.3}Fe_{2.7}O_4/SiO_2$/zeolite A	Al	13.80	(±0.24)	5.11	1.00
	Si	15.90	(±0.28)	5.66	1.11
	Na	7.30	(±0.25)	3.18	0.62
	Fe	47.50	(±0.18)	8.50	3.23
	Co	15.50	(±0.08)	2.63	1.00

The Fe_3O_4 and $Co_{0.3}Fe_{2.7}O_4$ particles in the zeolite A were observed by TEM (Figure 6.6). The images were taken before the particles were separated by the magnet, and the Fe_3O_4/SiO_2/zeolite A images show there were some particles with no or very little Fe_3O_4, but most particles had the expected amount of Fe_3O_4 in them. The zeolite A of $Co_{0.3}Fe_{2.7}O_4/SiO_2$/zeolite A contained some big $Co_{0.3}Fe_{2.7}O_4$ particles that were aggregated, and the zeolite A particles were also aggregated around the $Co_{0.3}Fe_{2.7}O_4$ particles (the zeolite A are light grey particles in the images).

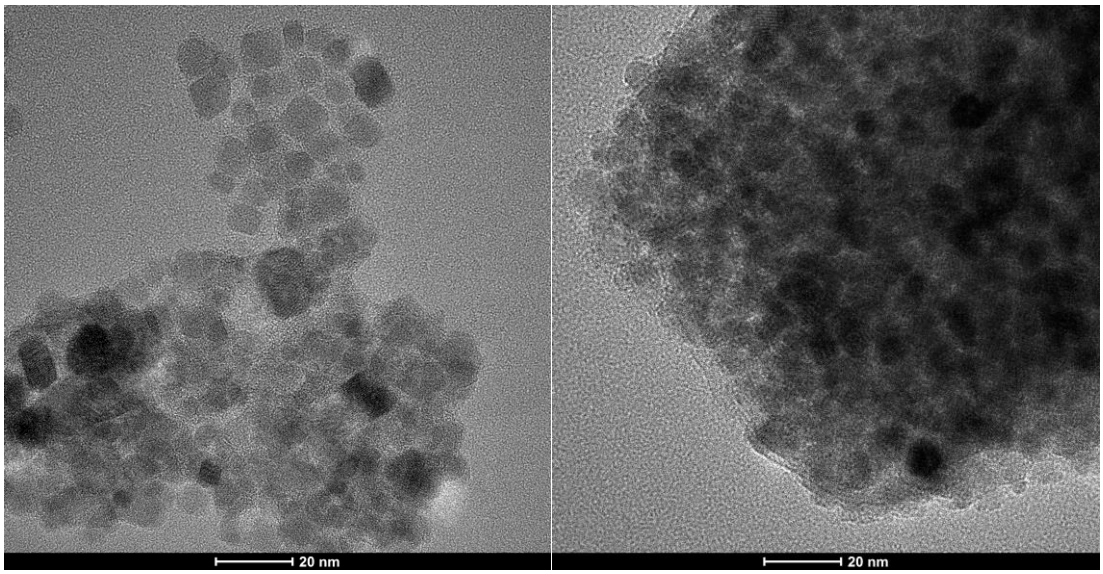

Figure 6.6 *TEM images of Fe_3O_4/SiO_2/zeolite A (left) and $Co_{0.3}Fe_{2.7}O_4/SiO_2$/zeolite A (right).*

The SEM-EDS images of the Fe_3O_4/SiO_2/zeolite A are shown in Figure 6.7. Al, Si and Na were detected around the samples, but Fe and O were detected more strongly, meaning these were Fe_3O_4-rich samples.

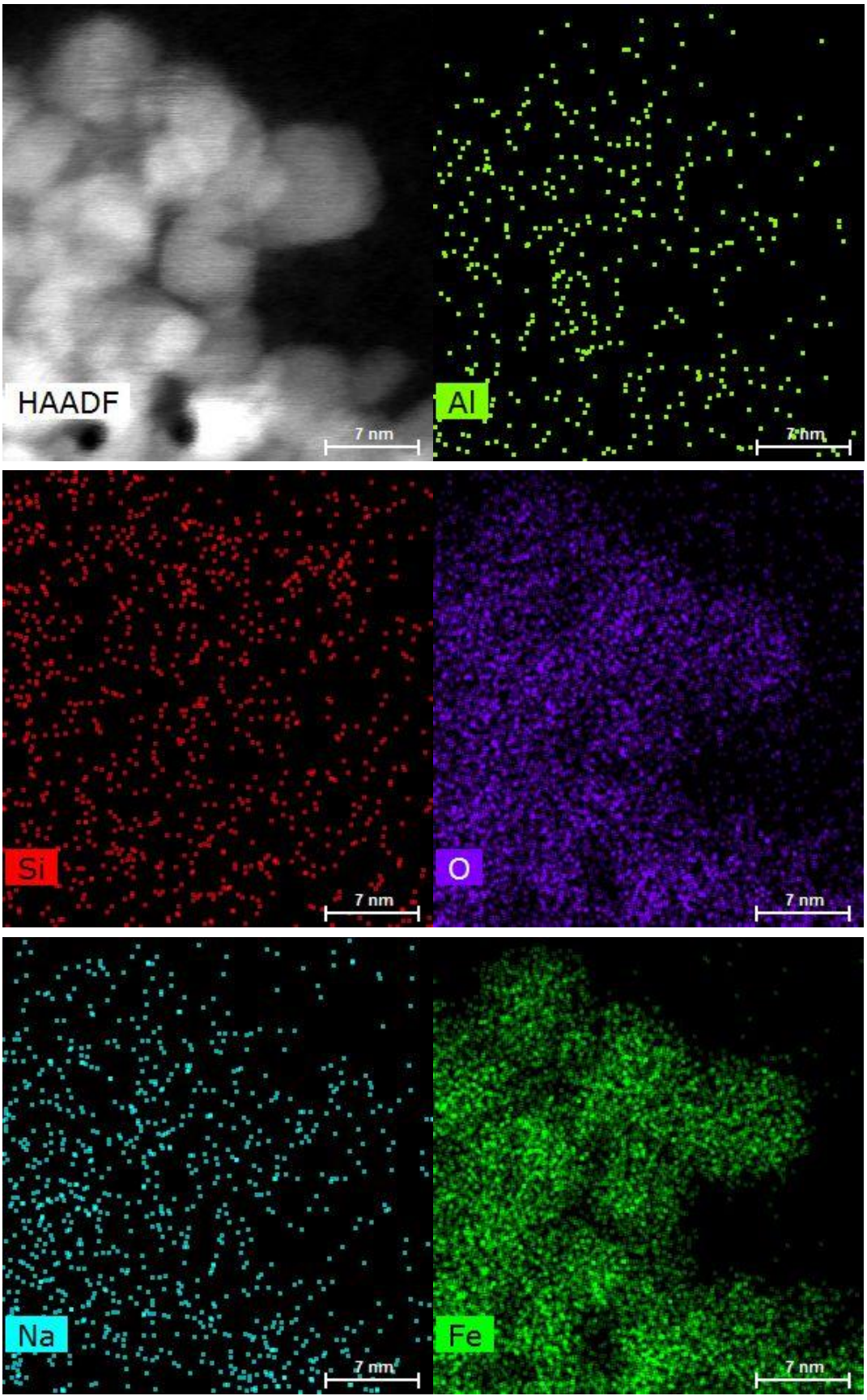

Figure 6.7 *TEM-EDS elemental mapping images of Fe_3O_4/SiO_2/zeolite A.*

The elemental mapping images of the $Co_{0.3}Fe_{2.7}O_4/SiO_2$/zeolite A were clearer than those of the Fe_3O_4/SiO_2/zeolite A due to the magnification levels. They also showed more Fe, Co and O than Al, Si and Na. The Si image shows there was more Si on the edge of the aggregated samples, and Fe, Co and O were detected strongly in the most aggregated parts (the white area on the HAADF image). From these images, it can be assumed that most of the $Co_{0.3}Fe_{2.7}O_4/SiO_2$ particles were incorporated into the zeolite A, and there were fewer particles on the edge of the zeolite A; therefore, it can be determined that there was no $Co_{0.3}Fe_{2.7}O_4/SiO_2$ outside the zeolite A.

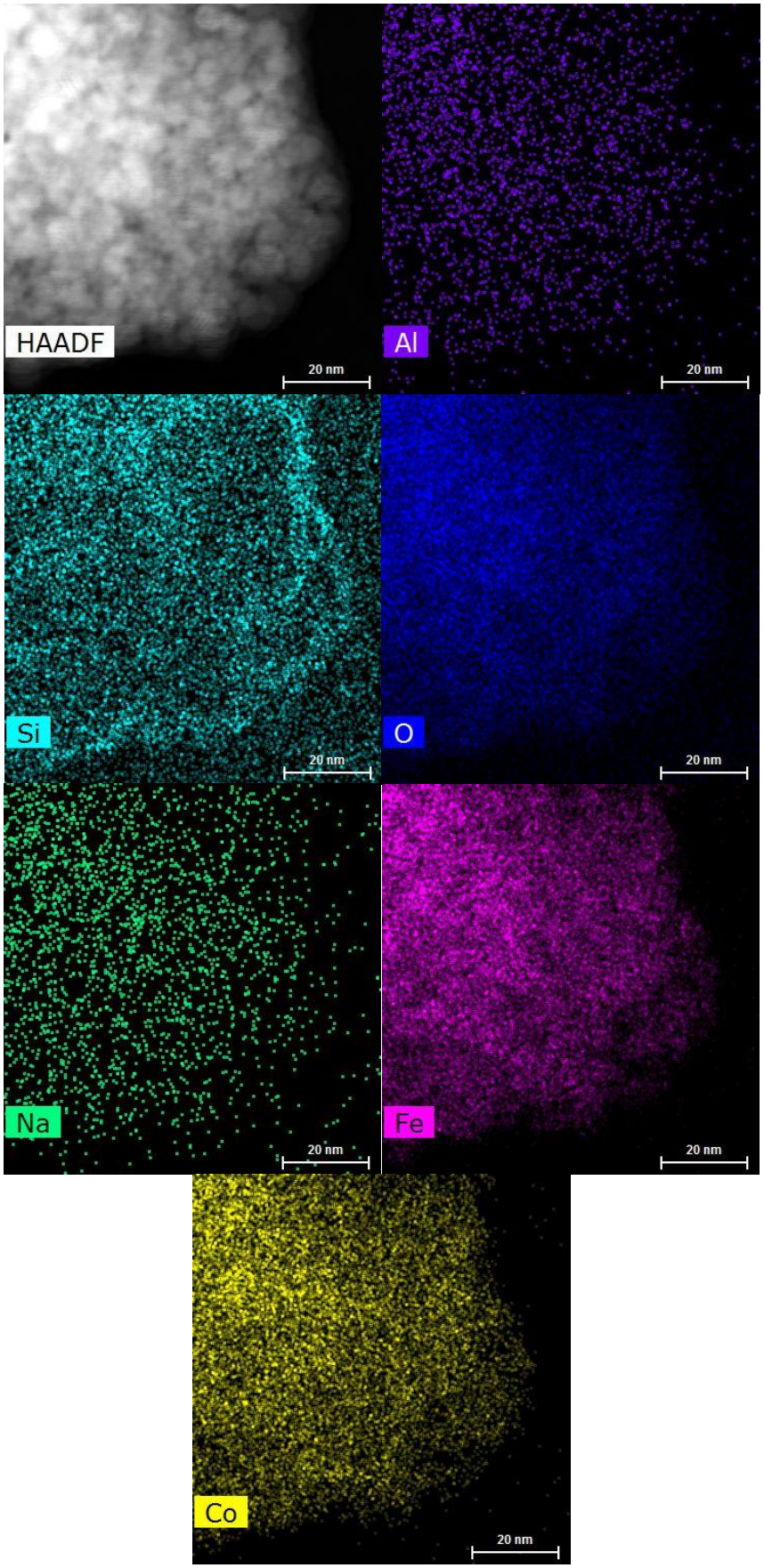

Figure 6.8 *TEM-EDS elemental mapping images of* $Co_{0.3}Fe_{2.7}O_4/SiO_2$*/zeolite A.*

6.3.1.2 Magnetic Properties

The magnetisation curves of the Fe_3O_4/SiO_2/zeolite A and $Co_{0.3}Fe_{2.7}O_4/SiO_2$/zeolite A are shown in Figures 6.9 and 6.10. Both curves saturated the origin points, and the maximum and minimum magnetisations had a central inversion shape; the tiny hysteresis of the curves did not move from the origin points, and the shapes were almost symmetrical. The maximum magnetisation of Fe_3O_4/SiO_2/zeolite A was 4.5 emu/g higher than for Fe_3O_4/CHA-Na, and that for $Co_{0.3}Fe_{2.7}O_4/SiO_2$/zeolite A was 9.2 emu/g higher than for $Co_{1.1}Fe_{1.9}O_4$/CHA-Na. The differences are negligible especially Fe_3O_4/SiO_2/zeolite A, because both products were attracted by the neodymium magnet even in water. These results might be due to a difference in the amount of M_xO_y in the zeolite: both Fe_3O_4/SiO_2/zeolite A and $Co_{0.3}Fe_{2.7}O_4/SiO_2$/zeolite A might have more Fe_3O_4 and $Co_{0.3}Fe_{2.7}O_4$ in the zeolite A than the M_xO_y/CHA-Na.

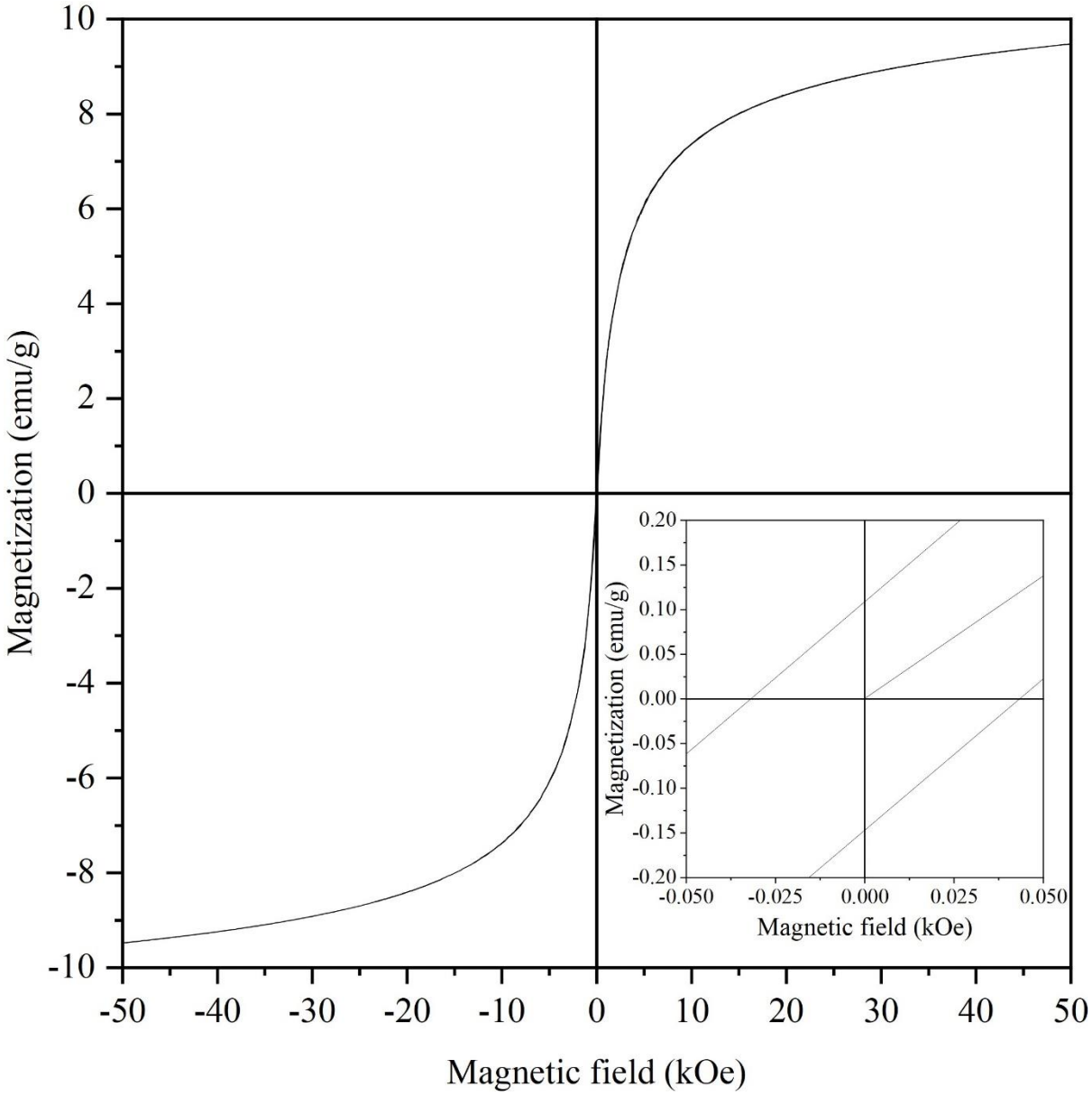

Figure 6.9 *Magnetisation loop of the Fe_3O_4/SiO_2/zeolite A.*

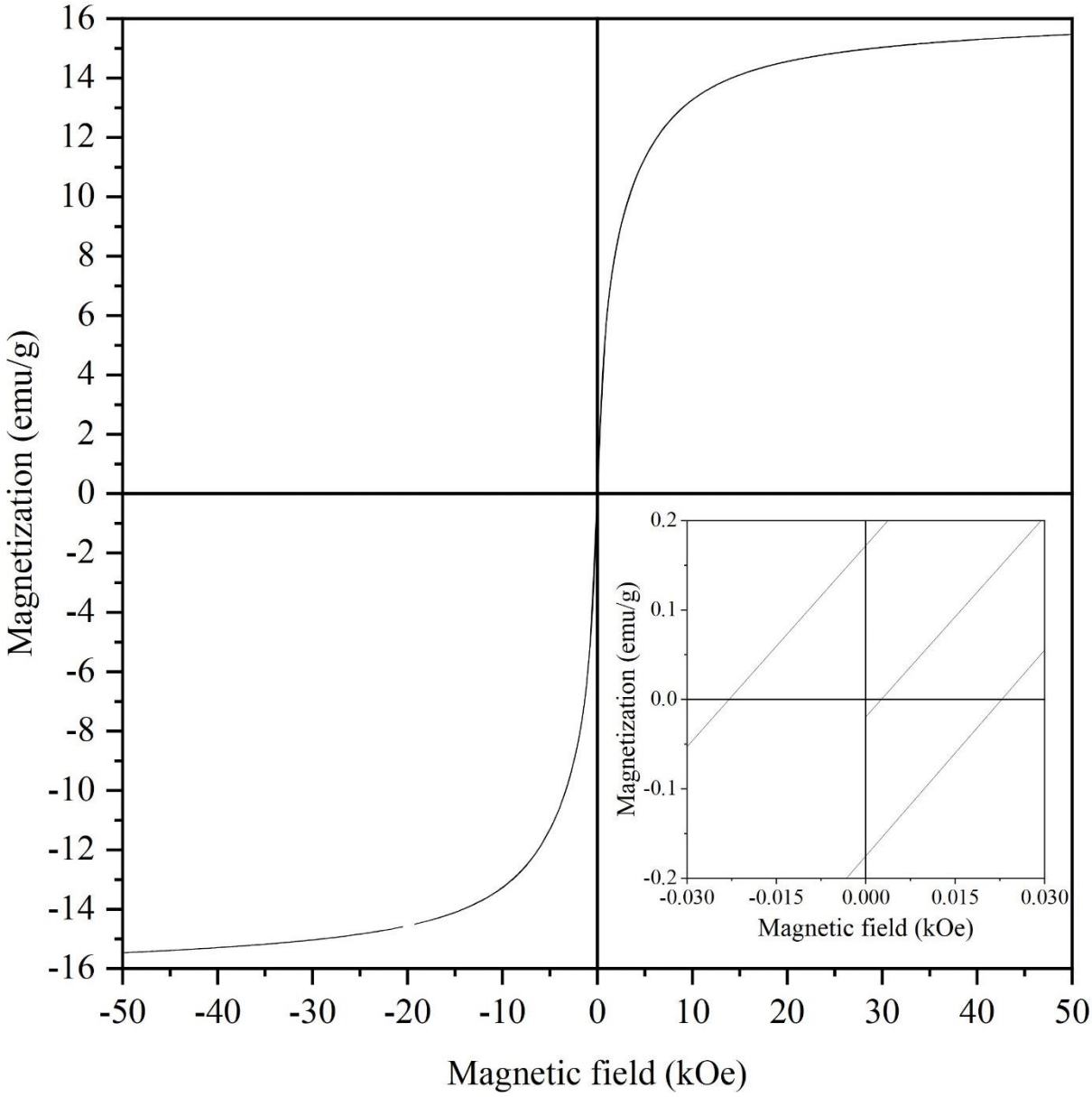

Figure 6.10 *Magnetisation loop of the $Co_{0.3}Fe_{2.7}O_4/SiO_2$/zeolite A.*

The superparamagnetism of the products was evaluated from the hysteresis gaps (Table 6.2). For both products, the M_r/M_s of the gaps was less than 0.1, and the values that were calculated from the maximum and minimum magnetisations were similar. This means the products were superparamagnetic.

Table 6.2 *Relationship between the magnetisation hysteresis gaps and superparamagnetism at 300 K.*

	H_c (kOe)	M_s (emu/g)	M_r (emu/g)	M_r/M_s
Fe_3O_4/SiO_2/zeolite A	-0.032	9.476	0.110	0.012
	0.029	-9.477	-0.147	0.016
$Co_{0.3}Fe_{2.7}O_4/SiO_2$/zeolite A	-0.022	15.500	0.170	0.011
	0.023	-15.500	-0.178	0.011

The magnetic properties of the products were also evaluated from their ZFC/FC curves (Table 6.11 and 6.12). The blocking temperatures of both were lower than room temperature. However, the blocking temperatures of both products were higher than for the corresponding M_xO_y/SiO_2; in particular, the blocking temperature of $Co_{0.3}Fe_{2.7}O_4/SiO_2$/zeolite A was higher than 273.15 K. Therefore, if these particles were used at the blocking temperature lower than 283.79 K they would not be superparamagnetic and it would be difficult to redisperse them in a solution at ambient temperature after exchanging the collected Sr with Na for reuse. However, if it is used lower than 283.79 K, it can keep having superparamagnetic, and it can be supposed the particles do not aggregate after attracted by the neodymium magnet.

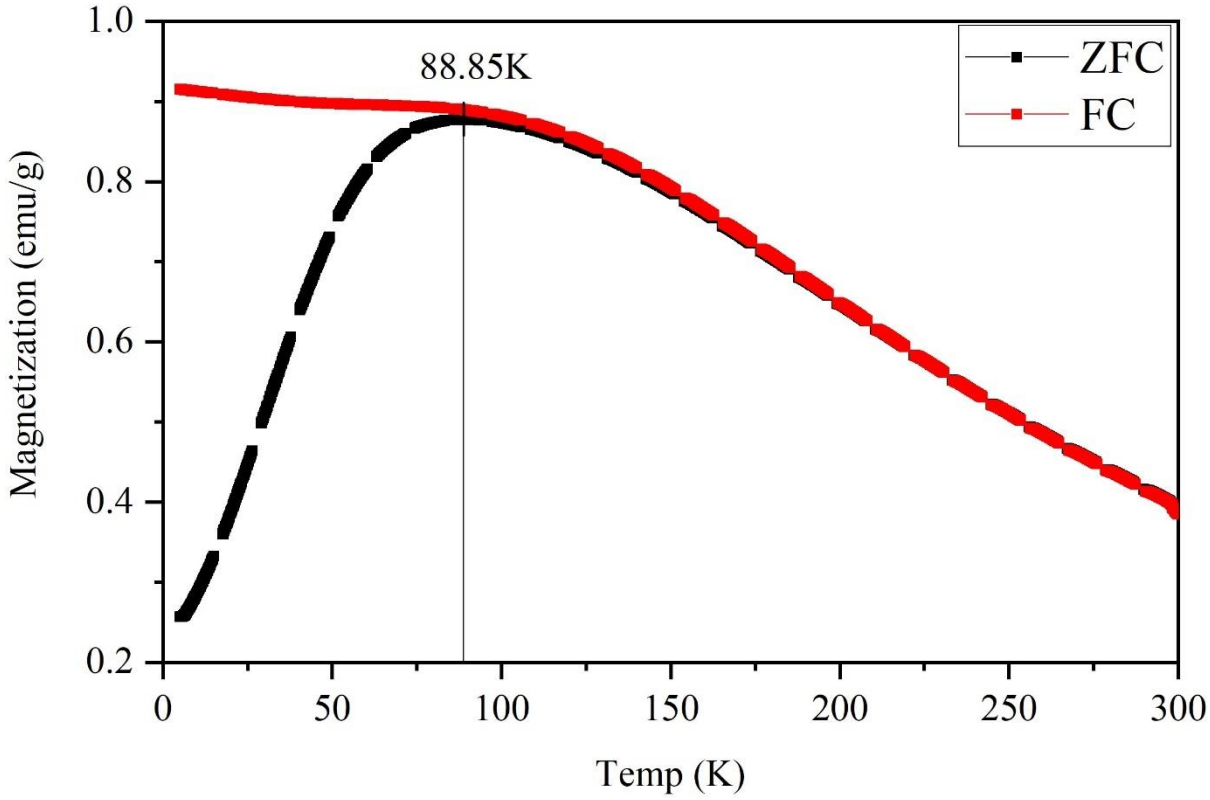

Figure 6.11 *ZFC/FC curves of the Fe_3O_4/SiO_2/zeolite A.*

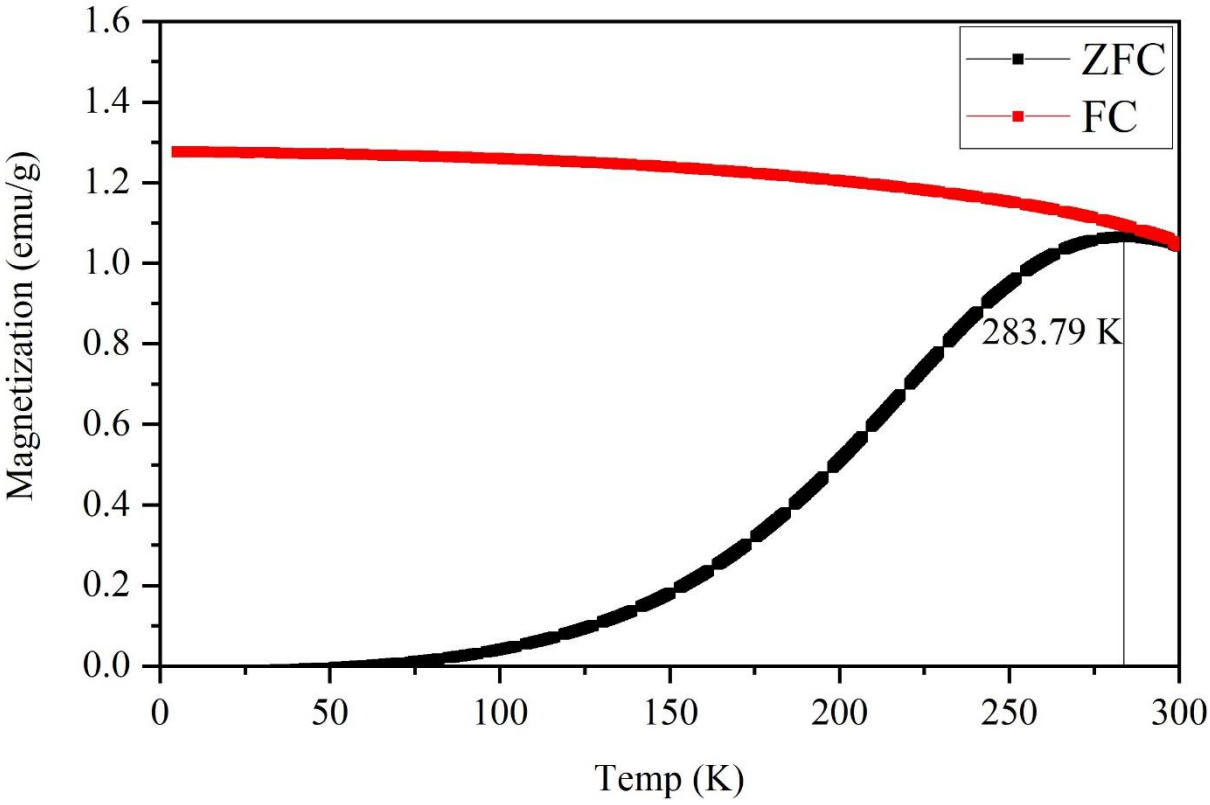

Figure 6.12 *ZFC/FC curves of the $Co_{0.3}Fe_{2.7}O_4/SiO_2$/zeolite A.*

6.3.1.3 Sr adsorption

6.3.1.3.1 Adsorption isotherms

The Sr adsorption isotherms of the Fe_3O_4/SiO_2/zeolite A, the $Co_{0.3}Fe_{2.7}O_4/SiO_2$/zeolite A and the bare zeolite A are shown in Figure 6.13. The standard error when the initial concentration was 278 ppm was ±44.72 ppm (Table 6.3), however, the standard errors of the initial concentrations between 238 to 165 ppm were less than ±10 ppm that the errors were negligible. Therefore, it could be supposed the adsorption isotherms were reliable. The bare zeolite A had the highest Sr capacity: it was about 70 mg/g higher than the other products at 55 mg/l. The isotherm curves of both Fe_3O_4/SiO_2/zeolite A and $Co_{0.3}Fe_{2.7}O_4/SiO_2$/zeolite A had almost the same shapes, showing they seemed to reach their maximum Sr capacities at around 5 mg/l. The particle sizes of the Fe_3O_4/SiO_2 and the $Co_{0.3}Fe_{2.7}O_4/SiO_2$ in the zeolite A were almost the same; therefore, it could be assumed their Sr capacities were also almost the same. However, the M_xO_y/CHA-Na had a higher Cs adsorption capacity, which was almost the same as for the bare CHA-Na. It could be assumed that the SiO_2 layer on the M_xO_y affected the pores of the zeolite A for Sr adsorption. The Na ratios of the Fe_3O_4/SiO_2 and the $Co_{0.3}Fe_{2.7}O_4/SiO_2$ were almost the same as for the bare zeolite A, and the Sr atom radius (200 pm) was bigger than Na atom radius (180 pm). Faghihian et al. (2014)[17] also reported that the difference in Sr equilibrium adsorption capacity between Fe_3O_4/zeolite A and bare Fe_3O_4 was bigger than the difference in their Cs equilibrium adsorption capacity. The number of

pores of the zeolite A might be reduced by the M_xO_y/SiO_2, because the particle size was a few nanometres bigger than the bare Fe_3O_4 (the average diameter was 8.0 nm) and $Co_{0.3}Fe_{2.7}O_4$ (The average diameter was 7.5 nm).

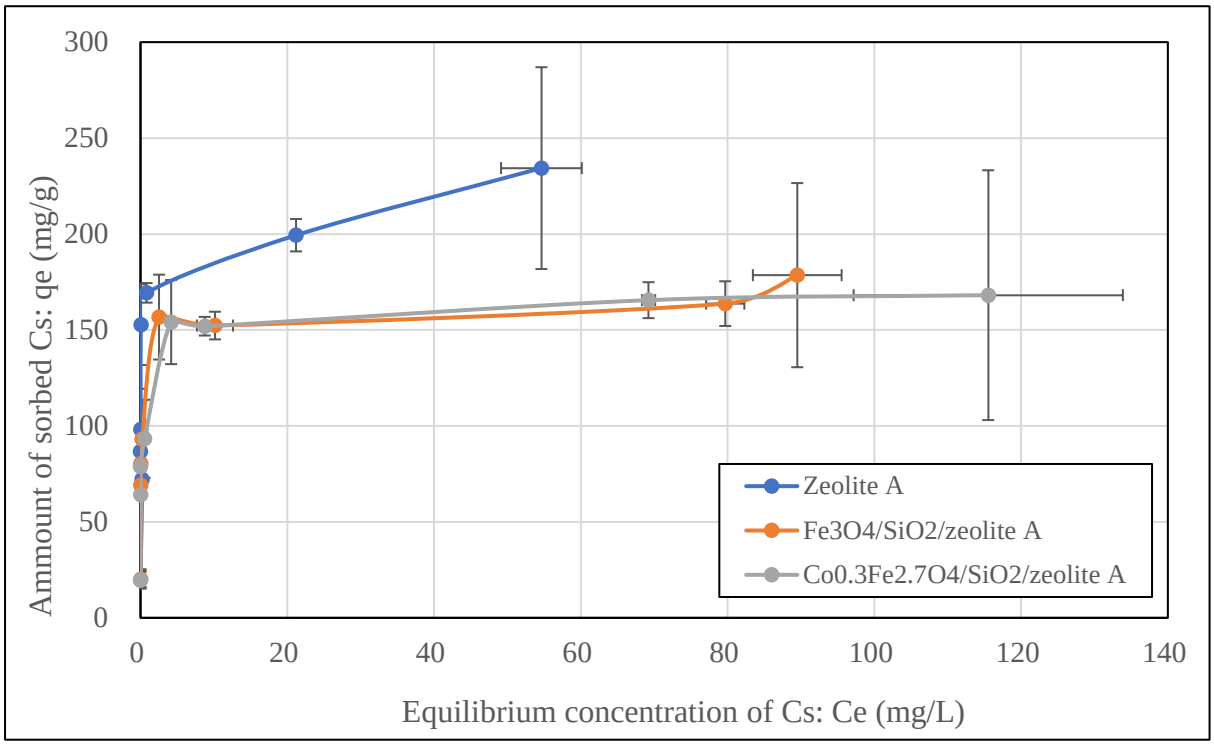

Figure 6.13 *Sr adsorption isotherm curves of M_xO_y/SiO_2/zeolite A.*

The initial pH of the Sr concentrated solution and the final pH after the Sr adsorption experiments are given in Table 6.3. The final pH values of the $Co_{0.3}Fe_{2.7}O_4/SiO_2$/zeolite A were smallest for all of the different initial Sr concentrations, and the values of the Fe_3O_4/SiO_2/zeolite A were near those of the bare zeolite A. At lower initial Sr concentrations,

the final pH of all samples increased to 8 or 9. They might be stable and able to absorb more Sr at a higher pH.

Table 6.3 *Initial $Sr(NO_3)_2$ concentrations and initial and final pH of bare zeolite A and M_xO_y/SiO_2/zeolite A. The measurement was used the auto-hold mode that the pH values were measured when they moved within ± 3 digit for 10 sec.*

ppm	Initial pH	Final pH		
		Zeolite A	Fe_3O_4/SiO_2/Zeolite A	$Co_{0.3}Fe_{2.7}O_4/SiO_2$/Zeolite A
278.43 (±44.72)	6.53	7.49	7.53	7.08
237.70 (±8.64)	6.16	7.11	6.84	6.72
164.97 (±4.86)	6.44	7.24	7.14	7.01
152.08 (±20.96)	6.31	7.56	7.04	6.85
95.66 (±20.73)	6.48	8.32	7.39	7.16
81.76 (±1.68)	8.15	8.16	8.16	8.04
68.97 (±1.32)	7.23	8.98	8.55	8.27
20.07 (±4.46)	7.36	9.63	9.11	8.77

The Sr adsorption isotherms of the products were also compared with the Langmuir and Freundlich isotherm models (Figures 6.14 to 6.16). The Sr adsorption isotherm curve of the bare zeolite A was similar to the Freundlich isotherm model. That means the maximum Sr equilibrium capacity of zeolite A could be higher in more concentrated Sr solutions.

The empirical isotherm curves of both Fe_3O_4/SiO_2/zeolite A and $Co_{0.3}Fe_{2.7}O_4/SiO_2$/zeolite A were similar to the Langmuir isotherm curves. That means they seemed to reach maximum Sr capacities, and the empirical curves became almost parallel to the Ce axis.

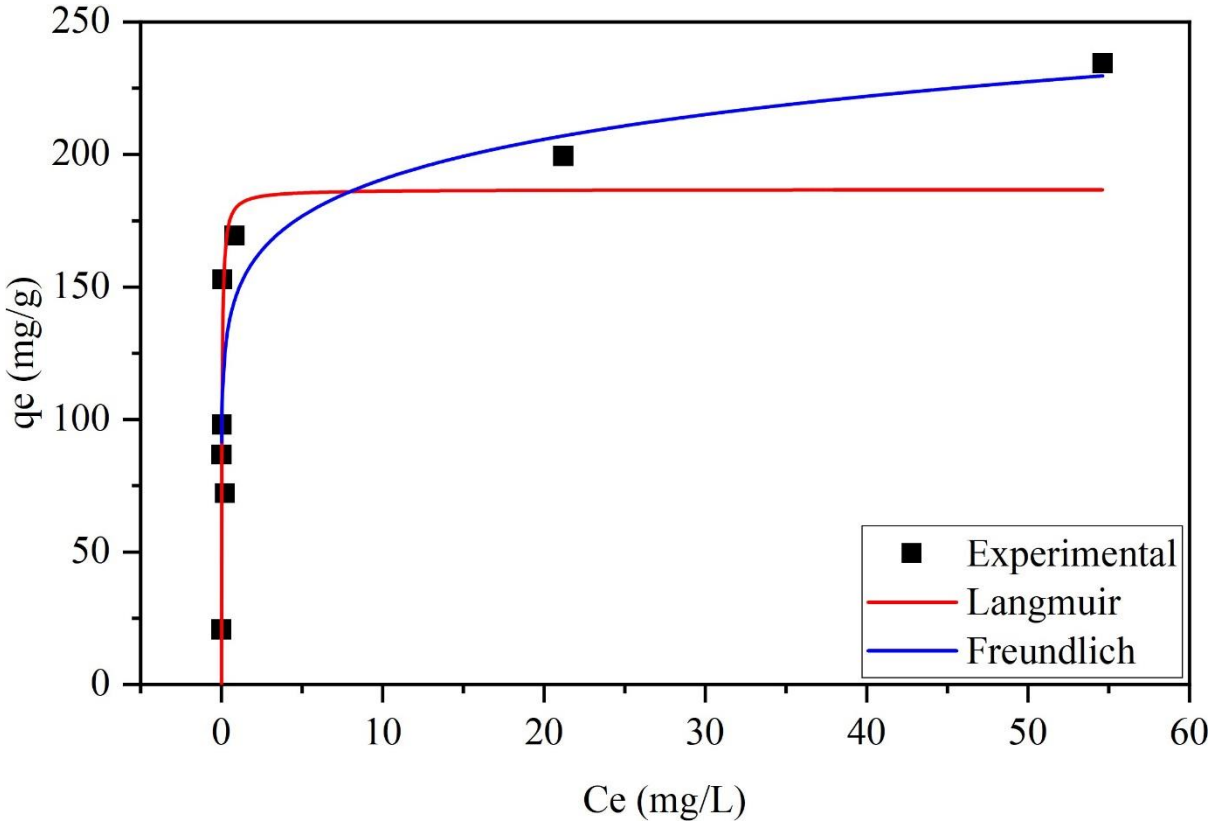

Figure 6.14 *Langmuir and Freundlich fitting curves of the bare zeolite A*

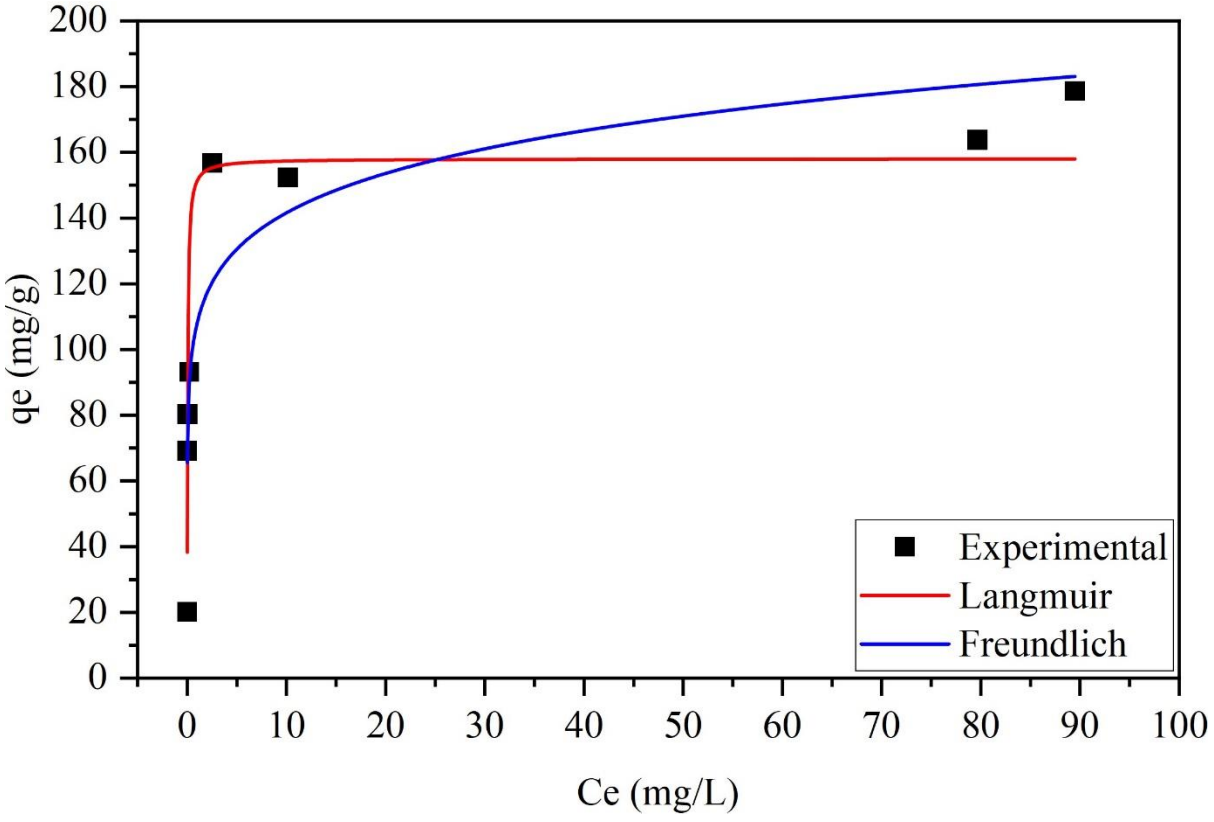

Figure 6.15 *Langmuir and Freundlich fitting curves of the Fe_3O_4/SiO_2/zeolite A*

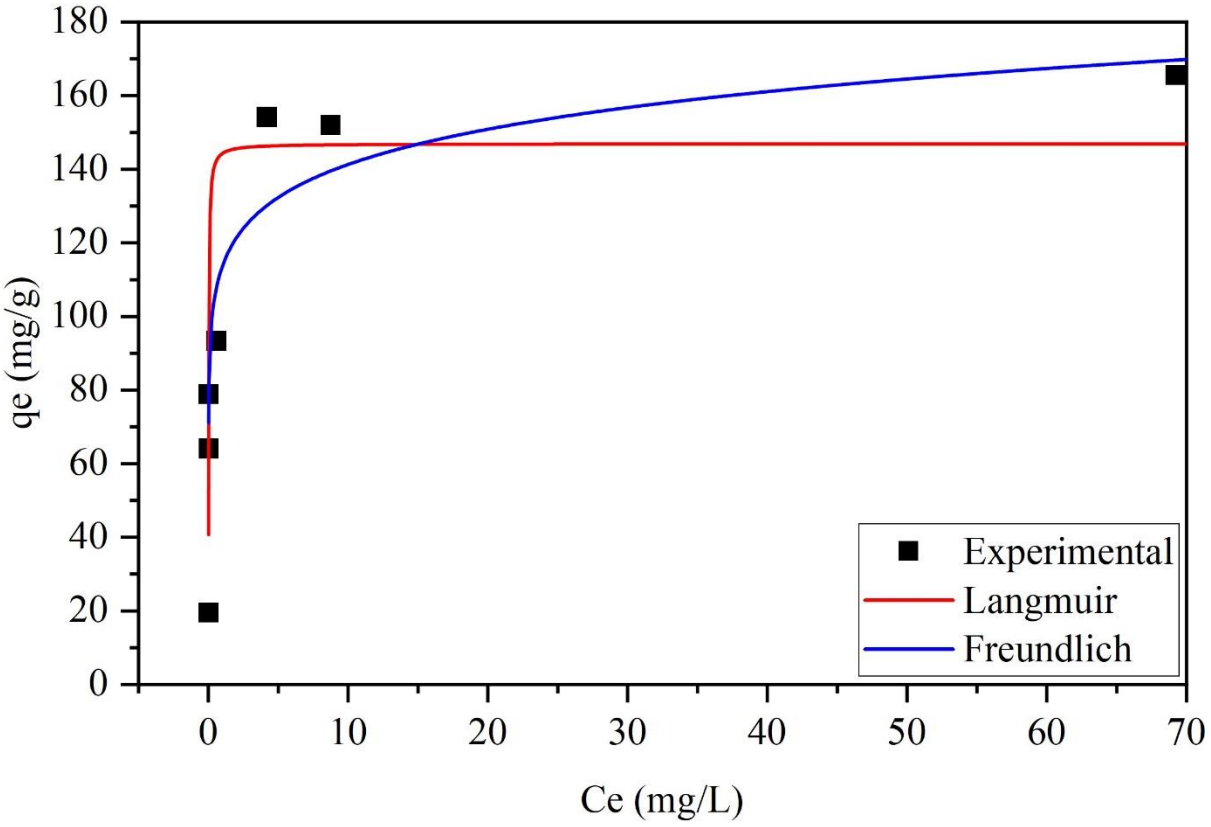

Figure 6.16 *Langmuir and Freundlich fitting curves of the* $Co_{0.3}Fe_{2.7}O_4/SiO_2$*/zeolite A*

6.3.1.3.2 Time-dependent Sr adsorption

The time-dependent Sr adsorption of the products is shown in Figures 6.17 and 6.18. The initial Sr concentration was 94 ppm, and it was adsorbed quickly onto the products. The bare zeolite A adsorbed the Sr within 10 to 30 min, but the other products took 120 min to adsorb most of the Sr onto them. It could be supposed that the pores for Sr adsorption in the zeolite A were clogged by the M_xO_y/SiO_2 particles, so the Sr adsorption took about 90 to 110 min more than with the bare zeolite A.

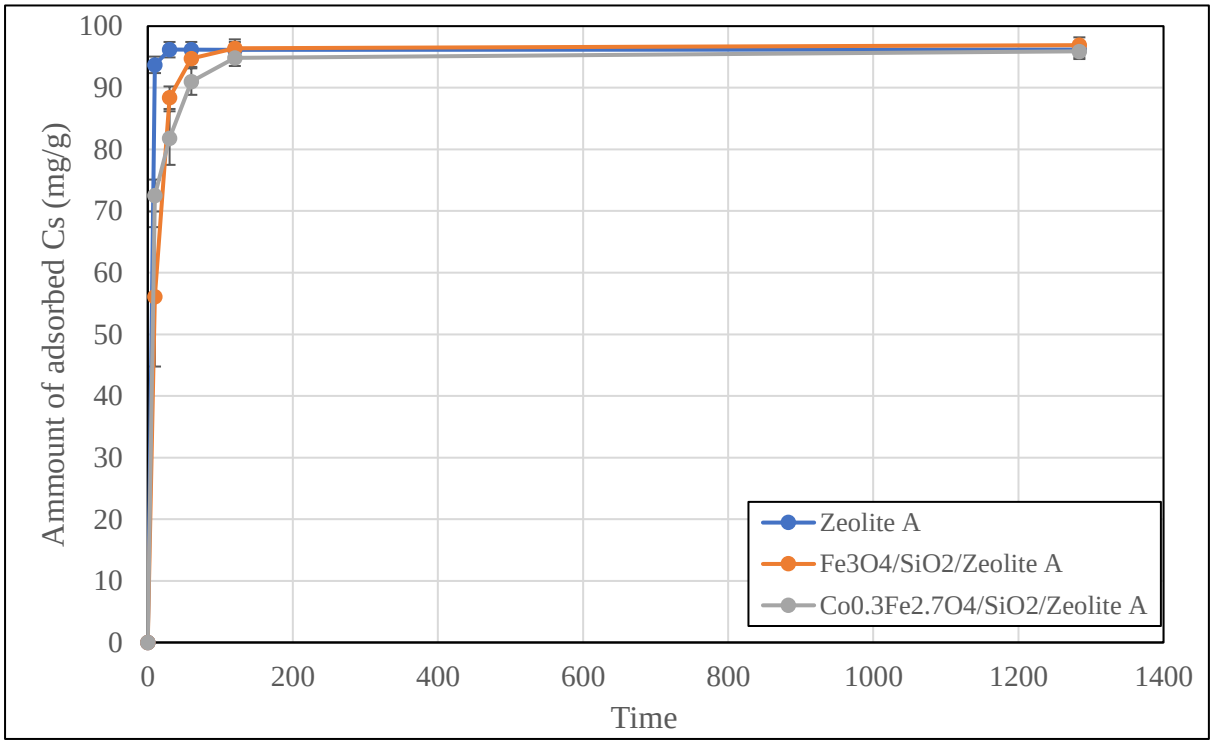

Figure 6.17 *Sr adsorption of the M_xO_y/SiO_2/zeolite A depending on time. The numbers after the samples were the duplicate experiments.*

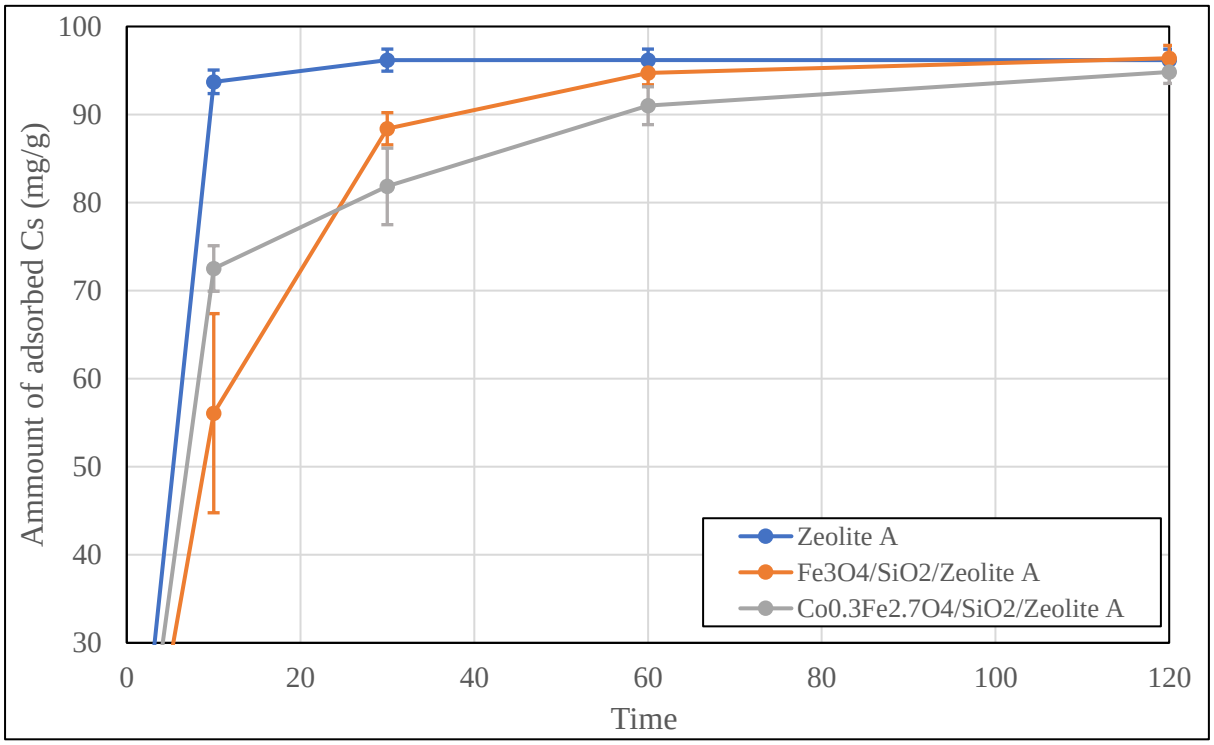

Figure 6.18 *Sr adsorption of the M_xO_y/SiO_2/zeolite A depending on time (Greater data of Figure 6.17). The numbers after the samples were the duplicate experiments.*

Table 6.4 shows the pH changes of the products while the Sr adsorptions. The pH changes of both Fe_3O_4/SiO_2/zeolite A and $Co_{0.3}Fe_{2.7}O_4/SiO_2$/zeolite A are smaller than the bare zeolite A. It might relate the Sr adsorption capacities of the products, which means there was more exchanged Na with Sr in the solution batch of the bare zeolite A, therefore, it could be assumed the pH values of the bare zeolite A were higher than both Fe_3O_4/SiO_2/zeolite A and $Co_{0.3}Fe_{2.7}O_4/SiO_2$/zeolite A.

Table 6.4 *Initial to final pH of Sr exchange solution for the Sr adsorption depending on time.*

Time	Zeolite A		Fe_3O_4/SiO_2/zeolite A		$Co_{0.3}Fe_{2.7}O_4/SiO_2$/zeolite A	
0	7.42 (Initial Sr: 94.03 ppm)*					
10	8.87	(±0.75)	6.89	(±0.17)	6.58	(±0.13)
30	8.75	(±0.16)	7.07	(±0.44)	6.51	(±0.07)
60	8.62	(±0.52)	6.70	(±0.07)	6.50	(±0.08)
120	8.87	(±0.28)	7.06	(±0.60)	6.60	(±0.02)
1480	9.43	(±0.06)	8.40	(±0.11)	8.17	(±0.08)

**The measurement was used only the auto-hold mode that the pH values were measured when they moved within ± 3 digit for 10 sec.*

6.3.1.3.3 pH-dependent Sr adsorption

The pH-dependent Sr adsorption onto the products is shown in Figure 6.19, and the initial Sr concentrations are in Table 6.5. The initial Sr concentrations were set between 112 and 130 ppm, and it was highest at pH 7.00. The highest Sr adsorption onto the bare zeolite A was at pH 7.00, and it decreased from 122.58 mg/g (±3.99mg/g) to 109.43 mg/g (±3.29 mg/g) at pH 9.96. If the batch becomes bigger for the Sr adsorption, the adsorption difference will be also larger, and it could be thought the Sr adsorption efficiency will be much lower than at

pH 7.00 in the bigger batch. Both Fe_3O_4/SiO_2/zeolite A and $Co_{0.3}Fe_{2.7}O_4$/SiO_2/zeolite A had the highest Sr capacities at pH 9.96, but the capacity differences at pH 7.00 were just a few to 10 mg/g. Faghihian et al. (2014)[17] also reported on the dependency of Sr adsorption onto bare zeolite A and Fe_3O_4/zeolite A on the solution pH, and their result was similar to this initial Sr solution pH-dependence result. From this result, it can be understood that the final pH of Fe_3O_4/SiO_2/zeolite A and $Co_{0.3}Fe_{2.7}O_4$/SiO_2/zeolite A of the Sr adsorption isotherms and time-dependent Sr adsorption were lower than for the bare zeolite A especially at pH 7.00. Because it could be assumed both Fe_3O_4/SiO_2/zeolite A and $Co_{0.3}Fe_{2.7}O_4$/SiO_2/zeolite A have the nanoparticles around the zeolite A pores for Sr adsorption sites, and they affected the less Sr capacities than the bare zeolite A.

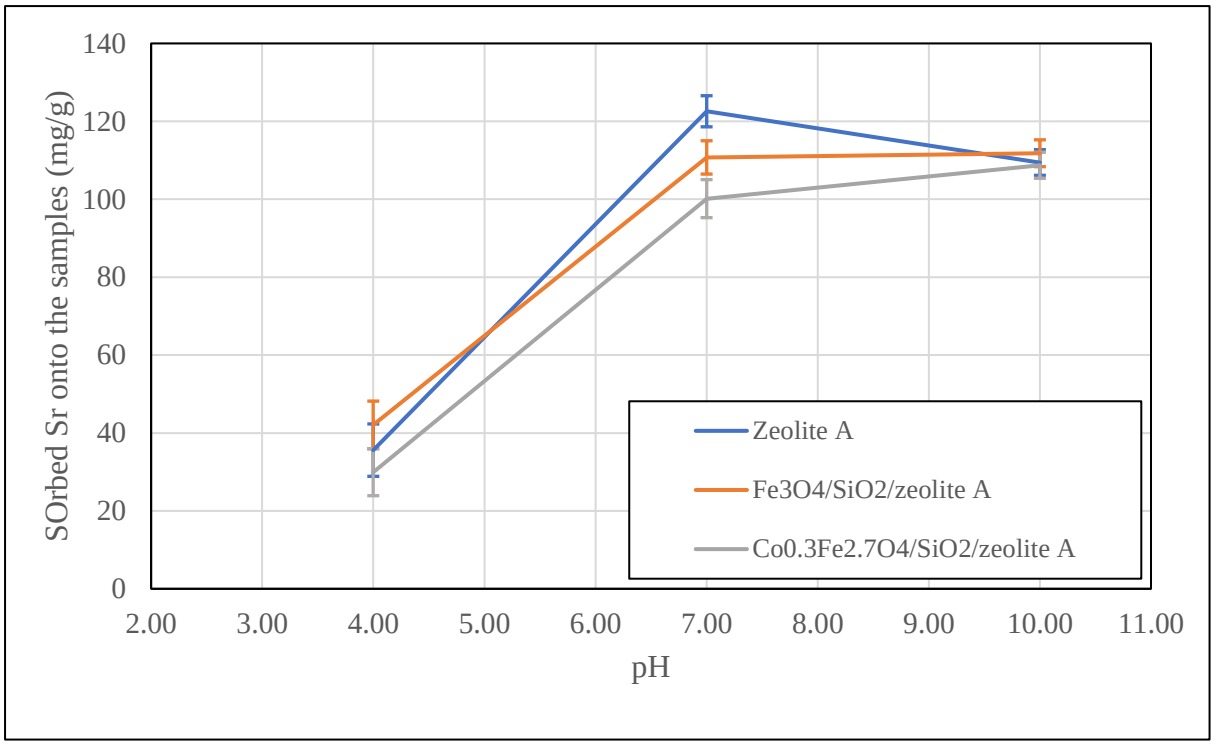

Figure 6.19 *Amount of Sr adsorbed onto M_xO_y/SiO_2/zeolite A at different pH. The numbers after the samples were the duplicate experiments.*

Table 6.5 *Initial Sr concentration of $Sr(NO_3)_2$ with pH for the M_xO_y/SiO_2/zeolite A.*

pH	Sr (ppm)	
4.06	128.51	(±3.12)
7.00	130.61	(±3.96)
9.96	111.97	(±3.37)

The initial and final solution pH values stabilised by HEPES and CAPS for the Sr adsorption are in Table 6.6. The solution initially with pH 4 moved to between about pH 4.06 to 5.88. The Fe_3O_4/SiO_2/zeolite A and $Co_{0.3}Fe_{2.7}O4/SiO_2$/zeolite A seemed to be stabilised even though it was mixed with HEPES, because when a pH value is stabilized by a buffer, the pH value can move within 1.00. However, the pH value of the bare zeolite A was not stabilised by the HEPES when the initial pH value was 4, it might be due to the less HEPES

in the bare zeolite A solution. The solutions that had initial pH 7.00 and 9.96 changed their pH values slightly. HEPES and CAPS could be used at the pH 7 and 9.96 conditions.

Table 6.6 *Initial and final pH of the stabilised pH of M_xO_y/SiO_2/zeolite A.*

Initial	Zeolite A	Fe_3O_4/SiO_2/zeolite A	$Co_{0.3}Fe_{2.7}O4/SiO_2$/zeolite A
4.06*	5.88 (±0.10)	4.96 (±0.01)	4.98 (±0.14)
7.00*	7.13 (±0.01)	7.06 (±0.09)	6.98 (±0.04)
9.96*	9.70 (±0.04)	9.76 (±0.04)	9.71 (±0.03)

**The measurement was used only the auto-hold mode that the pH values were measured when they moved within ± 3 digit for 10 sec.*

6.3.2 M_xO_y/SiO_2/zeolite X

6.3.2.1 Phase identification of M_xO_y/SiO_2/zeolite X

The XRD patterns of the Fe_3O_4/SiO_2/zeolite X are shown with those of the bare Fe_3O_4/SiO_2 and the bare zeolite X for comparison in Figure 6.20. Most peaks of the Fe_3O_4/SiO_2 also appeared in the same position on the bare zeolite X pattern, and Fe_3O_4/SiO_2 peaks that did not match those of the zeolite X were difficult to identify in the Fe_3O_4/SiO_2/zeolite X pattern. However, the peak of the product at around 41.4° was broad, so it seemed to contain both zeolite X and Fe_3O_4/SiO_2. This suggests that both materials might be in the product. The XRD patterns of Fe_3O_4/SiO_2/zeolite X also had a sharp peak around 52°, this also could be thought a Fe(0) peak of the Fe oxidisation while the synthesis.

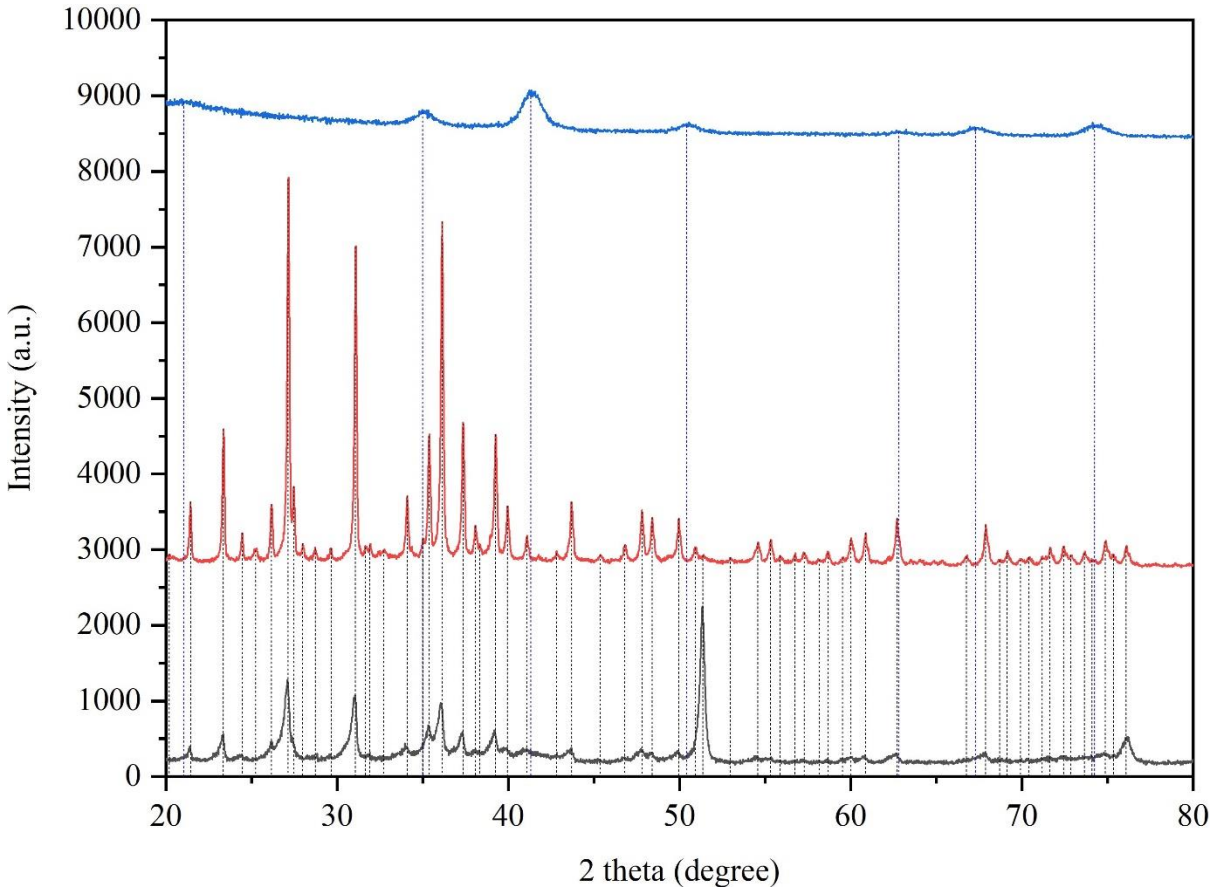

Figure 6.20 *XRD patterns of the Fe_3O_4 (blue), the zeolite X (red) and the Fe_3O_4/SiO_2/zeolite X (black)*

The XRD patterns of the $Co_{0.3}Fe_{2.7}O_4/SiO_2$/zeolite X are shown in Figure 6.21. Most of the $Co_{0.3}Fe_{2.7}O_4/SiO_2$ pattern also appeared in the bare zeolite X peaks; however, the peak at around 41.4° was again broad, suggesting that there might be both $CoFe_2O_4/SiO_2$ and zeolite X peaks there.

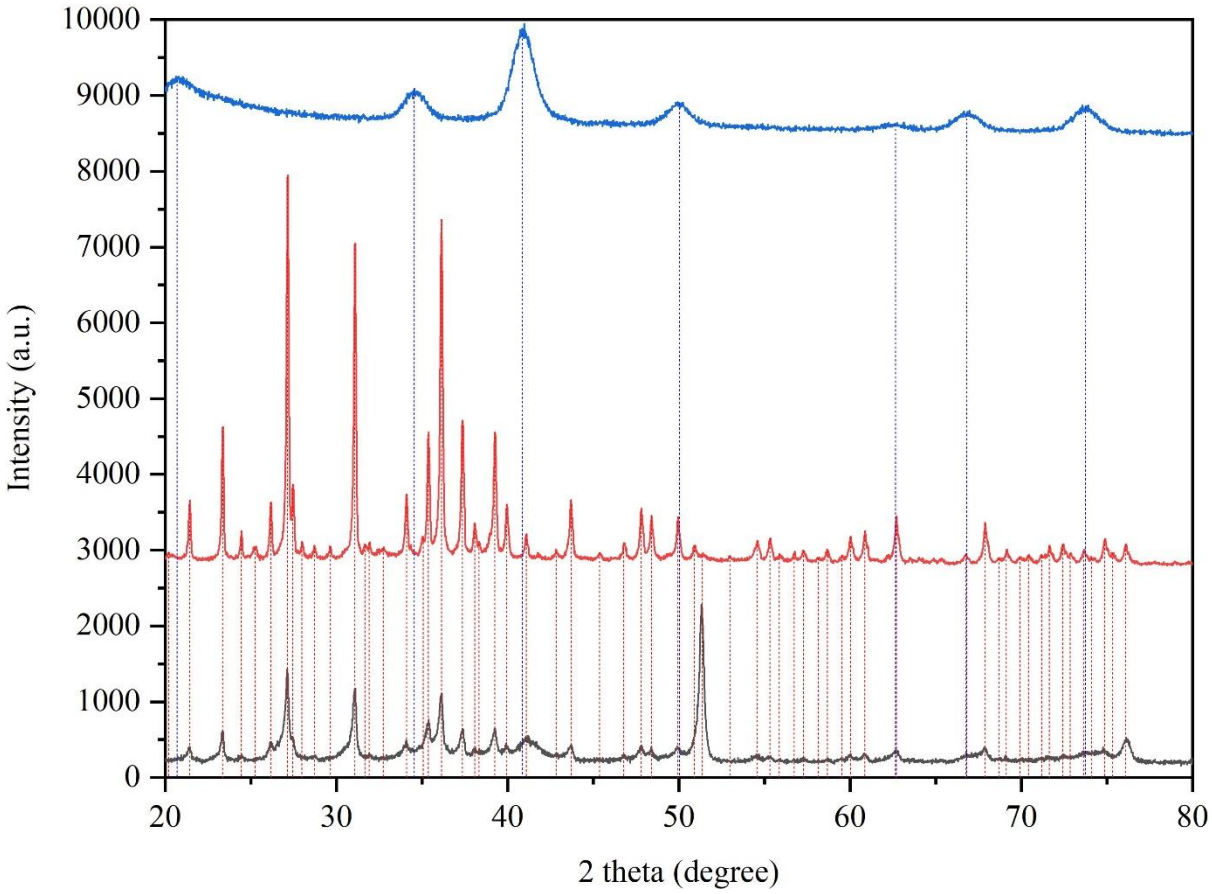

Figure 6.21 *XRD patterns of the $Co_{0.3}Fe_{2.7}O_4$ (blue), the zeolite X (red) and the $Co_{0.3}Fe_{2.7}O_4/SiO_2$/zeolite X (black).*

The presence of Fe_3O_4 and $Co_{0.3}Fe_{2.7}O_4$ in the products was also checked using the Raman spectra (Figure 6.22). The Fe_3O_4/SiO_2/zeolite X had a Fe_3O_4 peak at 695 cm^{-1}, and the $Co_{0.3}Fe_{2.7}O_4/SiO_2$/zeolite X also had two peaks at 590 and 677 cm^{-1} that the bare zeolite X did not have. The peaks seem to be the $CoFe_2O_4$ peaks. Low-silica zeolite X had Raman peaks at 1065, 920, 770, 730 620, 515, 465, 380 and 330 cm^{-1}.[131] The elemental composition of this synthesised zeolite X was slightly different to that of the low-silica zeolite X, but the Raman patterns were similar. The other peaks of both products appeared at positions that were close but slightly different to those of the zeolite X peaks. The crystal lattice of the zeolite X of the

products might be distorted by the M_xO_y/SiO_2, so the peak positions might be shifted from the original zeolite X positions, indeed, both Fe_3O_4/SiO_2/zeolite X and $Co_{0.3}Fe_{2.7}O_4/SiO_2$/zeolite X had a broad zeolite X peak at around 41.4° in Figure 6.20 and 6.21 that was not observed by the bare zeolite X. This $Co_{0.3}Fe_{2.7}O_4/SiO_2$/zeolite X patterns also had a sharp peak of Fe (0) at round 52°, and the reason could be assumed the same as the Fe_3O_4/SiO_2/zeolite X.

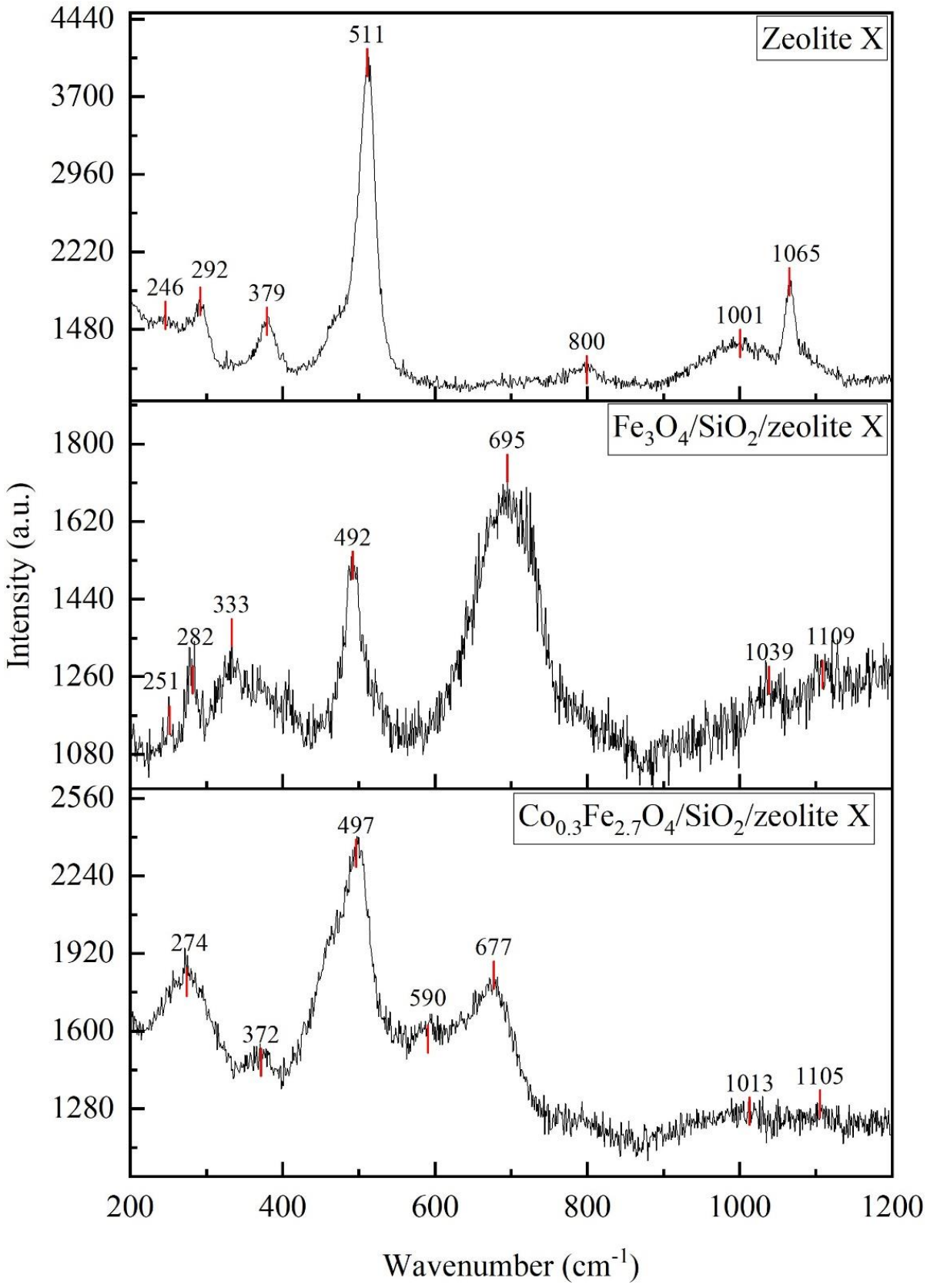

Figure 6.22 *Raman spectra of zeolite X, Fe_3O_4/SiO_2/zeolite X and $Co_{0.3}Fe_{2.7}O_4/SiO_2$/zeolite X.*

The particle shapes and elemental composition images of the Fe_3O_4/SiO_2/zeolite X, which were made using the conventional oven and captured by the SEM-EDS, are shown in Figure 6.23. There were many big particles, and the EDS images show they were Fe-rich. It could be assumed the reason was same as for the M_xO_y/SiO_2/zeolite A. The Al, Si and Na SEM-EDS images show the big particles that seem to be also coated by the zeolite X, but it could be thought they were from the characteristic X-rays that came from around the big particles. The $Co_{0.3}Fe_{2.7}O_4/SiO_2$/zeolite X also contained big particles (Figure 6.24). The aggregated $Co_{0.3}Fe_{2.7}O_4/SiO_2$ was over 20 μm, and the biggest particle mostly contained the elements Si, O, Fe and Co. It could be assumed the big particle was also formed before or during the crystallisation of the zeolite X, and zeolite X formed on the aggregated particle. The smaller particles were rich in Al, Si and Na.

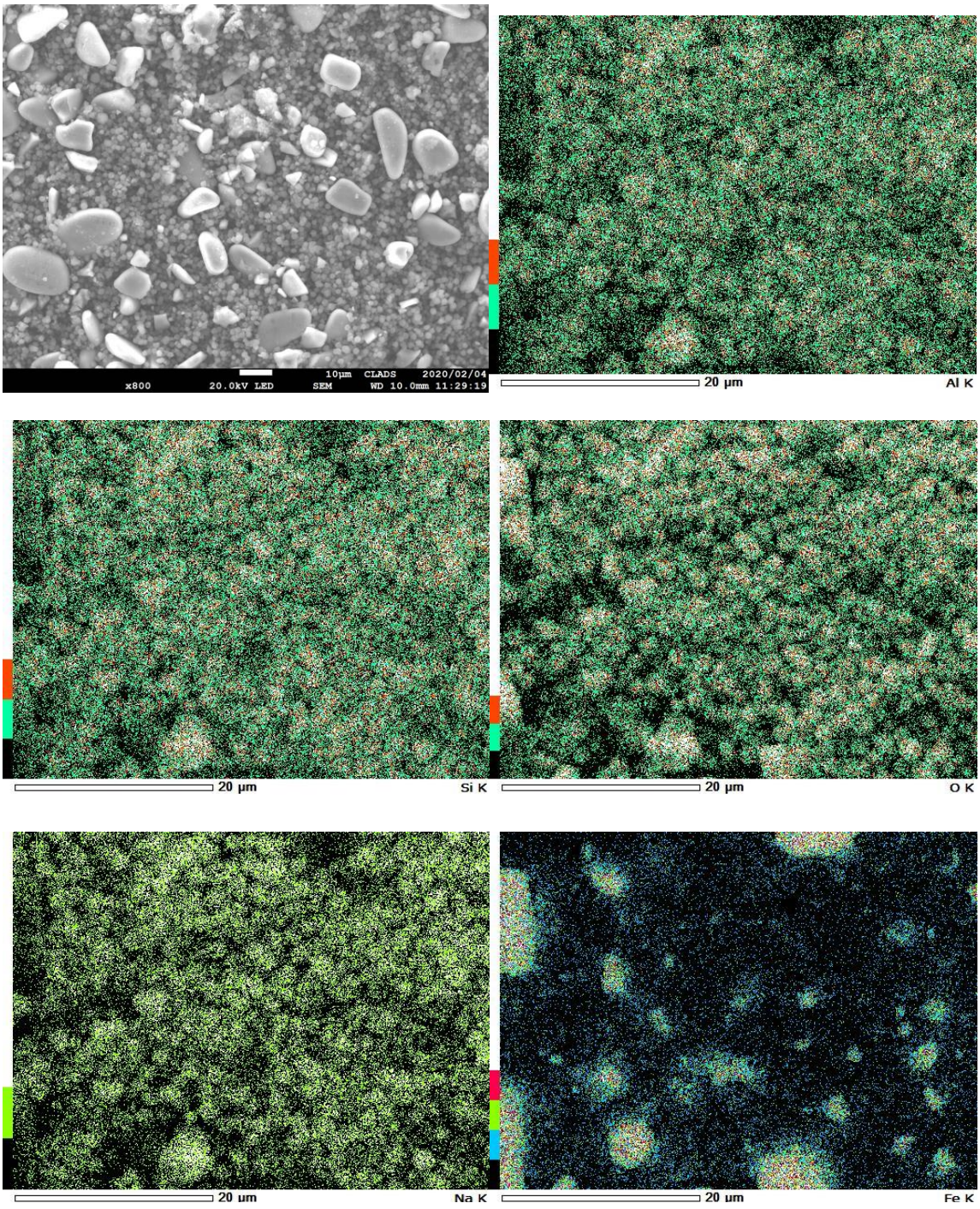

Figure 6.23 *SEM-EDS elemental mapping images of the Fe_3O_4/SiO_2/zeolite X.*

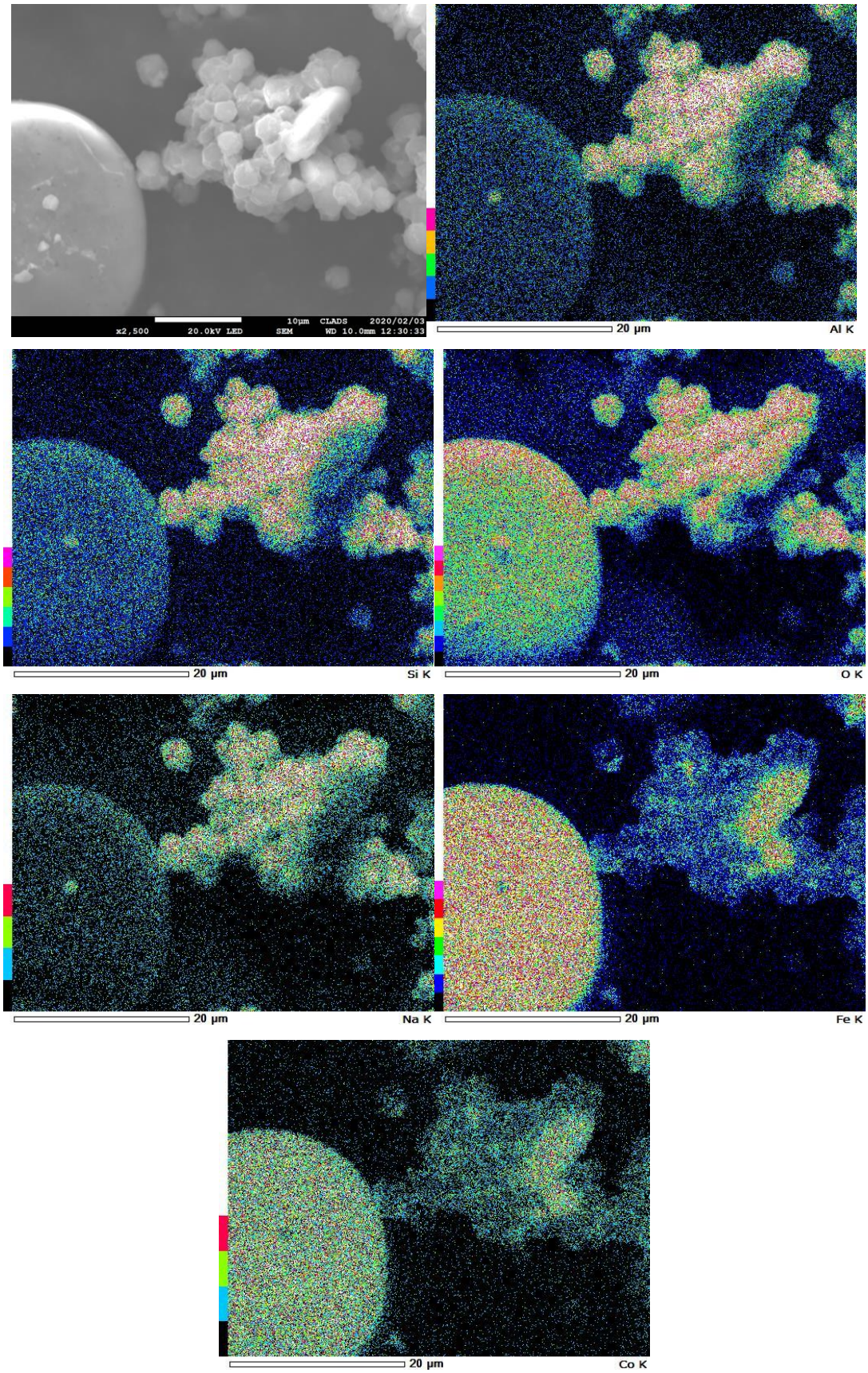

Figure 6.24 *SEM-EDs elemental mapping images of the* $Co_{0.3}Fe_{2.7}O_4/SiO_2$*/zeolite X.*

The elemental compositions of the products and the bare zeolite X measured by the XRF are in Table 6-7. The Si to Al ratio in both Fe_3O_4/SiO_2/zeolite X and $Co_{0.3}Fe_{2.7}O_4/SiO_2$/zeolite X was about 0.3 lower than in the bare zeolite X, as was seen in M_xO_y/SiO_2/zeolite A (see Chapter 6.3.1.1). The Na to Al ratio of the Fe_3O_4/SiO_2/zeolite X was the same as in the bare zeolite X; however, the Na to Al ratio of the $Co_{0.3}Fe_{2.7}O_4/SiO_2$/zeolite X was 0.12 higher than the bare zeolite X and the Fe_3O_4/SiO_2/zeolite X. The ratio of Co and Fe to Al in $Co_{0.3}Fe_{2.7}O_4/SiO_2$/zeolite X was smaller than the Fe to Al ratio in Fe_3O_4/SiO_2/zeolite X. There might have been a little bit less $Co_{0.3}Fe_{2.7}O_4/SiO_2$ in the zeolite X, so there was less Si, Fe and Co, and more Na than in the other products. Furthermore, the Co and/or Fe ratio in the zeolite X was about 1 smaller than in the M_xO_y/SiO_2/zeolite A: the zeolite X of the M_xO_y/SiO_2/zeolite X was richer than the M_xO_y/SiO_2/zeolite A. The differences might be due to the difference of the cage sizes of the zeolite X from the zeolite A, and some of the $M_x\mathbf{O}_y$ particles might be incorporated in the bigger cages, therefore, the ratio of Co and or Fe ratio was smaller than the zeolite A.

Table 6.7 *Elemental compositions of zeolite X, Fe_3O_4/SiO_2/zeolite X and $Co_{0.3}Fe_{2.7}O_4/SiO_2$/zeolite X (the ratio of Co and Fe are highlighted in yellow).*

Sample	Formula	Concentration (wt%)		Atomic weight (g/mol)	Amount of material (kmol)	Ratio
Zeolite X	Al	30.10	(±0.45)	26.98	11.16	1.00
	Si	52.80	(±0.71)	28.09	18.80	1.68
	Na	15.20	(±0.37)	22.99	6.61	0.59
Fe_3O_4/SiO_2/zeolite X	Al	10.10	(±0.23)	26.98	3.74	1.00
	Si	14.90	(±0.30)	28.09	5.30	1.42
	Na	5.07	(±0.22)	22.99	2.21	0.59
	Fe	69.90	(±0.26)	55.85	12.52	3.34
$Co_{0.3}Fe_{2.7}O_4/SiO_2$/zeolite X	Al	13.20	(±0.32)	26.98	4.89	1.00
	Si	18.70	(±0.39)	28.09	6.66	1.36
	Na	8.01	(±0.38)	22.99	3.48	0.71
	Fe	38.50	(±0.17)	55.85	6.89	1.92
	Co	21.20	(±0.13)	58.93	3.60	1.00

The TEM images of the Fe_3O_4/SiO_2/zeolite X are shown in Figure 6.25, and the TEM-EDS images are in Figure 6.26. The zeolite X particles encapsulated many Fe_3O_4/SiO_2 nanoparticles, but most of them were incorporated inside the zeolite X and not on the surface (the grey parts were just zeolite X). At the Fe-rich parts of the product, there was less Al and Na, it could be known the parts had the aggregated Fe_3O_4/SiO_2 particles. The SEM-EDS mapping image of Si also had Si characteristic X-rays from around the particle, but it could be supposed the particle Si was the highly purple coloured part.

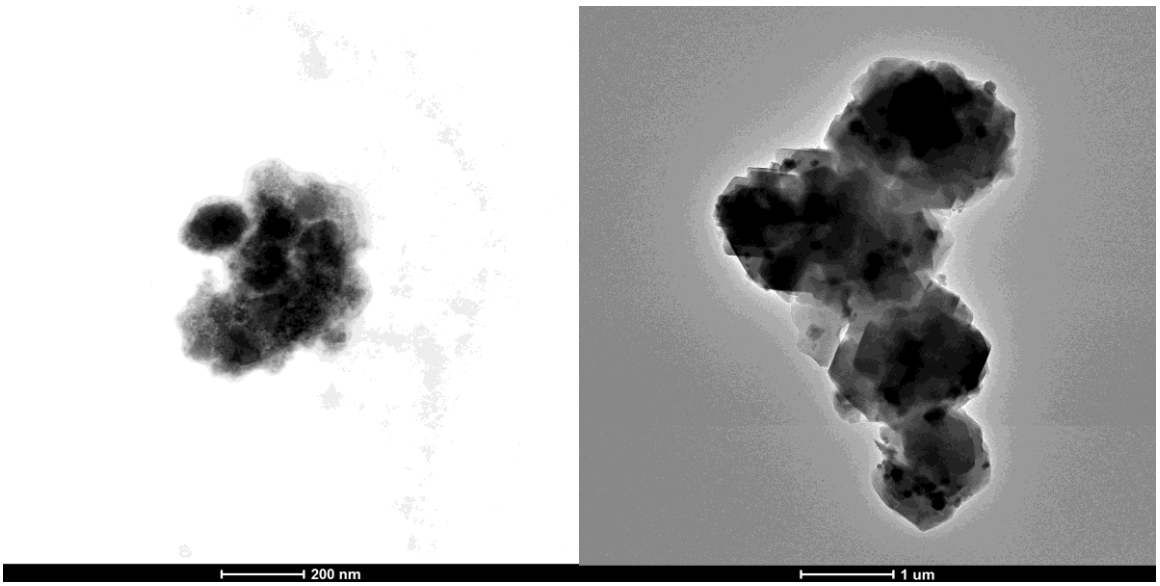

Figure 6.25 *TEM images of the Fe_3O_4/SiO_2/zeolite X.*

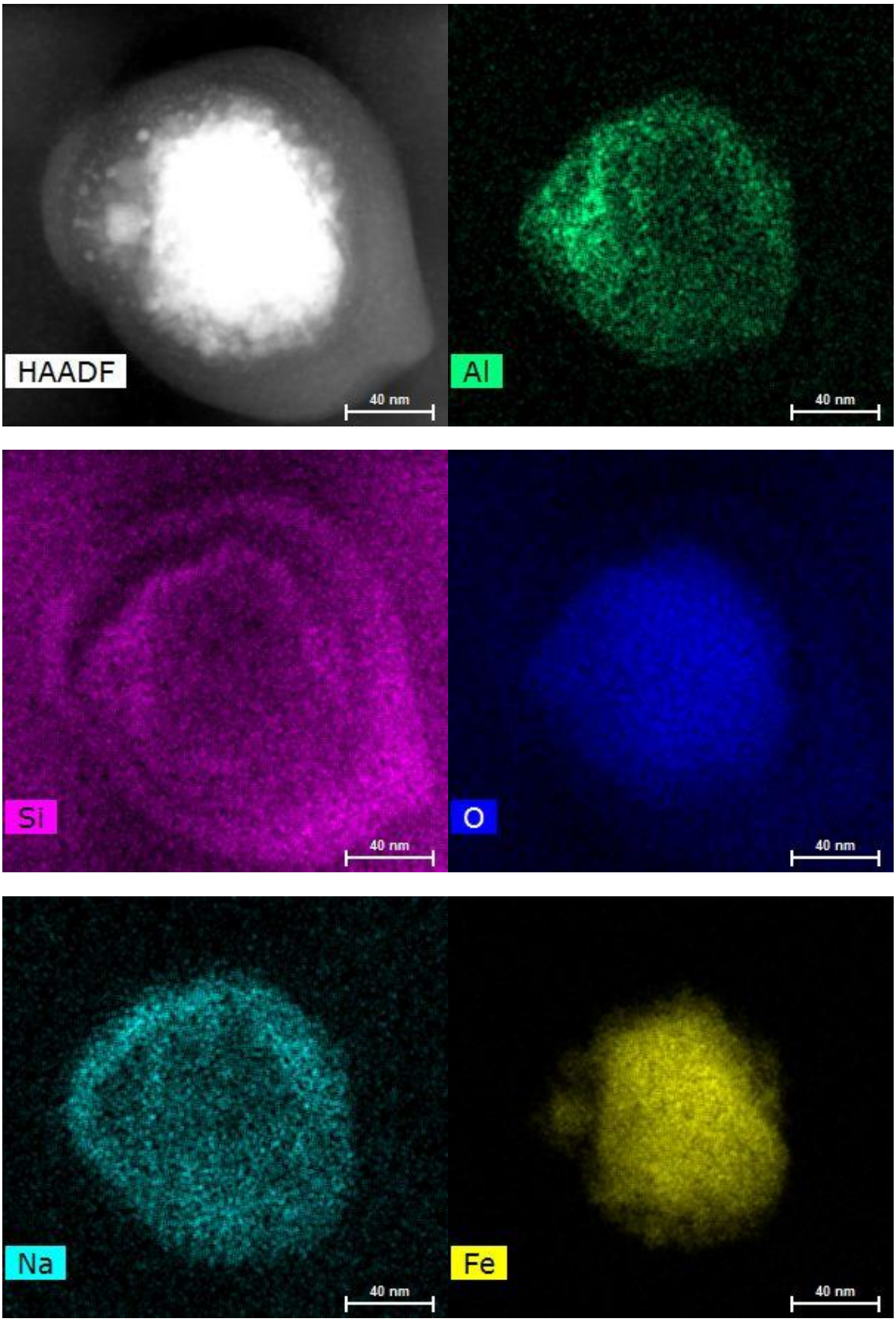

Figure 6.26 *TEM-EDS elemental images of the Fe_3O_4/SiO_2/zeolite X.*

6.3.2.2 Magnetic properties

The magnetisation loops of the Fe_3O_4/SiO_2/zeolite X and the $Co_{0.3}Fe_{2.7}O_4/SiO_2$/zeolite X are shown in Figures 6.27 and 6.28. The maximum magnetisation of the $Co_{0.3}Fe_{2.7}O_4/SiO_2$/zeolite X (10.9 emu/g) was higher than that of the Fe_3O_4/SiO_2/zeolite X (8.5 emu/g), consistent with the other product results. The tiny hysteresis of the product was through the origin point; however, the hysteresis of the Fe_3O_4/SiO_2/zeolite X was shifted to the positive side of the magnetic field. The maximum magnetisations of the products were a few emu/g smaller for than the M_xO_y/SiO_2/zeolite A due to there being more zeolite X than M_xO_y/SiO_2 in it.

The M_r/M_s values for both products were also calculated. The values for $Co_{0.3}Fe_{2.7}O_4/SiO_2$/zeolite X were less than 0.1, and the negative magnetic field side of M_r/M_s of the Fe_3O_4/SiO_2/zeolite X was also less than 0.1 (Table 6.8).

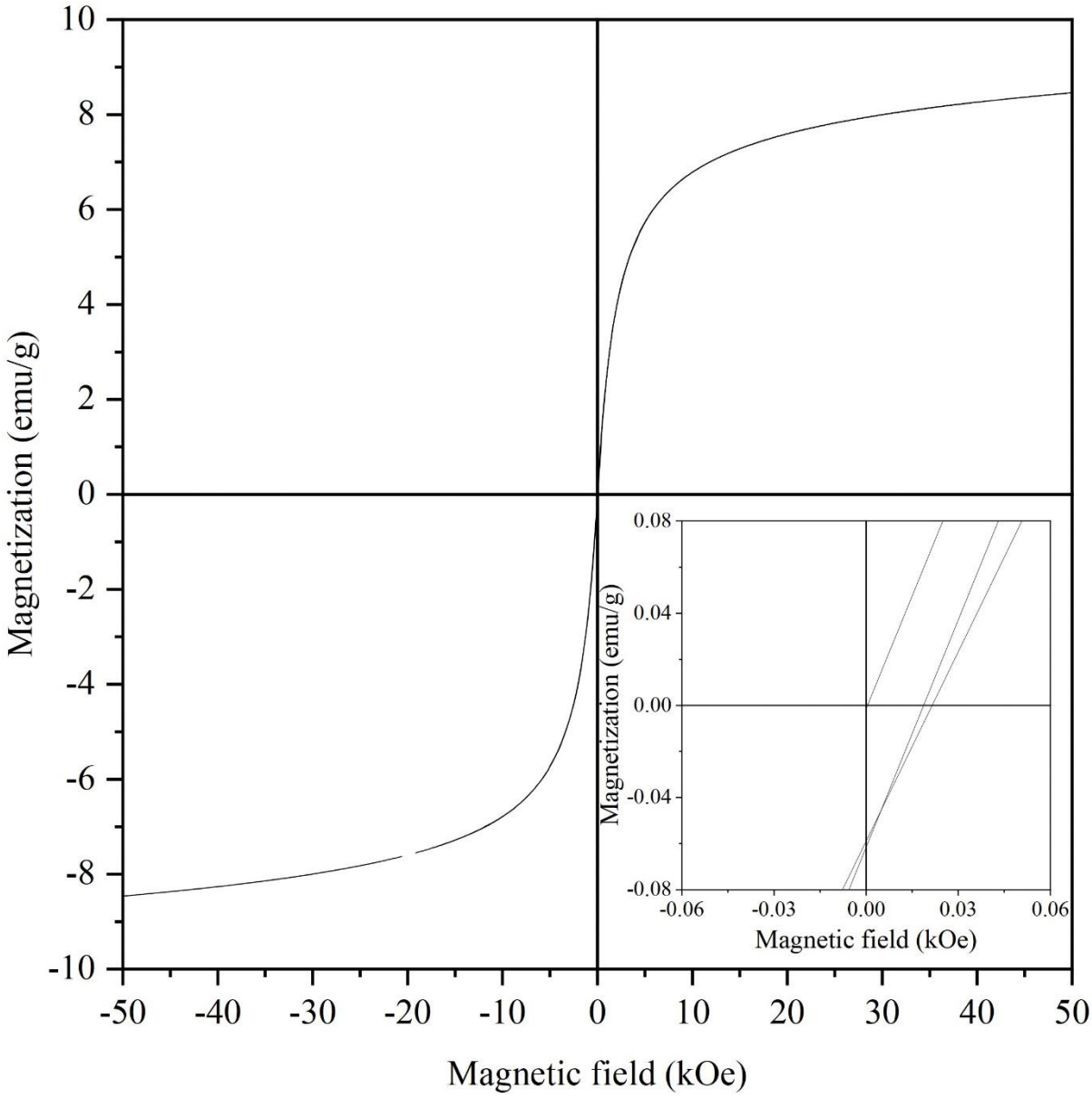

Figure 6.27 *Magnetisation loop of the Fe_3O_4/SiO_2/zeolite X.*

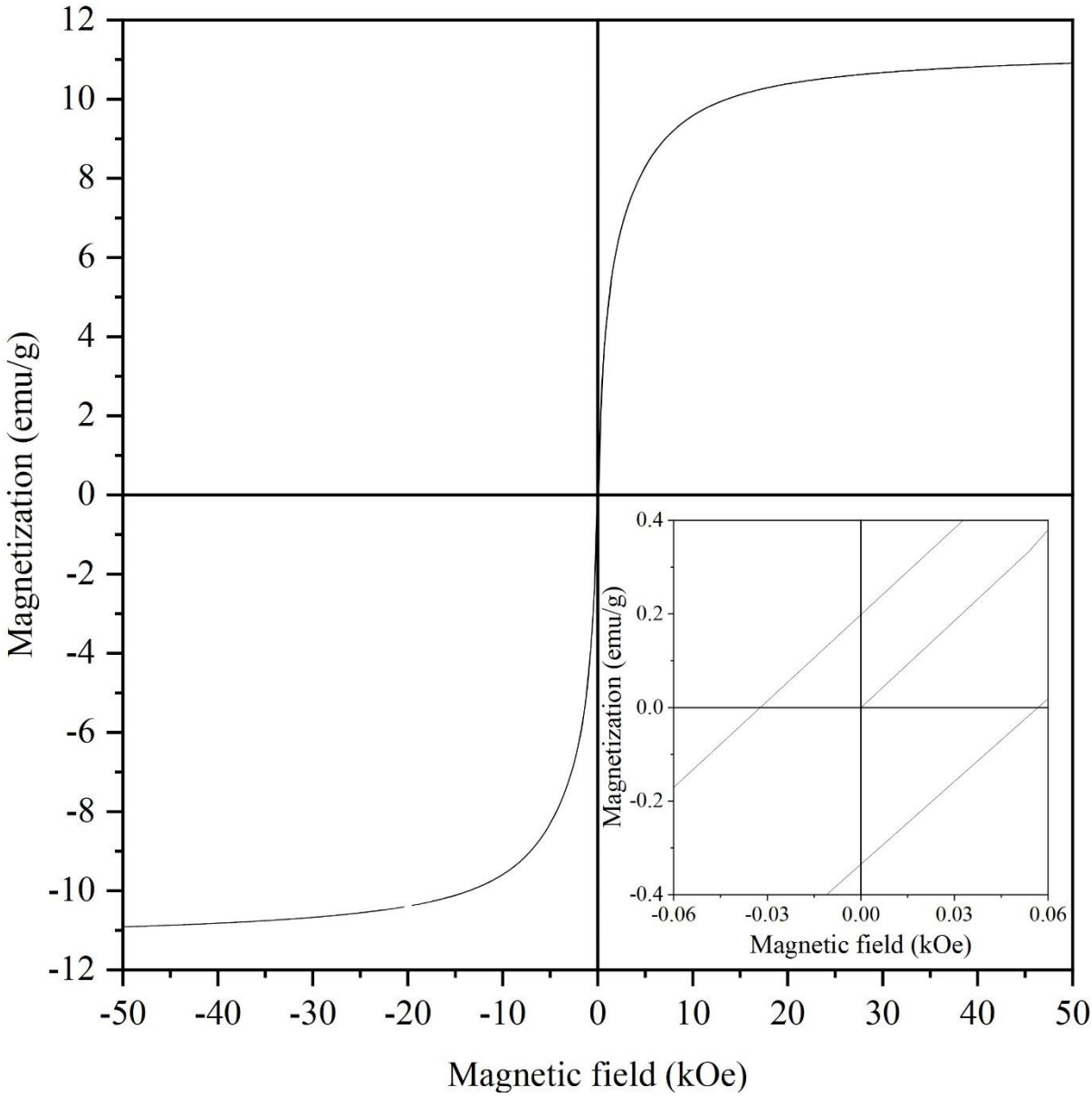

Figure 6.28 *Magnetisation loop of the $Co_{0.3}Fe_{2.7}O_4/SiO_2$/zeolite X.*

Table 6.8 *Relationship between the magnetisation hysteresis gaps and superparamagnetism (at 300 K)*

	H_c (kOe)	M_s (emu/g)	M_r (emu/g)	M_r/M_s
Fe_3O_4/SiO_2/zeolite X	0.019	8.500	-0.060	-0.007
	0.022	-8.500	-0.060	0.007
$Co_{0.3}Fe_{2.7}O_4/SiO_2$/zeolite X	-0.032	10.900	0.200	0.018
	0.057	-10.900	-0.333	0.031

The ZFC/FC curves of the Fe_3O_4/SiO_2/zeolite X and the $Co_{0.3}Fe_{2.7}O_4/SiO_2$/zeolite X are shown in Figures 6.29 and 6.30. The blocking temperatures of both products were below 273.15 K, but the $Co_{0.3}Fe_{2.7}O_4/SiO_2$/zeolite X had the higher blocking temperature (262.10 K), as was seen with the M_xO_y/SiO_2/zeolite A (55.61 K); however, both products' blocking temperatures were lower than those of the M_xO_y/SiO_2/zeolite A. It could be supposed the smaller amount of M_xO_y in zeolite X decreased the blocking temperatures.

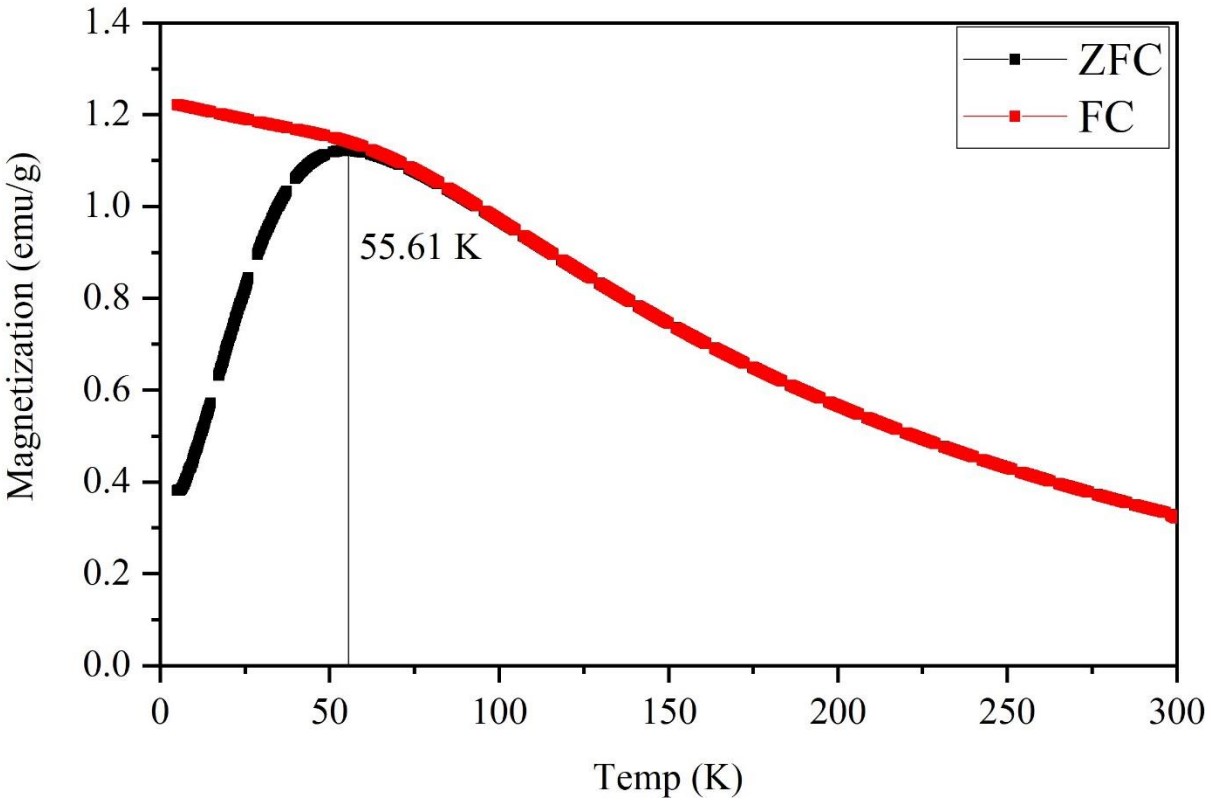

Figure 6.29 ZFC/FC curves of the Fe_3O_4/SiO_2/zeolite X.

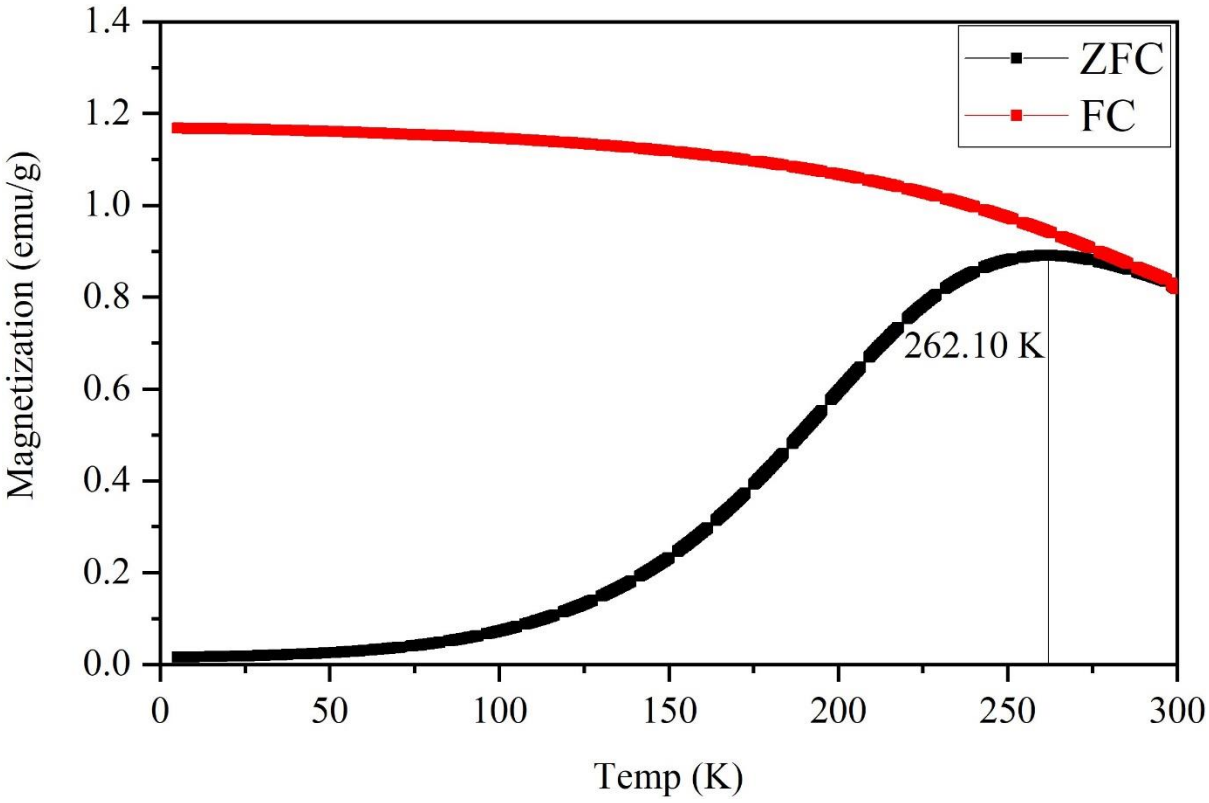

Figure 6.30 *ZFC/FC curves of the $Co_{0.3}Fe_{2.7}O_4/SiO_2$/zeolite X.*

6.3.2.3 Sr adsorption

6.3.2.3.1 Sr adsorption isotherms

The Sr adsorption isotherms of the products and the bare zeolite X are shown in Figure 6.31. The bare zeolite X had the highest adsorption isotherm curve, and it reached equilibrium at around 1.77 mg/l. Both products reached equilibrium at around 10 mg/l, and the maximum amount of adsorbed Sr was about 20 mg/g lower than for the bare zeolite X. The M_xO_y/SiO_2 particles seemed to have distorted the Sr adsorption capacities of the zeolite X, and the amount of zeolite X in the products seemed to be less than the bare zeolite X. The Sr adsorption capacities onto the products was about 50 mg/g lower than for

M_xO_y/SiO_2/zeolite A, even though the amount of M_xO_y particles in zeolite X was less than in the M_xO_y/SiO_2/zeolite A. The maximum Sr adsorption equilibrium of the bare zeolite X was already reached at around 2 mg/l; it did not increase such as the bare zeolite A.

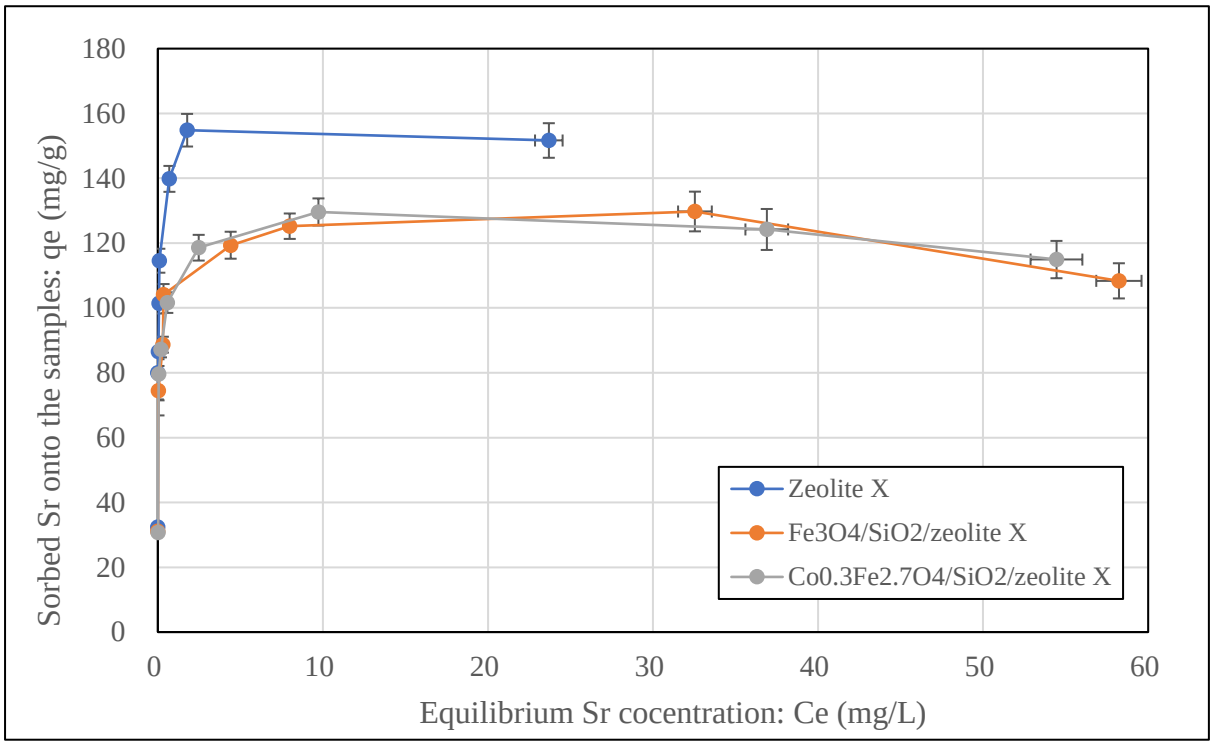

Figure 6.31 *Sr adsorption isotherm curves of M_xO_y/SiO_2/zeolite X*

The initial and final pH values of the concentrated Sr solutions used in this experiment are in Table 6.9. At the lower initial Sr concentrations, the final pH values were higher than for the higher initial Sr concentrations, and the values for the bare zeolite X were the highest. It could be assumed the higher pH values meant the zeolite X could adsorb Sr more efficiently.

The final pH values of the higher initial Sr concentrations were smaller than the initial pH vales, especially the initial concentration was 175.90 ppm. The reason could be thought there was more $Sr(NO_3)_2$ than the lower initial Sr concentration solutions, and it could be thought exchanged Na with Sr formed $NaNO_3$ and it decreased the final solution pH.

Table 6.9 *Initial $Sr(NO_3)_2$ concentrations, and initial and final pH of zeolite X and M_xO_y/SiO_2/zeolite X. The measurement was used the auto-hold mode that the pH values were measured when they moved within ± 3 digit for 10 sec.*

ppm	Initial pH	Final pH		
		Zeolite X	Fe3O4/SiO2/zeolite X	CoFe2O4/SiO2/zeolite X
175.90 (±4.52)	7.41	7.02	6.65	6.79
166.33 (±5.30)	7.28	8.10	6.93	6.86
135.73 (±3.83)	7.08	8.59	7.59	7.34
119.06 (±3.83)	6.77	9.30	7.57	6.95
100.50 (±3.10)	6.80	9.01	7.72	7.52
88.37 (±2.43)	6.48	9.66	7.29	6.92
77.28 (±7.91)	6.78	8.91	7.97	7.44
33.39 (±0.85)	7.02	9.34	7.73	7.84

The Sr adsorption isotherm curves were also compared with the Langmuir and Freundlich isotherm curves (Figures 6.32 to 6.34). All of the empirical curves were similar to the Langmuir curves, but the bare zeolite X curve was higher than the Langmuir curve. The zeolite X had a higher Sr capacity than the calculated capacity such as the bare zeolite A. The zeolite X particle sizes might be smaller, and they had more surfaces and Sr adsorption sites, therefore it could be assumed the adsorption curve was similar to the Freundlich curve.

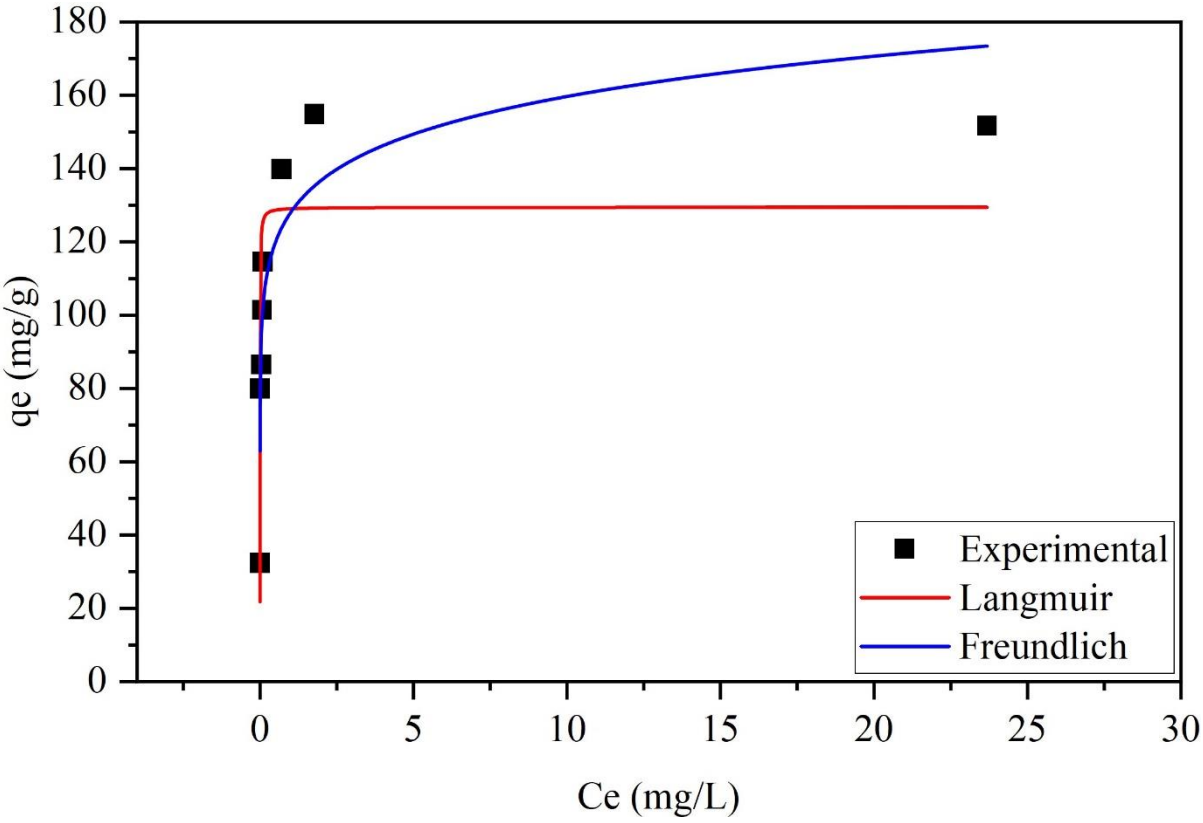

Figure 6.32 *Langmuir and Freundlich fitting curves of the Fe_3O_4/SiO_2/zeolite X*

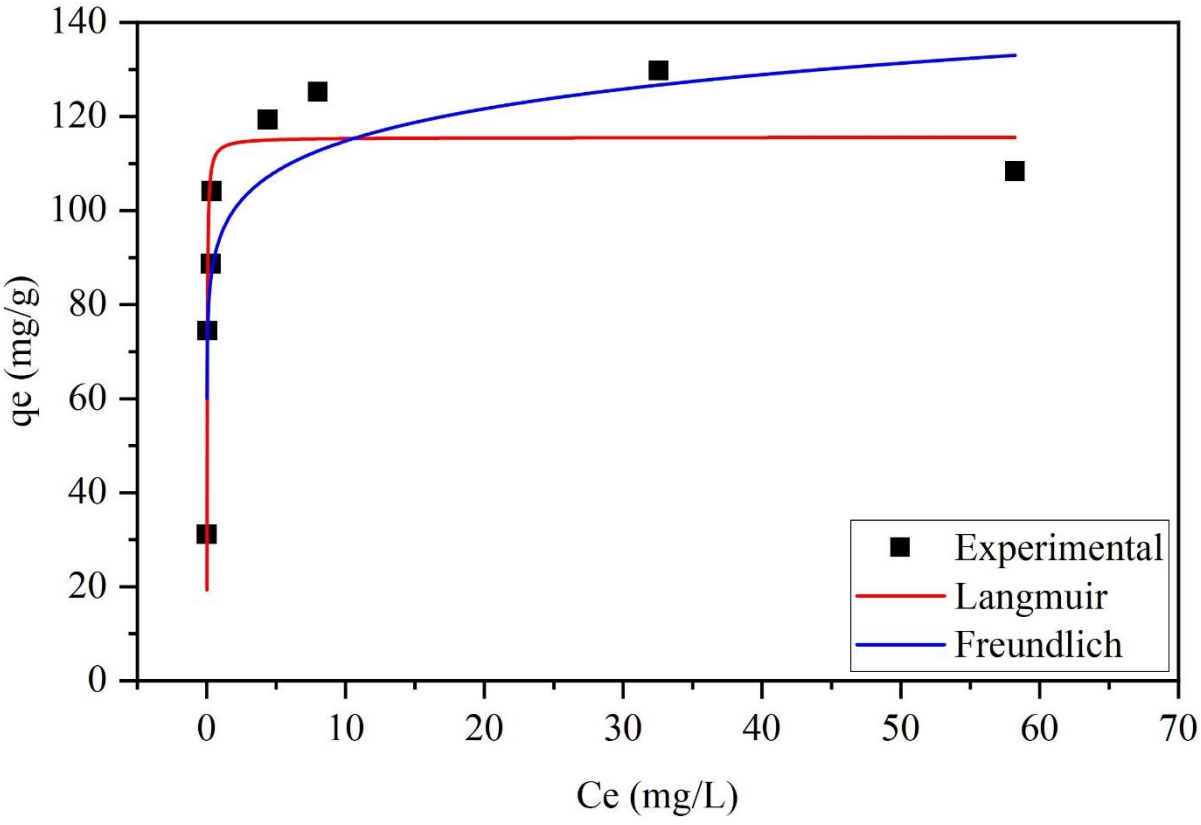

Figure 6.33 *Langmuir and Freundlich fitting curves of the Fe_3O_4/SiO_2/zeolite X*

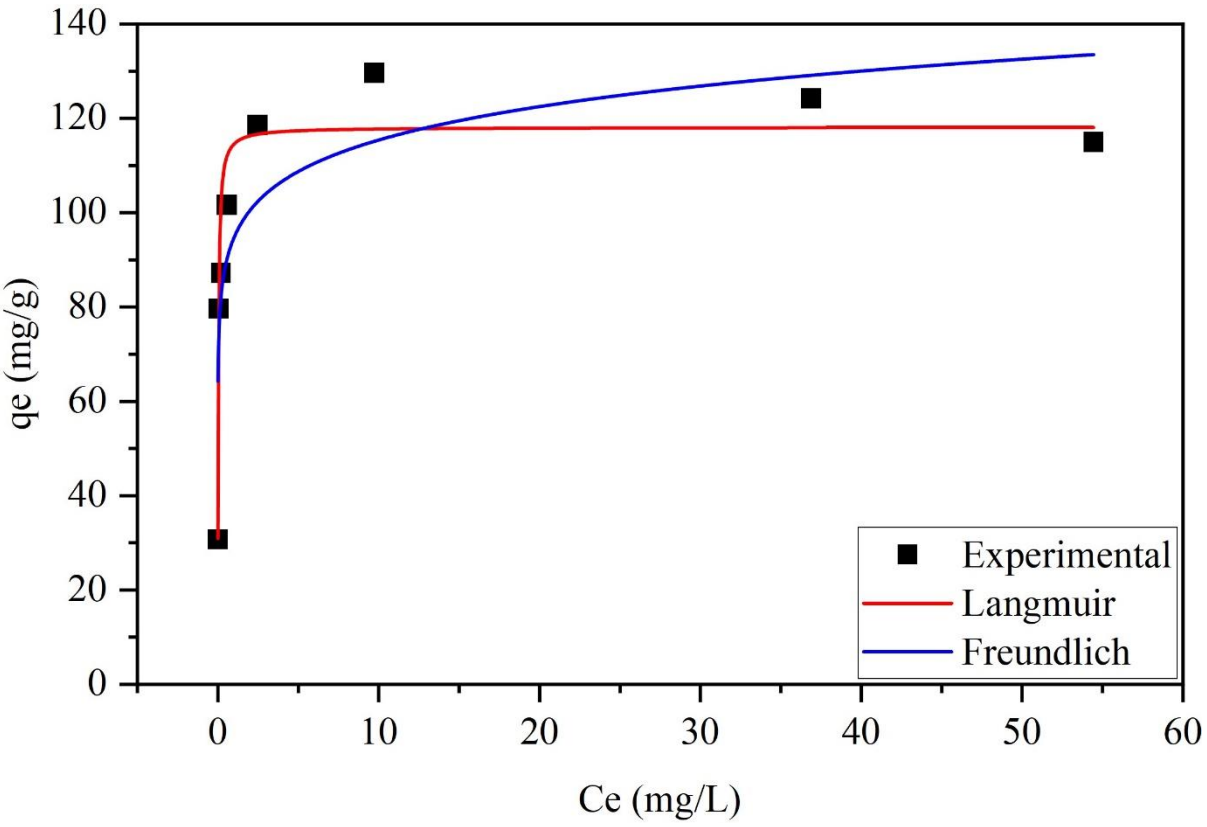

Figure 6.34 *Langmuir and Freundlich fitting curves of the* $Co_{0.3}Fe_{2.7}O_4/SiO_2$*/zeolite X*

6.3.2.3.2 Time-dependent Sr adsorption

The time-dependent Sr adsorption of the products and the bare zeolite X are shown in Figures 6.35 and 6.36. The bare zeolite X adsorbed most of the Sr within 10 min of starting the experiment, as was seen with the bare zeolite A. Both Fe_3O_4/SiO_2/zeolite X and $Co_{0.3}Fe_{2.7}O_4/SiO_2$/zeolite X took 60 min to adsorb most of the Sr. This was about 60 min quicker than the results seen with M_xO_y/SiO_2/zeolite A.

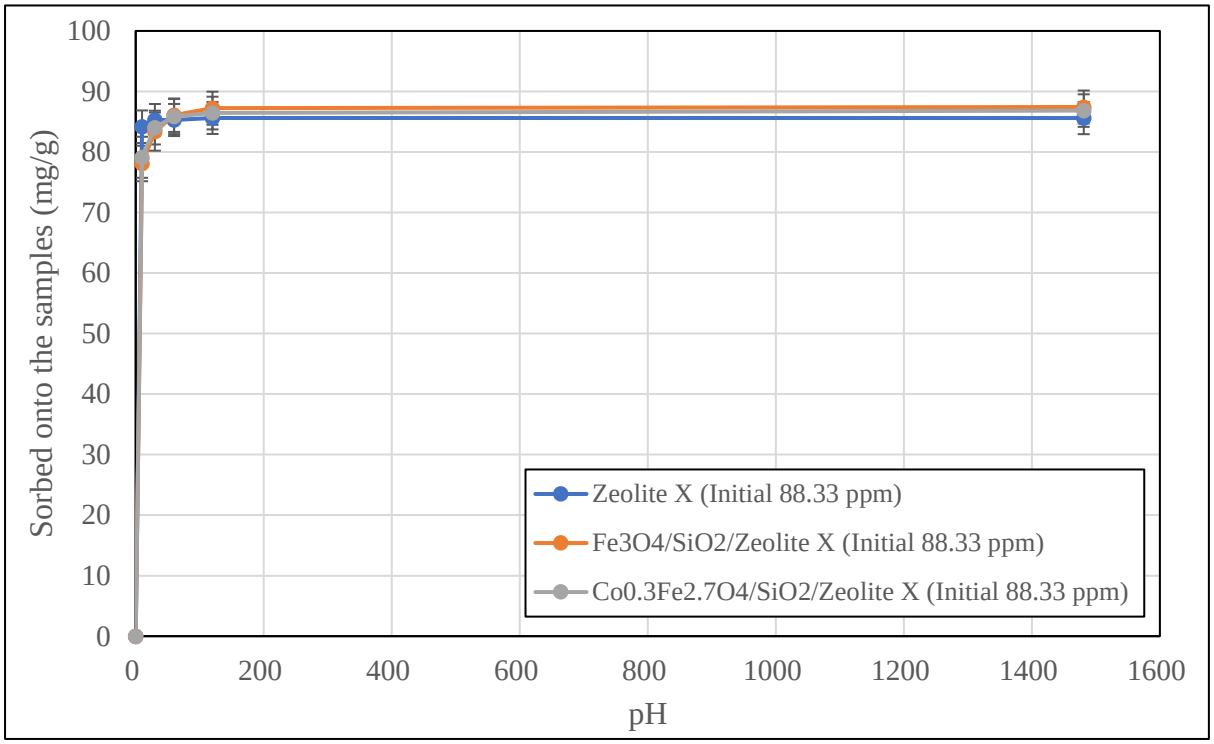

Figure 6.35 *Sr adsorption of the M_xO_y/SiO_2/zeolite X depending on time. The numbers after the samples were the duplicate experiments*

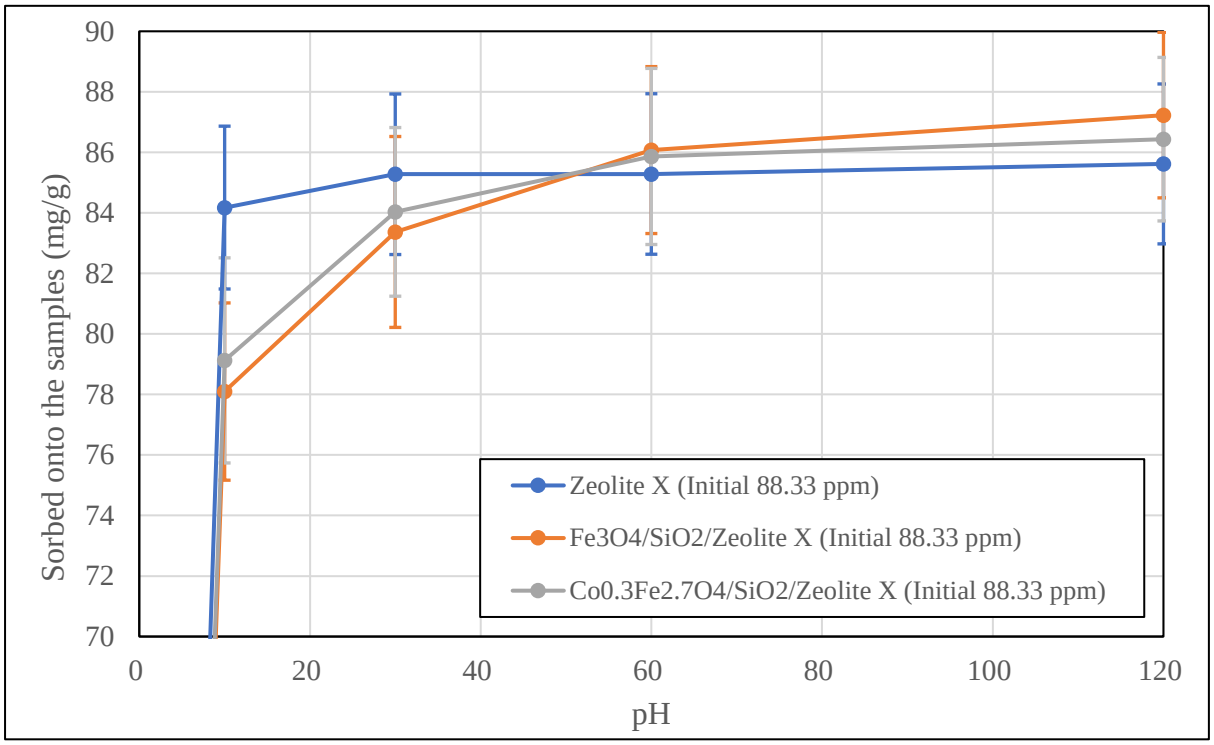

Figure 6.36 *Sr adsorption of M_xO_y/SiO_2/zeolite X depending on time (Greater data of Figure 6.37). The numbers after the samples were the duplicate experiments.*

The initial and final pH values of the products and the bare zeolite X are presented in Table 6-10. The bare zeolite X had the highest final pH values, and the $Co_{0.3}Fe_{2.7}O_4/SiO_2$/zeolite X had lowest final pH values, as was seen with $Co_{0.3}Fe_{2.7}O_4/SiO_2$/zeolite A (See Chapter 6.3.2.1.2). There might be one more reason: it might be due to the $Co_{0.3}Fe_{2.7}O_4$ particles such as changing the optimum zeolite pH for the Sr adsorption, and the $Co_{0.3}Fe_{2.7}O_4$ elements might be contacted with the Sr and Na within the zeolite frameworks.

Table 6.10 *Initial to final pH of Sr exchange solution for Sr adsorption with time.*

Time	Zeolite X	Fe_3O_4/SiO_2/zeolite X	$Co_{0.3}Fe_{2.7}O_4/SiO_2$/zeolite X
0	6.48*		
10	9.88 (±0.29)	7.65 (±0.55)	6.10 (±0.70)
30	9.99 (±0.06)	6.98 (±0.03)	6.79 (±0.05)
60	9.92 (±0.18)	8.85 (±1.39)	6.58 (±0.15)
120	9.85 (±0.14)	7.44 (±0.35)	6.70 (±0.01)
1481	9.81 (±0.01)	7.67 (±0.35)	7.00 (±0.13)

**The measurement was used the auto-hold mode that the pH values were measured when they moved within ± 3 digit for 10 sec.*

6.3.2.3.3 pH-dependent Sr adsorption

The final pH value differences for the products and the bare zeolite X were revealed by the Sr adsorption experiments using different stabilised pH values (Figure 6.37). The bare zeolite X had the highest Sr capacity at pH 7.00, and the Sr adsorption capacity of the

$Co_{0.3}Fe_{2.7}O_4/SiO_2$/zeolite X was highest and most stable between pH 7 and 10. The Fe_3O_4/SiO_2/zeolite X had its highest Sr capacity at pH 7, and it decreased by about 1 to 13 mg/g at pH 10.

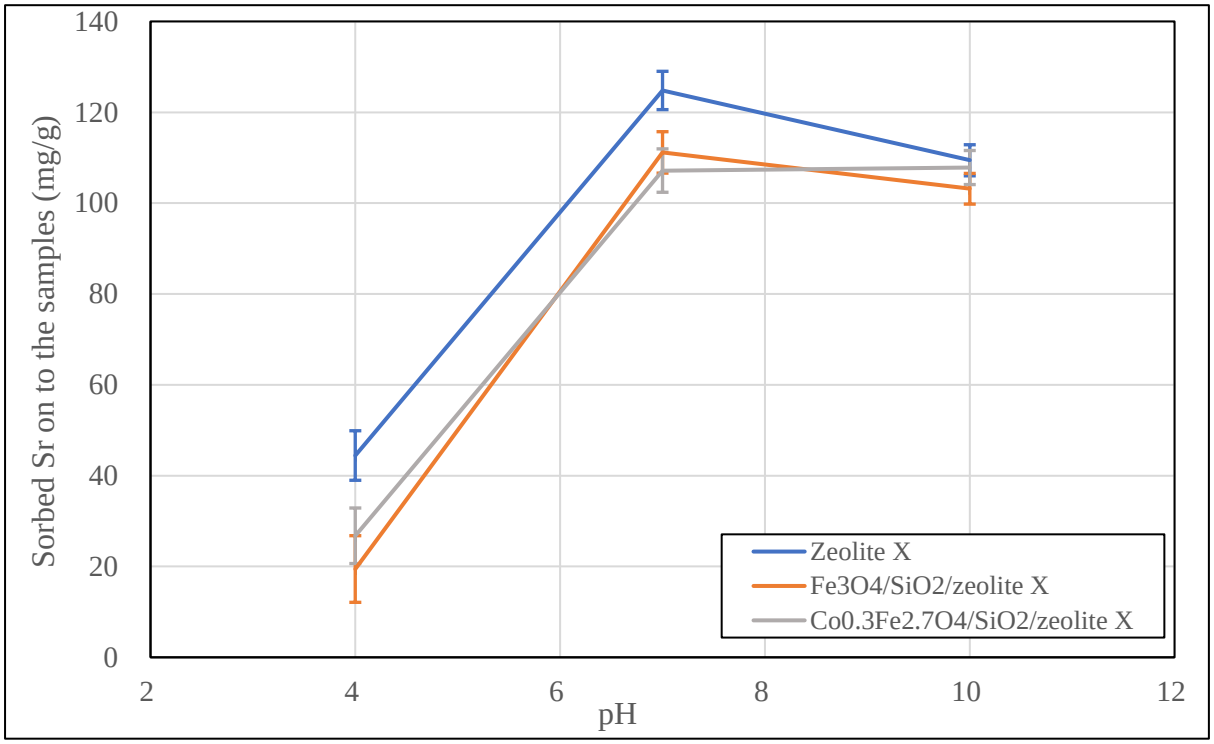

Figure 6.37 *Sr adsorption on to the M_xO_y/SiO_2/zeolite X depending on different initial pH*

The initial and final pH values of the stabilised concentrated Sr solutions are in Table 6.11. The pH values moved over 1.00, apart from the bare zeolite X at pH 4.06. The concentration of the HEPES in the pH 4.06 solutions may not have been enough to stabilise the pH, or the bare zeolite X may have been a stronger alkaliser than the other products.

Table 6.11 *Initial and final pH of the zeolite X and M_xO_y/SiO_2/zeolite X with different initial pH*

Initial	Zeolite X		Fe_3O_4/SiO_2/zeolite X		$Co_{0.3}Fe_{2.7}O_4/SiO_2$/zeolite X	
4.06*	5.30	(±0.08)	4.85	(±0.06)	4.82	(±0.08)
7.00*	7.12	(±0.06)	7.05	(±0.07)	7.11	(±0.03)
9.96*	9.92	(±0.02)	9.80	(±0.10)	9.71	(±0.04)

**The measurement was used the auto-hold mode that the pH values were measured when they moved within ± 3 digit for 10 sec.*

6.3.3 M_xO_y/SiO_2/CHA-Na

6.3.3.1 Phase identification of M_xO_y/SiO_2/CHA-Na

The XRD patterns of the Fe_3O_4/SiO_2/CHA-Na, the Fe_3O_4/SiO_2 and the bare CHA-Na are shown in Figure 6.38. The CHA-Na peaks of Fe_3O_4/SiO_2/CHA-Na at 51.3° and 76.2° were much bigger than for the bare CHA-Na, and they were not observed on the Fe_3O_4/CHA-Na XRD patterns. It could be assumed the reason is the same as the Chapter 5.10.1 and from Fe(0).

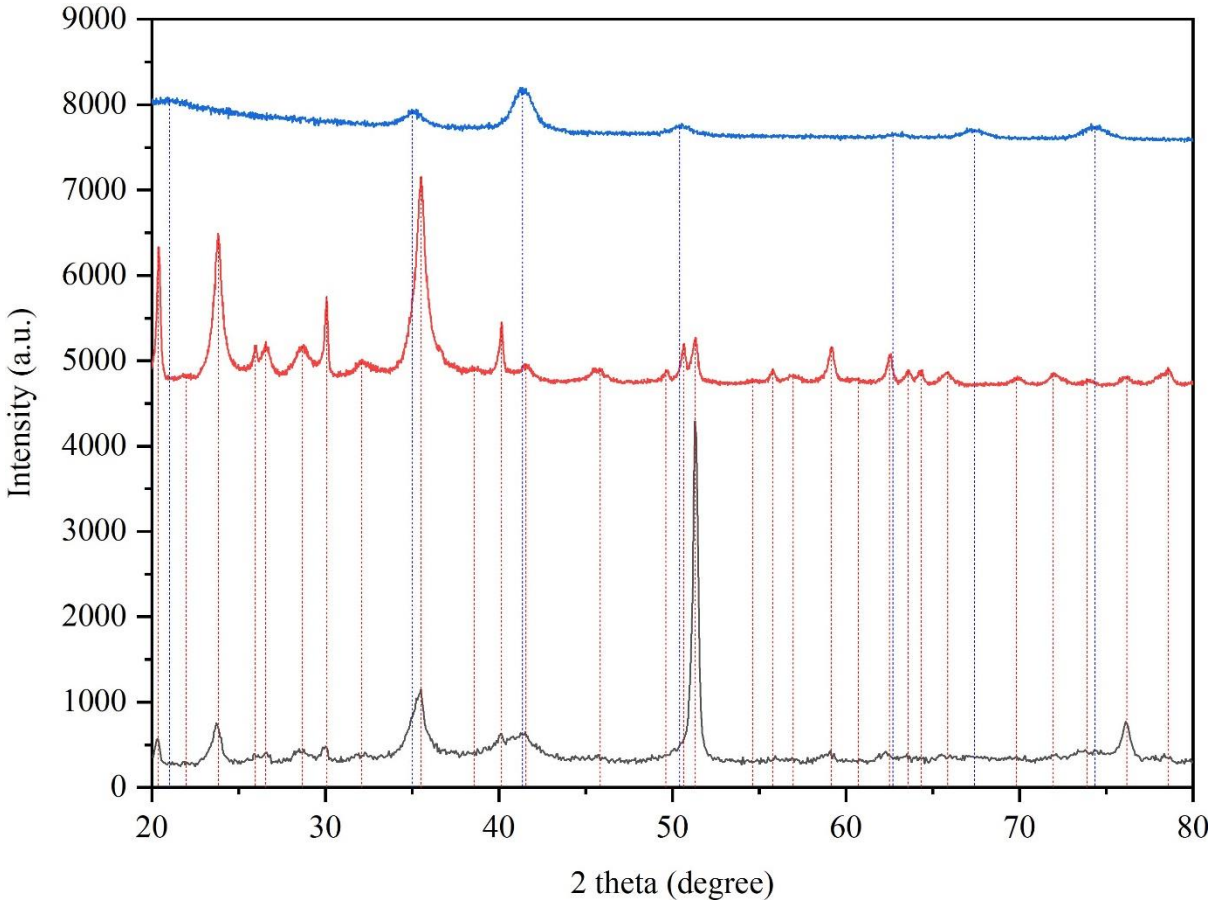

Figure 6.38 XRD *patterns of the Fe_3O_4 (blue), the CHA-Na (red) and the Fe_3O_4/SiO_2/CHA-Na (black).*

The XRD patterns of the $Co_{0.3}Fe_{2.7}O_4/SiO_2$/CHA-Na, the $Co_{0.3}Fe_{2.7}O_4/SiO_2$ and the bare CHA-Na are shown in Figure 6.39. Again, the $Co_{0.3}Fe_{2.7}O_4/SiO_2$/CHA-Na had much bigger peaks than the bare CHA-Na at 51.3° and 76.2°, but the peaks were smaller than seen for the Fe_3O_4/SiO_2/CHA-Na. The $Co_{0.3}Fe_{2.7}O_4$ peaks can be also observed at 34.5° and 41.0°, and the peak at 66.8° appeared strongly that could be assumed from Fe(0) by the oxidisation in air atmosphere.

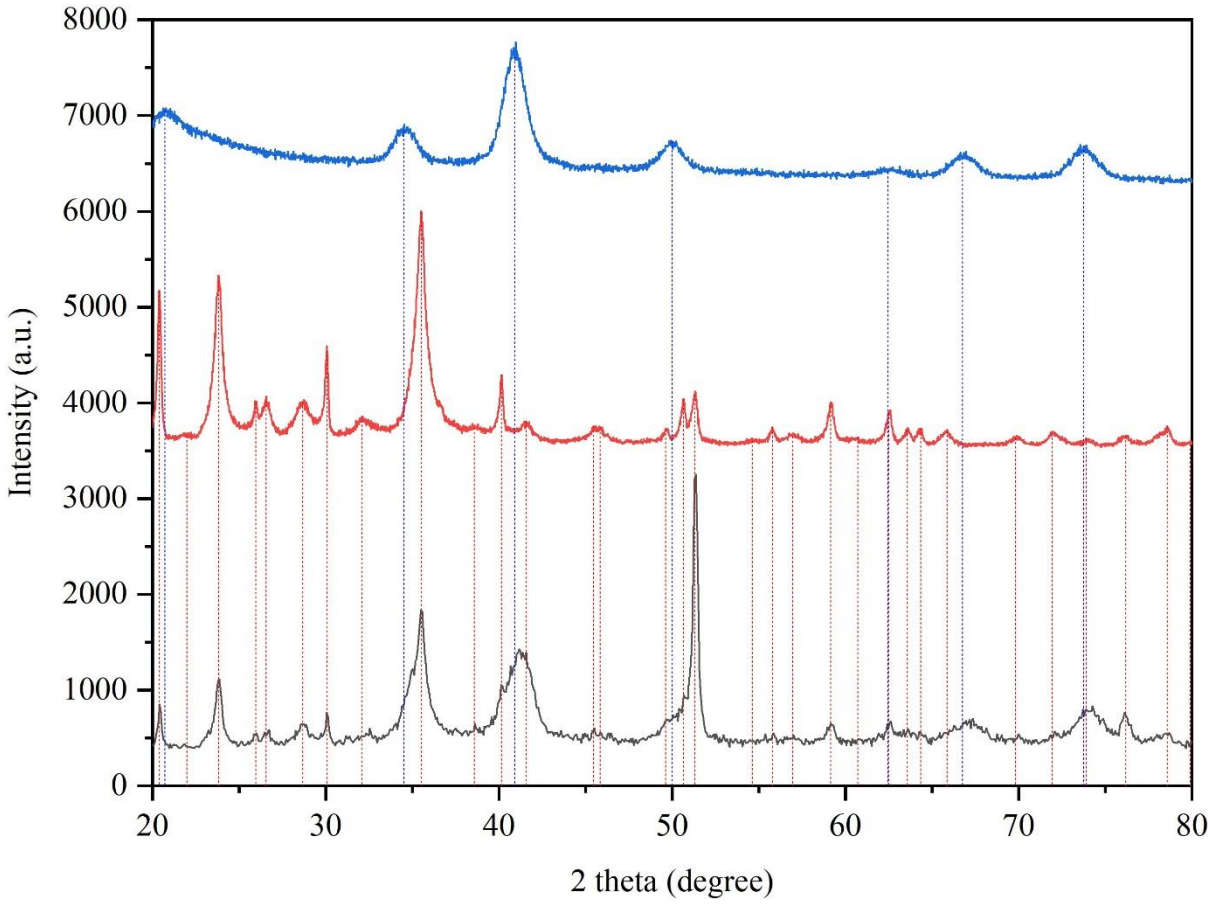

Figure 6.39 *XRD patterns of the $Co_{0.3}Fe_{2.7}O_4$ (blue), the CHA-Na (red) and the $Co_{0.3}Fe_{2.7}O_4/SiO_2$/CHA-Na (black).*

The Raman peaks of the products and the bare CHA-Na are shown in Figure 6.40. The CHA-Na peaks appeared on the Fe_3O_4/SiO_2/CHA-Na and $Co_{0.3}Fe_{2.7}O_4/SiO_2$/CHA-Na, but only the Fe_3O_4 and $Co_{0.3}Fe_{2.7}O_4$ peaks could not be observed. The layers of the CHA-Na on the products might be thicker than for M_xO_y/CHA-Na.

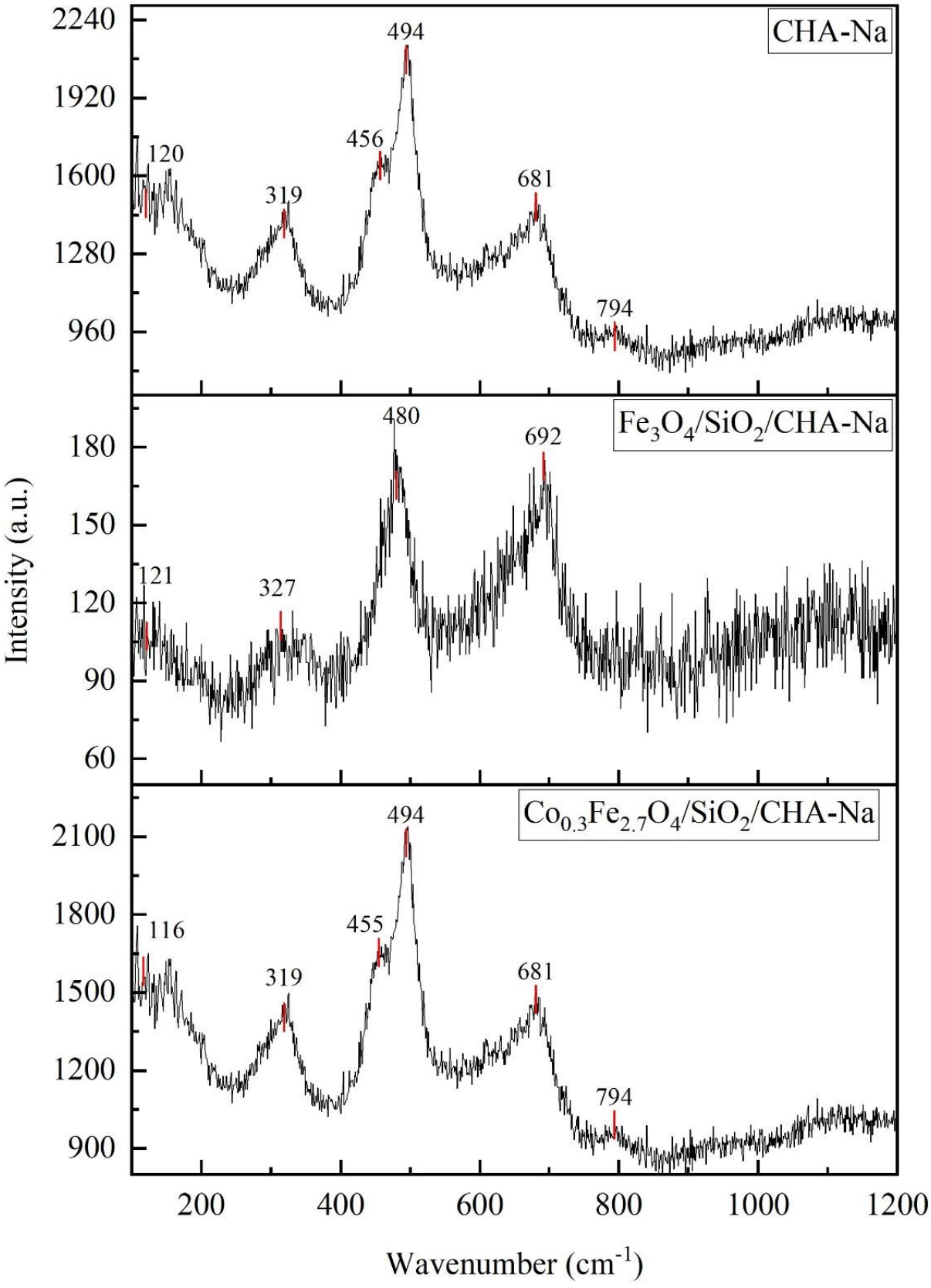

Figure 6.40 *Raman spectra of the M_xO_y/SiO_2/CHA-Na.*

The SEM-EDX images of the Fe_3O_4/SiO_2/CHA-Na are shown in Figures 6.41 and 6.42. The samples were made using the rotation oven and separated using the magnet. Therefore, they are Fe_3O_4-rich particles. There were fewer big aggregated Fe_3O_4 particles, and they were also smaller than the magnetic zeolite particles that were made using the conventional oven. The EDX images suggested that the product did not to contain K, and it was Na-rich.

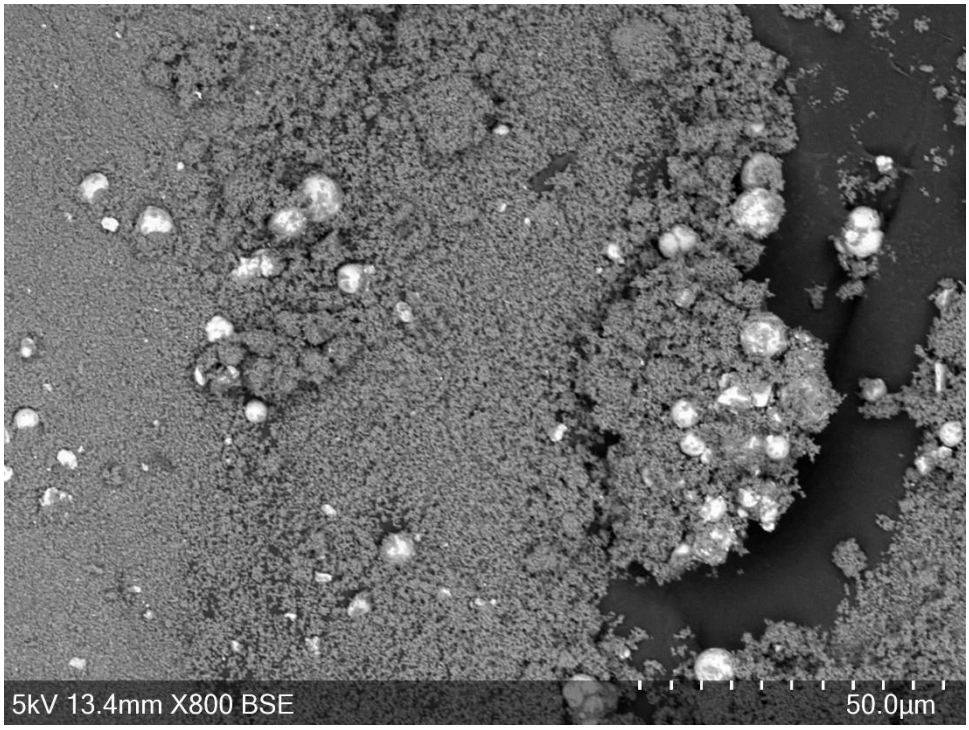

Figure 6.41 *SEM image of Fe_3O_4/SiO_2/CHA-Na.*

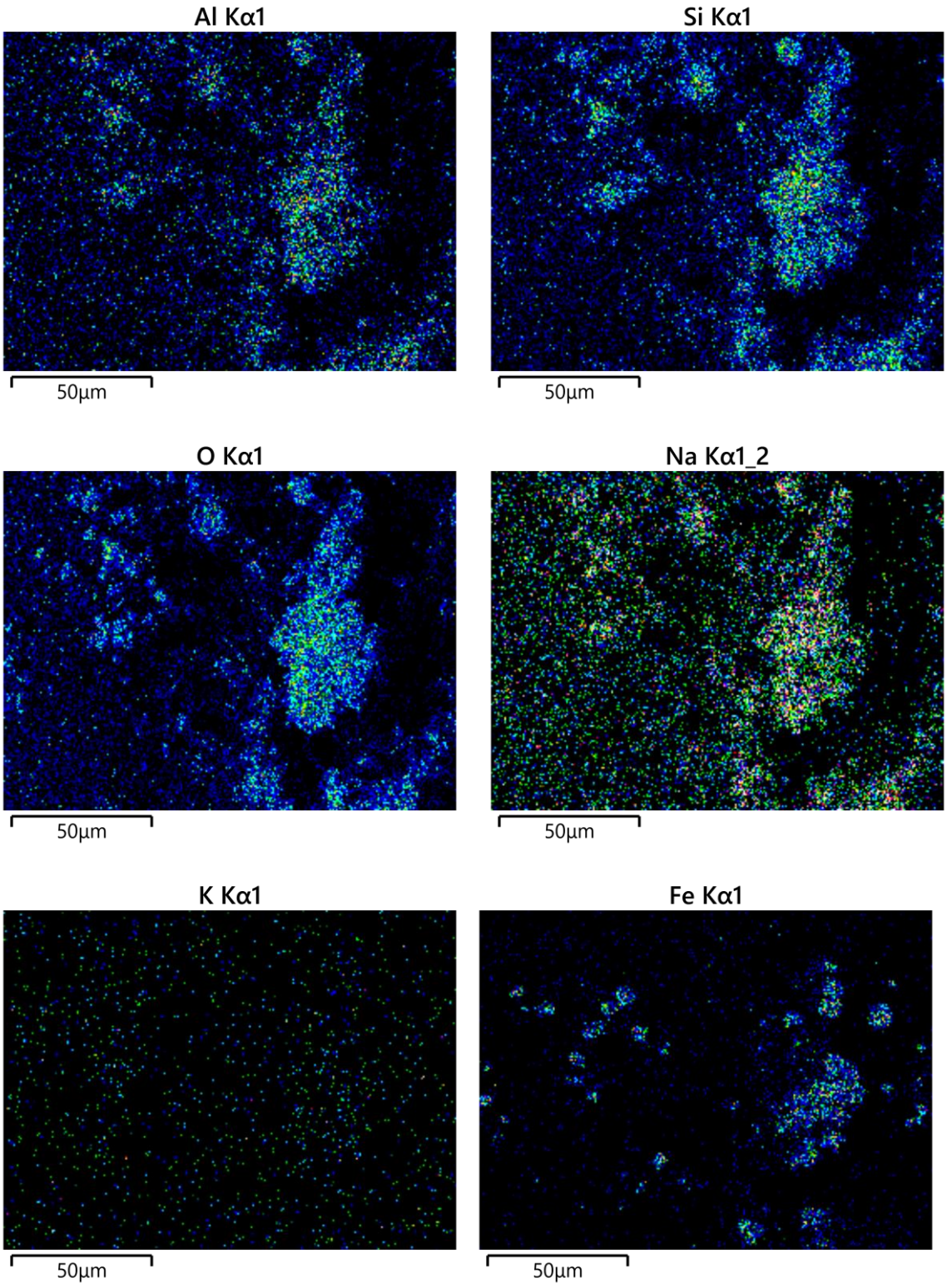

Figure 6.42 *SEM-EDX elemental mapping images of the Fe_3O_4/SiO_2/CHA-Na.*

The SEM-EDX images of the $Co_{0.3}Fe_{2.7}O_4/SiO_2$/CHA-Na are shown in Figures 6.43 to 6.45. Again, there were bigger aggregated $Co_{0.3}Fe_{2.7}O_4$ particles, but the shapes were like the already synthesised $Co_{0.3}Fe_{2.7}O_4/SiO_2$/CHA-Na particles that were aggregated. The EDX images also showed a small amount of Al and Na on the aggregated particles. It might be due to the Fe rich by the aggregations of the $Co_{0.3}Fe_{2.7}O_4/SiO_2$/CHA-Na.

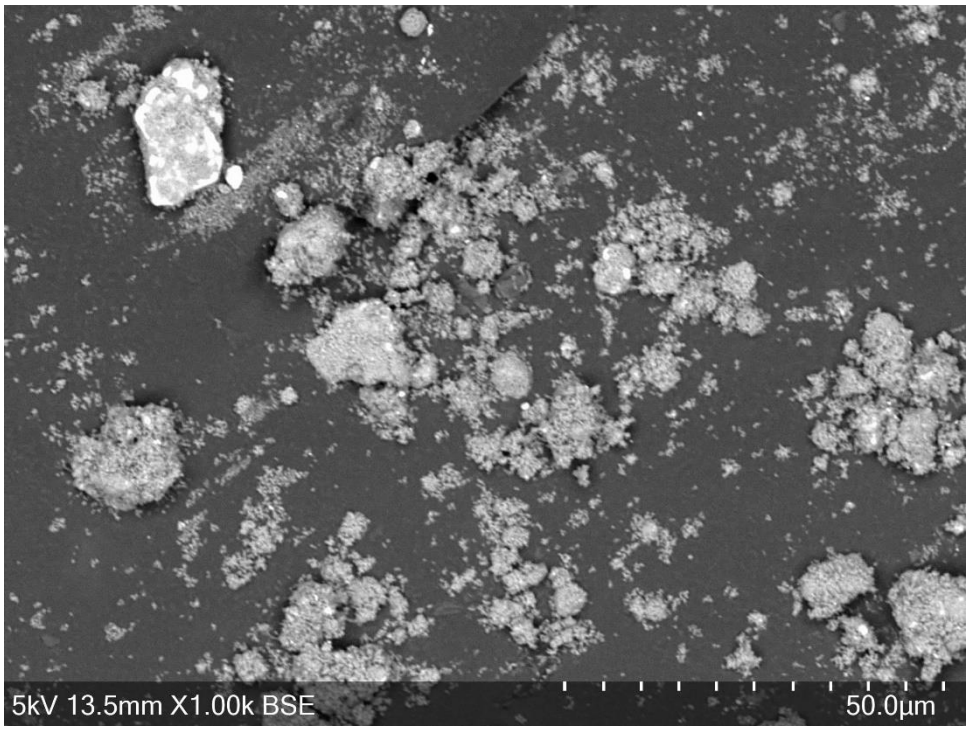

Figure 6.43 *SEM image of the $Co_{0.3}Fe_{2.7}O_4/SiO_2$/CHA-Na.*

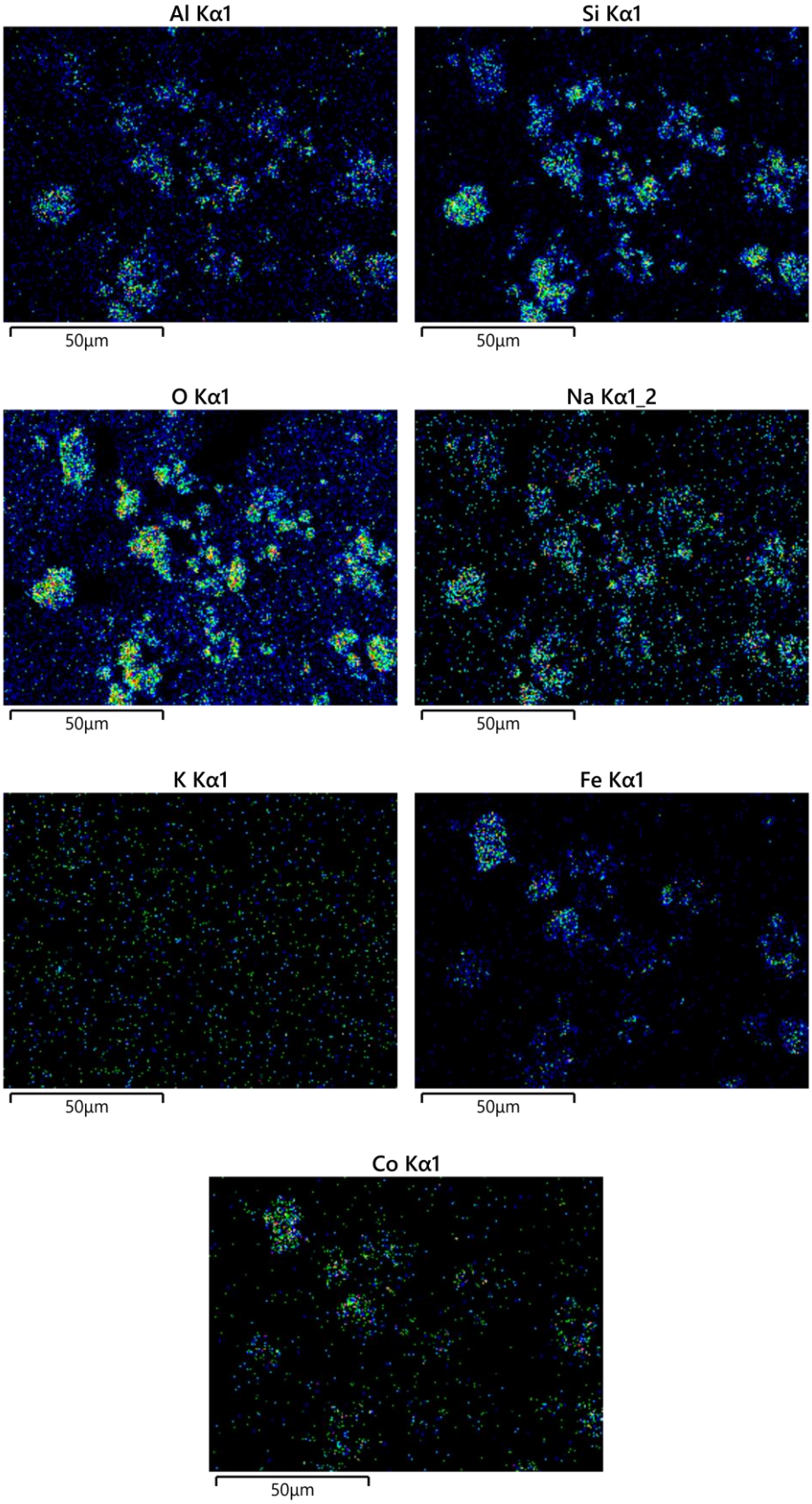

Figure 6.44 *SEM-EDX elemental mapping images of the* $Co_{0.3}Fe_{2.7}O_{49}/SiO_2$*/CHA-Na.*

The elemental compositions of the products and the bare CHA-Na observed by XRF are shown in Table 6.12. The Si to Al ratio of the products increased by between about 0.38 and 0.54 compared to the bare CHA-Na, and the Na to Al ratio decreased by about 0.2. It could be assumed the reason is the same as the Chapter 6.3.1.1, which Si source of the CHA-Na formation was used from M_xO_y/SiO_2 rather than the reagents, and the M_xO_y was also incorporated with the SiO_2 into the CHA-Na. The Fe to Al ratio of Fe_3O_4/SiO_2/CHA-Na was much higher than the total ratio of Co and Fe to Al of the $Co_{0.3}Fe_{2.7}O_4/SiO_2$/CHA-Na. That is why the XRD peak intensity sizes of Fe_3O_4/SiO_2/CHA-Na were bigger than for the $Co_{0.3}Fe_{2.7}O_4/SiO_2$/CHA-Na. The ratio of Fe to Al and/or Co to Al for Fe_3O_4/SiO_2/CHA-Na was over twice as high as for the Fe_3O4/CHA-Na and $Co_{1.1}Fe_{1.9}O_4$/CHA-Na. That means Fe_3O_4/SiO_2/CHA-Na had more Fe_3O_4 particles and less CHA-Na than the Fe_3O4/CHA-Na and $Co_{1.1}Fe_{1.9}O_4$/CHA-Na, and it could be supposed the Fe_3O_4/SiO_2/CHA-Na had less Cs adsorption capacities.

Table 6.12 *Elemental compositions of the M_xO_y/SiO_2/CHA-Na (the ratio of Co and Fe are highlighted in yellow).*

Sample	Formula	Concentration (wt%)		Amount of material (mmol)	Ratio
CHA-Na	Al	22.40	(±0.36)	8.30	1.00
	Si	58.70	(±0.62)	20.90	2.52
	Na	17.20	(±0.67)	7.48	0.90
	K	1.61	(±0.06)	0.41	0.05
Fe_3O_4/SiO_2/CHA-Na	Al	4.11	(±0.12)	1.52	1.00
	Si	11.60	(±0.22)	4.13	2.71
	Na	2.41	(±0.13)	1.05	0.69
	K	0.00	(±0.00)	0.00	0.00
	Fe	81.80	(±0.23)	14.65	9.61
$Co_{0.3}Fe_{2.7}O_4/SiO_2$/CHA-Na	Al	4.02	(±0.12)	1.49	1.00
	Si	12.00	(±0.21)	4.27	2.87
	Na	2.24	(±0.12)	0.97	0.65
	K	0.00	(±0.00)	0.00	0.00
	Fe	62.90	(±0.19)	11.26	3.53
	Co	18.80	(±0.08)	3.19	1.0

6.3.3.2 Magnetic properties

The magnetisation loops of the products are shown in Figures 6.45 and 6.46 The maximum magnetisation of $Co_{0.3}Fe_{2.7}O_4/SiO_2$/CHA-Na was also about 10 emu/g higher than that of the Fe_3O_4/SiO_2/CHA-Na, and the tiny hysteresis of Fe_3O_4/SiO_2/CHA-Na was shifted to the positive magnetic field side from the origin. The hysteresis of $Co_{0.3}Fe_{2.7}O_4/SiO_2$/CHA-Na went through the origin point, but it was slightly shifted to the positive magnetic field side and was not asymmetric. The maximum magnetisation of the Fe_3O_4/SiO_2/CHA-Na was 8.4 emu/g higher than for the Fe_3O_4/CHA-Na, and that of the $Co_{0.3}Fe_{2.7}O_4/SiO_2$/CHA-Na was also 18.4 emu/g higher than for the $Co_{1.1}Fe_{1.9}O_4$/CHA-Na. It could be thought that the

maximum magnetisation differences were due to the number of M_xO_y particles in the CHA-Na.

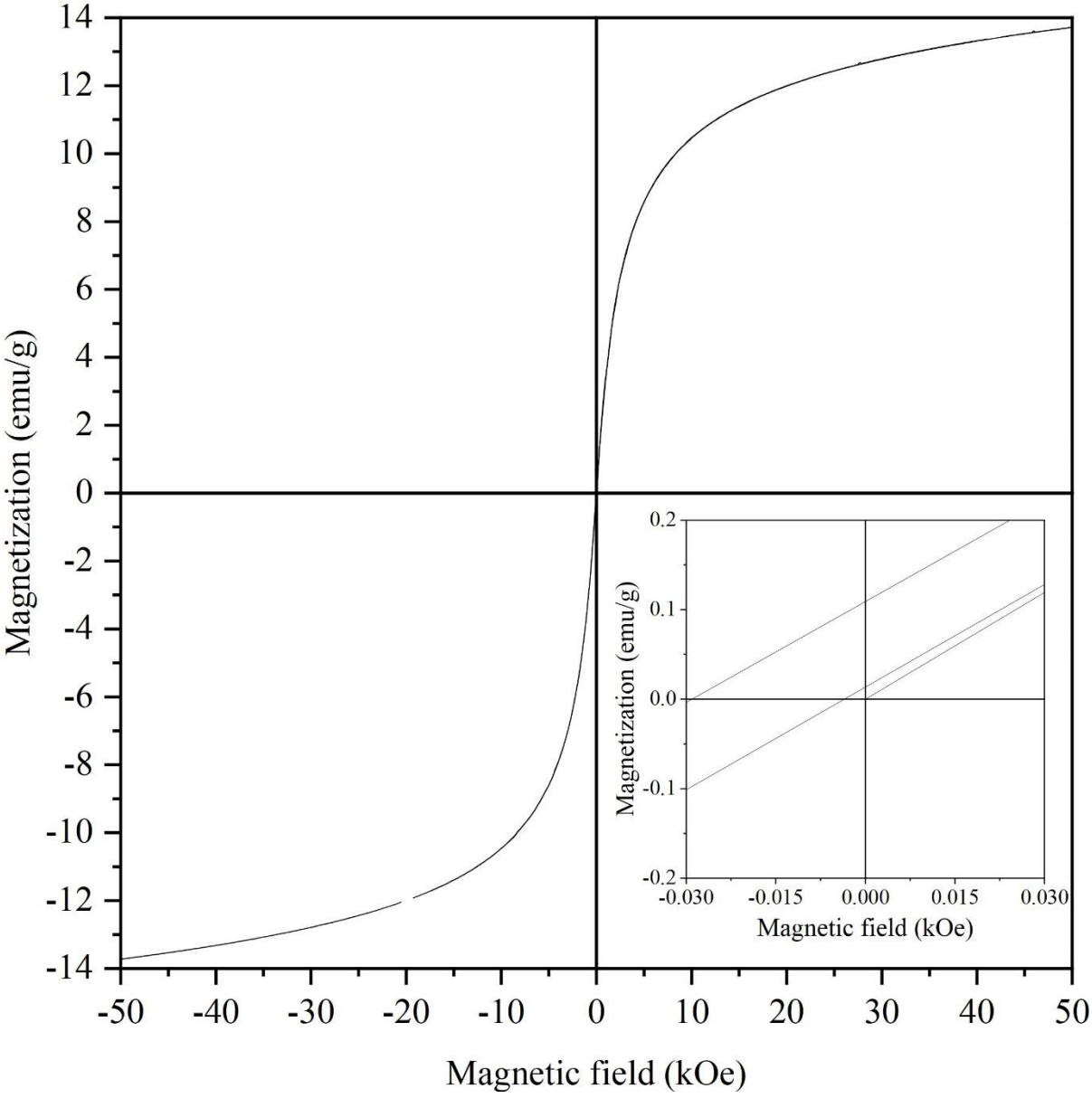

Figure 6.45 *Magnetisation curve of the Fe_3O_4/SiO_2/CHA-Na.*

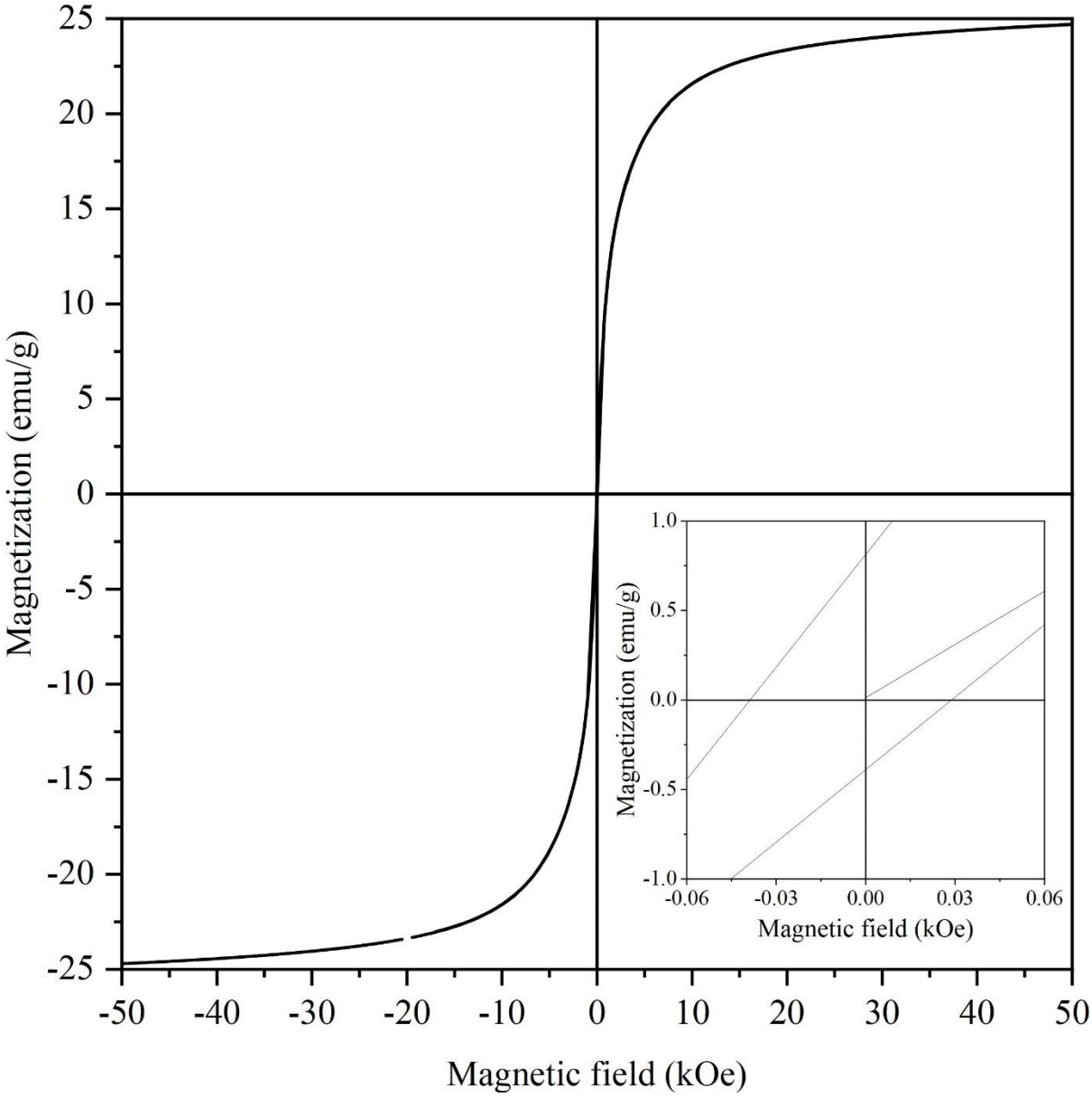

Figure 6.46 *Magnetisation curve of the $Co_{0.3}Fe_{2.7}O_4/SiO_2$/CHA-Na.*

The M_r/M_s values of the products are shown in Table 6.13. The M_r/M_s of the $CoFe_2O_4/SiO_2$/CHA-Na was less than 0.1, and the M_r/M_s of the maximum magnetisation of Fe_3O_4/SiO_2/CHA-Na was also less than 0.1.

Table 6.13 *Relationship between the magnetisation hysteresis gaps and superparamagnetism (at 300 K).*

	H_c (kOe)	M_s (emu/g)	M_r (emu/g)	M_r/M_s
Fe_3O_4/SiO_2/CHA-Na	-0.029	13.700	0.108	0.008
	-0.003	-13.700	0.014	-0.001
$Co_{0.3}Fe_{2.7}O_4/SiO_2$/CHA-Na	-0.038	24.700	0.800	0.032
	0.029	-24.700	-0.400	0.016

The ZFC/FC curves of the products are shown in Figures 6.47 and 6.48 The blocking temperatures were less than 273.15 K, and that of Fe_3O_4/SiO_2/CHA-Na was much smaller than that of $Co_{0.3}Fe_{2.7}O_4/SiO_2$/CHA-Na, as seen with the other products. The blocking temperature of Fe_3O_4/SiO_2/CHA-Na was 27.04 K higher than for Fe_3O_4/CHA-Na, and that of the $Co_{0.3}Fe_{2.7}O_4/SiO_2$/CHA-Na was 86.09 K higher than for the $Co_{1.1}Fe_{1.9}O_4$.

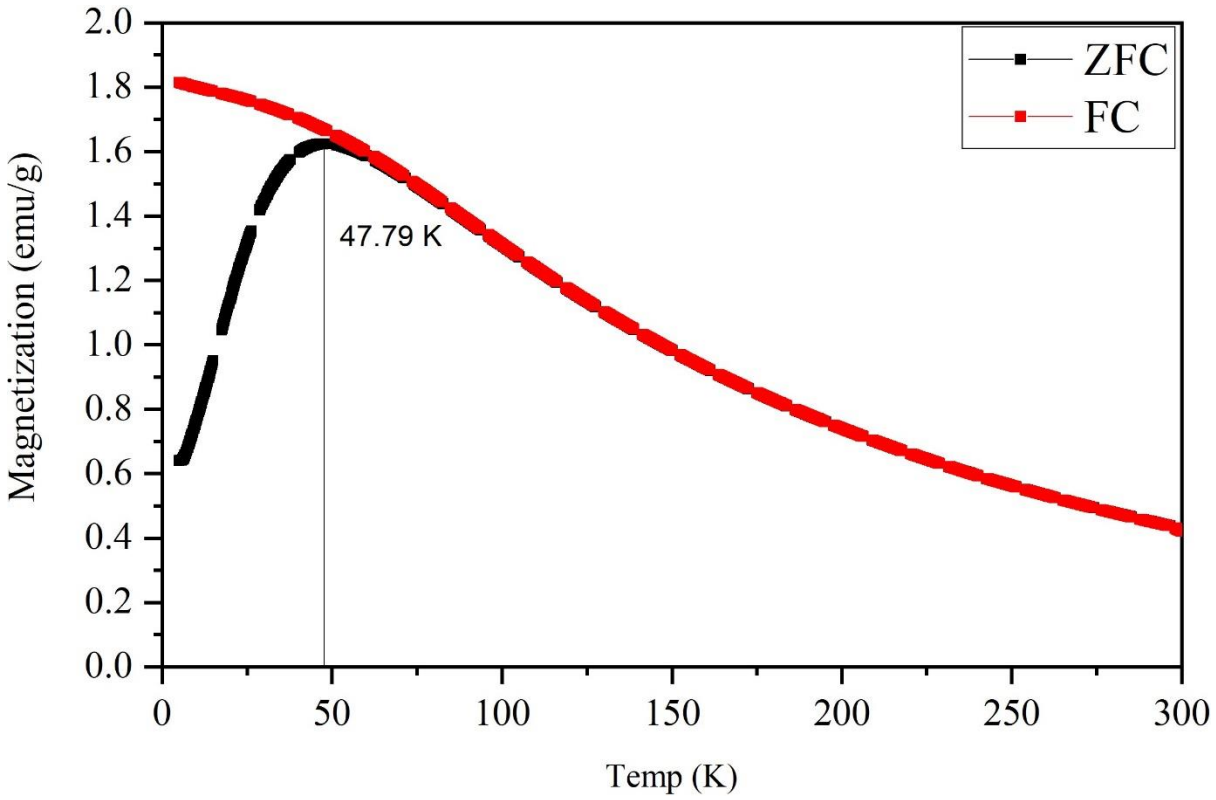

Figure 6.47 *ZFC/FC curves of the Fe_3O_4/SiO_2/CHA-Na.*

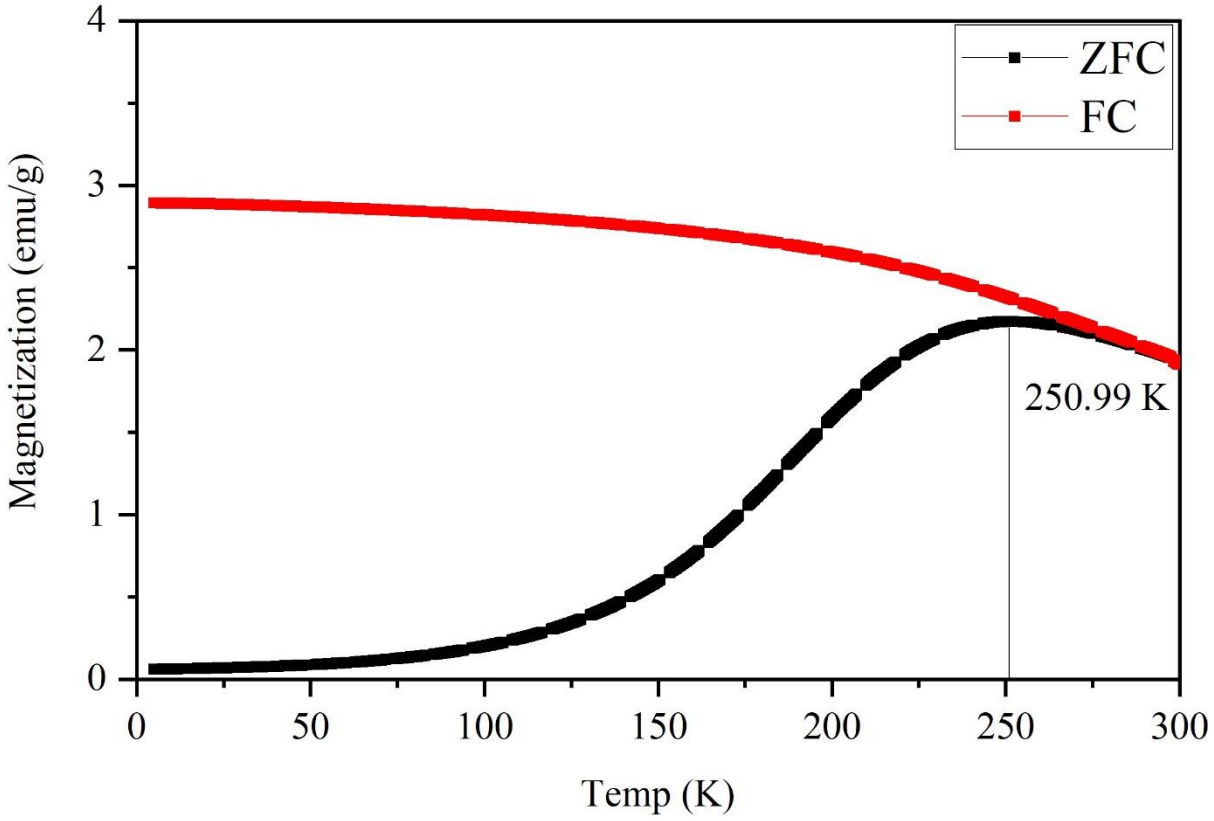

Figure 6.48 *ZFC/FC curves of the* $CoFe_{2.66}O_{4.99}/SiO_2$*/CHA-Na.*

6.3.3.3 Cs adsorption

6.3.3.3.1 Cs adsorption isotherms

The adsorption isotherms of the products and the bare CHA-Na are shown in Figures 6.49 and 5.50 Both products reached Cs adsorption equilibrium at around 5 mg/l, and the Cs adsorption capacity was about 20 mg/g lower than that of the bare CHA-Na. That means the maximum Cs adsorption equilibrium of both products was also just 20 mg/g lower than for the M_xO_y/CHA-Na, but this can be understood from the amount of incorporated M_xO_y: the products had over twice as many M_xO_y particles than the M_xO_y/CHA-Na.

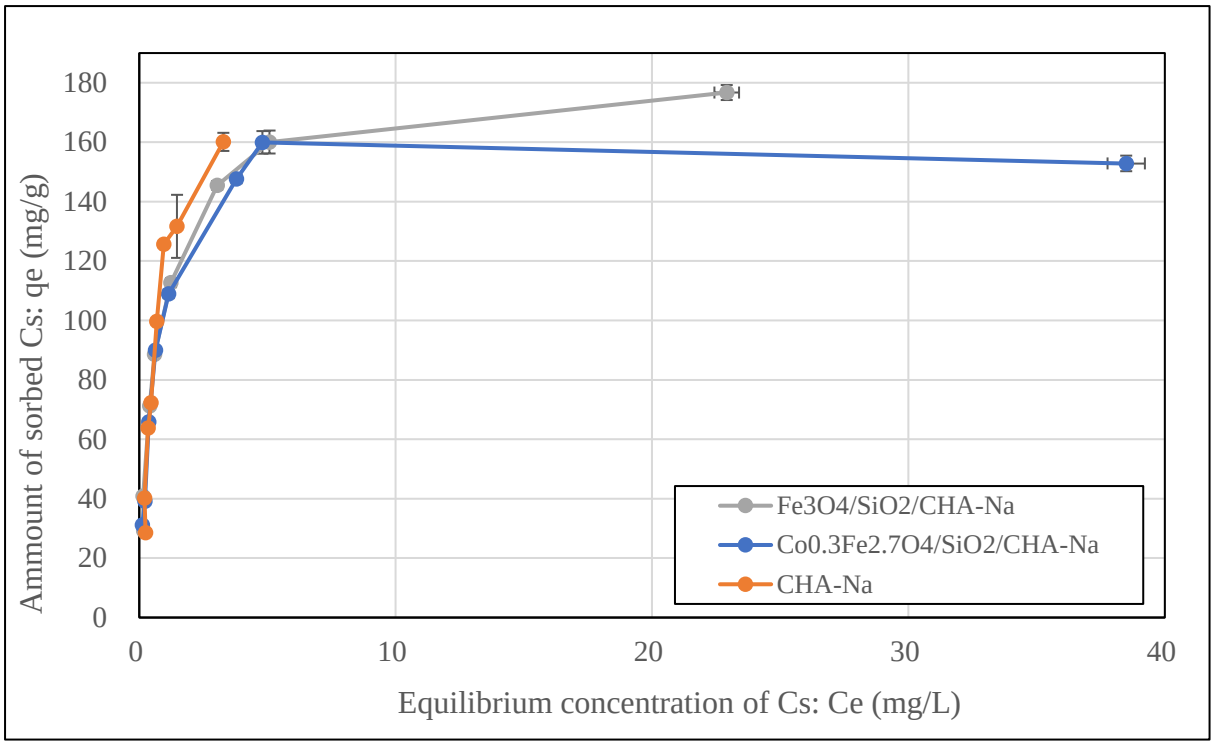

Figure 6.49 *Cs adsorption isotherm curves of the M_xO_y/SiO_2/CHA-Na.*

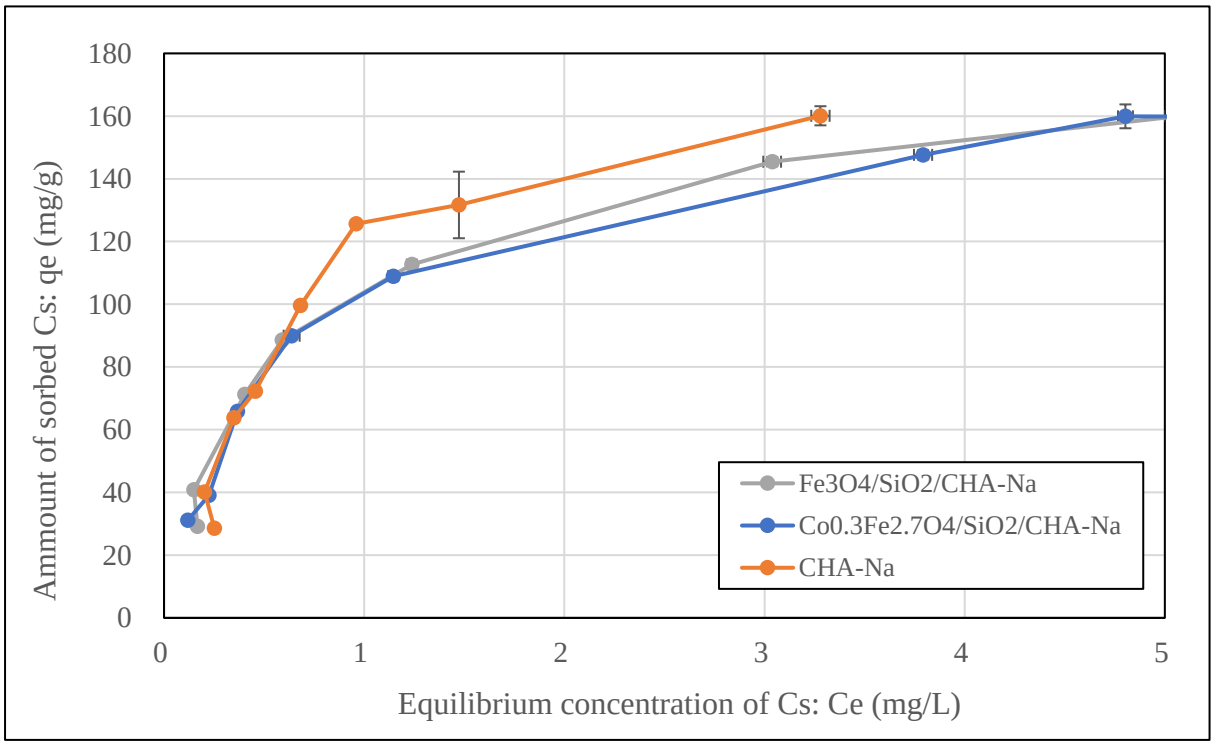

Figure 6.50 *Cs adsorption isotherm curves of the M_xO_y/SiO_2/CHA-Na (Greater data of Figure 6.49).*

The final pH values of the Cs adsorption isotherms of the products were about 0.5 higher than for the bare CHA-Na with an initial Cs concentration of 39–40 ppm, and the final pH values of the products and the bare CHA-Na were lower than those of the initial Cs concentrated solution (Table 6.14).

Table 6.14 *Initial $CsNO_3$ concentrations and initial and final pH of M_xO_y/SiO_2/CHA-Na. The measurement was used only the auto-hold mode that the pH values were measured when they moved within ± 3 digit for 10 sec.*

ppm	Initial pH	Final pH		ppm	Initial pH	Final pH
		Fe_3O_4/SiO_2 /CHA-Na	$Co_{0.3}Fe_{2.7}O_4/SiO_2$ /CHA-Na			CHA-Na
202.34 (±2.08)	7.99	6.79	6.86	160.70 (±2.95)	5.34	5.63
174.58 (±4.00)	7.38	7.01	7.04	138.76 (±11.05)	5.29	5.83
147.07 (±1.40)	7.20	7.54	7.19	121.45 (±0.78)	5.46	6.24
122.88 (±1.46)	7.54	7.13	6.84	95.87 (±0.84)	5.48	6.18
111.10 (±1.03)	7.29	7.29	7.04	75.75 (±1.20)	5.46	6.43
88.99 (±0.95)	7.33	7.14	6.87	63.12 (±0.85)	5.71	6.02
39.34 (±0.79)	6.78	6.99	7.11	40.36 (±0.42)	5.96	6.43
17.62 (±0.52)	7.73	7.31	7.13	30.30 (±0.61)	5.60	6.48

The adsorption isotherms of the products calculated by the Langmuir and Freundlich models are shown in Figures 6.51 and 6.52 The experimentally obtained Cs adsorption isotherm curves of both products were fitted with the Langmuir mode. That means the products had maximum Cs adsorption capacities, and the Cs adsorption sites onto the CHA-Na were not distorted by the M_xO_y/SiO_2 nanoparticles much.

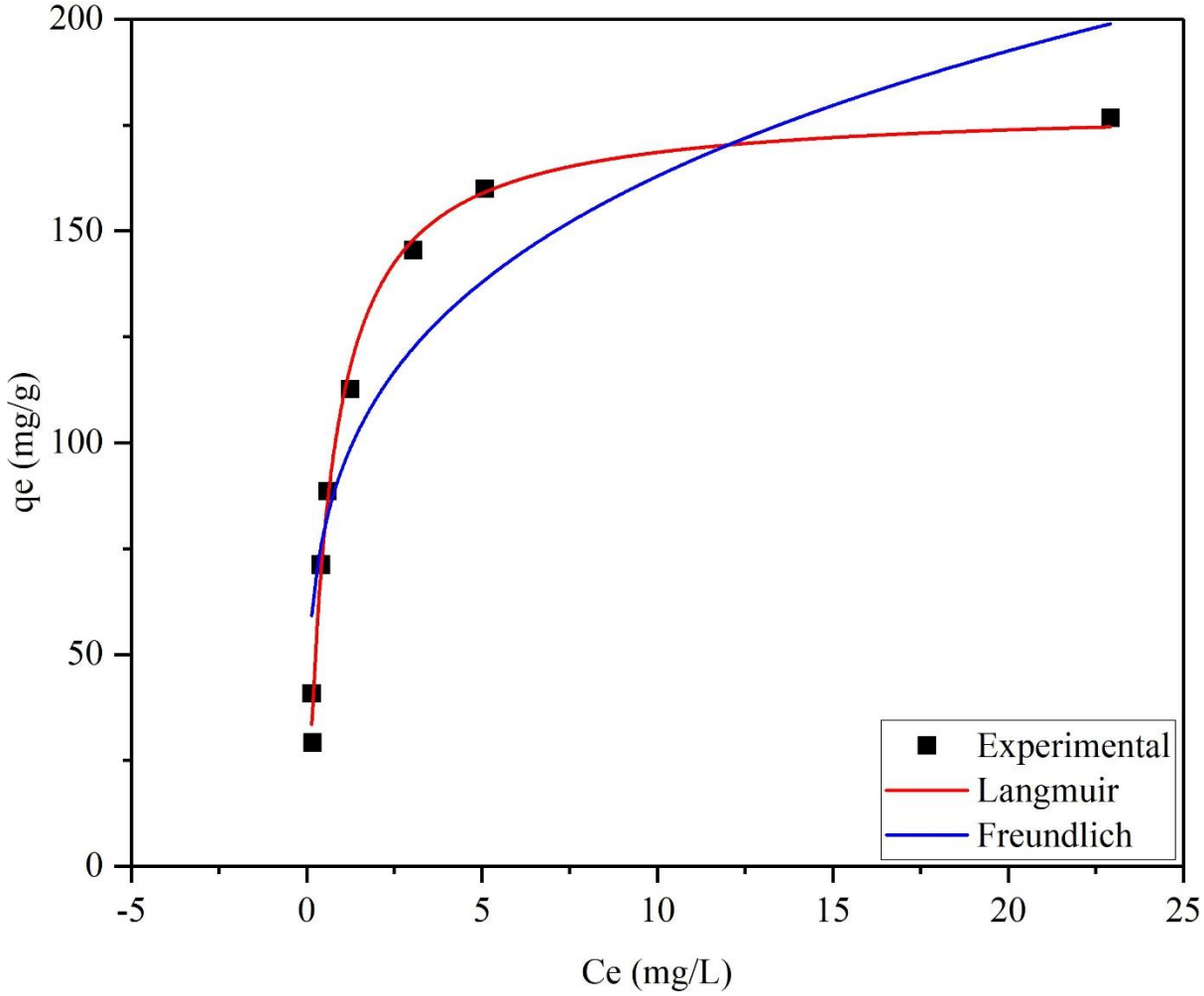

Figure 6.51 *Langmuir and Freundlich fitting curves of the Fe_3O_4/SiO_2/CHA-Na.*

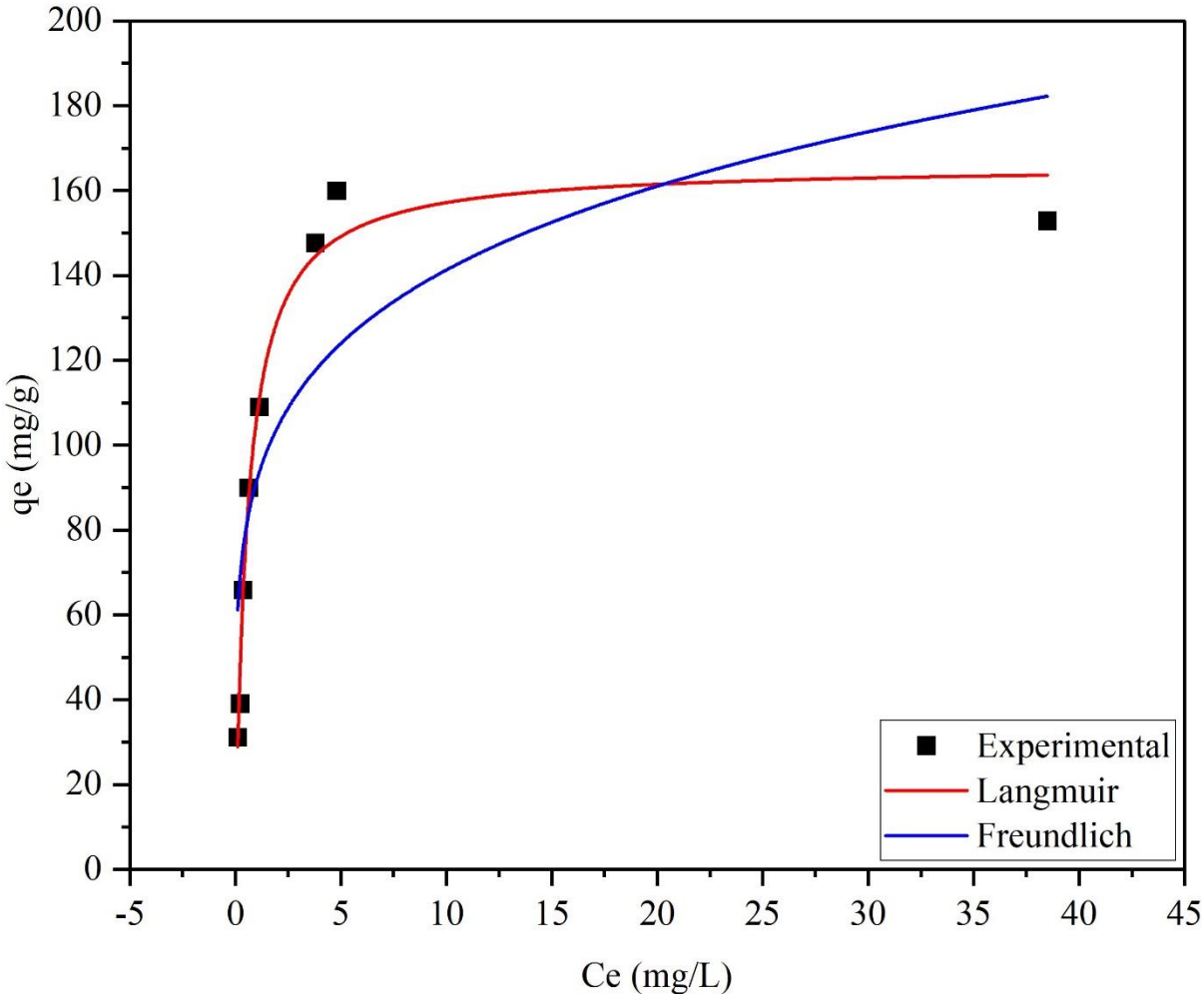

Figure 6.52 *Langmuir and Freundlich fitting curves of the* $Co_{0.3}Fe_{2.7}O_4/SiO_2$*/CHA-Na.*

6.3.3.3.2 Time-dependent Cs adsorption

The time-dependent Cs adsorption curves of the products and the bare CHA-Na are shown in Figures 6.53 and 6.54 All of the products and the bare CHA-Na adsorbed most Cs within 10 min of starting the experiment. This was 30 min faster than for the M_xO_y/CHA-Na. This was due to the M_xO_y/SiO_2 particle sizes in the CHA-Na or the different synthesis methods (whether or not coprecipitation was used).

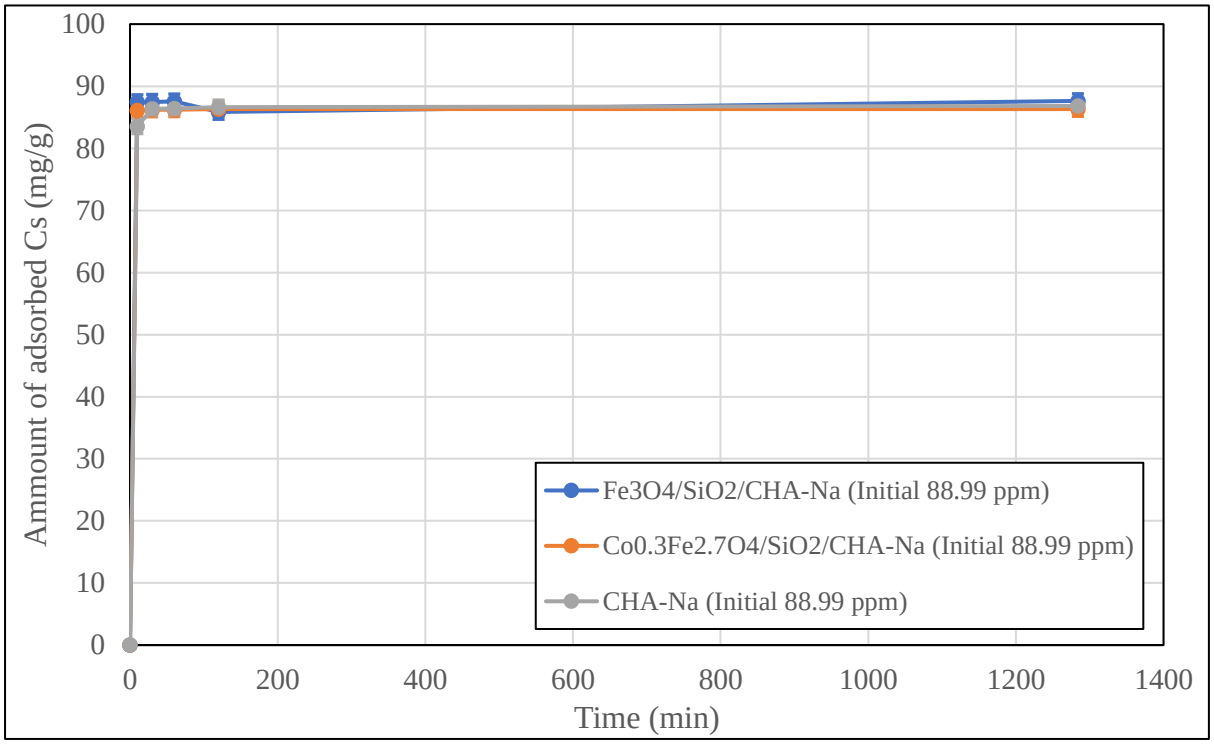

Figure 6.53 *Cs adsorption of the M_xO_y/SiO_2/CHA-Na depending on time. The numbers after the samples were the duplicate experiments.*

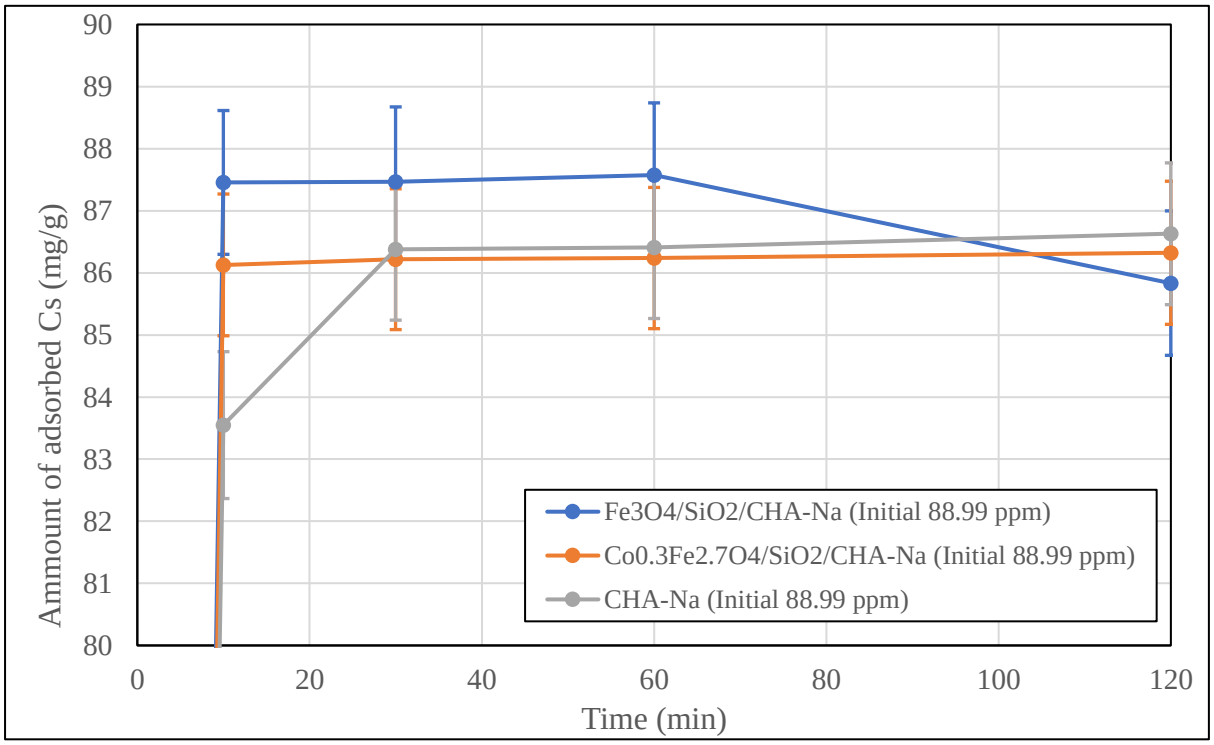

Figure 6.54 *Cs adsorption of the M_xO_y/SiO_2/CHA-Na depending on time (Greater data of Figure 6.53). The numbers after the samples were the duplicate experiments.*

The pH changes from the initial solutions of the products are shown in Table 6.15. Most of the final pH values had decreased from their initial values, with the exception of the CHA-Na after starting 10, 120 and 1440 min. The reason might be the adsorption experimental solution batches had less cation: Most cation was adsorbed onto the samples or formed acid form such as $NaNO_3$.

Table 6.15 *Initial to final pH of Sr exchange solution for the Cs adsorption depending on time.*

Time	CHA-Na		Fe_3O_4/SiO_2/CHA-Na		$Co_{0.3}Fe_{2.7}O_4/SiO_2$/CHA-Na	
0	7.33*					
10	7.45	(±0.64)	6.42	(±0.08)	5.80	(±0.10)
30	6.71	(±0.03)	6.55	(±0.25)	6.09	(±0.17)
60	6.93	(±0.23)	6.51	(±0.62)	6.38	(±0.09)
120	8.20	(±0.45)	7.22	(±0.21)	6.81	(±0.03)
1440	7.58	(±0.16)	7.09	(±0.16)	6.71	(±0.15)

**The measurement was used only the auto-hold mode that the pH values were measured when they moved within ± 3 digit for 10 sec.*

6.3.3.3.3 pH-dependent Cs adsorption

The products and the bare CHA-Na had their highest Cs adsorption capacities at pH 4.04. The Fe_3O_4/SiO_2/CHA-Na had the lowest adsorption capacity at pH 10.03. The $Co_{0.3}Fe_{2.7}O_4/SiO_2$/CHA-Na and the bare CHA-Na had the lowest Cs adsorption capacities at pH 6.89, and the capacities recovered slightly at pH 10.03. These results were very similar to those for the M_xO_y/CHA-Na.

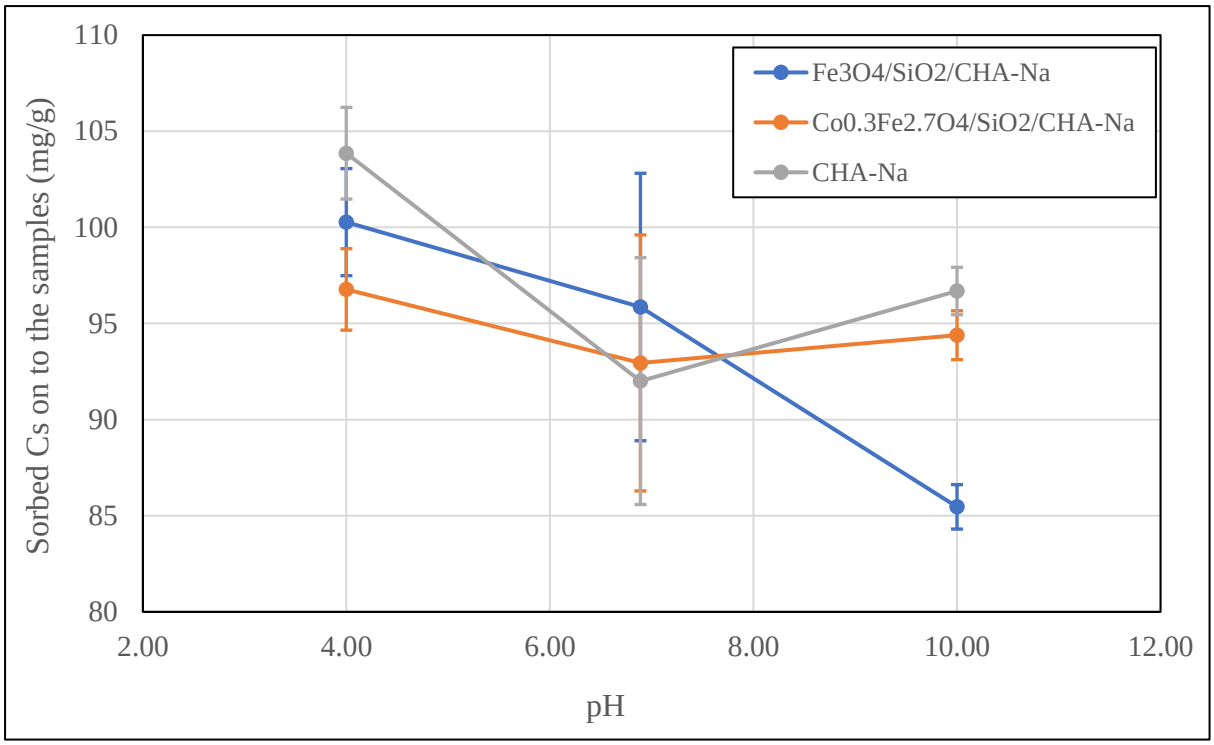

Figure 6.55 *Cs adsorption onto M_xO_y/SiO_2/CHA-Na depending on different initial pH. The numbers after the samples were the duplicate experiments.*

Table 6.16 *Initial Cs concentration of $CsNO_3$ on different pH.*

pH	Cs (ppm)	
4.04	107.06	(±2.10)
6.89	98.88	(±6.72)
10.03	96.30	(±1.16)

The initial and final pH of the solutions stabilised by HEPES and CAPS are shown in Table 6.17. The final pH values did not move much from the initial pH; they only moved within 0.5 units.

Table 6.17 *Initial and final pH of M_xO_y/SiO_2/CHA-Na depending on different initial pH.*

Initial pH	Fe_3O_4/SiO_2/CHA-Na	$Co_{0.3}Fe_{2.7}O_4/SiO_2$/CHA-Na	CHA-Na
4.04*	4.17 (±0.02)	4.28 (±0.11)	4.28 (±0.04)
6.89*	6.94 (±0.04)	6.92 (±0.09)	6.97 (±0.01)
10.03*	9.99 (±0.01)	9.95 (±0.01)	10.01 (±0.05)

**The measurement was used only the auto-hold mode that the pH values were measured when they moved within ± 3 digit for 10 sec.*

6.4 Conclusion

Three types of MSZ were synthesized from M_xO_y/SiO_2: M_xO_y/SiO_2/zeolite A, M_xO_y/SiO_2/zeolite X and M_xO_y/SiO_2/CHA-Na. Phase ID was confirmed by XRD and Raman spectroscopy, they were slightly different from the bare zeolite with broader XRD peaks and slightly shifted Raman peak positions. However, the maximum magnetisations of the products were a few emu/g higher than M_xO_y/CHA-Na at 50 kOe, especially the $Co_{0.3}Fe_{2.7}O_4/SiO_2$/CHA-Na that was 18.4 emu/g higher than for the $Co_{1.1}Fe_{1.9}O_4$/CHA-Na.

From the elemental composition results of the M_xO_y/SiO_2/zeolite A and M_xO_y/SiO_2/zeolite X, the SiO_2 of the SiO_2/M_xO_y might be used for the zeolite synthesis, and the SiO_2 layer of the particles might become thinner after using the zeolite synthesis, however, it could be expected the SiO_2/M_xO_y particles were well supported in the zeolite frameworks by making bonds with the zeolite framework elements.

The M_xO_y particle aggregations in the MSZ was resolved by crystallising in the rotation oven, and it was confirmed by the SEM images of M_xO_y/SiO_2/CHA-Na.

The blocking temperature of the ZFC/FC curves of the $Co_{0.3}Fe_{2.7}O_4/SiO_2$/zeolite A was 283.79 K that was lower than ambient temperature (293.15 K), and it means the particles were not superparamagnetic at ambient temperature. However, if the particles are used less than the blocking temperature, they can work as superparamagnetic: they do not aggregate after they are attracted by an external magnetic field.

The Sr adsorption capacities of the M_xO_y/SiO_2/zeolite A and M_xO_y/SiO_2/zeolite X were over 25 mg/g less than bare zeolite A and zeolite X. The Cs adsorption capacity of M_xO_y/SiO_2/CHA-Na was also less by about 13 mg/g than the bare CHA-Na.

The rate of Cs adsorption onto the M_xO_y/SiO_2/CHA-Na was 30 min quicker than onto the M_xO_y/CHA-Na, and the rate of Sr adsorption onto the M_xO_y/SiO_2/zeolite X was 30 min quicker than onto the M_xO_y/SiO_2/zeolite A. The reason is expected there was more Cs adsorption sites on the particle surfaces of the M_xO_y/SiO_2/CHA-Na than the M_xO_y/CHA-Na, and it might be due to the M_xO_y/SiO_2 incorporation while the CHA-Na synthesis. The Sr adsorption speed on to the M_xO_y/SiO_2/zeolite A was 90 to 110 min slower than the bare zeolite A, but if the M_xO_y/SiO_2/zeolite particles are used in a larger batch such as the adsorption towers at F1 site, it can be thought the adsorption speed differences do not much affect to the adsorption efficiency. Because the contaminated water is normally filtered few times, therefore it does not need to be removed by the adsorbents once.

The pH dependence of the Cs and Sr adsorption capacities revealed there was a few mg/g capacity differences between Fe_3O_4 and $Co_{0.3}Fe_{2.7}O_4$ in the zeolite. The Cs capacities onto the Fe_3O_4/SiO_2/CHA-Na at pH 10 were about 10 mg/g lower than the $Co_{0.3}Fe_{2.7}O_4/SiO_2$/CHA-Na and the bare CHA-Na.

7 Conclusion

Two types of magnetic zeolite were studied for their ability to remove Cs and Sr from radioactive contaminated water: these are MSZ and MZ. The MZ (M_xO_y/zeolite) was synthesised through a simple one-pot synthesis using the autoclave. Fe_3O_4 and $Co_{1.1}Fe_{1.9}O_4$ were used as the M_xO_y of the M_xO_y/zeolite, and CHA-Na was used as the zeolite. The MSZ was synthesised in three steps as M_xO_y, then M_xO_y/SiO_2 and finally M_xO_y/SiO_2/zeolite. The M_xO_y/SiO_2/zeolite consisted of Fe_3O_4 or Fe-rich $Co_{0.3}Fe_{2.7}O_4$. The M_xO_y particles were then coated by a thin layer of SiO_2 (the layer thickness was less than 2 nm) to protect the M_xO_y using the Stöber method. Finally, the M_xO_y/SiO_2 was coated with zeolite seeds that were either zeolite A, zeolite X or CHA-Na. The products were characterised by XRD, Raman spectroscopy, SEM-EDS and TEM-EDS and XRF to confirm and reveal the crystal morphologies and elemental compositions. MPMS and VSM were used to obtain the magnetic properties, and ICP-MS was used to measure the Sr or Cs adsorption capacities onto the synthesised MZ and MSZ. The M_xO_y particle size was measured using the DLS method by dispersing the samples in several types of solutions. The mixture of ethanol, DCM and 1-hexanol worked well to disperse and stabilise the Fe_3O_4 particles. However, both already dried Fe_3O_4 and the $Co_{0.3}Fe_{2.7}O_4$ aggregated and formed sedimentations even in this mixture.

The conditions for the synthesis of the Fe_3O_4 used for the MZ and the MSZ were also studied to produce suitable nanosized Fe_3O_4 particles for further use. The synthesis pressure in the autoclave was theoretically determined from the synthesis temperature and duration, and the various synthesis conditions were compared. The best synthesis conditions were used for the $Co_{0.3}Fe_{2.7}O_4$ synthesis.

The synthesised MZ and MSZ had some differences. The CHA-Na crystal of M_xO_y/CHA-Na was less affected by the M_xO_y particles than the M_xO_y/SiO_2/zeolite. They affected the Cs or Sr adsorption sites: M_xO_y/SiO_2/zeolite adsorbed less Cs or Sr than M_xO_y/CHA-Na. The M_xO_y particles were incorporated in the CHA-Na evenly, and the CHA-Na shapes seemed not to be affected by the incorporation. However, M_xO_y/SiO_2/zeolite A and M_xO_y/SiO_2/zeolite X had aggregated M_xO_y particles in the zeolite, and they changed the zeolite shapes. These were crystallised using the conventional oven. On the other hand, M_xO_y/CHA-Na was synthesised using the rotation oven to avoid aggregation. Therefore, the M_xO_y/SiO_2/zeolite used for the Sr and Cs adsorption experiments were also synthesised using the rotation oven. This seemed to resolve the M_xO_y aggregation problem, as confirmed by the SEM-EDS images of the M_xO_y/SiO_2/CHA-Na. However, the problem may be due to whether the coprecipitation method was used in the synthesis. Furthermore, the synthesis method used for the M_xO_y/SiO_2 might also have an effect: the sonication could control the water bath temperature and the sonication frequency limitedly.

The amount of M_xO_y particles incorporated in the zeolite also differed between the MZ and the MSZ: the Co and/or Fe compositions and the maximum magnetisations revealed that the M_xO_y/SiO_2/zeolite had over twice as many M_xO_y particles than the M_xO_y/CHA-Na. Therefore, the maximum magnetisations of the M_xO_y/SiO_2/zeolite were also over twice as high as the M_xO_y/CHA-Na. However, both the MZ and the MSZ were superparamagnetic at ambient temperatures.

The Cs adsorption capacities of M_xO_y/CHA-Na were similar to those of the bare CHA-Na, and they were higher than for the M_xO_y/SiO_2/CHA-Na. The adsorption capacity difference was due to the amount of M_xO_y particles. The amounts of Co and/or Fe in both M_xO_y/SiO_2/zeolite A and M_xO_y/SiO_2/zeolite X were lower than in the M_xO_y/SiO_2/CHA-Na. However, the Sr adsorption capacities were lower than those of the bare zeolite A and zeolite X.

Time -dependent Cs and Sr adsorption onto the MZ and the MSZ revealed the speed of the adsorptions. The Cs adsorption onto the M_xO_y/SiO_2/CHA-Na was 30 min quicker than onto the M_xO_y/CHA-Na, and the Sr adsorption onto the M_xO_y/SiO_2/zeolite X was 30 min quicker than for the M_xO_y/SiO_2/zeolite A.

The adsorption speeds seemed to be affected by the amount of M_xO_y and the SiO_2 coating in the zeolite: the morphology had changed, or the Cs and Sr adsorption sites of the zeolite were distorted or clogged by the M_xO_y. However, it could be supposed the speed

differences from the bare zeolite do not affect to a larger batch such as the adsorption towers at F1 site, because the filtration system normally filters the contaminated water few times. That means most radioactive Cs or Sr do no need to be removed by the filtration process once.

The pH-dependent Cs and Sr adsorption capacities onto the MZ and the MSZ revealed the optimal adsorption pH. However, the adsorption capacities onto them depending on pH were slightly different depending on Fe_3O_4 or cobalt ferrite (just a few mg/g difference). The optimal adsorption pH could be useful for further studies into the ability of MZ and MSZ to adsorb and desorb the elements efficiently to allow their reuse.

These characteristic results regarding MZ and MSZ show that both of them can be improved to optimise their magnetic properties and Cs and Sr adsorption capacities. In particular, the morphology of the products should be studied further to determine the most appropriate heating methods and the optimum amount of M_xO_y to incorporate, for example. The reusability of the products was not evaluated in this study. Therefore, this should also be studied in the future by adsorbing and desorbing the elements a few times.

For future work, the abilities of MZ and the MSZ to adsorb more radioactive Cs and Sr and be reused many times in contaminated water from nuclear reactors should be studied. Then if there is enough time, efficient disposal of the used MZ and MSZ to minimise the amount of radioactive waste should be considered. Because there has been no place to dispose the used zeolite in from the adsorption towers such as KURION and ALPS, and the

volume of the waste has been increased. New types of adsorbents or technics for the decontamination has been sought to reduce the wastes. If a new adsorbent such as the MZ or MSZ can be used instead the normal zeolite in the adsorption towers, they can reuse by the cation adsorption and desorption processes, and the only collected radioactive cations can be concentrated and disposed. However, the MZ and MSZ are not tested how strong durability they have, and how they will affect to packaging materials such as concrete or grass when they packed after using. Therefore, if they are applicable for the F1 site decontaminating, the materials are still needed to study more including after using the decontamination process.

8 References

1. Kataoka, I., *Review of thermal-hydraulic researches in severe accidents in light water reactors.* Journal of Nuclear Science and Technology, 2013. **50**(1): p. 1-14.
2. Council, N.R., *Lessons Learned from the Fukushima Nuclear Accident for Improving Safety of U.S. Nuclear Plants*. 2014, Washington, DC: The National Academies Press. 394.
3. Radiation, U.N.S.C.o.t.E.o.A., *Sources, Effects and Risks of Ionizing Radiation, United Nations Scientific Committee on the Effects of Atomic Radiation (UNSCEAR) 2016 Report: Report to the General Assembly, with Scientific Annexes*. 2017: United Nations.
4. Cui, L., et al., *Environmental Remediation of the difficult-to-return zone in Tomioka Town, Fukushima Prefecture.* Scientific Reports, 2020. **10**(1): p. 10165.
5. Lehto, J., et al., *Removal of Radionuclides from Fukushima Daiichi Waste Effluents.* Separation & Purification Reviews, 2019. **48**(2): p. 122-142.
6. Ochiai, E., *Hiroshima to Fukushima Biohazards of radiation*. 2014, Germany: Springer.
7. Company, T.E.P., *TEPCO Draft Study Responding to the Subcommittee Report on Handling ALPS Treated Water*. 2020, Tokyo Electric Power Company.
8. Tsukada, T., et al., *Early construction and operation of highly contaminated water treatment system in Fukushima Daiichi Nuclear Power Station (I) – Ion exchange properties of KURION herschelite in simulating contaminated water.* Journal of Nuclear Science and Technology, 2014. **51**(7-8): p. 886-893.
9. Semmler, J., et al., *Assessment of decontamination, decommissioning, and remediation methodologies at Fukushima*. 2014: Canada. p. 15.
10. Adhemar, B., *Lessons Learned: AREVA's Experience in JAPAN March to July 2011*. 2013: International Atomic Energy Agency (IAEA). p. 23.
11. Toshiba. *Toshiba's Simplified Active Water Retrieve and Recovery System II Now Removing Cesium and Strontium from Contaminated Water at Fukushima Daiichi*. 2019; Available from: https://www.toshiba-energy.com/en/info/info2019_0712.htm.
12. Company, T.E.P., *Status of Contaminated Water Treatment and Tritium at Fukushima Daiichi Nuclear Power Station*. 2014, Tokyo Electric Power Company.
13. Tusa, E. *Efficiency of Fortum's CsTreatR and SrTreatR in cesium and strontium removal in Fukushima Daiichi NPP*. in *Proceedings of the European Nuclear Conference - ENC 2014*. 2014. European Commission (EC).
14. Smart, L.E., *Solid State Chemistry: An Introduction, Fourth Edition*. 2017: Taylor & Francis Group.

15. Auerbach, S.M., K.A. Carrado, and P.K. Dutta, *Handbook of zeolite science and technology*. 2003: CRC press.
16. Townsend, R.P. and E.N. Coker, *Chapter 11 Ion exchange in zeolites.* Studies in Surface Science and Catalysis, 2001. **137**: p. 467-524.
17. Faghihian, H., et al., *Evaluation of a new magnetic zeolite composite for removal of Cs^+ and Sr^{2+} from aqueous solutions: Kinetic, equilibrium and thermodynamic studies.* Comptes Rendus Chimie, 2014. **17**(2): p. 108-117.
18. Munthali, M.W., et al., *Proton Adsorption Selectivity of Zeolites in Aqueous Media: Effect of Si/Al Ratio of Zeolites.* Molecules, 2014. **19**(12): p. 20468-20481.
19. Coombs, D.S., et al., *Recommended nomenclature for zeolite minerals: report of the subcommittee on zeolites of the International Mineralogical Association, Commission on new Minerals and Mineral names.* Canadian Mineralogist, 1997. **35**(6): p. 1571-1606.
20. Alberti, A., et al., *Position of cations and water molecules in hydrated chabazite. Natural and Na-, Ca-, Sr- and K-exchanged chabazites.* Zeolites, 1982. **2**(4): p. 303-309.
21. Association, I.Z. *Chabazite Series*. [Website] 2017; Available from: http://www.iza-online.org/natural/Datasheets/Chabazite/chabazite.htm.
22. Vener, M.V., X. Rozanska, and J. Sauer, *Protonation of water clusters in the cavities of acidic zeolites: $(H_2O)n{\cdot}H$-chabazite, n = 1–4.* Physical Chemistry Chemical Physics, 2009. **11**(11): p. 1702-1712.
23. Baek, W., et al., *Cation exchange of cesium and cation selectivity of natural zeolites:*
Chabazite, stilbite, and heulandite. Microporous and Mesoporous Materials, 2018. **264**: p. 159-166.
24. Khan, G., et al., *Linde Type-A zeolite synthesis and effect of crystallization on its surface acidity.* 2010.
25. Mimura, H. and T. Kanno, *Distribution and Fixation of Cesium and Strontium in Zeolite A and Chabazite.* Journal of Nuclear Science and Technology, 1985. **22**(4): p. 284-291.
26. Abd El-Rahman, K.M., et al., *Thermodynamic modeling for the removal of Cs^+, Sr^{2+}, Ca^{2+} and Mg^{2+} ions from aqueous waste solutions using zeolite A*. Vol. 268. 2006. 221-230.
27. Nakano, T. and Y. Nozue, *Orbital degeneracy and magnetic properties of potassium clusters incorporated into nanoporous crystals of zeolite A*. Vol. 7. 2007. 443-462.
28. Kim, H.S., D.Y. Chung, and W.T. Lim, *Single-Crystal Structures of Sr^{2+} and Cs^+-Exchanged Zeolites X and Y, $|Sr_{40}Cs_{12}|[Si_{100}Al_{92}O_{384}]$-FAU and $|Sr_{29}Cs_{17}|[Si_{117}Al_{75}O_{384}]$-FAU*. Journal of Chemical Crystallography, 2014. **44**(5): p. 269-278.
29. Oliveira, L.C.A., et al., *Magnetic zeolites: a new adsorbent for removal of metallic contaminants from water.* Water Research, 2004. **38**(17): p. 3699-3704.
30. Baile, P., L. Vidal, and A. Canals, *A modified zeolite/iron oxide composite as a sorbent for magnetic dispersive solid-phase extraction for the preconcentration of nonsteroidal*

anti-inflammatory drugs in water and urine samples. Journal of Chromatography A, 2019. **1603**: p. 33-43.

31. Baile, P., L. Vidal, and A. Canals, *Magnetic dispersive solid-phase extraction using ZSM-5 zeolite/Fe_2O_3 composite coupled with screen-printed electrodes based electrochemical detector for determination of cadmium in urine samples.* Talanta, 2020. **220**: p. 121394.
32. Majid, Z., A.A. AbdulRazak, and W.A.H. Noori, *Modification of Zeolite by Magnetic Nanoparticles for Organic Dye Removal.* Arabian Journal for Science and Engineering, 2019. **44**(6): p. 5457-5474.
33. Sajjadi, S.P., *Sol-gel process and its application in Nanotechnology.* Journal of Polymer Engineering and Technology, 2005. **13**: p. 38-41.
34. Parashar, M., V.K. Shukla, and R. Singh, *Metal oxides nanoparticles via sol–gel method: a review on synthesis, characterization and applications.* Journal of Materials Science: Materials in Electronics, 2020. **31**(5): p. 3729-3749.
35. Niederberger, M., *Nonaqueous Sol–Gel Routes to Metal Oxide Nanoparticles.* Accounts of Chemical Research, 2007. **40**(9): p. 793-800.
36. Pinna, N. and M. Niederberger, *Surfactant-Free Nonaqueous Synthesis of Metal Oxide Nanostructures.* Angewandte Chemie International Edition, 2008. **47**(29): p. 5292-5304.
37. Niederberger, M. and N. Pinna, *Solvent-Controlled Synthesis*, in *Metal Oxide Nanoparticles in Organic Solvents: Synthesis, Formation, Assembly and Application*, M. Niederberger and N. Pinna, Editors. 2009, Springer London: London. p. 53-95.
38. Stöber, W., A. Fink, and E. Bohn, *Controlled growth of monodisperse silica spheres in the micron size range.* Journal of Colloid and Interface Science, 1968. **26**(1): p. 62-69.
39. Mine, E., et al., *Direct coating of gold nanoparticles with silica by a seeded polymerization technique.* Journal of Colloid and Interface Science, 2003. **264**(2): p. 385-390.
40. Dang, F., et al., *Sonochemical coating of magnetite nanoparticles with silica.* Ultrasonics Sonochemistry, 2010. **17**(1): p. 193-199.
41. Im, S.H., et al., *Synthesis and characterization of monodisperse silica colloids loaded with superparamagnetic iron oxide nanoparticles.* Chemical Physics Letters, 2005. **401**(1): p. 19-23.
42. Lu, Y., et al., *Modifying the Surface Properties of Superparamagnetic Iron Oxide Nanoparticles through A Sol−Gel Approach.* Nano Letters, 2002. **2**(3): p. 183-186.
43. Waseda, Y., E. Matsubara, and K. Shinoda, *X-Ray Diffraction Crystallography : Introduction, Examples and Solved Problems.* 2011.
44. Chipera, S. and D. Bish, *Fitting Full X-Ray Diffraction Patterns for Quantitative Analysis: A Method for Readily Quantifying Crystalline and Disordered Phases.* Advances in Materials Physics and Chemistry, 2013. **3**: p. 47-53.

45. Azzaza, S., S. Alleg, and J.-J. Suňol, *Microstructure characterization and thermal stability of the ball milled iron powders.* Journal of Thermal Analysis and Calorimetry, 2015. **119**(2): p. 1037-1046.
46. Wilson, J., J. Cuadros, and G. Cressey, *An In situ Time-Resolved XRD-PSD Investigation into Na-Montmorillonite Interlayer and Particle Rearrangement during Dehydration.* Clays and Clay Minerals, 2004. **52**(2): p. 180-191.
47. Zhigachev, A.O., *The effect of specimen surface curvature on x-ray diffraction peak profiles.* Review of Scientific Instruments, 2013. **84**(9): p. 095105.
48. Potts, P.J. and P.C. Webb, *X-ray fluorescence spectrometry.* Journal of Geochemical Exploration, 1992. **44**(1): p. 251-296.
49. Viter, R. and I. Iatsunskyi, *Optical Spectroscopy for Characterization of Metal Oxide Nanofibers*, in *Handbook of Nanofibers*, A. Barhoum, M. Bechelany, and A.S.H. Makhlouf, Editors. 2019, Springer International Publishing: Cham. p. 523-556.
50. Smith, E. and G. Dent, *Modern Raman Spectroscopy: A Practical Approach*. 2005.
51. Larkin, P., *Infrared and Raman Spectroscopy; Principles and Spectral Interpretation*. 2011.
52. Panalytical, M. *Dynamic light scattering: an introduction in 30 minutes*. 2020; Available from: https://www.malvernpanalytical.com/en/learn/knowledge-center/technical-notes/TN101104DynamicLightScatteringIntroduction.
53. Ltd., M.I., *Zetasizer nano user manual*. 2013, Malvern Instruments Ltd.: Worcestershire.
54. Bhattacharjee, S., *DLS and zeta potential – What they are and what they are not?* Journal of Controlled Release, 2016. **235**: p. 337-351.
55. Riddick, T.M., *Control of colloid stability through zeta potential*. 1968, Wynnewood, Pa.: Livingston.
56. Altshuler, E. and R. García, *Josephson junctions in a magnetic field: Insights from coupled pendula.* American Journal of Physics, 2003. **71**(4): p. 405-408.
57. Seidel, P., *Applied Superconductivity : Handbook on Devices and Applications*. 2015, Weinheim, GERMANY: John Wiley & Sons, Incorporated.
58. Clarke, J., *The SQUID handbook Vol 1 Fundamentals and technology of SQUIDs and SQUID systems*. 2004, Germany: Wiley VCH.
59. Ul-Hamid, A., *Components of the SEM*, in *A Beginners' Guide to Scanning Electron Microscopy*, A. Ul-Hamid, Editor. 2018, Springer International Publishing: Cham. p. 15-76.
60. Science, T.F. *Transmission Electron Microscopy vs Scanning Electron Microscopy: Electron microscopy reference focusing on the difference between transmission electron microscopy (TEM) and scanning electron microscopy (SEM)*. Available from: https://www.thermofisher.com/uk/en/home/materials-science/learning-center/applications/sem-tem-difference.html.

61. McLaren, A.C., *Transmission Electron Microscopy of Minerals and Rocks*. 2 ed. Cambridge Topics in Mineral Physics and Chemistry. 1991, Cambridge: Cambridge University Press.
62. Charles, B. and K.J. Fredeen, *Concepts, instrumentation and techniques in inductively coupled plasma optical emission spectrometry.* Perkin Elmer Corporation, 1997. **3**: p. 2.
63. Thomas, R., *Practical Guide to ICP-MS : A Tutorial for Beginners*. 2013, Baton Rouge, UNITED STATES: CRC Press LLC.
64. Wilschefski, S.C. and M.R. Baxter, *Inductively Coupled Plasma Mass Spectrometry: Introduction to Analytical Aspects.* The Clinical biochemist. Reviews, 2019. **40**(3): p. 115-133.
65. Chiou, C.T., *Partition and adsorption of organic contaminants in environmental systems*. 2003: John Wiley & Sons.
66. Swenson, H. and N.P. Stadie, *Langmuir's Theory of Adsorption: A Centennial Review.* Langmuir, 2019. **35**(16): p. 5409-5426.
67. Skopp, J., *Derivation of the Freundlich Adsorption Isotherm from Kinetics.* Journal of Chemical Education, 2009. **86**(11): p. 1341.
68. Cornell, R.M. and U. Schwertmann, *The Iron Oxides: Structure, Properties, Reactions, Occurrences and Uses*. 2006: Wiley.
69. Mahmoudi, M., et al., *Superparamagnetic Iron Oxide Nanoparticles: Synthesis, Surface Engineering, Cytotoxicity and Biomedical Applications*. 2010, Hauppauge, UNITED STATES: Nova Science Publishers, Incorporated.
70. Tapeinos, C., *Magnetic Nanoparticles and Their Bioapplications*, in *Smart Nanoparticles for Biomedicine*, G. Ciofani, Editor. 2018, Elsevier. p. 131-142.
71. Lu, Y., J. Yu, and S. Cheng, *Magnetic composite of Fe_3O_4 and activated carbon as a adsorbent for separation of trace Sr(II) from radioactive wastewater.* Journal of Radioanalytical and Nuclear Chemistry, 2015. **303**(3): p. 2371-2377.
72. Pinna, N., et al., *Magnetite Nanocrystals: Nonaqueous Synthesis, Characterization, and Solubility.* Chemistry of Materials, 2005. **17**(11): p. 3044-3049.
73. Chicea, D., E. Indrea, and C. Cretu, *Assesing Fe_3O_4 nanoparticle size by DLS, XRD and AFM.* Journal of optoelectronics and advanced materials, 2012. **14**(5): p. 460.
74. Bui, T.Q., et al., *Size-dependent magnetic responsiveness of magnetite nanoparticles synthesised by co-precipitation and solvothermal methods.* Journal of Science: Advanced Materials and Devices, 2018. **3**(1): p. 107-112.
75. Ayyappan, S., J. Philip, and B. Raj, *A facile method to control the size and magnetic properties of $CoFe_2O_4$ nanoparticles.* Materials Chemistry and Physics, 2009. **115**(2): p. 712-717.

76. Hou, Y.H., et al., *Structural, electronic and magnetic properties of partially inverse spinel $CoFe_2O_4$: a first-principles study.* Journal of Physics D: Applied Physics, 2010. **43**(44): p. 445003.
77. Zhao, F., et al., *Synthesis of $CoFe_2O_4$–Zeolite Materials and Application to the Adsorption of Gallium and Indium.* Journal of Chemical & Engineering Data, 2015. **60**(5): p. 1338-1344.
78. Huang, Y., et al., *Preparation of magnetic clinoptilolite/$CoFe_2O_4$ composites for removal of Sr^{2+} from aqueous solutions: Kinetic, equilibrium, and thermodynamic studies.* Journal of Saudi Chemical Society, 2017. **21**(1): p. 58-66.
79. Mathew, D.S. and R.-S. Juang, *An overview of the structure and magnetism of spinel ferrite nanoparticles and their synthesis in microemulsions.* Chemical Engineering Journal, 2007. **129**(1): p. 51-65.
80. Anjum, S., et al., *Tuning of Magnetic and Optical Properties of $Co_{0.8}Zn_{0.2}Fe_2O_4$ Spinel Ferrite Thin Films Based on Post Annealing Temperature.* Journal of Superconductivity and Novel Magnetism, 2018. **31**(12): p. 4095-4106.
81. Wulfsberg, G., *Inorganic Chemistry*. 2000: University Science Books.
82. Kominami, H., et al., *Synthesis of Microcrystalline Hematite and Magnetite in Organic Solvents and Effect of a Small Amount of Water in the Solvents.* Journal of the American Ceramic Society, 1999. **82**(7): p. 1937-1940.
83. Lazor, P., O.N. Shebanova, and H. Annersten, *High-pressure study of stability of magnetite by thermodynamic analysis and synchrotron X-ray diffraction.* Journal of Geophysical Research: Solid Earth, 2004. **109**(B5).
84. Yaws, C.L., *The Yaws handbook of vapor pressure: Antoine coefficients*. 2015: reffered 2015)Gulf Professional Publishing.
85. Masubuchi, Y., et al., *Magnetite/maghemite mixture prepared in benzyl alcohol for the preparation of α"-$Fe_{16}N_2$ with α-Fe.* Journal of the European Ceramic Society, 2011. **31**(14): p. 2471-2474.
86. Rabenau, A., *The Role of Hydrothermal Synthesis in Preparative Chemistry.* Angewandte Chemie International Edition in English, 1985. **24**(12): p. 1026-1040.
87. Ferreira, T.A.S., et al., *Structural and morphological characterization of $FeCo_2O_4$ and $CoFe_2O_4$ spinels prepared by a coprecipitation method.* Solid State Sciences, 2003. **5**(2): p. 383-392.
88. Rafique, M.Y., et al., *Influence of $NaBH_4$ on the size, composition, and magnetic properties of $CoFe_2O_4$ nanoparticles synthesized by hydrothermal method.* Journal of Nanoparticle Research, 2012. **14**(10): p. 1189.
89. Coduri, M., et al., *Local Structure and Magnetism of Fe_2O_3 Maghemite Nanocrystals: The Role of Crystal Dimension.* Nanomaterials (Basel, Switzerland), 2020. **10**(5): p. 867.

90. Kolen'ko, Y.V., et al., *Large-Scale Synthesis of Colloidal Fe_3O_4 Nanoparticles Exhibiting High Heating Efficiency in Magnetic Hyperthermia.* The Journal of Physical Chemistry C, 2014. **118**(16): p. 8691-8701.
91. Chandramohan, P., et al., *Cation distribution and particle size effect on Raman spectrum of $CoFe_2O_4$.* Journal of Solid State Chemistry, 2011. **184**(1): p. 89-96.
92. Lu, X., et al., *Superdispersible PVP-Coated Fe_3O_4 Nanocrystals Prepared by a "One-Pot" Reaction.* The Journal of Physical Chemistry B, 2008. **112**(46): p. 14390-14394.
93. Chung, Y.-C. and J.-Y. Huang, *Water-borne composite coatings using nanoparticles modified with dopamine derivatives.* Thin Solid Films, 2014. **570**: p. 376-382.
94. Guerrini, L., R.A. Alvarez-Puebla, and N. Pazos-Perez, *Surface Modifications of Nanoparticles for Stability in Biological Fluids.* Materials (Basel), 2018. **11**(7).
95. Li, X.-H., et al., *Synthesis and Magnetic Properties of Nearly Monodisperse $CoFe_2O_4$ Nanoparticles Through a Simple Hydrothermal Condition.* Nanoscale research letters, 2010. **5**(6): p. 1039-1044.
96. Shen, L., B. Li, and Y. Qiao, *Fe_3O_4 Nanoparticles in Targeted Drug/Gene Delivery Systems.* Materials (Basel, Switzerland), 2018. **11**(2): p. 324.
97. Ye, H.-J., W.-Z. Shao, and L. Zhen, *Tetradecylphosphonic acid modified $BaTiO_3$ nanoparticles and its nanocomposite.* Colloids and Surfaces A: Physicochemical and Engineering Aspects, 2013. **427**: p. 19-25.
98. Lowry, G.V., et al., *Guidance to improve the scientific value of zeta-potential measurements in nanoEHS.* Environmental Science: Nano, 2016. **3**(5): p. 953-965.
99. Cardoso, B.D., et al., *Magnetoliposomes containing magnesium ferrite nanoparticles as nanocarriers for the model drug curcumin.* Royal Society open science, 2018. **5**(10): p. 181017-181017.
100. Chitu, L., et al., *Structure and magnetic properties of $CoFe_2O_4$ and Fe_3O_4 nanoparticles.* Materials Science and Engineering: C, 2007. **27**(5): p. 1415-1417.
101. Tomitaka, A., et al., *Evaluation of magnetic and thermal properties of ferrite nanoparticles for biomedical applications*. 2011.
102. Zhao, S., et al., *Synthesis of Magnetic Nanoparticles of Fe_3O_4 and $CoFe_2O_4$ and Their Surface Modification by Surfactant Adsorption.* Bulletin of the Korean Chemical Society, 2006. **27**.
103. Lien, Y.-H. and T.-M. Wu, *Preparation and characterization of thermosensitive polymers grafted onto silica-coated iron oxide nanoparticles.* Journal of Colloid and Interface Science, 2008. **326**(2): p. 517-521.
104. Khosroshahi, M.E. and L. Ghazanfari, *Amino surface modification of Fe_3O_4/SiO_2 nanoparticles for bioengineering applications.* Surface Engineering, 2011. **27**(8): p. 508-573.

105. Aghazadeh, B. and M. Nikpassand, *"2-Amino glucose" as a substrate for synthesis of magnetically recoverable nanocatalyst $NiFe_2O_4$@SiO_2@amino glucose for the green synthesis of novel bis (1,2-dihydro-4-hydroxy-2-oxoquinolin-3-yl)methanes.* Carbohydrate Research, 2019. **483**: p. 107755.
106. Villa, S., et al., *Functionalization of Fe_3O_4 NPs by Silanization: Use of Amine (APTES) and Thiol (MPTMS) Silanes and Their Physical Characterization.* Materials, 2016. **9**(10): p. 826.
107. Bumb, A., et al., *Synthesis and characterization of ultra-small superparamagnetic iron oxide nanoparticles thinly coated with silica.* Nanotechnology, 2008. **19**(33): p. 335601-335601.
108. Cannas, C., et al., *CoFe2O4 and CoFe2O4/SiO2 Core/Shell Nanoparticles: Magnetic and Spectroscopic Study.* Chemistry of Materials, 2010. **22**(11): p. 3353-3361.
109. Stjerndahl, M., et al., *Superparamagnetic Fe_3O_4/SiO_2 Nanocomposites: Enabling the Tuning of Both the Iron Oxide Load and the Size of the Nanoparticles.* Langmuir, 2008. **24**(7): p. 3532-3536.
110. Wei, X., et al., *Polymorphous transformation of rod-shaped iron oxides and their catalytic properties in selective reduction of NO by NH_3.* RSC Advances, 2015. **5**(81): p. 66141-66146.
111. Fernández, E., L. Vidal, and A. Canals, *Zeolite/iron oxide composite as sorbent for magnetic solid-phase extraction of benzene, toluene, ethylbenzene and xylenes from water samples prior to gas chromatography-mass spectrometry.* Journal of Chromatography A, 2016. **1458**: p. 18-24.
112. Cao, J.-l., et al., *Magnetic P zeolites: Synthesis, characterization and the behavior in potassium extraction from seawater.* Separation and Purification Technology, 2008. **63**(1): p. 92-100.
113. Nyankson, E., et al., *Characterization and Evaluation of Zeolite A/Fe_3O_4 Nanocomposite as a Potential Adsorbent for Removal of Organic Molecules from Wastewater.* Journal of Chemistry, 2019. **2019**: p. 8090756.
114. Karmaoui, M. and J.A. Hriljac, *New magnetic zeolite nanocomposites for nuclear waste cleanup*. 2016, University of Birmingham: Birmingham.
115. Aono, H., et al., *Synthesis of chabazite and merlinoite for Cs^+ adsorption and immobilization properties by heat-treatment.* Solid State Sciences, 2020. **100**: p. 106094.
116. Abtahi, M., et al., *Removal of cesium through adsorption from aqueous solutions: A systematic review.* Journal of Advances in Environmental Health Research, 2018. **6**(2): p. 96-106.
117. Kesraoui-Ouki, S., C.R. Cheeseman, and R. Perry, *Natural zeolite utilisation in pollution control: A review of applications to metals' effluents.* Journal of Chemical Technology & Biotechnology, 1994. **59**(2): p. 121-126.

118. Velikyan, I., H. Maecke, and B. Langstrom, *Convenient Preparation of ^{68}Ga-Based PET-Radiopharmaceuticals at Room Temperature.* Bioconjugate Chemistry, 2008. **19**(2): p. 569-573.
119. B, L., et al., *The power of databases: the RRUFF project. In: Highlights in Mineralogical Crystallography*. 2015, Berlin, Germany: W. De Gruyter.
120. Crane, R. and D. Sapsford, *Tunable formation of copper metal, oxide, chloride and hydroxyl chloride nanoparticles from aqueous copper solutions using nanoscale zerovalent iron particles.* Nanomaterials and Nanotechnology, 2019. **9**: p. 1847980419886173.
121. Li, X., et al., *Galvanic corrosion of zero-valent iron to intensify Fe^{2+} generation for peroxymonosulfate activation.* Chemical Engineering Journal, 2021. **417**: p. 128023.
122. He, J., et al., *Graphene-doped carbon/Fe_3O_4 porous nanofibers with hierarchical band construction as high-performance anodes for lithium-ion batteries.* Electrochimica Acta, 2017. **229**: p. 306-315.
123. Nene, A., M. Takahashi, and P. Somani, *Fe_3O_4 and Fe Nanoparticles by Chemical Reduction of Fe(acac)$_3$ by Ascorbic Acid: Role of Water.* World Journal of Nano Science and Engineering, 2016. **6**: p. 20-28.
124. He, Y.T. and S.J. Traina, *Transformation of magnetite to goethite under alkaline pH conditions.* Clay Minerals, 2007. **42**(1): p. 13-19.
125. Tourinho, F.A., R. Franck, and R. Massart, *Aqueous ferrofluids based on manganese and cobalt ferrites.* Journal of Materials Science, 1990. **25**(7): p. 3249-3254.
126. Esposito, S., et al., *Magnetic metal-ceramic nanocomposites obtained from cation-exchanged zeolite by heat treatment in reducing atmosphere.* Microporous and Mesoporous Materials, 2018. **268**: p. 131-143.
127. Abasian, P., et al., *Incorporation of magnetic NaX zeolite/DOX into the PLA/chitosan nanofibers for sustained release of doxorubicin against carcinoma cells death in vitro.* International Journal of Biological Macromolecules, 2019. **121**: p. 398-406.
128. Robson, H., *How to read a patent.* Microporous and Mesoporous Materials, 1998. **22**(4): p. 551-662.
129. Peng, H., M. Ding, and J. Vaughan, *The Anion Effect on Zeolite Linde Type A to Sodalite Phase Transformation.* Industrial & Engineering Chemistry Research, 2018. **57**(31): p. 10292-10302.
130. Pambudi, T., E. Wahyuni, and M. Mudasir, *Recoverable Adsorbent of Natural Zeolite/Fe_3O_4 for Removal of Pb (II) in Water.* 2020.
131. Depla, A., et al., *Zeolites X and A crystallization compared by simultaneous UV/VIS-Raman and X-ray diffraction.* Physical Chemistry Chemical Physics, 2011. **13**(30): p. 13730-13737.

9 APPENDIX

Table 9.1 Elemental compositions of CHA-Na after Cs adsorptions depending on pH

	Formula	Concentration (wt%)		Amount of material (mmol)	Ratio
pH 4	Al	2.68	(±0.11)	0.99	1.00
	Si	9.33	(±0.06)	3.32	3.35
	Na	0.23	(±0.12)	0.10	0.10
	K	0.43	(±0.07)	0.11	0.11
	Cs	86.50	(±0.03)	6.51	6.56
pH 7	Al	3.06	(±0.08)	1.13	1.00
	Si	8.67	(±0.06)	3.09	2.72
	Na	0.97	(±0.17)	0.42	0.37
	K	0.88	(±0.13)	0.23	0.20
	Cs	86.00	(±0.03)	6.47	5.71
pH 10	Al	3.50	(±0.08)	1.30	1.00
	Si	11.55	(±0.05)	4.11	3.17
	Na	1.62	(±0.13)	0.70	0.54
	K	0.46	(±0.07)	0.12	0.09
	Cs	82.45	(±0.03)	6.20	4.78

Table 9.2 *Elemental compositions of Fe_3O_4/CHA-Na after Cs adsorptions depending on pH*

	Formula	Concentration (wt%)		Amount of material (mmol)	Ratio
pH 4	Al	0.98	(±0.09)	0.36	1.00
	Si	3.81	(±0.19)	1.36	3.75
	Na	0.06	(±0.02)	0.02	0.07
	K	0.00	(±0.00)	0.00	0.00
	Cs	40.55	(±1.32)	3.05	8.44
	Fe	54.50	(±0.33)	9.76	27.00
pH 7	Al	1.11	(±0.12)	0.41	1.00
	Si	4.40	(±0.26)	1.56	3.82
	Na	0.31	(±0.07)	0.13	0.33
	K	0.00	(±0.00)	0.00	0.00
	Cs	50.85	(±2.12)	3.83	9.34
	Fe	43.00	(±0.36)	7.70	18.80
pH 10	Al	1.28	(±0.13)	0.47	1.00
	Si	4.07	(±0.26)	1.45	3.07
	Na	0.80	(±0.12)	0.35	0.74
	K	0.00	(±0.00)	0.00	0.00
	Cs	35.15	(±1.58)	2.64	5.60
	Fe	58.45	(±0.45)	10.47	22.15

Table 9.3 Elemental compositions of $Co_{1.1}Fe_{1.9}O_4$/CHA-Na after Cs adsorptions depending on pH *(the ratio of Co and Fe are highlighted in yellow).*

	Formula	Concentration (wt%)		Atomic weight (g/mol)	Amount of material (mmol)	Ratio
pH 4	Al	0.96	(±0.08)	26.98	0.35	1.00
	Si	3.40	(±0.18)	28.09	1.21	3.41
	Na	0.07	(±0.02)	22.99	0.03	0.09
	K	0.00	(±0.00)	39.10	0.00	0.00
	Cs	36.90	(±1.29)	132.91	2.78	7.84
	Fe	43.70	(±0.29)	55.85	7.82	3.11
	Co	14.85	(±0.14)	58.93	2.52	1.00
pH 7	Al	1.07	(±0.10)	26.98	0.40	1.00
	Si	4.16	(±0.23)	28.09	1.48	3.73
	Na	0.00	(±0.00)	22.99	0.00	0.00
	K	0.00	(±0.00)	39.10	0.00	0.00
	Cs	37.35	(±1.56)	132.91	2.81	7.09
	Fe	41.35	(±0.33)	55.85	7.40	2.79
	Co	15.65	(±0.17)	58.93	2.66	1.00
pH 10	Al	1.32	(±0.14)	26.98	0.49	1.00
	Si	4.64	(±0.29)	28.09	1.65	3.39
	Na	0.36	(±0.09)	22.99	0.15	0.32
	K	0.34	(±0.06)	39.10	0.09	0.18
	Cs	47.80	(±2.19)	132.91	3.60	7.38
	Fe	33.05	(±0.34)	55.85	5.92	3.00
	Co	11.63	(±0.16)	58.93	1.97	1.00

Table 9.4 *Elemental compositions of zeolite A after Sr adsorptions depending on pH*

	Formula	Concentration (wt%)		Amount of material (mmol)	Ratio
pH 4	Al	38.20	(±2.62)	14.16	1.00
	Si	52.70	(±3.57)	18.76	1.33
	Na	7.35	(±1.29)	3.20	0.23
	Sr	0.00	(±0.00)	0.00	0.00
pH 10	Al	20.65	(±1.15)	7.65	1.00
	Si	31.95	(±1.62)	11.37	1.49
	Na	5.95	(±0.71)	2.59	0.34
	Sr	41.30	(±0.24)	4.71	0.62

Table 9.5 *Elemental compositions of Fe_3O_4/SiO_2/zeolite A after Sr adsorptions depending on pH*

	Formula	Concentration (wt%)		Atomic weight (g/mol)	Amount of material (mmol)	Ratio
pH 4	Al	5.98	(±0.33)	26.98	2.22	1.00
	Si	8.27	(±0.43)	28.09	2.94	1.33
	Na	0.56	(±0.12)	22.99	0.24	0.11
	Sr	5.11	(±0.05)	87.62	0.58	0.26
	Fe	80.00	(±0.60)	55.85	14.32	6.46
pH 7	Al	5.08	(±0.30)	26.98	1.88	1.00
	Si	8.74	(±0.42)	28.09	3.11	1.65
	Na	1.16	(±0.16)	22.99	0.50	0.27
	Sr	12.90	(±0.06)	87.62	1.47	0.78
	Fe	72.10	(±0.54)	55.85	12.91	6.86
pH 10	Al	4.77	(±0.28)	26.98	1.77	1.00
	Si	7.80	(±0.41)	28.09	2.78	1.57
	Na	1.12	(±0.16)	22.99	0.49	0.28
	Sr	14.85	(±0.06)	87.62	1.69	0.96
	Fe	70.95	(±0.56)	55.85	12.70	7.19

Table 9.6 Elemental compositions of $Co_{0.3}Fe_{2.7}/O_4/SiO_2$/zeolite A after Sr adsorptions depending on pH *(the ratio of Co and Fe are highlighted in yellow).*

	Formula	Concentration (wt%)		Amount of material (mmol)	Ratio
pH 4	Al	7.42	(±0.30)	2.75	1.00
	Si	9.00	(±0.36)	3.20	1.17
	Na	0.62	(±0.10)	0.27	0.10
	Sr	5.22	(±0.05)	0.60	0.22
	Fe	60.65	(±0.42)	10.86	3.80
	Co	16.85	(±0.18)	2.86	1.00
pH 7	Al	3.10	(±0.22)	1.15	1.00
	Si	4.53	(±0.30)	1.61	1.40
	Na	0.81	(±0.13)	0.35	0.31
	Sr	9.51	(±0.06)	1.09	0.95
	Fe	62.40	(±0.51)	11.17	3.41
	Co	19.30	(±0.22)	3.28	1.00
pH 10	Al	4.47	(±0.29)	1.66	1.00
	Si	6.66	(±0.39)	2.37	1.43
	Na	1.07	(±0.17)	0.46	0.28
	Sr	12.43	(±0.06)	1.42	0.86
	Fe	56.30	(±0.51)	10.08	3.20
	Co	18.55	(±0.24)	3.15	1.00

Table 9.7 *Elemental compositions of zeolite X after Sr adsorptions depending on pH*

	Formula	Concentration (wt%)		Amount of material (mmol)	Ratio
pH 4	Al	28.45	(±1.15)	10.54	1.00
	Si	40.90	(±1.55)	14.56	1.38
	Na	2.23	(±0.37)	0.97	0.09
	Sr	28.15	(±0.23)	3.21	0.30
pH 7	Al	17.50	(±1.04)	6.49	1.00
	Si	35.40	(±1.67)	12.60	1.94
	Na	3.63	(±0.54)	1.58	0.24
	Sr	43.15	(±0.22)	4.92	0.76
pH 10	Al	18.90	(±0.95)	7.01	1.00
	Si	32.65	(±1.41)	11.62	1.66
	Na	4.61	(±0.54)	2.00	0.29
	Sr	43.80	(±0.22)	5.00	0.71

Table 9.8 *Elemental compositions of Fe_3O_4/SiO_2/zeolite X after Sr adsorptions depending on pH*

	Formula	Concentration (wt%)		Amount of material (mmol)	Ratio
pH 4	Al	5.92	60.36)	2.19	1.00
	Si	8.49	(±0.48)	3.02	1.38
	Na	1.04	(±0.17)	0.45	0.21
	Sr	1.94	(±0.02)	0.22	0.10
	Fe	80.15	(±0.67)	14.35	6.55
pH 7	Al	5.49	(±0.28)	2.03	1.00
	Si	10.93	(±0.43)	3.89	1.91
	Na	1.02	(±0.14)	0.44	0.22
	Sr	18.05	(±0.08)	2.06	1.01
	Fe	64.25	(±0.48)	11.50	5.66
pH 10	Al	5.92	(±0.31)	2.19	1.00
	Si	10.38	(±0.45)	3.69	1.68
	Na	1.46	(±0.18)	0.64	0.29
	Sr	17.30	(±0.08)	1.97	0.90
	Fe	65.00	(±0.51)	11.64	5.31

Table 9.9 *Elemental compositions of $Co_{0.3}Fe_{2.7}/O_4/SiO_2$/zeolite X after Sr adsorptions depending on pH (the ratio of Co and Fe are highlighted in yellow).*

	Formula	Concentration (wt%)		Atomic weight (g/mol)	Amount of material (mmol)	Ratio
pH 4	Al	6.67	(±0.36)	26.98	2.47	1.00
	Si	10.44	(±0.50)	28.09	3.72	1.50
	Na	0.92	(±0.15)	22.99	0.40	0.16
	Sr	3.18	(±0.04)	87.62	0.36	0.15
	Fe	59.95	(±0.54)	55.85	10.73	3.82
	Co	16.55	(±0.23)	58.93	2.81	1.00
pH 7	Al	0.32	(±0.32)	26.98	0.12	1.00
	Si	0.47	(±0.47)	28.09	0.17	1.42
	Na	0.15	(±0.15)	22.99	0.06	0.55
	Sr	0.08	(±0.08)	87.62	0.01	0.08
	Fe	0.44	(±0.44)	55.85	0.08	2.22
	Co	0.21	(±0.21)	58.93	0.04	1.00
pH 10	Al	5.89	(±0.36)	26.98	2.18	1.00
	Si	10.85	(±0.55)	28.09	3.86	1.77
	Na	1.53	(±0.22)	22.99	0.67	0.31
	Sr	14.20	(±0.07)	87.62	1.62	0.74
	Fe	51.40	(±0.54)	55.85	9.20	3.45
	Co	15.70	(±0.24)	58.93	2.66	1.00

Table 9.10 *Elemental compositions of Fe_3O_4/SiO_2/CHA-Na after Sr adsorptions depending on pH*

	Formula	Concentration (wt%)		Amount of material (mmol)	Ratio
pH 4	Al	0.98	(±0.09)	0.36	1.00
	Si	3.81	(±0.19)	1.36	3.75
	Na	0.06	(±0.02)	0.02	0.07
	K	0.00	(±0.00)	0.00	0.00
	Cs	40.55	(±1.32)	3.05	8.44
	Fe	54.50	(±0.33)	9.76	27.00
pH 7	Al	1.11	(±0.12)	0.41	1.00
	Si	4.40	(±0.26)	1.56	3.82
	Na	0.31	(±0.07)	0.13	0.33
	K	0.00	(±0.00)	0.00	0.00
	Cs	50.85	(±2.12)	3.83	9.34
	Fe	43.00	(±0.36)	7.70	18.80
pH 10	Al	1.28	(±0.13)	0.47	1.00
	Si	4.07	(±0.26)	1.45	3.07
	Na	0.80	(±0.12)	0.35	0.74
	K	0.00	(±0.00)	0.00	0.00
	Cs	35.15	(±1.58)	2.64	5.60
	Fe	58.45	(±0.45)	10.47	22.15

Table 9.11 *Elemental compositions of $Co_{0.3}Fe_{2.7}/O_4/SiO_2$/CHA-Na after Sr adsorptions depending on pH (the ratio of Co and Fe are highlighted in yellow).*

	Formula	Concentration (wt%)		Atomic weight (g/mol)	Amount of material (mmol)	Ratio
pH 4	Al	0.96	(±0.08)	26.98	0.35	1.00
	Si	3.40	(±0.18)	28.09	1.21	3.41
	Na	0.07	(±0.02)	22.99	0.03	0.09
	K	0.00	(±0.00)	39.10	0.00	0.00
	Cs	36.90	(±1.29)	132.91	2.78	7.84
	Fe	43.70	(±0.29)	55.85	7.82	3.11
	Co	14.85	(±0.14)	58.93	2.52	1.00
pH 7	Al	1.07	(±0.10)	26.98	0.40	1.00
	Si	4.16	(±0.23)	28.09	1.48	3.73
	Na	0.00	(±0.00)	22.99	0.00	0.00
	K	0.00	(±0.00)	39.10	0.00	0.00
	Cs	37.35	(±1.56)	132.91	2.81	7.09
	Fe	41.35	(±0.33)	55.85	7.40	2.79
	Co	15.65	(±0.17)	58.93	2.66	1.00
pH 10	Al	1.32	(±0.14)	26.98	0.49	1.00
	Si	4.64	(±0.29)	28.09	1.65	3.39
	Na	0.36	(±0.09)	22.99	0.15	0.32
	K	0.34	(±0.06)	39.10	0.09	0.18
	Cs	47.80	(±2.19)	132.91	3.60	7.38
	Fe	33.05	(±0.34)	55.85	5.92	3.00
	Co	11.63	(±0.16)	58.93	1.97	1.00

Table 9.12 *The final concentrations and standard errors of the bare CHA-Na and M_xO_y/CHA-Na for the Cs adsorption isotherm curves.*

CHA-Na (ppm)		Fe_3O_4/CHA-Na (ppm)		$CoFe_2O_4$/CHA-Na (ppm)	
160.10	(±3.05)	157.65	(±2.98)	157.11	(±3.00)
131.67	(±10.62)	131.12	(±10.62)	135.60	(±10.96)
125.63	(±0.82)	119.89	(±0.78)	118.85	(±0.79)
99.64	(±0.90)	95.10	(±0.84)	94.18	(±0.84)
72.26	(±1.16)	75.49	(±1.21)	74.00	(±1.19)
63.77	(±0.88)	58.47	(±0.79)	62.92	(±0.85)
40.15	(±0.43)	38.52	(±0.41)	39.94	(±0.42)
28.57	(±0.58)	31.05	(±0.62)	28.97	(±0.58)

Table 9.13 *The final concentrations and standard errors of the bare CHA-Na and M_xO_y/CHA-Na for the time-dependent Cs adsorption.*

Time	CHA-Na		Fe_3O_4/CHA-Na		$Co_{0.3}Fe_{2.7}O_4$/CHA-Na	
10	73.46	(±1.38)	72.64	(±1.95)	75.09	(±0.94)
30	74.03	(±1.26)	74.86	(±1.28)	76.39	(±1.13)
60	74.11	(±1.30)	74.94	(±1.19)	76.40	(±1.22)
120	74.56	(±1.34)	74.95	(±1.19)	76.51	(±1.25)
1284	74.70	(±1.37)	74.90	(±1.23)	76.73	(±1.27)

Table 9.14 *The final concentrations and standard errors of the bare CHA-Na and M_xO_y/CHA-Na for the pH-dependent Cs adsorption.*

pH	CHA-Na		Fe_3O_4/CHA-Na		$Co_{0.3}Fe_{2.7}O_4$/CHA-Na	
4.04	103.86	(±1.55)	102.02	(±1.66)	106.79	(±1.76)
6.89	92.00	(±4.77)	98.18	(±4.68)	96.62	(±4.43)
10.03	96.69	(±1.55)	90.91	(±1.61)	93.17	(±1.63)

Table 9.15 *The final concentrations and standard errors of the bare zeolite A and M_xO_y/SiO_2/zeolite A for the Sr adsorption isotherm curves.*

Zeolite A		Fe_3O_4/SiO_2/zeolite A		$Co_{0.3}Fe_{2.7}O_4/SiO_2$/zeolite A	
234.35	(±52.59)	178.57	(±47.98)	168.14	(±65.09)
199.38	(±8.44)	163.73	(±11.65)	165.55	(±9.37)
169.36	(±5.11)	152.31	(±7.20)	151.97	(±4.85)
152.78	(±21.07)	156.72	(±22.11)	154.12	(±21.92)
98.09	(±21.27)	93.12	(±20.23)	93.30	(±20.34)
86.74	(±1.79)	80.35	(±1.66)	78.89	(±1.64)
72.20	(±1.39)	69.15	(±1.33)	64.10	(±1.24)
20.73	(±4.60)	20.15	(±4.48)	19.56	(±4.35)

Table 9.16 *The final concentrations and standard errors of the bare zeolite A and M_xO_y/SiO_2/zeolite A for the time-dependent Sr adsorption.*

Time	Zeolite A		Fe_3O_4/SiO_2/Zeolite A		$Co_{0.3}Fe_{2.7}O_4/SiO_2$/Zeolite A	
10	93.72	(±1.34)	56.08	(±11.31)	72.51	(±2.59)
30	96.18	(±1.25	88.39	(±1.83)	81.84	(±4.35)
60	96.18	(±1.25)	94.74	(±1.35)	91.00	(±2.15)
120	96.17	(±1.25)	96.41	(±1.44)	94.83	(±1.29)
1284	96.18	(±1.25)	96.91	(±1.27)	95.91	(±1.25)

Table 9.17 *The final concentrations and standard errors of the bare zeolite A and M_xO_y/SiO_2/zeolite A for the pH-dependent Sr adsorption.*

pH	Zeolite A		Fe_3O_4/SiO_2/zeolite A		$Co_{0.3}Fe_{2.7}O_4/SiO_2$/zeolite A	
4.06	35.59	(±6.72)	42.07	(±6.10)	29.92	(±6.03)
7.00	122.58	(±3.99)	110.74	(±4.28)	100.15	(±4.88)
9.96	109.43	(±3.29)	111.81	(±3.45)	108.72	(±3.34)

Table 9.18 *The final concentrations and standard errors of the bare zeolite X and M_xO_y/SiO_2/zeolite X for the Sr adsorption isotherm curves.*

Zeolite X		Fe_3O_4/SiO_2/zeolite X		$CoFe_2O_4/SiO_2$/zeolite X	
151.66	(±5.33)	108.36	(±5.42)	114.92	(±5.42)
154.83	(±5.03)	129.75	(±6.13)	124.21	(±6.13)
139.82	(±3.99)	125.22	(±3.92)	129.61	(±3.92)
114.57	(±3.69)	119.35	(±4.16)	118.58	(±4.16)
101.41	(±3.13)	104.14	(±3.23)	101.64	(±3.23)
86.55	(±2.38)	88.66	(±2.46)	87.16	(±2.46)
79.96	(±8.19)	74.47	(±7.63)	79.65	(±7.63)
32.35	(±0.82)	31.15	(±0.79)	30.74	(±0.79)

Table 9.19 *The final concentrations and standard errors of the bare zeolite X and M_xO_y/SiO_2/zeolite X for the time-dependent Sr adsorption.*

Time	Zeolite X		Fe_3O_4/SiO_2/Zeolite X		$Co_{0.3}Fe_{2.7}O_4/SiO_2$/Zeolite X	
10	84.17	(±2.69)	78.10	(±2.93)	79.12	(±3.39)
30	85.28	(±2.65)	83.37	(±3.15)	84.03	(±2.79)
60	85.28	(±2.65)	86.07	(±2.76)	85.86	(±2.91)
120	85.62	(±2.64)	87.23	(±2.74)	86.43	(±2.70)
1481	85.59	(±2.65)	87.43	(±2.72)	86.84	(±2.69)

Table 9.20 *The final concentrations and standard errors of the bare zeolite X and M_xO_y/SiO_2/zeolite X for the pH-dependent Sr adsorption.*

pH	Zeolite X		Fe_3O_4/SiO_2/zeolite X		$Co_{0.3}Fe_{2.7}O_4/SiO_2$/zeolite X	
4.06	44.43	(±5.45)	19.45	(±7.33)	26.76	(±6.12)
7.00	124.80	(±4.22)	111.16	(±4.56)	107.17	(±4.78)
9.96	109.43	(±3.42)	103.16	(±3.38)	107.84	(±3.75)

Table 9.21 *The final concentrations and standard errors of the bare CHA-Na and M_xO_y/SiO_2/CHA-Na for the Cs adsorption isotherm curves.*

CHA-Na		Fe_3O_4/SiO_2/CHA-Na		$Co_{0.3}Fe_{2.7}O_4/SiO_2$/CHA-Na	
160.10	(±3.05)	176.71	(±2.52)	152.85	(±2.62)
131.67	(±10.62)	160.05	(±3.86)	159.92	(±3.81)
125.63	(±0.82)	145.46	(±1.46)	147.65	(±1.49)
99.64	(±0.90)	112.70	(±1.52)	108.97	(±1.48)
72.26	(±1.16)	88.57	(±1.04)	89.97	(±1.09)
63.77	(±0.88)	71.24	(±1.01)	65.83	(±0.93)
40.15	(±0.43)	40.81	(±0.82)	39.08	(±0.79)
28.57	(±0.58)	29.23	(±0.49)	31.16	(±0.52)

Table 9.22 *The final concentrations and standard errors of the bare CHA-Na and M_xO_y/SiO_2/CHA-Na for the time-dependent Cs adsorption.*

Time	CHA-Na		Fe_3O_4/SiO_2/CHA- Na		$Co_{0.3}Fe_{2.7}O_4/SiO_2$/CHA-Na	
10	83.55	(±1.18)	87.46	(±1.16)	86.13	(±1.14)
30	86.38	(±1.14)	87.47	(±1.20)	86.22	(±1.13)
60	86.41	(±1.14)	87.58	(±1.16)	86.24	(±1.14)
120	86.63	(±1.14)	85.84	(±1.16)	86.32	(±1.15)
1284	86.81	(±1.14)	87.63	(±1.15)	86.30	(±1.14)

Table 9.23 *The final concentrations and standard errors of the bare CHA-Na and M_xO_y/SiO_2/CHA-Na for the pH-dependent Cs adsorption.*

pH	CHA-Na		Fe_3O_4/SiO_2/CHA-Na		$Co_{0.3}Fe_{2.7}O_4/SiO_2$/CHA-Na	
4.04	103.86	(±2.79)	100.27	(±2.12)	96.77	(±2.38)
6.89	92.00	(±6.95)	95.86	(±6.66)	92.95	(±6.42)
10.03	96.69	(±1.16)	85.46	(±1.27)	94.39	(±1.23)